Non-equilibrium strongly-correlated quantum dynamics in photonic resonator arrays



Thomas Grujic

Balliol College, Oxford

A thesis submitted to the Mathematical and Physical Sciences Division for the degree of Doctor of Philosophy in the University of Oxford

Michaelmas Term, 2013

Atomic and Laser Physics,

University of Oxford

Non-equilibrium strongly-correlated quantum dynamics in photonic resonator arrays

Thomas Grujic, Balliol College, Oxford

Hilary Term 2013

Abstract

Strong effective photon-photon interactions mediated by atom-photon couplings have been routinely achievable in QED setups for some time now. Recently, there have been several proposals to push the physics of interacting photons into many-body distributed architectures. The essential idea is to coherently couple together arrays of QED resonators, such that photons can hop between resonators while interacting with each other inside each resonator. These proposed structures have attracted intense theoretical attention while simultaneously inspiring experimental efforts to realise this novel regime of strongly-correlated many-body states of light. A central challenge of both theoretical and practical importance is to understand the physics of such coupled resonator arrays (CRAs) beyond equilibrium, when unavoidable (or sometimes even desired) photon loss processes are accounted for.

This thesis presents several studies whose purpose can roughly be divided in two aims. The first part studies just what constitutes a valid physical and computational representation of non-equilibrium driven-dissipative CRAs. Addressing these questions constitutes essential groundwork for further investigations of CRA phenomena, as numerical experiments are likely to guide and interpret near-future experimental array observations. The relatively small body of existing work on CRAs out of equilibrium has often truncated their full, rich physics. It is important to establish the effects and validity of these approximations. To this end we introduce powerful numerical algorithms capable of efficiently simulating the full dynamics of CRAs, and use them to characterise the non-equilibrium steady states of arrays reached under the combined influence of dissipation and pumping.

Having established the rigour necessary to realistically describe CRAs, we examine two novel phenomena observable in near-future small arrays. Firstly we relate a counter-intuitive 'super bunching' in the statistics of photons emitted from arrays engineered to demonstrate strong effective photon-photon repulsion at the single and two-photon level, to an interplay between the underlying eigen-structure and details of the non-equilibrium operation. Secondly we characterise a dynamical phenomenon in which domains of 'frozen' photons remain trapped in sufficiently nonlinear arrays. Finally we present a preliminary characterisation of a previously unexplored phase diagram of arrays under coherent two-photon pumping. Competition between the coherence injected by the pumping, photon interactions and delocalisation processes lead to interesting new physical signatures.

Acknowledgements

First thanks go to my supervisor Prof. Dieter Jaksch, who allowed me great flexibility and self-direction in my PhD work, for which I am very grateful. I often learnt more from five minutes speaking with him than from a week of reading papers – his crystal clear feedback and insight was always deeply considered and constructive.

Dr. Stephen Clark, pillar of the group, has helped me enormously in the past years, having seemingly inexhaustible patience and generosity with his time. He has assisted me at every stage of my work, always taking the time to understand my questions even when they were very naive and I'm sure he had better things to do!

I'd like to thank Prof. Dimitris Angelakis, who helped initiate the field of coupled quantum resonator arrays that is the central theme of this thesis. Dimitris invited me numerous times to the Center for Quantum Technologies in Singapore, which was always great fun.

Though our joint work does not appear in this thesis, I very much enjoyed working with Juan Jose Mendoza Arenas, who helped out with the writing of this thesis through his very thorough knowledge of matrix product state calculations.

I'm incredibly grateful for the Clarendon Scholarship which allowed me to study at Oxford in the first place.

Thomas Grujic, Balliol College, 2013

Contents

Abstract i

Acknowledgements ii

List of Figures xiii

Chapter 1. Introduction 1

1.1 Background and motivation 1

1.2 Brief review of cavity QED 5

1.2.1 Modes of a simple optical resonator 6

1.2.2 Quantised oscillator - photons 7

1.2.3 Two-level systems 8

1.2.4 The Jaynes-Cummings interaction and photon blockade . 8

1.3 Coupled resonator arrays (CRAs) – the Jaynes-Cummings-Hubbard model 12

1.4 Survey of existing work on CRAs 17

1.4.1 CRAs as quantum simulators 17

1.4.2 Equilibrium physics – a novel phase diagram 18

1.4.3 Beyond equilibrium 19

1.5 Candidate architectures for realising CRAs 21

1.6 Thesis overview 29
1.7 Contribution and publications 31

Chapter 2. Simulating large lossy arrays 33

2.1 Lindblad master equations 35
2.2 Solving master equations 35
2.2.1 Exact diagonalisation 36
2.2.2 Numerically exact time evolution 36
2.2.3 Quantum trajectories 37
2.2.4 Trajectory Algorithm 37
2.2.5 Equivalence of the trajectory approach and master equation simulation 39
2.2.6 Calculation of steady state observables 41
2.3 Matrix product states (MPS) 42
2.3.1 The time evolving block decimation (TEBD) method . . . 45
2.4 Trajectory simulations with MPS 46
2.5 Matrix product operators (MPOs) - Mixed states and TEBD master equation simulation 46
2.6 Describing infinite systems 50

Chapter 3. Describing coupled resonator arrays 53

3.1 The system 55
3.1.1 Local description 57
3.1.2 Comparing Kerr and Jaynes-Cummings nonlinearities . . 59
3.1.3 Coupled nonlinear resonators 60
3.1.4 Driving and losses 60
3.2 Single resonator steady states: Kerr versus Jaynes-Cummings nonlinearities 63

3.2.1 The photonic limit of the Jaynes-Cummings model 66
3.2.2 The atomic limit of the Jaynes-Cummings model 67
3.3 Many-body signatures in steady state observables 68
3.4 Larger resonator arrays 72
3.5 The strong nonlinearity limit: fermionization and crystallization of photons in CRAs 74
3.5.1 Fermionization in coupled resonator arrays 74
3.5.2 Polariton crystallization 77
3.6 Discussion 79

Chapter 4. Robustness of bistabilities in driven photonic resonator arrays 83

4.1 Model 86
4.2 Semi-classical approximation 87
4.3 Mean field 89
4.4 Fully quantum model 93
4.5 A quantum trajectory treatment 97
4.6 Conclusions 100

Chapter 5. Repulsively induced photon super-bunching in driven resonator arrays 103

5.1 System 105
5.2 Two-resonator 'dimer' 106
5.3 Bunching in larger systems 114
5.4 Photon statistics in Jaynes-Cummings arrays 115
5.5 Discussion 117

Chapter 6. Frozen photons in Jaynes Cummings arrays 119

6.1 System 120
6.2 Photon localisation under a semi-classical treatment 122
6.3 The fully quantum regime 124
6.4 Probing the frozen dynamics in an experiment 127
6.5 Discussion 129

Chapter 7. Parametrically pumped resonator arrays 131

7.1 Examples of topological signatures in the extended Bose-Hubbard model 134
7.1.1 Non-local order and ground state phases 134
7.1.2 Entanglement spectra 137
7.2 Infinite parametrically driven arrays 138
7.2.1 Limits of the model 138
7.3 Finite systems 142
7.3.1 Hardcore limit - Kitaev model and topological behaviour . 143
7.3.2 Relaxing the hardcore constraint 146
7.4 Discussion 147

Chapter 8. Conclusions 149

8.1 Summary of results 149
8.2 Future prospects 151

Appendix A. Derivation of the Lindblad quantum master equation 155

A.0.1 The Lindblad form of the master equation 156
A.0.2 Evolution of the system density operator 157

Appendix B. Matrix product states 165

B.1 Entanglement properties of 1D quantum systems 165
B.1.1 Schmidt decompositions 165

B.1.2 Entanglement spectra 166
B.2 Operations with matrix product states 167
B.3 Time evolving matrix product states 171
B.3.1 The Suzuki-Trotter approximation 171
B.3.2 The TEBD algorithm 174

Appendix C. Exact diagonalisation notes **175**

C.0.3 Set-up 175
C.0.4 N-excitation sector 178
C.0.5 Permutationally invariant subsystems 179
C.0.6 Constructing the Liouvillian directly in the shrunken basis 181

Appendix D. Example trajectory code **183**

Bibliography **191**

List of Figures

1.1 Schematic of idealised resonator array . . . 3
1.2 The Jaynes-Cummings model . . . 10
1.3 Ground state phase diagrams for the Jaynes-Cummings-Hubbard and Bose-Hubbard models . . . 15
1.4 Schematic of a coupled resonator array as realised in a photonic crystal architecture . . . 23
1.5 Schematic of a coupled resonator array as realised in an etched optical waveguide system . . . 25
1.6 Schematic of a coupled resonator array as realised in a superconducting cQED geometry . . . 27

2.1 Sample quantum trajectories for two simple systems . . . 39
2.2 Illustration of the stochastic quantum trajectory averaging procedure 40
2.3 Elementary matrix-vector operation in our graphical language . . . 43
2.4 Graphical representation of the matrix product state (MPS) ansatz and MPS manipulations . . . 44
2.5 Graphical representation of the quantum trajectory matrix product state (MPS) algorithm . . . 47
2.6 Calculating expectation values with an MPO . . . 48
2.7 Graphical representation of an infinite matrix product state and associated manipulations . . . 51

3.1 Comparison of low-lying eigenstructure of the Jaynes-Cummings and Kerr-type interactions . . . 56
3.2 Comparison of steady-state observables for single resonators described by Jaynes-Cummings and Kerr-type nonlinearities . . . 65
3.3 Polaritonic level structure in 'atomic limit' . . . 68
3.4 Comparison of steady-state observables for small resonator arrays described by Jaynes-Cummings and Kerr-type nonlinearities . . . 70
3.5 Comparison of steady state resonator excitation for mesoscopic driven arrays described by both the Jaynes-Cummings-Hubbard and Bose-Hubbard Hamiltonians . . . 73
3.6 Comparison of 'fermionised photon' spectra for the two models in the strongly interacting regime . . . 80
3.7 Steady state 'crystallised photon' density-density correlations for 16-site arrays described by the two models . . . 81

4.1 Schematics of arrays at different levels of approximation 85
4.2 Stability regions for the semi-classical treatment of the spin model . . 88
4.3 Stability regions for the mean-field treatment of the spin model . . . 93
4.4 Analysis of steady states and their stability for the mean-field model . 94
4.5 TEBD results for steady state spectra of spin systems for increasing size 96
4.6 TEBD results for steady state spectra of spin systems for increasing MPS parameter χ 97
4.7 Comparison of TEBD master equation and quantum trajectory results for the spin system 99

5.1 Schematics of driven-dissipative Bose-Hubbard and Jaynes-Cummings-Hubbard resonator arrays. Illustration of the driving scheme for Chapter 5 104
5.2 'Phase diagram' of emitted photon statistics for a Bose-Hubbard dimer as a function of resonator coupling and nonlinearity 108
5.3 Spectral function of a driven two-site 'dimer' showing the relevant transitions in the system 113
5.4 Evolution of steady state photon statistics for increasing system size. 115
5.5 Quantum trajectory results for steady state photon statistics for larger systems 116
5.6 'Phase diagram' of emitted photon statistics for a Jaynes-Cummings-Hubbard dimer as a function of resonator coupling and nonlinearity. 117

6.1 Schematic of the system and initial conditions considered in Chapter 6 121
6.2 Semi-classical prediction of a localized-delocalized photon transition. 124
6.3 Rigorous quantum simulation of the time evolution of photon domains at weak and strong nonlinearities 125
6.4 An exploration of the localisation-delocalisation transition for different system sizes and initial excitation. 126
6.5 Projection of the initial array state into the system eigenbasis for different initial excitations. 128
6.6 Comparison of localisation-delocalisation transition for lossless and lossy arrays. 130

7.1 Schematic of parametric pumping in resonator arrays. 132
7.2 Ground state phase diagram of the extended Bose-Hubbard model . . 135
7.3 Typical configurations of Haldane and Mott insulating ground states of the extended Bose-Hubbard model 136
7.4 Ground state quantities calculated along a cut in Fig. 7.2 137
7.5 Comparison of Bose-Hubbard mean field ground state phase diagrams for different units 139
7.6 Ground state observables for the hardcore limit of the parametrically driven model 140
7.7 Rigorous ground state phase diagram of the Bose-Hubbard model . . 142

7.8 Ground state observables along a cut in Fig. 7.7 143

7.9 Investigation of parametric driving effects on the ground state Bose-Hubbard phase diagram 144

7.10 Two types of pairing in the Kitaev model 145

7.11 Spectral gaps for finite Tonks gas systems 145

7.12 Entanglement and eigenvalue spectral gaps for finite Tonks gas systems 146

7.13 Entanglement spectral gap for finite systems with finite nonlinearities 147

A.1 Representation of the interaction between a quantum system and its environment 156

B.1 Schematic illustration of the full density matrix as an outer product of matrix product states 169

B.2 Illustration of the calculation of two-site correlators in the MPS formalism 169

B.3 Application of a two-site gate on a matrix product state 170

B.4 Simplified schematic of a TEBD simulation time-step 172

Chapter 1

Introduction

This thesis is concerned with the non-equilibrium quantum physics of strongly correlated photons in coupled resonator arrays (CRAs). In this first chapter, we motivate the study and experimental realisation of such strongly interacting photonic systems. We briefly introduce the essential concepts and review the major strands of research in this relatively youthful field. The importance of including photon loss processes in the description of these devices is stressed. Lossy arrays must of course be driven in order to maintain a non-trivial array state. Realistic descriptions of CRAs are therefore fundamentally non-equilibrium in nature, as we discuss. Candidate systems for realising strongly interacting photonic gases in CRAs are presented, and their relative merits contrasted. The chapter concludes with a summary of the rest of the thesis.

1.1 Background and motivation

Understanding strongly-correlated many-particle quantum systems remains one of the key challenges of quantum physics today. Such many-body systems are of great interest in solid-state materials, where strong local electronic correlations are fundamental to phenomena such as high temperature superconductivity [1] and the

fractional quantum Hall effect [2]. Experimental observation of microscopic properties of strongly-correlated condensed matter systems is difficult because of the short length- and time-scales involved. Meanwhile on the theoretical side, even simplified models capturing the essential details of these correlations remain extremely difficult to treat analytically or numerically.

Another route towards studying strongly correlated systems which has been met with considerable success in recent years is to artificially construct quantum systems capable of simulating the physics of interest in the original systems [3]. Such fabricated quantum simulators are easier to manipulate experimentally than the original simulated system. This allows reconstruction of the original system's properties in regions of parameter space which are inaccessible to experimental observation of the simulated system.

The first systems acting in a quantum simulation capacity were arrays of Josephson junctions [4, 5, 6] emulating properties of interacting bosons. Further progress followed with cold atoms in optical lattices [7], the physics of which can be neatly described by the Bose-Hubbard Hamiltonian [8]. Early famous optical lattice experiments demonstrated clear simulation of the superfluid-Mott insulating quantum phase transition [9] and the realisation of a Tonks-Girardeau gas [10].

Coupled resonator arrays, the central system of interest in this thesis, were originally proposed as a new direction in the field of quantum simulation. The essential idea is to couple together many confining photonic resonators, each with an associated element (such as an atom) coupling to the resonator field generating effective photon nonlinearities at the single-quantum level [11, 12, 13, 14, 15]. An illustrative sketch is provided in Fig. 1.1. The combination of photon tunnelling between resonators, and effective local repulsion leads to the idea of novel quantum 'fluids' of light [16] delocalised over the structure. Interactions between single photons may be large enough to induce sizeable correlations in such fluids. The ability to tune

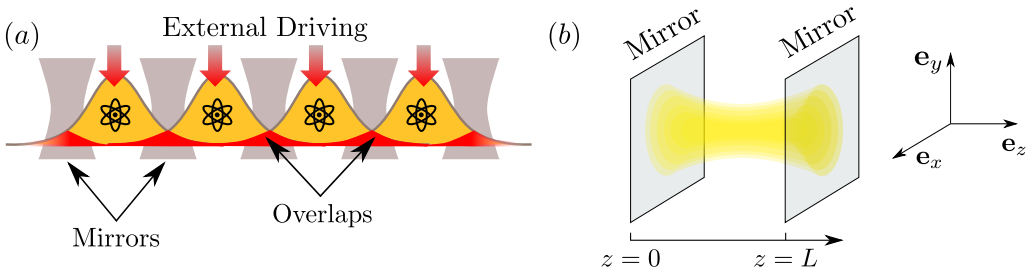


Figure 1.1. (a) Schematic of an idealised coupled resonator array. Partially transmitting mirrors lead to localised modes with significant modal overlap (red) between neighbouring resonators enabling coherent photon tunnelling. The presence of elements coupling to the optical fields, such as an atom or multiple atoms in each resonator, may lead to nonlinearities at the two-photon level. CRAs are additionally open to external driving and monitoring at the single resonator level. (b) Schematic of a single idealised optical resonator, consisting of two perfectly conducting (reflecting) mirrors along the z-axis separated by a distance L.

the magnitude of interactions and possibly also the resonator coupling amplitudes raises the intriguing possibility of using coupled resonator arrays as photonic quantum simulators of quantum lattice models. Potential implementations of these platforms offer attractive features for the initialisation, manipulation, and measurement of exotic quantum states of light. Adjacent photon resonators may be separated by lengths on the order of μm – mm, depending on the implementation details. This allows 'sites' to be resolved relatively easily, so that quantum states may be prepared locally and expectation values could be measured directly on the light emitted from a single resonator. As the elementary excitations are partly photonic in nature, quantum states may be initialised via external lasers capable of resolving individual resonators. This is in contrast to, for example, quantum simulation schemes based on cold atoms in optical lattices, where single-site resolution has only recently been demonstrated [17, 18] and the initial loading of atoms is a complex, if well established process.

Despite this potential advantage over optical lattice setups, it is anticipated that the scalability and absence of imperfections afforded by optical lattice simulation

schemes will be difficult to match in CRAs. Some amount of disorder in any fabrication process is inevitable. We also note that at the time of writing, CRAs have not been demonstrated experimentally, though promising efforts are underway, as we briefly review in Section 1.5.

The first generation of works concerning CRAs drew heavily on analogies with equilibrium physics and quantum simulation schemes in the more established field of optical lattices. These studies ignored for the most part perhaps the main qualitative difference between these two classes of system – the unavoidable presence of photon loss. Loss processes were initially treated as merely a hindrance, limiting the available time for observing coherent quantum dynamics. However, near-future photonic devices will necessarily operate under driven-dissipative conditions on account of unavoidable photon loss. Rather than being seen as a problem, the naturally open nature of CRAs and the inherent ability to address and observe single resonators from the side (or infer photonic statistics by measurements on the atom) make these systems ideal platforms for the exploration of novel non-equilibrium many-body photonic effects. Non-equilibrium quantum processes are notoriously difficult to treat theoretically, as equilibrium principles of detailed balance no longer hold [19] Very recently however, impressive analytic progress has been made in the particular case of boundary-driven spin chains [20, 21, 22, 23, 24, 25, 26], which in many ways are quantum analogs of the totally asymmetric exclusion process (TASEP) [27, 28], a canonical model for 1D non equilibrium transport processes. Much of this thesis is devoted to CRA dynamics in the strongly non-equilibrium regime, where driving and losses are non-perturbative competing processes determining array properties.

CRAs are in many ways perfectly poised to play an important role in the exploration of driven-dissipative quantum systems, as they lie at the fruitful confluence of non-equilibrium statistical mechanics, quantum optics and condensed matter physics. Many ideas from condensed matter physics, where the assumption of infi-

nite systems is usually valid, are finding novel application in CRA structures, as new fabrication techniques allow traditional QED devices to enter the meso- or perhaps even macroscopic regime. Conversely, it is hoped that CRA devices acting in a quantum simulation capacity may shed new light on difficult problems in conventional condensed matter physics.

1.2 Brief review of cavity QED

Much of the promise of CRAs builds on the spectacular advances in the isolation and manipulation of both real and artificial atoms over the last decades. Recently, experimental progress has allowed access to the deeply quantum regime where coupling between single photons and atoms is observable. Clear experimental signatures of these quantum optical phenomena require operating in the strong coupling regime, where the coupling between confined light fields and atomic transitions is substantially larger than relevant photon loss and decoherence rates. Such conditions have been attainable in quantum electrodynamics (QED) setups for some years now [29]. This opened the possibility of engineering strong effective photon-photon interactions, mediated by single atomistic emitters.

In this section we give a concise review of the fundamental ingredients in cavity QED relevant to this thesis, following the approach of [30]. Specifically, we begin by deriving the allowed optical modes of a simplified resonator. We then outline the quantisation procedure for these modes. Next, introducing a two-level quantum system into the resonator, we show how the resonator-TLS interaction naturally gives rise to the Jaynes-Cummings-Hamiltonian so ubiquitous in quantum optics contexts and central to this thesis.

1.2.1 Modes of a simple optical resonator

Figure 1.1 (b) shows an idealised optical resonator consisting of two parallel, perfectly reflecting (conducting) mirrors lying in the (x, y) plane at $z = 0$ and $z = L$. We take the electric $\mathbf{E}$ field to be polarised along the x-axis such that $\mathbf{E}(\mathbf{r}, t) = \mathbf{e}_x E_x(z, t)$. The forms of the permissible electric field solutions inside the resonator follow from Maxwell's source-free equations [31], together with the boundary conditions that the electric field vanish at the mirrors. We obtain discrete electric field solutions indexed by m, and a magnetic field polarised along the y-axis, $\mathbf{B}(\mathbf{r}, t) = \mathbf{e}_y B_y(z, t)$:

$$E_x^{(m)}(z,t) = E_0 \sin(\omega_m t)\sin(k_m z) \tag{1.1}$$

$$B_y^{(m)}(z,t) = \left(\frac{E_0}{c}\right)\cos(\omega_m t)\cos(kz) = B_0\cos(\omega_m t)\cos(kz), \tag{1.2}$$

where $k_m = m\pi/L$ for integer $m > 0$ and $\omega_m = ck_m$. The classical field energy $E^{(m)}$ of each resonator mode m is then obtained as an integral of the electric and magnetic local energy densities $u_E = \frac{1}{2}\epsilon_0|\mathbf{E}|^2$, $u_B = \frac{1}{2\mu_0}|\mathbf{B}|^2$ over the resonator volume:

$$\begin{aligned} E^{(m)} &= \frac{1}{2}\int dV \left[\epsilon_0 |E_x^{(m)}|^2(z,t) + \frac{1}{\mu_0}|B_y^{(m)}|^2(z,t)\right] \\ &= \frac{V}{4}\epsilon_0 E_0^2\left(\sin^2(\omega_m t) + \cos^2(\omega_m t)\right). \end{aligned} \tag{1.3}$$

Here V is the volume of the resonator. Defining the new co-ordinates

$$q^{(m)}(t) = \sqrt{\frac{\epsilon_0 V}{2\omega_m^2}} E_0 \sin(\omega_m t) \tag{1.4}$$

$$p^{(m)}(t) = \sqrt{\frac{V}{2\mu_0}} B_0 \cos(\omega_m t) = \sqrt{\frac{\epsilon_0 V}{2}} E_0 \cos(\omega_m t), \tag{1.5}$$

the electromagnetic energy for mode m takes the form $E^{(m)} = \frac{1}{2}\left[(p^{(m)})^2 + \omega_m^2 (q^{(m)})^2\right]$, mathematically identical to the energy of a simple harmonic oscillator, where p and q respectively play the roles of a momentum and position. From now we consider only one mode, which in these introductory sections we take to be the lowest lying one corresponding to $m = 1$, and drop the sub- and super-scripts referring to the mode index m. We assume that the energy spacing between this and higher-lying modes is sufficiently large that the lowest-lying mode is effectively isolated from the others.

1.2.2 Quantised oscillator - photons

Quantising the modes of this electromagnetic resonator proceeds by promoting the coordinate $q(t)$ and momentum $p(t)$ to the status of quantum mechanical operators, yielding the Hamiltonian $\hat{H}_{\rm res} = \frac{1}{2}(\hat{p}^2 + \omega^2 \hat{q}^2)$. The operators $\hat{q}$ and $\hat{p}$ obey the canonical commutation relation $[\hat{q}, \hat{p}] = i\hbar\hat{1}$. It is useful to introduce the operators

$$\hat{a} = \frac{\omega\hat{q} + i\hat{p}}{\sqrt{2\hbar\omega}} \tag{1.6}$$

$$\hat{a}^\dagger = \frac{\omega\hat{q} - i\hat{p}}{\sqrt{2\hbar\omega}}, \tag{1.7}$$

with commutation relation $[\hat{a}, \hat{a}^\dagger] = \hat{1}$ following from the underlying commutation relation of $\hat{p}$ and $\hat{q}$. The mode Hamiltonian can now be written in the form $\hat{H}_{\rm res} = \hbar\omega\left(\hat{a}^\dagger\hat{a} + \frac{1}{2}\right)$, and the electric field is expressed as $E_x(z,t) = E_0(\hat{a} + \hat{a}^\dagger)\sin(kz)$.

The properties of $\hat{H}_{\rm res}$ follow from the commutation relations for $\hat{a}$ and $\hat{a}^\dagger$. We briefly state the important results here, relegating the details to appropriate quantum optics textbooks [32, 33, 34]. The number operator $\hat{n} = \hat{a}^\dagger\hat{a}$ satisfies the commutation relations $[\hat{n}, \hat{a}] = -\hat{a}$, $[\hat{n}, \hat{a}^\dagger] = \hat{a}^\dagger$, so that $\hat{a}$ and $\hat{a}^\dagger$ respectively decrease and increase the eigenvalues of $\hat{n}$ by one. There exists a lowest vacuum state $|0\rangle$

satisfying $\hat{n}|0\rangle = 0$ so that the eigenvalues of $\hat{n}$ are the integers $0, 1, 2, \ldots$. The corresponding eigenvectors are called the number, or Fock states, and satisfy $\hat{n}|n\rangle = n|n\rangle$. We have the useful relations $\hat{a}|n\rangle = \sqrt{n}|n-1\rangle$ and $\hat{a}^\dagger|n\rangle = \sqrt{n+1}|n+1\rangle$. The Fock states can be constructed from the vacuum state $|0\rangle$ by repeated application of the creation operators as $|n\rangle = \frac{1}{\sqrt{n!}}(\hat{a}^\dagger)^n|0\rangle$. The Hamiltonian can be written $\hbar\omega\left(\hat{n} + \frac{1}{2}\right)$, so that the Fock states are also energy eigenstates $\hat{H}_{\text{res}}|n\rangle = \hbar\omega_c(n + 1/2)|n\rangle$.

1.2.3 Two-level systems

We now consider the addition of a single two-level system (TLS) into the resonator. A TLS is a truncated description of a real or artificial atom, whose full quantised level structure is complicated. Often, for instance when the atom interacts with electromagnetic fields in a narrow frequency range around a transition frequency between two of its levels, the rest of the eigen-structure can be safely ignored [35]. We denote the two remaining relevant levels by $|g\rangle$ and $|e\rangle$, with corresponding energies $E_e - E_g = \omega_a > 0$. The TLS Hamiltonian $\hat{H}_{\text{TLS}}$ and dipole transition operator $\hat{\mathbf{d}} = q\hat{\mathbf{R}}$ are represented as 2×2 matrices in this space. Setting the zero of energy at the lower energy level, we have $\hat{H}_{\text{TLS}} = \omega_a\hat{\sigma}^+\hat{\sigma}^-$, where $\hat{\sigma}^+ = |e\rangle\langle g|$ and $\hat{\sigma}^- = |g\rangle\langle e|$ are raising and lowering operators between the levels. Assuming that the two levels are of opposite parity, the odd-parity dipole operator is non-diagonal, so that it can be written $\hat{\mathbf{d}} = \mathbf{d}^*\hat{\sigma}^+ + \mathbf{d}\hat{\sigma}^-$, where $\mathbf{d} = \langle e|\hat{\mathbf{d}}|g\rangle$.

1.2.4 The Jaynes-Cummings interaction and photon blockade

Considering now the interaction between the TLS (located at z inside the resonator) and field mode, the coupling is described by $\hat{H}_{\text{int}} = -\hat{\mathbf{d}} \cdot \hat{\mathbf{E}}(z, t)$. With $\hat{d} = \hat{\mathbf{d}} \cdot \mathbf{e}_x$ we

have

$$\hat{H}_{\text{int}} = -E_0(\hat{a} + \hat{a}^\dagger) \sin\left(\frac{\pi z}{L}\right) \hat{d} \tag{1.8}$$

Defining the position-dependent Jaynes-Cummings coupling strength $g(z) = -E_0 \sin\left(\frac{\pi z}{L}\right) d$, and making use of the relation $\hat{\sigma}_x = \hat{\sigma}^+ + \hat{\sigma}^-$, the interaction is expanded as

$$\begin{aligned} \hat{H}_{\text{int}} &= g(z)(\hat{\sigma}^+ + \hat{\sigma}^-)(\hat{a} + \hat{a}^\dagger) \\ &= g(z)(\hat{\sigma}^+\hat{a} + \hat{\sigma}^-\hat{a} + \hat{\sigma}^+\hat{a}^\dagger + \hat{\sigma}^-\hat{a}^\dagger) \end{aligned} \tag{1.9}$$

Ideally, the TLS is positioned at the field anti-node such that $g = g_{\max} = E_0 d$. The second and third terms in the last line of Eq. (1.9) correspond to non-excitation number conserving processes, the destruction of a resonator photon accompanied by the de-excitation of the TLS, and vice-versa. When $|\omega_c - \omega_a| \ll \omega_c$, these are highly non-resonant processes, as revealed by transforming to an interaction picture defined through the transformation $\hat{H}'_{\text{int}} = \exp(-i(\hat{H}_{\text{res}} + \hat{H}_{\text{TLS}})t)\hat{H}\exp(i(\hat{H}_{\text{res}} + \hat{H}_{\text{TLS}})t)$:

$$\hat{H}'_{\text{int}} = g\left(\hat{\sigma}^+\hat{a}e^{i(-\omega_c+\omega_a)t} + \hat{\sigma}^-\hat{a}e^{-i(\omega_c+\omega_a)t} + \hat{\sigma}^+\hat{a}^\dagger e^{i(\omega_c+\omega_a)t} + \hat{\sigma}^-\hat{a}^\dagger e^{(-i(-\omega_c+\omega_a))t}\right). \tag{1.10}$$

Performing the rotating wave approximation [35], we neglect the high-frequency terms rotating at $\omega_c + \omega_a$. Transformation back to the Schrodinger equation finally yields the standard form of the Jaynes-Cummings (JC) Hamiltonian [36, 34], originally defined in 1963 [37]:

$$\begin{aligned} \hat{\mathcal{H}}_{\text{JC}} &= \hat{H}_{\text{res}} + \hat{H}_{\text{TLS}} + \hat{H}_{\text{int}} \\ &= \omega_c\hat{a}^\dagger\hat{a} + \omega_0\hat{\sigma}^+\hat{\sigma}^- + g\left(\hat{a}^\dagger\hat{\sigma}^- + \hat{a}\hat{\sigma}^+\right). \end{aligned} \tag{1.11}$$

For decades an idealisation, recent experimental advances in the quality of optical

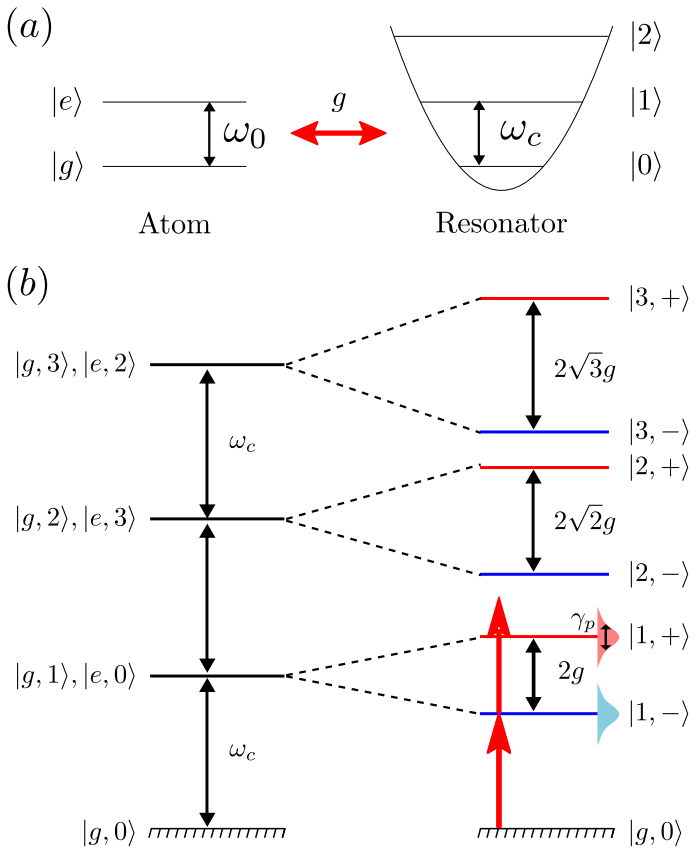


Figure 1.2. The Jaynes-Cummings model consists of a single two-level system coupled to a quantised single-mode field as represented by a harmonic oscillator. The strength of the coupling between the TLS and field is characterised by a rate g. Vertical arrows indicate that a loss of excitation in the field appears as a gain in the TLS, and vice versa. The Lorentzian shapes (not to scale) drawn on the $|1, \pm\rangle$ levels indicate the finite line width ($\approx \gamma_p$) of the JC levels induced by resonator losses.

resonators and the ability to trap and control single atomistic systems mean that the JC Hamiltonian now accurately describes physical quantum optics setups [30]. Figure 1.2 (a) shows the levels of an uncoupled TLS and resonator while Fig. 1.2 (b) shows the level scheme of the resonant ($\omega_c = \omega_0$) JC model. The more general non-resonant case is taken up in Chapter 3. The spectrum consists of an infinite series of doublets above a non-degenerate ground state. The splitting of the n-th doublet is equal to $2\sqrt{n}g$. The anharmonicity of the JC spectrum means that a pump field on resonance with, for instance, the lower state of the $n = 1$ one-excitation doublet as

shown in the figure, the closest two excitation state is then detuned by a frequency $(2-\sqrt{2})g$. If this detuning is comparable to or larger than the natural resonator line-width γ_p, a second photon is strongly inhibited from entering the resonator. This phenomenon is known as photon blockade, by analogy with the electronic Coulomb blockade [38, 39]. Photon blockade was anticipated in [40] and more fully elaborated in [41]. The blockade effect can be seen as an effective photon-photon interaction at the two-photon level. The requirement for observing strong quantum nonlinear effects is that the Jaynes-Cummings coupling parameter g be larger than the resonator loss rate γ_p. Minimising the loss rate γ_p is equivalent to producing high-quality resonators with large Q-factor (or a more convenient measure in the optical domain - the finesse [32]). The Q-factor is a measure of the confining power of a resonator, defined as the ratio of its natural frequency to its decay rate.

Clear experimental observation of the Jaynes-Cummings spectrum, as measured by the transmitted anti-bunching of an incident photon stream, was first made in a macroscopic optical cavity [29]. Slightly weaker signatures were soon after observed with a single quantum dot in a photonic crystal nanocavity [42, 43, 44]. The strongest results yet have been obtained in the microwave domain in circuit QED [45, 46] (though observing single microwave photons is certainly not trivial), as the ratio of coupling to loss g/γ_p achievable in these systems is currently at least an order of magnitude higher than in optical setups.

Though we focus on JC nonlinearities (and approximations to JC physics) to provide strong effective photon-photon interactions in this thesis, we note the existence of alternative schemes. Notably, giant photon nonlinearities have been predicted [47, 48, 49] in single mode cavities filled with an electromagnetically-induced transparency (EIT) medium [50, 51, 52], with experimental observation in [53]. Feshbach resonances [54] have also been proposed to enhance the optical nonlinearity of polaritons.

1.3 Coupled resonator arrays (CRAs) – the Jaynes-Cummings-Hubbard model

In this section we go beyond single-resonator QED physics, and introduce coupled resonator arrays (CRAs) as the central systems of interest in this thesis. We define the relevant system parameters and Hamiltonians, and additionally briefly review the equilibrium physics of these arrays, which has been well explored in the literature.

The photon blockade effect discussed in the last section is at the heart of CRAs. Many-body strongly-correlated states of light are realised by coherently coupling together multiple Jaynes-Cummings resonators into so-called coupled resonator arrays (CRAs). Extending the simple picture of a single resonator as a pair of perfect mirrors (Fig. 1.1 (b)), conceptually CRAs may be thought of as adjacent resonators sharing partially transmitting mirrors as boundaries (Fig. 1.1 (a)). The field modes of neighbouring resonators then couple, giving rise to coherent photon tunnelling processes. Assuming discrete translational invariance of the CRA with periodicity L, the tunnelling rate, or inter-resonator coupling constant J can be calculated by solving for the normalised global electric field $E(z)$ and integrating the overlap over a single resonator $J = \int_0^L E(z)E(z+L)dz$. The more general case of resonators with arbitrary geometry and refractive index profile is treated in [55].

The governing CRA Hamiltonian in many cases has come to be known as the Jaynes-Cummings-Hubbard (JCH) model. For a one-dimensional CRA with M resonators, the basic Hamiltonian is

$$\hat{H}_{\mathrm{JCH}} = \sum_{j=1}^{M} \left(\hat{a}_j^\dagger \hat{a}_j + \hat{\sigma}_j^+ \hat{\sigma}_j^- \right) + \sum_{j=1}^{M} g \left(\hat{a}_j^\dagger \hat{\sigma}_j^- + \hat{a}_j \hat{\sigma}_j^+ \right) - J \sum_{j=1}^{M-1} \left(\hat{a}_j^\dagger \hat{a}_{j+1} + h.c. \right), \quad (1.12)$$

where the subscript j refers to the j^{th} resonator in the array. The JCH Hamiltonian

describes local photon-photon interactions (second term) competing with delocalisation processes induced by the coupling (third term), giving rise to nontrivial photonic quantum states extended across these structures. Additionally in much of this thesis, we maintain external fields which coherently drive the photonic resonator fields, to combat loss processes. The addition of driving terms to the system Hamiltonian breaks number conservation, and significantly changes the physics. Full details are given in Chapter 3.

Many early works were concerned with the ground state phase diagram of the JCH model, and its departures from the well-known Bose-Hubbard (BH) Hamiltonian realised with cold atoms in optical lattices. The canonical Bose-Hubbard Hamiltonian is

$$\hat{H}_{\mathrm{BH}} = \frac{U}{2}\sum_j \hat{n}_j\left(\hat{n}_j - 1\right) - J\sum_j \left(\hat{a}_j^\dagger \hat{a}_{j+1} + h.c.\right), \tag{1.13}$$

where U is a rate controlling an interaction strength quadratic in the particle number. The BH model has also been used to approximate the full dynamics of the JCH Hamiltonian. In Chapter 3 we evaluate if this is a physically valid procedure, or if the extra degrees of freedom available in the JCH Hamiltonian lead to different features.

We now summarise the essential features of the JCH and BH phase diagrams under a mean-field treatment. Illustrating the procedure for the case of the JCH, we take the limit $M \to \infty$ and add a chemical potential (μ) term [56], which in the grand canonical statistical ensemble controls the filling of the system.

$$\hat{H}_{\mathrm{JCH}}^{\mathrm{GC}} = \hat{H}_{\mathrm{JCH}} - \mu\sum_j \left(\hat{a}_j^\dagger \hat{a}_j + \hat{\sigma}_j^+ \hat{\sigma}_j^-\right) \tag{1.14}$$

Rigorous general solution of the ground states of Hamiltonian 1.14 is far from

trivial. We may however gain appreciable physical insight into the ground state (GS) phases by making the assumption that the ground state is a translationally invariant product state $|\Psi_{\rm GS}\rangle = \prod_j \left(\sum_i c_i|i\rangle\right)$, where the c_i are amplitudes for the local basis states $|i\rangle$ (canonically a polaritonic basis for JC-type couplings, and Fock states for Bose-Hubbard models). Such a *Gutzwiller ansatz* [57] therefore treats the local physics exactly, while breaking inter-site correlations. It is known to qualitatively reproduce many important features of lattice model ground states, while failing to capture higher-order details. We take up an investigation of the validity of employing a similar ansatz in non-equilibrium settings in Chapter 4.

Making the substitution for $|\Psi_{\rm GS}\rangle$ in $\hat{H}^{\rm GC}_{\rm JCH}|\Psi_{\rm GS}\rangle = \omega|\Psi_{\rm GS}\rangle$, we find that the two-site kinetic energy terms $\hat{a}^\dagger_j\hat{a}_{j+1} + h.c.$ decouple as $\hat{a}^\dagger_j\hat{a}_{j+1} + \hat{a}_j\hat{a}^\dagger_{j+1} = \Phi\hat{a}_{j+1} + \hat{a}^\dagger_j\Phi^* - |\Phi|^2$, where $\Phi = \langle\hat{a}\rangle$. The order parameter Φ enters the theory as a mean-field describing the influence of hopping between neighbouring sites.

The decoupling leaves us with an effective Hamiltonian which is a sum of single-site mean-field Hamiltonians $\sum_j \hat{\mathcal{H}}^{\rm MF}_{\rm JCH}$, where

$$\hat{\mathcal{H}}^{\rm MF}_{\rm JCH} = \omega_c\hat{a}^\dagger\hat{a} + \omega_a\hat{\sigma}^+\hat{\sigma}^- + g\left(\hat{a}^\dagger\hat{\sigma}^- + \hat{a}\hat{\sigma}^+\right) - 2J\left(\Phi\hat{a}^\dagger + \Phi^*\hat{a} - |\Phi|^2\right) - \mu\hat{a}^\dagger\hat{a}. \quad (1.15)$$

The ground state is a site-wise product of the ground state $|\Psi_{\rm MF}(\Phi)\rangle$ of $\hat{\mathcal{H}}^{\rm MF}_{\rm JCH}$ with energy $E_{\rm MF}(\Phi)$. The ground state $|\Psi_{\rm MF}(\Phi)\rangle$ can be determined straightforwardly by numerical diagonalisation of $\hat{\mathcal{H}}_{\rm MF}$ once an appropriate photon cut-off is introduced. The value of Φ is then determined self-consistently by minimising $E_{\rm MF}(\Phi)$.

Figure. 1.3 shows the value of the order parameter Φ measured with respect to the ground states for different regions of parameter space, for both the JCH and BH Hamiltonians. Regions with $\Phi = 0$ indicate Mott phases, characterised by a fixed number of excitations per site with no fluctuations. The nature of the Mott states

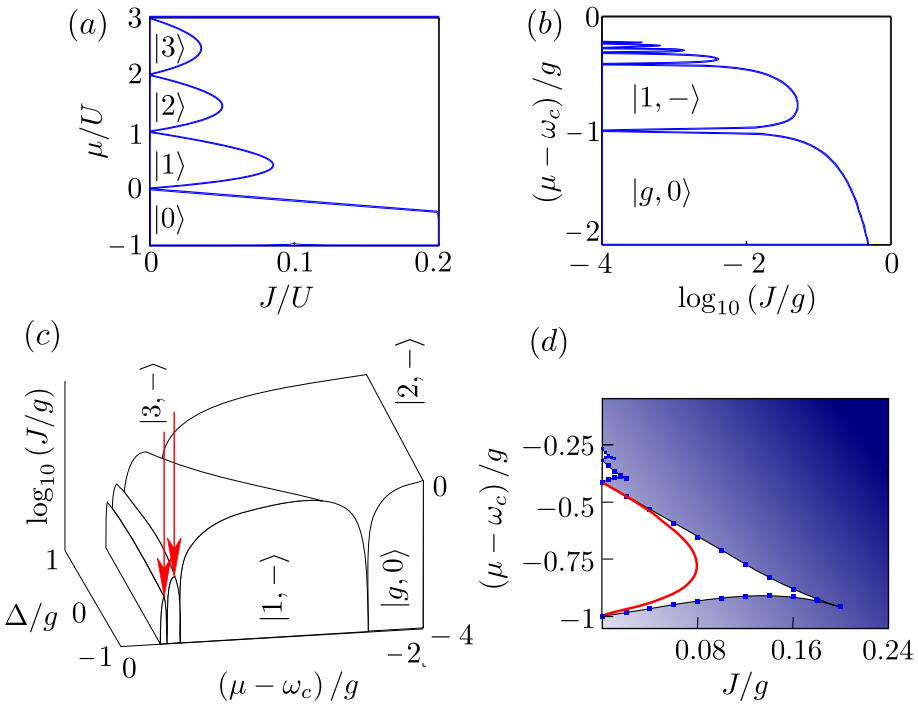


Figure 1.3. Mean field ground state phase diagram for (a) the Bose-Hubbard model and (b) the Jaynes-Cummings-Hubbard model. Both share several common features, with Mott insulating 'lobes' (characterised by vanishing order parameter $\Phi = \langle \hat{a} \rangle = 0$, white) surrounded by superfluid regions (blue) with a non-vanishing photon order parameter $\Phi \neq 0$. The Mott lobes are labelled with the Fock basis $\{|n\rangle\}$ in (a), and the polaritonic basis $\{|n, \pm\rangle\}, n \neq 0$ in (b), and $|g, 0\rangle$ denotes the 'empty' state of zero photons and the atom in its ground state. (c) Changing the relative detuning Δ between the characteristic resonator and atomic frequencies changes the makeup of the polaritonic excitations, and consequently the extent of the Mott lobes. (d) A comparison between the mean field (solid red curve) $|1, -\rangle$ Mott lobe boundary and rigorous DMRG calculations (solid black + blue markers) [58]. Note the different scales between (b) and (d). Re-entrant behaviour similar to the Bose-Hubbard model [59] is observed in the DMRG results, where monotonically increasing J crosses the phase boundary twice for some fixed μ.

is different between the models. For the BH Hamiltonian, the Mott lobes (under a mean-field treatment) are composed of product Fock states of $0, 1, 2, \cdots$ photons. The JCH Mott lobes meanwhile are also characterised by a fixed *total* local particle number, however this is shared between the photonic and atomic degrees of freedom – the Mott states are product polaritons e.g. $\cdots \otimes |1, -\rangle \otimes |1, -\rangle \otimes |1, -\rangle \otimes \cdots$. The total particle number fluctuation is zero. However, if the fluctuations of just one component (say, the photons) is measured, a non-zero variance is obtained even in the Mott regions. The novel features of CRA equilibrium physics due to their bipartite atom-photon nature were rigorously explored in the context of a two-resonator system in [60]. Figure 1.3 (c) additionally reflects the effect of the extra (atomic) degree of freedom that the JCH possesses, relative to the Bose-Hubbard model [61]. Varying the atom-resonator detuning Δ changes the makeup of the polaritons and consequently changes the features of the diagram, in particular the extent of the Mott lobes.

The superfluid phase meanwhile has a non-zero order parameter $\Phi \neq 0$, and the local photon number distribution changes from being a Kronecker delta function to being approximately Poissonian. The boundary between the $\Phi = 0$ and $\Phi \neq 0$ phases denotes a quantum phase transition of light for both models [56]. In general, we expect that when photon-photon interactions dominates over hopping, the system is in a Mott phase, and when the converse is true, the system will be in a superfluid phase.

1.4 Survey of existing work on CRAs

1.4.1 CRAs as quantum simulators

Proposals to use CRAs as platforms for quantum simulation date from the earliest works on these structures [12, 13, 14]. There is much interest in using CRAs as simulations for the JCH Hamiltonian to probe the polaritonic Mott-superfluid transition just discussed, analogously to the ground-breaking first evidence for the transition in optical lattices [9]. Beyond the JCH which is naturally realised in CRAs, there have been several proposals [12, 62, 63, 64, 65, 66] to simulate quantum spin chains, of great interest to fundamental condensed matter physics and more recently quantum information.

An early scheme to obtain an XY spin Hamiltonian from the JCH model relies on decoupling the upper $(+)$ and lower $(-)$ polaritons in the polaritonic Mott phase [12]. The local basis, effectively truncated at $\{|g,0\rangle, |1,-\rangle\}$ when the atom-photon coupling is large, is mapped onto a spin $\frac{1}{2}$.

Though we focus exclusively in this thesis on CRAs with resonator nonlinearities generated by JC-type couplings with single two-level atoms, generalisations beyond this 'standard' JCH model lead to a rich variety of quantum simulation ideas. For example, a scheme to realise both XY and ZZ spin couplings is found in [63]. The two lowest-lying states of three-level Λ-configuration atoms act as an effective spin $\frac{1}{2}$ in each resonator, with an effective magnetic field and coupling to nearest-neighbor resonators mediated by an external laser coupled to the third excited level. Time evolution of an effective XXZ spin model is simulated by alternately shining lasers which simulate either effective XX or ZZ couplings. Further details on realising the anisotropic Heisenberg model are found in [65]. Simulating a ZZ Ising coupling has also been proposed [67]. Simulating higher-spin Heisenberg models, of interest because of the lack of analytical results on their phase diagrams, may also be possible

[64]. The magnitude of the spin is controlled by the number of atoms in each resonator, and a relatively small number of constant laser fields are required.

A proposal to realise fractional quantum Hall [2] states in two dimensional CRAs was made in [68], by making use of the local addressability of individual resonators. The scheme involves the optical manipulation of the internal states of three-level atoms to simulate hard-core bosons (bosons in systems engineered such that there is very strong repulsion between them such that they are strongly inhibited from passing through each other) in Abelian vector potentials, leading to simulation of the Laughlin wave function [69]. In a non-equilibrium context, expected transmission spectra of CRAs exposed to synthetic gauge fields are calculated in [70], highlighting the extra features beyond single resonator QED signatures.

1.4.2 Equilibrium physics – a novel phase diagram

Much early attention was devoted to calculating the expected features of the Jaynes-Cummings-Hubbard ground state phase diagram. The work in [71] explores various analytic approximations to the phase diagram, comparing them with accurate numerical results. The existence of polaritonic Mott lobes beyond the mean-field calculations presented in Fig. 1.3 has also been confirmed using several more rigorous calculation schemes. The study in [72] used exact diagonalisation and cluster mean field approximations (in which more than one resonator is kept in the 'unit cell' of a Gutzwiller product ansatz for the ground state). An analytic strong-coupling approach to the phase diagram is presented in [73], accounting for quantum fluctuations beyond a mean-field treatment. Density-matrix renormalisation group (DMRG) calculations were applied to CRAs in [58], also confirming the extent of the Mott lobes. The characteristic shape of the $|1,-\rangle$ Mott lobe from these calculations is shown in Fig. 1.3 (d). The same numeric approach led in [74] to a proposed scheme to detect

the superfluid Mott-insulating quantum phase transition in a finite CRA by studying the excitation fluctuations as a function of array size. The work in [75] presents one of the few results for two-dimensional CRA ground states, using a Monte Carlo approach.

Continuing the theme of comparisons between Jaynes-Cummings-Hubbard physics and the more familiar Bose-Hubbard model, many early works presented studies of the expected spectral properties of CRAs. Many similarities between the models were highlighted, confirming for the most part that the JCH model also exhibits gapped particle and hole bands in the Mott phase, and Bogoliubov excitations in the superfluid. The single particle Mott excitation spectrum has been studied using a variational cluster approach in [11, 76] and with Monte Carlo methods in [77], and an analytic one-polariton approximation made in [78] in analogy with the one-electron approach of solid state physics. Anamolous features of JCH superfluid excitations are related in [79] to the special role of the zero polariton state.

Studies of the phase diagram of variants of the JCH include an exploration of arrays with multiple two-level systems (TLS) per resonator [58, 80], and arrays in the ultra-strong coupling regime where the rotating wave approximation is no longer valid [81]. Including the effect of disorder in either the number of atoms per resonator [58] or the array coupling parameters [80] lead to the emergence of polaritonic glassy phases similar to those in a disordered Bose-Hubbard model [8, 82].

A proposal to experimentally observe the Mott-superfluid transition in the specific architecture of coupled superconducting stripline resonators was made in [83].

1.4.3 Beyond equilibrium

The first works acknowledging the fundamentally lossy nature of CRAs attempted to bridge the gap with equilibrium physics by seeking signatures of the polaritonic

Mott-superfluid quantum phase transition in their dissipative dynamics. The work in [84, 85] proposed detecting the transition by analysing the coherence of light emitted (lost) from the CRA (described with a Bose-Hubbard Hamiltonian) which is initialised in a Mott state by an initial laser pulse. Similar ideas are presented in [86]. In [87] we show the existence of an anomalous 'super bunching' in the statistics of light emitted from arrays under continuous driving in the vicinity of the quantum phase transition (see also Chapter 5).

Moving beyond the relatively familiar physics of the quantum phase transition, various works began to explore the general expected emitted spectral features of driven-dissipative CRAs. The work in [88] demonstrates the effects of the interplay between photon tunnelling and strong interactions under pumping and loss, charting different zones of parameter space chiefly by the coherence properties of emitted light. Meanwhile the expected fluorescence spectrum of a driven-dissipative two-resonator system is related in [89] to excitations of the underlying Hamiltonian.

The dynamics of one- or two-particle transport have also been studied in several CRA variants. Single particle propagation in the JCH exhibits some unexpected properties such as pulse separation [90]. Single-particle propagation has also been considered in quantum communication contexts [91, 92], using CRAs as communication channels. The recent work [93] examines single-photon transport properties between the first and third resonators of a three-resonator system when only the central system features a JC-type coupling, in a microwave analog of the quantum optical Josephson interferometer [94]. The nature of the transport is qualitatively different in the strong coupling and ultra-strong coupling (when the rotating wave approximation is not valid) regimes. Exploiting a breakdown in the quantum blockade effect due to bistabilities in a classical driving field has been suggested to control photon transport in CRAs [95]. Radiation trapping [96] as a consequence of many-body bound atom-photon states may be experimentally measurable. In a similar

vein, [97] investigates two-polariton bound states in the JCH model which emerge beyond a critical g.

Other non-equilibrium CRA phenomena recently studied include novel dynamical photon localisation-delocalisation transitions [98, 99], single photon generation from strongly anti-bunched resonator array sources [100, 101], the non-equilibrium dynamics of entanglement generation [102, 103] and engineering synthetic gauge fields [70]. A 'fermionization' of photons in 1D structures in the strongly nonlinear regime was reported in [104], with spectroscopic evidence for the fermionization imprinted on the transmitted light from a driving laser. An intriguing photon 'crystallisation' is conjectured in [105], where driving lasers with appropriately chosen phases drive a 'current' of photons around a ring-like CRA. Evidence for photon crystallisation is found in photon density-density correlations arising from an interplay between driving, delocalisation and nonlinearity. We make contact with these last two effects in Chapter 3, where we demonstrate their existence in arrays rigorously described by the JCH Hamiltonian. Meanwhile the steady states of arrays with nonlinear nearest-neighbor couplings under coherent drive and loss have recently been predicted to exhibit photon crystal signatures with an associated periodic variation in the photon blockade [106].

1.5 Candidate architectures for realising CRAs

The JCH Hamiltonian of Eq. (1.12) generically describes coherently coupled bosonic fields, with each field exchanging quanta with a two-level system as described by the Jaynes-Cummings interaction of Eq. (1.11). It does not prescribe a specific physical implementation. It remains to be seen which of several candidate architectures will be successful in demonstrating extended JCH dynamics beyond the single resonator case. The present time is exciting for the field because of its youth, and the expecta-

tion that the first coupled resonator systems will be constructed in the near future. Here we briefly introduce the strongest contenders and discuss their advantages and limitations.

Photonic crystal cavities

Photonic crystals are in many ways the photonic analog of semiconductor periodic structures, operating in the infra-red to visible range [107]. They are characterised by a periodic variation of the refractive index on the length scale of the wavelength of light, induced for instance by drilling holes in an otherwise uniform substrate. This periodicity gives rise to photonic band gaps. Introducing localised defects in this regular structure, commonly by changing the size or material composition of the repeated features, leads to isolated photon modes inside the band gap. The defect modes are strongly spatially localized around the defect, leading to strong confinement of the photon mode in the plane of the crystal. The sharp refractive index difference at the interface between the (two-dimensional) photonic crystal and its surroundings (usually air) confines the mode in the direction perpendicular to the crystal plane, while still allowing access to mode observables. Figure 1.4 shows a schematic of such an arrangement.

Coherent optical coupling between neighbouring defect resonators formed in this way may be achieved by fabricating them close enough to each other such that the evanescent 'tails' of their modes overlap. Resonators may be arranged into many configurations, depending on the geometry of the host crystal.

In contrast to bulk nonlinear optics applications [108], material properties are insufficient to achieve the strong photon-photon interaction regime in the few-photon limit. Instead, a particularly promising route is to embed electronic quantum dots [109, 110, 111] inside the cavity defects [112, 113]. Quantum dots are small structures composed of a different material than the host cavity, which are capable of confin-

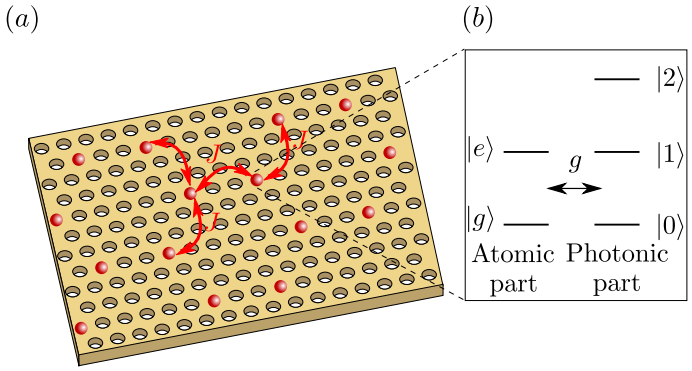


Figure 1.4. (a) Red circles denote defect cavities formed by removing holes from an otherwise periodic crystal lattice, and red arrows indicate coherent tunnelling between neighbouring defects. (b) Quantum dots featuring two cleanly isolated low-lying levels play the role of artificial atoms coupling in a Jaynes-Cummings interaction with the localised photon modes.

ing the electronic wave function in three dimensions. As a consequence, quantum dots possess quantised electronic levels. Transitions between levels can be isolated and addressed by external fields. By bringing one of these transitions into quasi-resonance with the cavity mode, a strong cavity-dot coupling is achieved, which can be accurately modelled as a Jaynes-Cummings type coupling. Achieving the maximal coupling g requires accurately positioning the dot to coincide with the maximum amplitude of the photonic mode. Current state-of-the-art cavity-quantum dot experiments can achieve ratios of the coupling to photon loss rates of $g/\gamma_p \approx 3$, sufficient to observe photon blockade but far inferior to superconducting setups (see below).

Research into photonic crystals is extremely active and fabrication techniques are already well established [114, 107] as they are of great interest for purely classical optical applications. Two dimensional photonic crystals in the form of photonic crystal fibres [115, 116, 107] have found commercial application due to their novel confining characteristics relative to conventional optical fibres, which allow them to guide exotic wavelengths of light for surgical and construction uses. While fully three-dimensional crystals still suffer from problems of disorder in the manufacturing process, they promise sizeable optical nonlinearities necessary to implement classical

all-optical logic operations. The one-dimensional subset of photonic crystals are known as coupled optical resonator waveguides, or CROWs [117, 55]. CROWs have been routinely fabricated for over a decade now, with uses in nonlinear signal processing and 'slow light' delay lines [118, 119, 120].

The advantages that photonic crystal platforms offer for novel strongly-interacting quantum photonics experiments include a large Q-factor approaching 10^6, and extremely small mode volumes on the order of λ^3, where λ is the operating wavelength. However, while strong signatures of photon blockade at the single photon level have been observed for a single photonic crystal defect cavity coupled to a quantum dot, at present there are technological problems with scaling to multi- or many-cavity geometries. This is because during the growth stage of quantum dots their size and location cannot be deterministically controlled. Present approaches involve selecting a quantum dot with desirable transition frequency characteristics, then fabricating a photonic crystal lattice around it with periodicity tailored to the dot's resonance.

Integrated optical waveguide arrays

Impressive first steps towards scaleable coupled resonator array physics were demonstrated some years ago with the fabrication of arrays of micro-cavities consisting of Bragg-inscribed optical fibre tips above concave mirrors etched in silicon [121], as in Figs. 1.5 (a) and (b). The cavities thus formed possess cleanly isolated modes, with cavity mode volumes comparable to the effective volume of atoms (approximately 10 times as large, though hundreds of times λ^3) allowing strong photon-atom interactions. Originally constructed with a view to developing sensitive and reliable atom detectors [122], subsequent increased control over experiments led to the possibility of single-atom loading [123].

More recently, improved designs replace the fibre arrays with UV laser inscribed waveguides. These waveguides are patterned by moving a substrate relative to an

intense writing laser capable of permanently increasing the substrate's refractive index. This technique is well established in the fields of telecommunications and optical information processing, where components are generally 'written' to interact with light at telecommunications wavelengths, $\approx 1.5\mu m$. This is not useful for atom-optics applications, as there are no suitable atomic transitions around this wavelength. It was however recently demonstrated [124] that waveguide writing using this technique is indeed possible around commonly used atomic transition frequencies, e.g. 780nm for Rubidium.

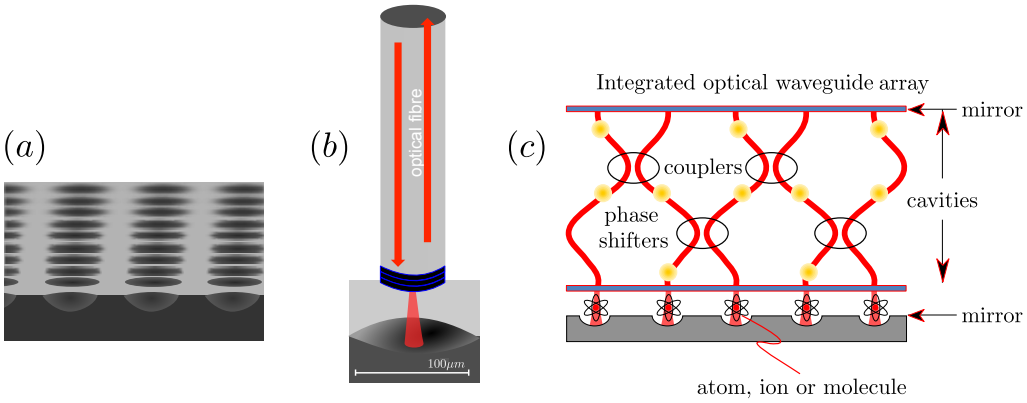


Figure 1.5. (a) Concave mirrors etched into silicon may be fabricated with high precision in large-scale arrays. (b) Resonators may be formed from these micro-mirrors by adding Bragg-inscribed fibres above them, with the internal field addressed through the fibres. (c) Coupled resonator array as realised by inscribing optical waveguides (red lines) in a substrate by modifying the local refractive index with a strong writing laser. Etched mirrors capping each waveguide form resonant 'cavities', each of which is tunnel-coupled to an auxiliary cavity into which atoms may be dropped.

Coupled cavity arrays may be realised using this technology by inducing waveguides in a substrate, and mirror coating both ends of the substrate slab, as shown schematically in Fig. 1.5 (c). The resulting waveguide 'cavities' are coupled by writing the guides close enough to each other for efficient evanescent coupling. Remarkably, this geometry allows for the possibility of tuneable resonator-resonator coupling by dynamically phase shifting the light in one of the resonators relative to its neighbour, reducing the effective overlap between the modes in the coupling

region [125]. This has been demonstrated through the temperature-dependence of the substrate refractive index, using deposited nichrome heating wires laid over the optical waveguides. The resonance frequency is tuneable over an entire free spectral range, though losses are still high.

Coupling these 'cavities' with single atoms is achieved by adding auxiliary microcavities formed between one of the slab mirrors and an external micro-mirror. Atoms can then be dropped under gravity from an atom cloud [122]. More recently the possibility of using well-isolated discrete transitions in molecules such as dibenzoterrylene (DBT) as effective two-level systems has been investigated [126]. It may be possible to fix the position of individual molecules by embedding them in an anthracene crystal matrix. However, phonon noise in the confining matrix must be 'cooled', requiring low operating temperatures. Another possible alternative consists of positioning DBT molecules directly on the surface waveguides, allowing direct access to the optical fields [127].

Superconducting quantum circuit QED systems

A third, particularly promising platform for observing clear, scalable JCH physics is that of circuit QED (cQED) setups, operating in the microwave regime [128, 129, 130, 131, 132]. Josephson junctions fabricated in superconducting quantum circuits act as non-dissipating nonlinear elements, inducing unequal spacings between discrete energy levels of the circuit. The lowest of these levels can then be cleanly isolated and addressed, so that these structures are often called 'artificial atoms'. Through appropriate design, the two lowest levels may be much closer together than all higher states, so that an effective two-level system is simulated to a good approximation.

Arrays of such Josephson junctions can be fabricated at micrometer length scales on a chip using mature lithographic technologies, and unlike real atoms can be de-

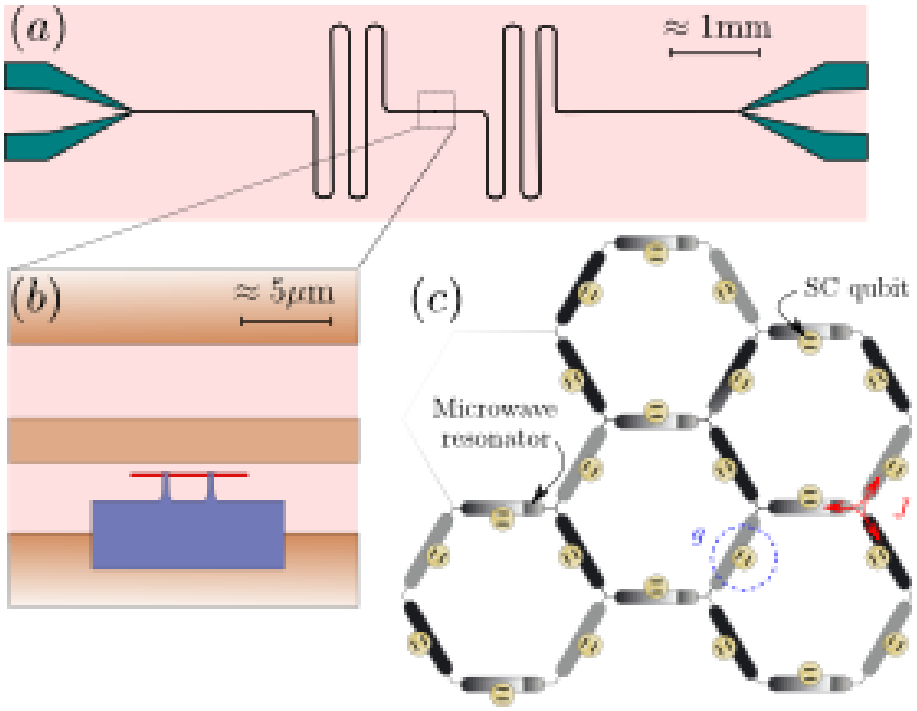


Figure 1.6. (a) Schematic of a superconducting coplanar waveguide resonator patterned into a thin film on the surface of a silicon chip. Green tapering structures fanning out to the edges of the chip connect to input and output lines. The total length of the resonator is 24 mm. The resonator consists of a centre conductor separated from two ground planes as shown in the zoom. (b) Magnified view of the effective TLS realised by a transmon quit, which consists of two superconducting islands (purple, large charge reservoir and thin red) positioned in the gap between the central and one of the two flanking rails of the stripline waveguide (brown) at the field antinode. (c) Many stripline resonators fabricated into a Jaynes-Cummings-Hubbard system.

signed with certain properties. It is also possible to dynamically control the properties of the artificial atoms *in-situ* through the use of external fields. These artificial atoms can then be inserted into and coupled to the bosonic fields of superconducting transmission line resonators, as in Fig. 1.6 [133]. The resulting interaction between the 'atoms' and resonator fields can be described by a Jaynes-Cummings type interaction [128]. Such setups have come to be known as circuit QED, by analogy with cavity QED experiments with real atoms [134].

The relative advantages of cQED type structures over optical implementations of

CRAs include the accurate and fixed positioning of the effective TLS at the resonator field antinode, and the extremely small mode volume of quasi-1D transmission line resonators ($\approx 10^{-6}$ cubic wavelengths). It is interesting to note that cQED setups are capable of demonstrating Jaynes-Cummings coupling rates comparable to the resonator frequency itself [132], though we will not investigate this ultra-strong coupling regime in this thesis. Clear quantum behaviour can be observed much more distinctly in cQED than in comparable optical systems, with coupling to loss ratios $g/\gamma_p \approx 10^2$ achievable in current experiments. However, cQED requires mK temperatures so that the characteristic thermal energy kT is much less than the microwave resonator energy $\hbar\omega_c$. Crucially for probing the internal quantum dynamics of these systems, reliable single microwave photon detectors have also not yet been demonstrated.

Table 1.1 summarises and compares the essential parameters characterising each of the three platforms discussed in this section. In addition to the three candidate architectures discussed, we note there are also other systems under consideration. Notably, strong coupling with atoms has been demonstrated [135] in fiber-coupled high-Q ($Q > 10^6$) micro-disk arrays [136]. Micro-disk arrays are fabricated via electron-beam lithography in regular scalable arrays, and may be coupled together efficiently with a tapered fiber optic filament, which is a standard optical fiber heated and stretched to a diameter less than the wavelength of light, so that an evanescent field extends beyond the fiber boundary allowing coupling to the disks. Quantum dots are grown non-deterministically on top of the disks, coupling to both the counter-propagating fields of a whispering gallery mode of the resonator. Again uniform placement and sizing of quantum dots at multiple resonators is an issue, though relatively strong coupling is achievable for a single resonator (effective mode volume a few multiples of a cubic wavelength and $g/\gamma_p \approx 5$).

Table 1.1. Comparison of maximum achievable CRA parameters for different architectures.

Parameter	Symbol	Photonic crystals	Integrated optics	Superconducting
Resonance frequency	$\omega_c/2\pi$	380 THz	380 THz	10 GHz
JC parameter	g/π, g/ω_c	5 GHz, 3×10^{-5}	1 GHz, 3×10^{-6}	100 MHz, 5×10^{-3}
Cavity decay lifetime	$1/\gamma_p, Q$	0.5 ns, 10^6	1 ns, 2×10^6	160 ns, 10^4
Atom decay lifetime	$1/\gamma_a$	1 ns	50 ns	2 μs
Coupling to loss ratio	g/γ_p	5	3	50
Resonator coupling	$J/2\pi$	300 GHz	3 GHz	10 MHz

1.6 Thesis overview

The structure of this thesis is as follows. Chapter 2 introduces the background theoretical and numeric machinery necessary to treat large, open one-dimensional quantum resonator arrays. We define the quantum master equation describing the dynamics of a quantum system open to its environment, which we use extensively throughout this thesis. Quantum trajectories are also introduced as a powerful method to simulate non-equilibrium dynamics of open systems. Details of the practical algorithm are summarised and simple examples provided. We also discuss in general terms the properties of our chief numerical workhorse, a class of representations known as matrix product states (MPS). Representing the state of CRAs is challenging, due to the exponential growth in Hilbert space dimension with increasing system size. MPS are capable of efficiently compressing the quantum state of one-dimensional systems. We summarise their most important properties and outline how accurate, near-exact calculations may be performed within this formalism.

Chapters 3 and 4 then take up the topic of what constitutes a physically realistic description of CRAs. Often in the literature, the joint photon-atom nature of excitations in resonator arrays is approximated by a purely bosonic interacting model (where the nonlinearities introduced by coupling to atoms is approximated by terms quadratic in the boson number). Neglecting the extra atomic degree of freedom truncates the richer physics demonstrated by the full JCH Hamiltonian. We explore

when it is valid to approximate the full physics of resonator arrays in this way, and characterise the additional features the driven-dissipative JCH model possesses relative to simpler bosonic descriptions. We then proceed to evaluate the prospects of observing two recently-proposed intriguing strongly correlated photonic phenomena in resonator arrays by properly simulating the relevant steady states [137].

Chapter 4 continues the theme of investigating what constitutes a physically valid description of CRAs. We study the effect of different, complementary numerical approximations to the state of the array on the predicted steady state properties. In particular, we focus on the possible existence of multiple stable steady states of driven quantum lattices. We find that low-level approximations neglecting or truncating long-ranged quantum correlations through the system predict bistable behaviour in certain parameter regimes. Employing a matrix product representation of the system state capable of encoding larger correlations 'washes out' this bistability, recovering a single unique stationary state for all parameter regimes. We note this bistability (or lack thereof) is qualitatively different that that found in single cavities in the large-excitation regime [138], as we examine the low-excitation, fully quantum regime of extended cavity arrays.

Having demonstrated the necessity of a rigorous physically accurate representation of resonator arrays, Chapters 5 and 6 proceed to explore two novel quantum optical phenomena which we anticipate are observable in near-future experimental array implementations. Chapter 5 investigates the possibility of observing signatures of celebrated equilibrium quantum phase transitions in a non-equilibrium photonic setting. We find a novel photon 'super bunching' in the statistics of emitted photons from arrays in the vicinity of where the equilibrium phase transition is expected [87]. The origins of this enhanced bunching are traced to the structure of the underlying Hamiltonian, and an approach to the thermodynamic limit of large array sizes is studied.

Chapter 6 departs from our focus on steady-state properties, presenting evidence for 'frozen' photon dynamics in sufficiently nonlinear resonator arrays. We show that arrays may be initialised in such a way that the initial pumped state has little overlap with propagating modes of the system, resulting in stationary domain walls of photons over appreciable timescales [99].

Chapter 7 follows up on an intriguing recent proposal to observe signatures of topological Majorana fermonic physics in CRAs [139]. This scheme involves a novel form of driving, parametrically pumping correlated photon pairs into adjacent resonators. This fascinating proposal leaves open many questions regarding the existence and nature of topologically nontrivial phases away from the ultra-strong nonlinearity regime considered in [139], and additionally the persistence of these phases in the thermodynamic limit of infinite CRAs. We present the foundations of a thorough characterisation of the expected phases of this novel system.

Finally a summary of the thesis is given in Chapter 8, together with an outlook on prospects for further research along the lines of the work presented here.

1.7 Contribution and publications

Here I summarise my own contribution to the work presented in this thesis, and link results presented in the following chapters to papers, either published already or in the pipeline.

By chronological submission date, the publication history following from the work in this thesis is as follows.

- The work in Chapter 3 led to the publication of *Non-equilibrium many-body effects in driven nonlinear resonator arrays* [137], for which I was the first author.

- The work in Chapter 5 led to the publication of *Non-equilibrium many-body effects in driven nonlinear resonator arrays* [87], for which I was the first author.

- The work in Chapter 6 led to the publication of *Frozen photons in Jaynes Cummings arrays* [99], for which I was the second author. However, I contributed all calculations, figures and wrote the bulk of the paper.

- The results in Chapter 5 have been written up and are currently being combined with a possible experimental implementation section from collaborators at the Center for Quantum Technologies (CQT) in Singapore National University for publication. I would remain first author.

In addition to the coherent body of work in this thesis, centred around driven dissipative effects in coupled optical resonator arrays, I have been involved with work on transport in incoherently boundary-driven quantum spin chains, which led to

- *Dephasing enhanced transport in non-equilibrium strongly-correlated quantum systems* [140]. I contributed to much of the work and writing behind this publication.

Chapter 2

Simulating large lossy arrays

In this Chapter we introduce the notation and techniques, both theoretical and numerical, we use to both describe and simulate mesoscopic sized driven-dissipative one-dimensional CRAs throughout this thesis.

We rely heavily on Lindblad quantum master equations (QMEs) [141, 142] to simulate the density matrix describing driven, lossy resonator arrays, where coherent dynamics acting in concert with irreversible photon loss to the surrounding vacuum leads to steady states. It is relatively straightforward to write down the governing QME for a coupled resonator array, but in general difficult to solve for quantities of interest.

The difficulties stem chiefly from the exponential growth in the Hilbert space dimension with the number of resonators. This growth is particularly limiting in our case, where we often wish to simulate the open dynamics of resonator arrays with both photons and atoms so that even the local dimension of Hilbert space is relatively large. Developing numerical algorithms to aid in studying the strongly-correlated many-body quantum systems is one of the most difficult problems in computational physics. The last decade has seen impressive progress in the development of computational representations of the state of quantum lattice systems as tensor networks [143, 144]. In particular, in one dimension a class of representations known as matrix

product states (MPS) has met with much success [145, 146]. While traditionally one dimensional models [147] served as simplifications for higher-dimensional, more 'realistic' quantum systems, experimental advances over the past decades have enabled the realisation of true 1D and quasi-1D physics in cold atom optical lattice setups [7, 9], atomic gases in hollow optical fibres [148, 149, 150, 151], and coupled optical resonator arrays, our main focus. In addition to faithfully representing the physics of resonator arrays, 1D models may be simulated near-exactly within the MPS formalism using a powerful algorithm known as time evolving block decimation (TEBD) [152, 153, 154, 155]. Many of the results in this thesis extensively use this scheme to calculate both equilibrium and non-equilibrium properties. We note the existence of a freely available software library written in the C language which provides highly optimised routines implementing the necessary tensor network manipulations underlying the TEBD algorithm [156]. In this thesis however we predominantly use older routines written in MATLAB, extending an existing code base [157], as the C library was developed towards the end of this PhD.

This chapter introduces the following material. Section 2.1 defines the generic form of QME we use throughout this thesis. A derivation of the quantum master equation and discussion of the necessary assumptions (and their validity) in arriving at this form are provided in Appendix A. Section 2.2 discusses approaches to solving QMEs for quantities of interest, via simple approaches and the more sophisticated quantum trajectory framework. Section 2.3 introduces a powerful compact ansatz for the quantum state of CRAs, which aids in avoiding the exponential scaling problem. The integration of this ansatz into algorithms to simulate QMEs is taken up in Sections 2.4 - 2.6. Our presentation of these algorithms is aimed at giving a high-level understanding of the MPS representation and the nature of manipulations underlying the TEBD algorithm. Further details may be found in Appendix B. We use all these techniques at various points in this thesis to calculate array properties

far from equilibrium.

2.1 Lindblad master equations

It is known that the most general form of a Markovian time-local master equation that preserves the trace, Hermiticity, and positivity of the system's density matrix ρ must be of so-called Lindblad form [142]:

$$\frac{d\rho}{dt} = \hat{\mathcal{L}}[\rho] = -i[\hat{H}, \rho] + \sum_{\alpha} \left(\hat{L}_\alpha \rho \hat{L}_\alpha^\dagger - \frac{1}{2} \left\{ \hat{L}_\alpha^\dagger \hat{L}_\alpha, \rho \right\} \right), \tag{2.1}$$

where the Lindblad operators $\hat{L}_\alpha = \sqrt{\gamma_\alpha} A_\alpha$ and $\hat{H}$ is the Hamiltonian describing the unitary part of the system's dynamics. The γ_α are identified as the characteristic rates at which 'jump operators' A_α act on the system. For instance, in the case of a lossy single-mode resonator with field destruction operator $\hat{a}$, γ describes the intensity loss rate of the resonator, characteristic of the jump operator $\hat{a}$ which acts to dissipate photons.

2.2 Solving master equations

In this thesis, we are concerned primarily with steady-state properties of arrays under the action of continous driving and dissipation. We denote by $\rho_{\text{ss}} = \lim_{t\to\infty} \rho(t)$ the system density matrix reached in the long-time limit. The steady state then satisifies $\dot{\rho} = \mathcal{L}[\rho_{\text{ss}}] = 0$. We characterise these steady states by measuring steady state observables as $\langle \hat{O} \rangle_{\text{ss}} = \text{Tr}\left(\hat{\text{O}} \rho_{\text{ss}} \right)$.

We now briefly discuss methods to calculate either ρ_{ss} directly, or steady state observables without the full density matrix.

2.2.1 Exact diagonalisation

The master equations of Lindblad type in Eq. (2.1) do not depend on the past history of the system, and are linear in the system density matrix. The stationarity condition $\mathcal{L}[\rho_{\text{ss}}] = 0$ may therefore be recast as a matrix eigenvector problem. The steady state density matrix ρ_{ss} (say of dimension $N \times N$) can be 'flattened' into a vector $\bar{\rho}_{\text{ss}}$ of length N^2, and the super operator may be cast as a matrix $\bar{\mathcal{L}}$ of dimension $N^2 \times N^2$ which premultiplies $\bar{\rho}_{\text{ss}}$. Generally $\bar{\mathcal{L}}$ is very sparse, allowing the flattened solution vector $\bar{\rho}_{\text{ss}}$ to be found efficiently using sparse matrix routines as the eigenvector of $\bar{\mathcal{L}}$ corresponding to the eigenvalue with zero magnitude (or very close to it in numerical solutions). The full density matrix ρ_{ss} may then be reconstructed from $\bar{\rho}_{\text{ss}}$, allowing the calculation of steady state quantities of interest.

This approach is only viable for small systems. Some optimisations of the exact diagonalisation approach are possible, as outlined in Appendix C, and Appendix D lists example MATLAB code illustrating the reshaping and diagonalisation operations necessary to solve for $\bar{\rho}_{\text{ss}}$.

2.2.2 Numerically exact time evolution

We can write the solution to Eq. (2.1) as $\rho_{\text{ss}} = \lim_{t\to\infty} e^{\hat{\mathcal{L}}t}\rho(0)$. An alternative to exact diagonalisation is therefore to evolve an initial state $\rho(0)$ until some convergence criteria is achieved. Typically this proceeds by discretising the simulation time into steps δt, and repeatedly applying the evolution operator $\exp(\hat{\mathcal{L}}\delta t)$. When simulating small systems, $\exp(\hat{\mathcal{L}}\delta t)$ may be calculated explicitly, then repeatedly applied to the system state in a series of matrix-vector multiplications. Larger systems, for which this exponentiation becomes intractable, may benefit from approximations to matrix exponentials requiring only matrix-vector multiplications [158]. Again, the sparseness of $\hat{\mathcal{L}}$ aids in both these approaches, though again the exponential

scaling of $\hat{\mathcal{L}}$ (with dimensions the square of the dimension of Hilbert space) severely limits the size of systems which may be addressed. We evolve yet larger systems by representing both the density matrix $\rho(t)$ and evolution generator $\exp(\hat{\mathcal{L}}\delta t)$ in the language of matrix product operators, to be introduced in Section 2.3.

2.2.3 Quantum trajectories

Often, even with the compression afforded by the matrix product operator ansatz, the representation of a lattice system's density matrix is simply too large to handle numerically. An alternative to simulating the dynamics of an open system by evolving its density matrix, which represents a statistical ensemble of constituent states, is to propagate stochastic realisations of individual system state vectors $\{|\Psi_i(t)\rangle\}$ [159, 160, 161]. These 'quantum trajectories' are piecewise deterministic processes, interrupted randomly by 'quantum jumps' due to the system's interaction with the environment. An approximation to the density matrix may be obtained by averaging the contributions $\Pi_i = \{|\Psi_i(t)\rangle\langle\Psi_i(t)|\}$ of many trajectories as described in more detail below.

The details of the 'unravelling' of the Lindblad master equation into stochastic wave functions is somewhat involved [142]. Here we give a practical recipe on how to generate quantum trajectories, and then show equivalence between the two approaches.

2.2.4 Trajectory Algorithm

For a set of Lindblad operators $\{\hat{L}_\alpha\}$, we construct a non-unitary effective Hamiltonian $\hat{H}_{\text{eff}}$:

$$\hat{H}_{\text{eff}} = \hat{H} - \frac{i}{2}\sum_\alpha \hat{L}_\alpha^\dagger \hat{L}_\alpha, . \tag{2.2}$$

Evolution under the Schrödinger equation with this effective Hamiltonian leads to a decay in the norm of the wave-function as a consequence of interactions with the environment. Trajectories are then generated as follows.

1. Begin the simulation by initialising the system in a state $|\Psi\rangle = |\Psi(0)\rangle$.

2. Draw a randomly chosen number $r \in [0, 1]$.

3. Evolve the system under the action of the non-Hermitian Hamiltonian of Eq. (2.2). While the state under this evolution is not properly normalised, physical expectation values are calculated using the normalised form $|\Psi(t)\rangle / \sqrt{||\langle|\Psi(t)|\Psi(t)\rangle||}$.

4. Continue the evolution until the norm falls below the randomly chosen number, i.e. when the condition $|||\Psi(t_{\text{jump}})\rangle|| < r$ is first met. One of the possible quantum jumps now occurs.

5. The jump operator to be applied is chosen by first generating the normalised probability distribution

$$P_\alpha = \frac{||\hat{L}_\alpha \Psi(t_{\text{jump}})\rangle||^2}{\sum_\beta ||\hat{L}_\beta \Psi(t_{.\text{jump}})\rangle||^2}, \tag{2.3}$$

   then randomly selecting a jump operator index j from this weighted distribution. The normalised state after the application of the chosen operator is

$$\frac{\hat{L}_j|\Psi(t_{\text{jump}})\rangle}{||\hat{L}_j|\Psi(t_{\text{jump}})\rangle||}. \tag{2.4}$$

We continue looping over steps 2-5 until the end of our simulation window.

Figure 2.1 shows example realisations of quantum trajectories for two simple systems, and example MATLAB code in Appendix D shows an implementation of the algorithm for a two-site Bose Hubbard lattice system subject to driving and loss.

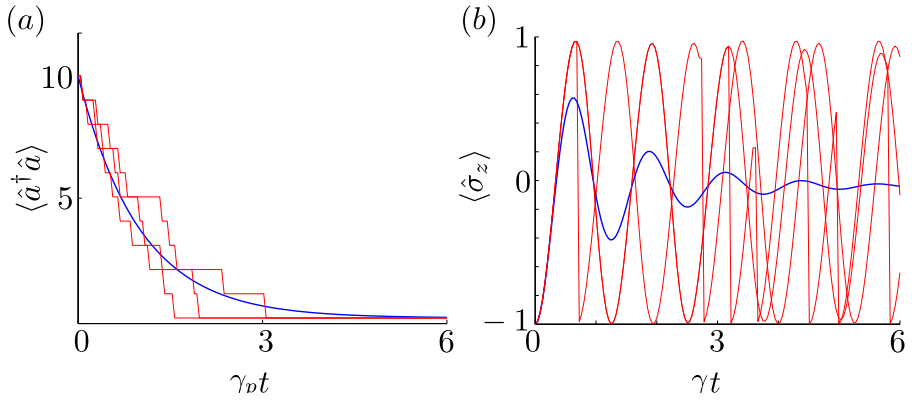


Figure 2.1. Example trajectories generated for two simple systems. Red lines are individual trajectory realisations, thicker blue lines are master equation results (which agree with the average over a large number of trajectories). (a) A harmonic resonator prepared in the $n = 10$ Fock state at time $t = 0$, left to evolve under lossy dynamics. The discrete nature of quantum jumps is obvious here, as the photon number decreases by exactly one at random intervals. Jump operator: $\sqrt{\gamma_p}\hat{a}$, and effective Hamiltonian: $\hat{H}_{\text{eff}} = -i\frac{\gamma_p}{2}\hat{a}^\dagger\hat{a}$, where γ_p is the loss rate. (b) A two-level system Rabi-flopping between the states $|\uparrow\rangle$, $|\downarrow\rangle$, with incoherent loss at rate γ from the upper level $|\uparrow\rangle$ leading into the lower level. We see the coherent oscillations interrupted at random times as the system is projected into the state $|\downarrow\rangle$. Jump operator $\sqrt{\gamma}\hat{\sigma}^-$ and effective Hamiltonian: $\hat{H}_{\text{eff}} = \Omega(\hat{\sigma}^+ + \hat{\sigma}^-) - i\frac{\gamma}{2}\hat{\sigma}^+\hat{\sigma}^-$, with $\Omega/\gamma = 1$.

2.2.5 Equivalence of the trajectory approach and master equation simulation

Here we verify that the average $\bar{\Pi}$ over a set $\{\Pi_i = |\Psi_i(t)\rangle\langle\Psi_i(t)|\}$ of very many trajectories is governed by the same Lindblad equation controlling the density matrix in Eq. (2.1), following [30]. Beginning with a $\bar{\Pi}(t)$ coinciding with the density matrix $\rho(t)$, we follow the evolution of the ensemble of trajectories over a small time interval δt. During this interval, either no jump occurs (with probability p_0), or one of the set of jumps occurs with total probability $1 - p_0$. From the form of the non-Hermitian Hamiltonian of Eq. (2.2) inducing the norm decay, the probability p_0 of no jump for trajectory i in the interval δt is $p_0 = 1-(\delta t)\sum_\alpha \langle\Psi_i(t)|\hat{L}_\alpha^\dagger\hat{L}_\alpha|\Psi_i(t)\rangle$. The probability p_j of a jump with corresponding Lindblad operator $\hat{L}_j$ is then identified

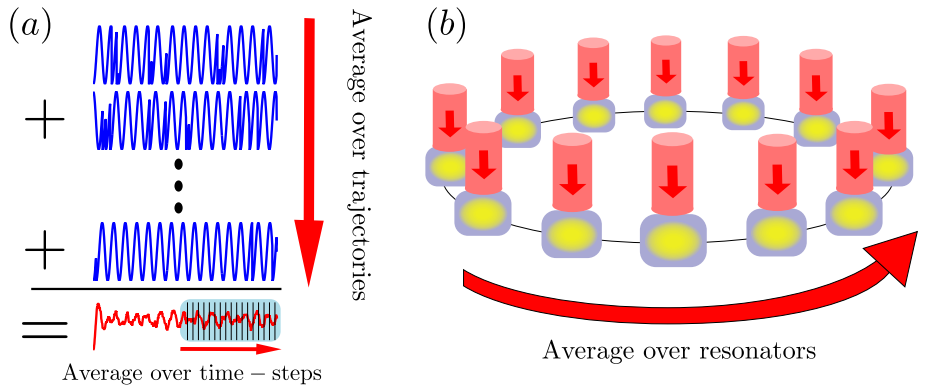


Figure 2.2. Illustration of the trajectory averaging procedure to find non-equilibrium steady states. (a) Averages are performed both over independent trajectory realisations, and time steps within the trajectories. (b) Translationally invariant periodic systems also benefit from an additional average over lattice sites, an advantage increasing with system size.

as $p_j = (\delta t)\langle\Psi_i(t)|\hat{L}_j^\dagger\hat{L}_j|\Psi_i(t)\rangle$. If after δt no jump has occurred, for trajectory i, the wave function is (normalised to first order in δt):

$$|\Psi_i(t+\delta t)\rangle_{\text{no jump}} = \frac{1 - i(\delta t)H_{\text{eff}}}{\sqrt{p_0}}|\Psi_i(t)\rangle. \tag{2.5}$$

Meanwhile if a jump j occurs in this time interval, the wave-function is projected into

$$|\Psi_i(t+\delta t)\rangle_{\text{jump}} = \frac{\hat{L}_j|\Psi_i(t)\rangle}{\sqrt{\langle\Psi_i(t)|\hat{L}_j^\dagger\hat{L}_j|\Psi_i(t)\rangle}}. \tag{2.6}$$

The ensemble average $\bar{\Pi}(t+\delta t)$ is then a mixture of some wave functions which have undergone jumps, and some which have not. The weights of these two components are p_0 and $1-p_0$ respectively. With $|\Psi(t+\delta t)\rangle = |\Psi'\rangle$,

$$\begin{aligned}\frac{d\bar{\Pi}}{dt} &\approx \frac{\bar{\Pi}(t+\delta t) - \bar{\Pi}(t)}{\delta t} \\ &= \frac{p_0\overline{\{|\Psi'\rangle\langle\Psi'|\}}_{\text{no jump}} + (1-p_0)\overline{\{|\Psi'\rangle\langle\Psi'|\}}_{\text{jump}} - \overline{\{|\Psi(t)\rangle\langle\Psi(t)|\}}}{\delta t}.\end{aligned} \tag{2.7}$$

Substituting for the probability p_0, and Eqns. (2.5) and (2.6) for the forms of the wave-functions both with and without a jump, we recover the evolution equation

$$\frac{d\bar{\Pi}}{dt} = -i[\hat{H}, \bar{\Pi}] + \sum_{\alpha} \left(\hat{L}_{\alpha} \bar{\Pi} \hat{L}_{\alpha}^{\dagger} - \frac{1}{2} \bar{\Pi} \hat{L}_{\alpha}^{\dagger} \hat{L}_{\alpha} - \frac{1}{2} \hat{L}_{\alpha}^{\dagger} \hat{L}_{\alpha} \bar{\Pi} \right), \tag{2.8}$$

showing that the Lindblad master equation and stochastic trajectory simulation method are equivalent, in the limit of a large number of trajectories.

2.2.6 Calculation of steady state observables

Given a set of R trajectories $\{|\Psi_i(t)\rangle\}$ evaluated at time intervals δt, we estimate expectation values $\langle \hat{O} \rangle(t) = \mathrm{Tr}(\hat{O}\rho(t))$ as

$$\langle \hat{O}(t) \rangle \approx \frac{1}{R} \sum_{r=1}^{R} \langle \Psi_r(t) | \hat{O} | \Psi_r(t) \rangle, \tag{2.9}$$

When estimating steady-state observables, the average is extended over time-steps as well [162, 163]:

$$\langle \hat{O} \rangle_{\mathrm{ss}} = \frac{1}{N_T - N_S} \sum_{n=N_s}^{N_T} \langle \hat{O}(n\delta t) \rangle \tag{2.10}$$

where we start the averaging procedure at a time-step N_S after the initial transient dynamics have died out, up until a final time-step N_T, as illustrated in Fig. 2.2. This important trick is possible because in the non-equilibrium steady state the stochastic wave-functions at each time step must average to the true steady state density matrix ρ_{ss} [164, 165, 166]. Hence the trajectory method is far more efficient at simulating non-equilibrium steady states than the transient dynamics. A single trajectory can yield estimates of steady state expectation values and multiple trajectory realizations give an indication of the statistical errors in calculated quantities. Chapter 4 discusses some subtle differences in accuracy between trajectory and full

QME simulation in the context of extended lattice systems.

2.3 Matrix product states (MPS)

An essential method in our numerical toolbox to simulate CRAs is a representation of the array state which overcomes the exponential scaling of the array description, without sacrificing physical accuracy. The dimension of Hilbert space is exponentially large for a representation in the bare basis, as seen by writing a pure state of a 1D M-site lattice generically as

$$|\psi\rangle = \sum_{j_1=1}^{d} \cdots \sum_{j_M=1}^{d} c_{j_1 \cdots j_M} |j_1, \ldots, j_M\rangle, \tag{2.11}$$

where $c_{j_1 \cdots j_M}$ is a set of d^M complex amplitudes and $|j_m\rangle$ is a basis spanning the local d-dimensional Hilbert space of site m. An alternative representation known as a Schmidt decompostion follows by breaking the system into two blocks to the left $\{1, \cdots, m\}$ and right $\{m+1, \cdots, M\}$ of site m:

$$|\psi\rangle = \sum_{\alpha=1}^{\chi_m} \lambda_\alpha^{[m]} |L_\alpha^m\rangle |R_\alpha^m\rangle. \tag{2.12}$$

Here $\lambda_\alpha^{[m]}$ are non-negative numbers called Schmidt coefficients and $|L_\alpha^m\rangle$ and $|R_\alpha^m\rangle$ form orthonormal bases spanning the left and right subsystems, respectively. The number of Schmidt coefficients χ_m is called the Schmidt rank. Importantly, the entropy of the probabilities $(\lambda_\alpha^{[m]})^2$ is a measure of the *entanglement* of the state [167]. It is known that for 1D systems with a Hamiltonian composed of nearest-neighbour terms, the ground and low-lying excited states have a very small amount of entanglement resulting in their Schmidt coefficients $\lambda_\alpha^{[m]}$ decaying rapidly with α

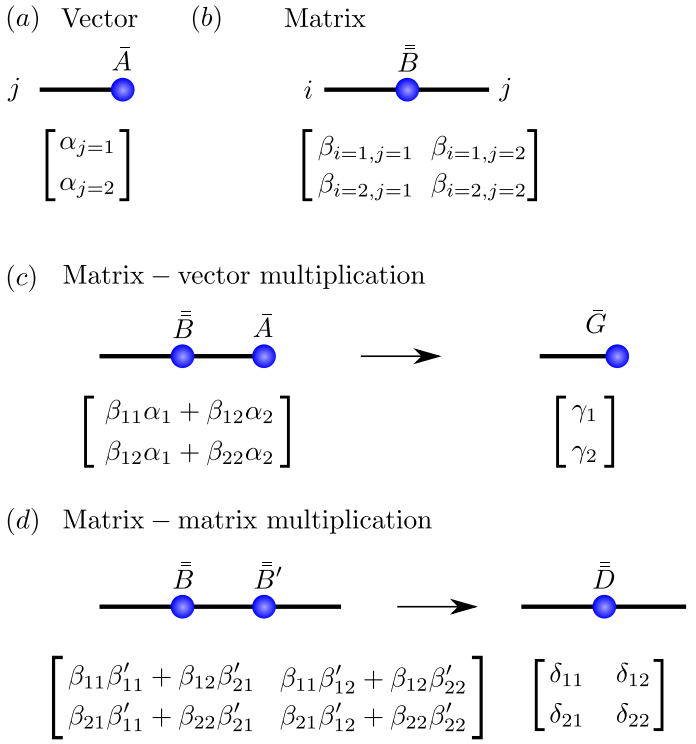


Figure 2.3. The basic elements of the graphical representation of matrix algebra which we employ heavily in this chapter to explain various steps of matrix product state algorithms. In this Figure capital latin symbols with one and two overbars represent vectors and matrices respectively. Black lines (or 'legs') represent the free indices of each quantity, i.e. the objects are fully specified by allowing each 'leg' to run over it's available values. Explicit examples are given for a vector of length 2 in (a), and a matrix of dimension 2×2 in (b). Matrix-vector and matrix-matrix multiplication are illustrated in (c) and (d) - these operations are represented graphically by joining the legs of two objects, and mathematically by 'contracting' these legs.

when arranged in descending order. This allows us to heavily truncate the description at a much smaller fixed χ while still providing a near exact description. This fact can be exploited to form a new, compact description of the state. Following [152] the expansion coefficients of the state in Eq. (2.11) can be brought into the canonical form

$$c_{j_1 j_2 \cdots j_M} = \sum_{\{\alpha\}=1}^{\{\chi\}} \Gamma^{[1]j_1}_{\alpha_1} \lambda^{[1]}_{\alpha_1} \Gamma^{[2]j_2}_{\alpha_1\alpha_2} \lambda^{[2]}_{\alpha_2} \cdots \Gamma^{[M]j_M}_{\alpha_{M-1}}, \tag{2.13}$$

where $\{\alpha\} = \{\alpha_1, \cdots, \alpha_{M-1}\}$ and $\{\chi\} = \{\chi_1, \cdots, \chi_{N-1}\}$. Here $\Gamma^{[m]j_m}$ is a set of

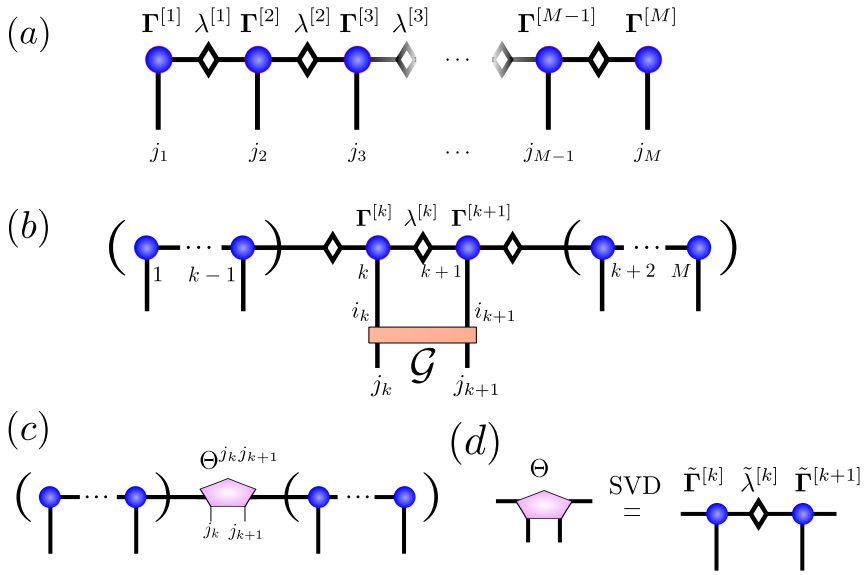


Figure 2.4. (a) Graphical representation of a matrix product state. Each site has an associated tensor (circles) and vector of Schmidt coefficient weights (diamonds). The 'legs' (straight lines) attached to the tensors represent tensor indices. Joining the legs of two tensors implies a contraction, or matrix multiplication over the corresponding indices. The 'free' vertical legs represent the indices corresponding to the physical state of each site. (b) A gate $\mathcal{G}$ is applied to sites k, $k+1$ of an MPS. The most general form of such a two-site gate is $\mathcal{G} = \sum_{j_{k,k+1}} \sum_{i_{k,k+1}} G^{j_k j_{k+1}}_{i_k i_{k+1}} |j_k\rangle|j_{k+1}\rangle\langle i_k|\langle i_{k+1}|$. (c) Applying $\mathcal{G}$ transforms the two neighbouring tensors into a single large intermediate tensor Θ which is not of MPS form. To restore standard MPS form, a singular value decomposition (SVD) is performed, breaking Θ into two tensors with dimensions $> \chi$. (d) These new tensors are truncated back to χ, introducing some truncation error which is many cases is very small.

$\chi_{m-1} \times \chi_m$ matrices indexed by the local state j_m at site m, while $\lambda^{[m]}$ is a diagonal matrix containing the Schmidt coefficients for the m-th bipartition. This is a matrix product description since once the all local configurations $j_1 j_2 \cdots j_M$ are specified the above sum over all the α's implements a sequence of matrix multiplications. The MPS representation lends itself to a convenient graphical interpretation as a tensor network as in Fig. 2.4 (a), with Fig.2.3 defining the basic matrix operations involved. By fixing the Schmidt ranks $\chi_m \leq \chi$ for all bipartitions m the number of parameters needed to describe $|\psi\rangle$ scales as $O(dM\chi^2)$, linear in the system size (there may be a dependence of the necessary χ for an accurate description on M,

though in most cases this is weak beyond small M).

2.3.1 The time evolving block decimation (TEBD) method

The TEBD algorithm [152, 153] provides an efficient means of updating the MPS representation after the action of a two-site operator on any two neighboring lattice sites. This proceeds by modifying the Γ matrices associated with each site and the λ's linking them, and requires a number of operations which scales as $O(d^4\chi^3)$. The resulting matrices are then systematically truncated back to a maximum rank of χ to reestablish a fixed rank MPS description. The graphical representation of MPS facilitates visualisation of the necessary operations, as in Figs 2.4 (b)-(d). Time evolution of the MPS is achieved by approximating evolution operators over incremental time steps δt into a product of two-site gates via a Suzuki-Trotter decomposition [168] (details in Appendix B).

TEBD may also be used to find the ground state of a quantum lattice in a fixed excitation number subspace, by evolving under imaginary time evolution from some initial guess state, i.e. making the replacement $\delta t \to -i\delta t$ [154]. The ground state component is projected out and magnified under such evolution. We note the existence of alternative efficient popular MPS-based methods to find ground states, known as DMRG (density-matrix renormalisation group) [169, 170, 171]. In this thesis we use TEBD to calculate ground states, so as to fit with our dynamical calculation scheme.

Since its inception, the time evolving block decimation (TEBD) algorithm has for the most part been formulated and deployed in the context of pure quantum states. In the following sections we sketch the less conventional adaptations which we rely on in this thesis. Namely, we have combined the matrix product state and TEBD machinery with the quantum trajectory algorithm, creating a powerful lattice

non-equilibrium steady state simulation tool. We also discuss the representation of a resonator array density matrix in the matrix product state language, and outlines how to directly simulate master equation evolution. Finally we discuss how the state of infinite arrays may be represented.

2.4 Trajectory simulations with MPS

Figure 2.5 describes graphically the implementation of the quantum trajectory algorithm as described in Section 2.2.3 in the MPS language. The one ingredient that cannot be conveniently visualised is the renormalisation of the state such that $\langle\Psi|\Psi\rangle = 1$ after a quantum jump. This is achieved by dividing the elements of the Γ matrices of an unnormalised site by $||\langle\Psi|\Psi\rangle||^{\frac{1}{2M}}$.

To our knowledge, we were amongst the first to exploit this powerful combination of the MPS formalism with quantum trajectories. We have found the combination to be very effective in calculating CRA steady state properties, allowing simulation in regimes inaccessible otherwise. Chapter 4 provides some explanation of the efficiency of this combination. We benefitted from access to a large computing cluster. Individual trajectories are independent, so that there is no need for sophisticated inter-process communication during simulation, but rather a simple final aggregation and averaging of results.

2.5 Matrix product operators (MPOs) - Mixed states and TEBD master equation simulation

Having described the combination of the quantum trajectory method with the MPS formalism, we now discuss how to directly evolve an array's density matrix in time under master equation dynamics as described by Eq. (2.1). Simulating mixed state

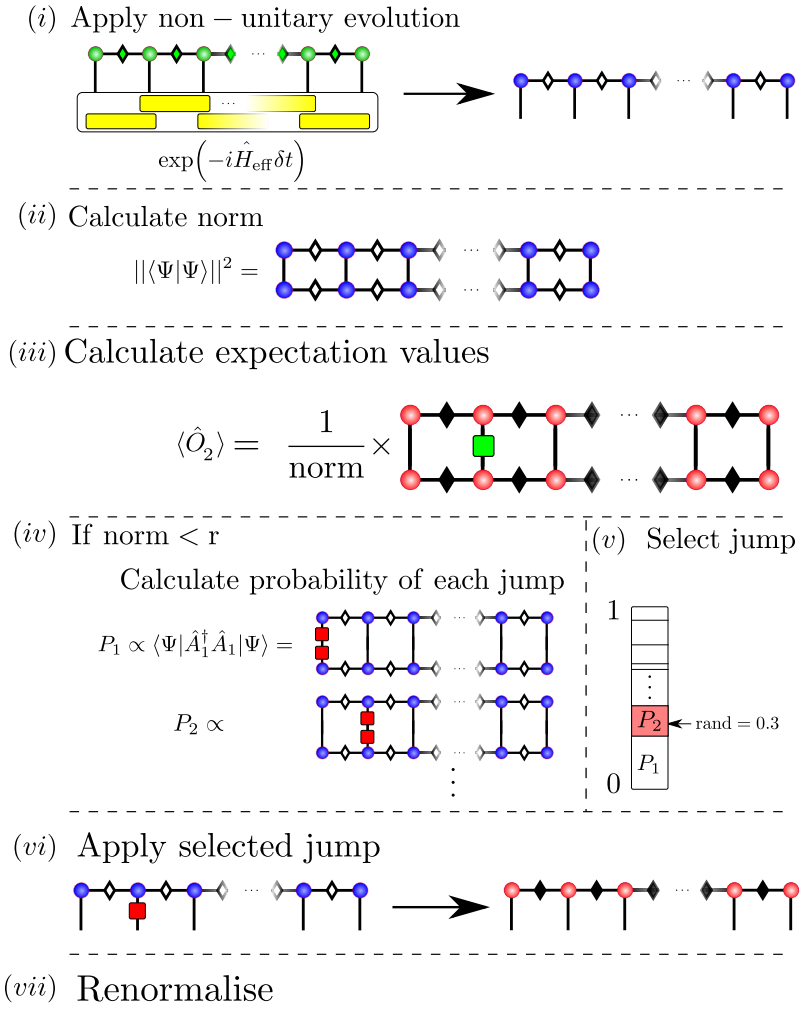


Figure 2.5. A single time step of the quantum trajectory algorithm as implemented with matrix product states and the TEBD procedure. (i) Evolution under the effective Hamiltonian of Eq. (2.2) is performed by breaking the evolution into a series of two-site 'gates' (yellow), applied to the initial MPS (green tensors), yielding a new MPS (blue). (ii) The norm of the wavefunction is calculated by contracting the MPS representation of the state ket (upper) with its bra (lower), yielding a scalar. (iii) Expectation values are calculated by 'sandwiching' the operator between the bra and ket, and renormalising to account for the norm decay. (iv) If the norm falls below the randomly chosen threshold as described in Sec. 2.2.4, we form a distribution of the probabilities of each quantum jump occurring, as in Eq. (2.3), and randomly sample a jump to apply, otherwise loop to (i). Jump operators are indicated by red boxes. (v) Applying the jump consists of contracting the matrix representing the jump operator with the corresponding physical index of the MPS, yielding a new MPS (red).

evolution within the TEBD framework was proposed near simultaneously in [172] and [173].

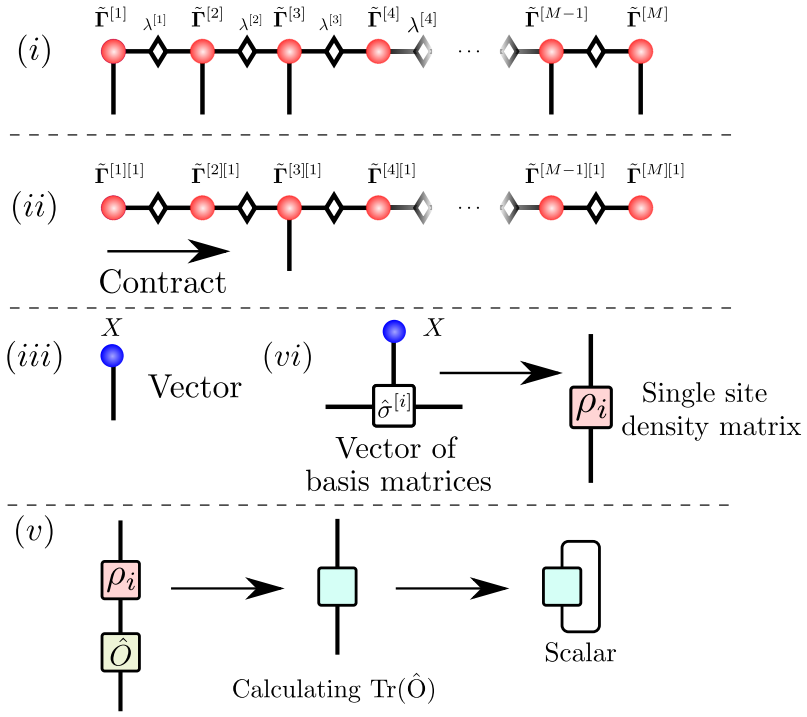


Figure 2.6. Illustration of the procedure to calculate expectation values with respect to an MPO representation of the density matrix ρ, shown in (i). (ii) To calculate the reduced density matrix at site i (here $i = 3$) we select the first matrix in the basis at all sites $\neq i$. Contracting the network results in a single vector of coefficients, represented in (iii). (iv) Contracting this vector with a vector of basis matrices yields the ρ_i. (v) Expectation values are calculated by contracting operators with ρ_i, and a trace is finally performed by contracting the two physical indices.

Our starting point is to expand the density matrix of an M-site array with local basis dimension d in the bare basis (analogously to the pure state expansion of Eq. (2.11)) as

$$\rho = \sum_{j_1=1}^{d^2} \cdots \sum_{j_M=1}^{d^2} c_{j_1 \cdots j_M} \left(\boldsymbol{\sigma}^{[1]j_1} \cdots \boldsymbol{\sigma}^{[M]j_M} \right). \tag{2.14}$$

The $\{\boldsymbol{\sigma}^j\}$ are a set of d^2 matrices of dimension $d \times d$ forming an orthonormal basis for the local Hilbert space. We take the first matrix $\boldsymbol{\sigma}^1$ to be proportional to the identity $\boldsymbol{I}$. The remaining $d^2 - 1$ basis matrices are traceless and Hermitian. As an

example, for $d = 2$ this basis could be proportional to the identity, and the Pauli matrices $\{\boldsymbol{I}, \boldsymbol{\sigma}^x, \boldsymbol{\sigma}^y, \boldsymbol{\sigma}^z\}$. Again the expansion coefficients c may be expressed as matrix products once the physical indices $j_1, j_2, \cdots, j_M$ are fixed, as in Fig. 2.4 (a). Figure 2.6 (i) shows the resulting graphical representation – the MPO structure is identical to the MPS representation of Fig. 2.4 (a), but the indices $j_1, \cdots, j_M$ run from 1 to d^2 rather than d.

Time evolving an MPO is very similar to time-evolving an MPS. The master equation generator $\exp(\mathcal{L}\delta t)$ is approximated by a series of two-site gates, which after contraction with the MPO and subsequent reshaping and truncation as per Figs. 2.4 (b)-(d) results in a new MPO.

Calculating expectation values from MPOs is significantly different from the pure state case. We outline the steps to obtain a single-site reduced density matrix from an MPO. The extension to multi-site reduced density matrices is straightforward. Substituting a matrix product for the expansion coefficients in Eq. (2.14) and tracing over all sites but i to obtain the reduced density matrix ρ_i:

$$\begin{aligned}
\rho_i &= \mathrm{Tr}_{i' \neq i} \sum_{j_1, \cdots, j_M = 1}^{d^2} \boldsymbol{\Gamma}^{[1]j_1} \lambda^{[1]} \boldsymbol{\Gamma}^{[2]j_2} \lambda^{[2]} \cdots \boldsymbol{\Gamma}^{[i]j_i} \lambda^{[i]} \cdots \boldsymbol{\Gamma}^{[M]j_M} \left(\boldsymbol{\sigma}^{[1]j_1} \cdots \boldsymbol{\sigma}^{[M]j_M} \right) \\
&= d^{M-1} \sum_{j_i=1}^{d^2} \boldsymbol{\Gamma}^{[1]1} \lambda^{[1]} \boldsymbol{\Gamma}^{[2]1} \lambda^{[2]} \cdots \boldsymbol{\Gamma}^{[i]j_i} \lambda^{[i]} \cdots \boldsymbol{\Gamma}^{[M]1} \boldsymbol{\sigma}^{[i]j_i} \\
&= \sum_{j_i=1}^{d^2} \gamma_{j_i} \boldsymbol{\sigma}^{[i]j_i} \qquad (2.15)
\end{aligned}$$

Moving from the first to the second lines, we have used the matrix identity $\mathrm{Tr}(X \otimes Y \otimes Z) = \mathrm{Tr}(X)\mathrm{Tr}(Y)\mathrm{Tr}(Z)$ and the fact that only the first matrix in the basis has non-zero trace. We see that ρ_i is then a linear combination of the local spanning basis matrices, and we assemble the coefficients into a vector $X = \{\gamma_1, ..., \gamma_{d^2}\}$. Calculation of local expectation values of operators $\hat{O}_{j_i}$ then follows from taking

the trace $\mathrm{Tr}(\rho_i \hat{O}_{j_i})$. This procedure also has a graphical interpretation, shown in Fig. 2.6.

2.6 Describing infinite systems

Incredibly, matrix product states are capable of describing infinite, translationally invariant quantum lattices [154]. Studying 1D quantum lattices directly in the thermodynamic limit removes finite-size artefacts and removes the need to extrapolate infinite system properties from scaling analyses. The key observation underlying the iTEBD (infinite TEBD) algorithm is that the state of an infinite lattice is shift-invariant, and so may be described by a single set of matrices $\mathbf{\Gamma}, \lambda$, independent of site m. As time evolution under TEBD consists of the repeated action of two-site gates, a two-site 'unit cell' is instead retained, as in Fig. 2.7 (a). We denote these two sites by A and B.

Simulation of time evolution or convergence to a ground state proceeds by updating the MPS structure under the repeated action of two-site gates $\mathcal{G}_{AB}$ and $\mathcal{G}_{BA}$. The gates preserve the translational invariance of the system, updating the MPS tensors in the unit cell. Somewhat counter-intuitively, the memory and processing requirements for the iTEBD algorithm are less than those for a finite-sized system, at fixed χ, as only two sites need to be updated at each time-step. Figure 2.6 (b) illustrates the algorithm, very similar to the finite-size case in Fig. 2.4.

However, we stress that the iTEBD algorithm is not capable of simulating non-unitary evolution (other than finding ground states through a fortunate property of the iMPS representation) 'out of the box'. An extension to simulate non-equilibrium dynamics was proposed in [174], however we have not implemented this algorithm (see Conclusions and Further work chapter).

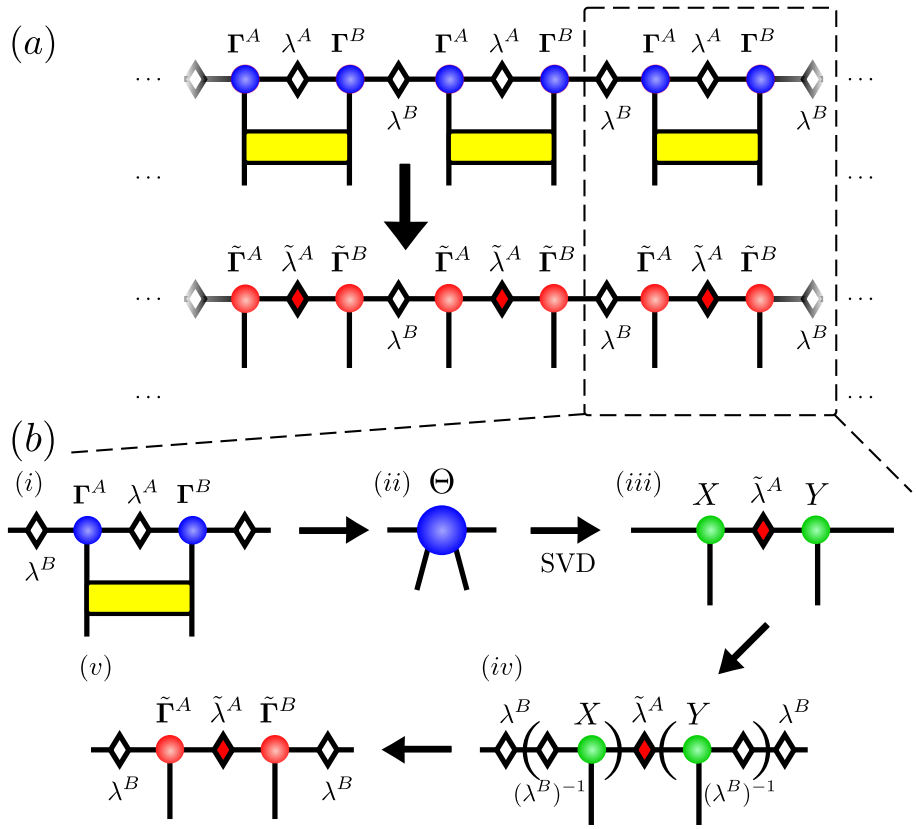


Figure 2.7. (a) Schematic of the procedure to update an iMPS (completely specified by just four tensors $\mathbf{\Gamma}^A, \mathbf{\Gamma}^B, \lambda^A, \lambda^B$) after the application of a two-site translationally invariant operator indicated by yellow rectangles (incremental unitary evolution operator for real time simulation, imaginary time evolution operator for ground state calculations). Contraction with the operator yields a new iMPS (red), again completely defined by the new tensors $\tilde{\mathbf{\Gamma}}^A, \tilde{\mathbf{\Gamma}}^B, \tilde{\lambda}^A, \lambda^B$. (b) Details on how the new tensors are formed. The whole 'unit cell' tensor network in (i) is contracted to form an intermediate tensor Θ, which is then split as in the usual TEBD scheme into two tensors X and Y and a diagonal matrix of weights $\tilde{\lambda}^A$. New tensors $\tilde{\mathbf{\Gamma}}^A$ and $\tilde{\mathbf{\Gamma}}^B$ are formed by absorbing the inverse of λ^B.

Chapter 3

Describing coupled resonator arrays

In this Chapter, we introduce the specific models we use to describe optically driven dissipative coupled resonator arrays (CRAs). We study their non-equilibrium steady states using the machinery introduced in the last chapter, analysing experimentally accessible quantities such as the total excitation number, the emitted photon spectra and photon coherence functions for different parameter regimes. The main focus of this Chapter is to evaluate whether it is viable to approximate the fully polaritonic nature of CRA excitations with simpler models, while retaining a proper description of the non-equilibrium physics. This is an important question, as ever since the first proposals to implement the Jaynes-Cummings-Hubbard (JCH) Hamiltonian in CRAs, analogies were made with the well-known Bose-Hubbard (BH) model [7]. The latter naturally emerges in CRAs when one assumes generic nonlinear resonator effects instead of a Jaynes-Cummings interaction, as has been done in many recent works [104, 85, 105, 94]. Indeed, the JCH and BH share many similarities, both describing bosons hopping coherently between nearest neighbor sites, with local nonlinearities. An equilibrium quantum phase transition [56] between Mott-insulating and superfluid-like phases exists for both models as discussed in Section 1.3. However, the BH Hamiltonian involves only a single species of bosons (photons in this case), while the excitations of the JCH model have both photonic

and atomic components. Consequently, the equilibrium physics of the JCH model is richer as shown in [61, 58, 71, 78, 72]. Studying the JCH out of equilibrium, as naturally implemented in open driven CRAs, is likely to highlight even more interesting differences with novel features beyond the realm of the driven BH model.

To address this issue, in this Chapter we therefore compare and contrast the expected behavior of CRAs assuming the local nonlinearity in the cavities is generated either by a generic Kerr effect, or a Jaynes-Cummings interaction. We find that the behavior of the experimentally accessible observables produced by the two models differs for realistic regimes of interactions even when the corresponding nonlinearities are of similar strength. We analyze in detail the extra features available in the Jaynes-Cummings-Hubbard (JCH) model originating from the mixed nature of the excitations and investigate the regimes where the Kerr approximation would faithfully match the JCH physics. We find that the latter is true for values of the light-matter coupling and losses beyond the reach of current technology. Throughout the study we operate in the weak pumping, fully quantum mechanical regime where approaches such as mean field theory fail, and instead use a combination of quantum trajectories and the time evolving block decimation algorithm to compute the relevant steady state observables. In our study we have assumed small to medium size arrays (from 3 up to 16 sites) and values of the ratio of coupling to dissipation rates $g/\gamma \sim 20$ which makes our results implementable with current designs in Circuit QED and with near future photonic crystal set ups, as described in Section 1.5.

In addition, most existing work to date on out of equilbrium CRAs has used mean-field approaches to treat the systems [84, 85, 86, 175, 176, 177]. Going beyond mean-field theory is crucial to provide physically accurate insights, especially in the experimentally realistic few-resonator regime. This requires a faithful representation of the full Liouville space of the resonator system which in most cases beyond two

resonators becomes challenging. For similar reasons of complexity, existing works to date on non-equilibrium resonator arrays exploring correlations and anti-bunching effects were always limited to minimal systems of two resonators [88, 100, 101, 102, 103]. More recent work includes a study of the fluorescence spectrum of again two coupled Jaynes-Cummings resonators [89, 178]. In the present chapter we simulate CRAs beyond the two resonator regime, always assuming the full JCH model, by exploiting a combination of the matrix product state time-evolving block decimation (TEBD) algorithm [152, 153] and quantum trajectories.

The structure of this chapter is as follows. In the first section we detail the Hamiltonians describing both JCH and BH physics, beginning with a description of the two types of nonlinearity at the single-resonator level. We then discuss our driving scheme and the inclusion of resonator loss in the model. In Section 3.2 we investigate the steady state spectra of single driven dissipative resonators, and demonstrate that Kerr physics can be achieved as a limiting case of the Jaynes-Cummings model. Section 3.3 treats arrays of a few sites as could be implemented in near future experimental setups, and results for yet larger arrays are presented in Section 3.4. In Section 3.5 we investigate the behavior of the system in the strongly repulsive regime and look for signatures of photon fermionization and crystallization in the JCH model. We then discuss the Chapter's main results in Section 3.6.

3.1 The system

We study a 1D system of M coupled single-mode resonators (indexed by j), as shown schematically in Fig. 3.1 (a) for a small system of $M = 3$ resonators. The Figure depicts a 'ring'-like geometry under periodic boundary conditions. Different parts of this thesis deal alternately with periodic and open boundary conditions, which we indicate when appropriate. The resonator frequency ω_c is the same for

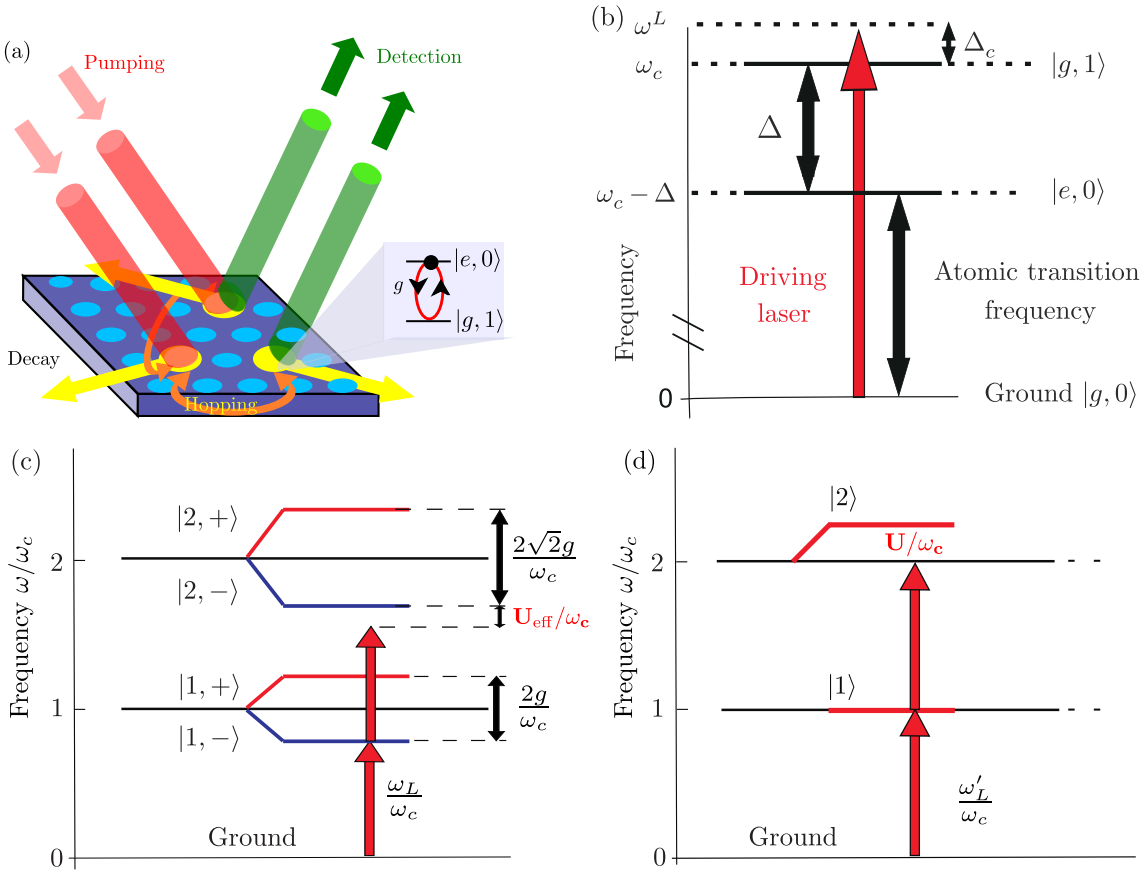


Figure 3.1. (a) A schematic of a three site set up. Here two-level systems are embedded in cavities in a 2D photonic crystal but alternative implementations involving Circuit QED architectures are also envisaged [131]. Coherent photon hopping between cavities results from modal overlap between neighboring cavities and photons can be lost due to decay mechanisms. (b) The relevant frequency scales and detunings used to describe a driven Jaynes-Cummings resonator (not to scale). (c) The low-lying eigen-levels for the Jaynes-Cummings interaction, showing the definition of the effective Kerr nonlinearity U_{eff}. (d) The low-lying excitations of a Kerr-nonlinear resonator. Arrows schematically show that a driving laser resonantly exciting a single-particle mode from the ground state is detuned from higher modes. Solid horizontal lines represent multiples of the cavity frequency. Dotted horizontal lines are a guide to the eye.

each resonator j. Coherent photon hopping between nearest-neighbor oscillators at a rate J arises as a result of an overlap between neighboring resonator modes $\langle j, j' \rangle$. Assuming each resonator is coherently interacting with a two-level system, the physics is well described by the JCH model as defined below. We will analyze the non-equilibrium system response and in parallel contrast the results with the case where a generic Kerr nonlinearity is assumed in place of the Jaynes-Cummings interaction as described by the well known BH model.

3.1.1 Local description

The local physics for both cases is captured by the two Hamiltonians

$$\hat{h}'_{JC} = \omega_c \hat{a}^\dagger \hat{a} + (\omega_c - \Delta)\, \hat{\sigma}^+ \hat{\sigma}^- + g\left(\hat{a}^\dagger \hat{\sigma}^- + \hat{a}\hat{\sigma}^+\right), \tag{3.1}$$

$$\hat{h}'_{BH} = \omega_c \hat{a}^\dagger \hat{a} + \frac{U}{2} \hat{a}^\dagger \hat{a}^\dagger \hat{a}\hat{a}, \tag{3.2}$$

where we have set $\hbar = 1$. The difference between the resonator frequency, and the atomic transition frequency is denoted by Δ and illustrated in Fig. 3.1 (b). The operator $\hat{a}^\dagger$ creates a photon, while the operators $\hat{\sigma}^\pm$ denote the usual raising and lowering operations between the ground and excited states of the two-level system.

The eigenstates of $\hat{h}'_{\rm JC}$ are known as 'dressed' states, or polaritons. They are mixed atom-photon excitations, which are also eigenstates of the total excitation number operator $\hat{\mathcal{N}} = \hat{\sigma}^+ \hat{\sigma}^- + \hat{a}^\dagger \hat{a}$ with eigenvalue n. The resonant case $\Delta = 0$ was briefly discussed in Chapter 1 – here we give the general eigen-frequencies and states for arbitrary atom-resonator detunings Δ. The ground state is $|0\rangle \equiv |g, 0\rangle$, with energy $E_0 = 0$. For a given excitation number $n \neq 0$, there are two polaritonic modes, designated $|n, \pm\rangle$, with associated frequencies

$$\omega_n^\pm = n\omega_c - (\Delta/2) \pm \sqrt{(\Delta/2)^2 + ng^2}. \tag{3.3}$$

The eigenstates can be written in the bare resonator-atom basis as $|n,\pm\rangle = \alpha_n^{\pm}|e,n-1\rangle + \beta_n^{\pm}|g,n\rangle$, with [34]

$$\alpha_n^{\pm} = (\chi_n \mp \Delta)/(\sqrt{2}\sqrt{\chi_n^2 \mp \Delta\chi_n}), \tag{3.4}$$

$$\beta_n^{\pm} = \pm 2g\sqrt{n}/(\sqrt{2}\sqrt{\chi_n^2 \mp \Delta\chi_n}). \tag{3.5}$$

Here $\chi_n = \sqrt{\Delta^2 + 4ng^2}$. It can be seen from these coefficients that setting a larger positive Δ results in an enhanced atomic component of the '-' polaritons, while negative Δ increases the photonic contribution, with the relative composition of polaritons reversed for the '+' species. The increased splitting of the polaritonic frequencies from the bare resonator frequency with increasing n gives rise to an effective interaction between incoming photons, leading to a well known phenomenon in Cavity QED, the photon blockade [29] (Section 1.2.4). Figure 3.1 (c) shows the eigen-structure schematically for the particular case $\Delta/g = 0$, illustrating the energy mismatch between adjacent polariton manifolds. Resonant excitation of the mode $|n,\pm\rangle$ by driving lasers requires an n-photon transition from the ground state $|0\rangle$ such that the resonant condition is to set the driving laser detuning $\Delta_c = \omega_L - \omega_c = \omega_n^{\pm}/n - \omega_c$ at

$$(\Delta_c)_n^{\pm} = \frac{1}{2n}\left(\Delta \pm \chi_n\right). \tag{3.6}$$

At atom-resonator resonance ($\Delta = 0$), this condition is $(\Delta_c)_1^{\pm} = \pm g$.

Meanwhile the local Hamiltonian for the BH model, $\hat{h}'_{\mathrm{BH}}$, describes a single-mode resonator with a Kerr-type nonlinearity in the particle number of strength U. The eigen-frequencies are $\omega_n = n\omega_c + \frac{U}{2}n(n-1)$, with corresponding eigenstates being the Fock number states $|n\rangle$. The eigen-structure of the three lowest-lying levels is shown in Fig. 3.1 (d). An n-photon excitation of the n^{th} mode occurs for the laser

detuning $\Delta_c = \omega_L - \omega_c = \omega_n/n - \omega_c$:

$$(\Delta_c)_n = \frac{U}{2}(n-1). \tag{3.7}$$

3.1.2 Comparing Kerr and Jaynes-Cummings nonlinearities

We now describe the manner in which we compare the two models in this Chapter. As the two Hamiltonians are patently different, care must be taken when comparing their behavior. We map the Jaynes-Cummings nonlinearity to an effective Kerr interaction via a frequency mismatch argument, as considered in both equilibrium and non-equilibrium contexts [72, 179]. In the following we focus on the '-' species of polaritons (see Eq. (3.3)), as the driving laser frequency necessary to resonantly excite the $|n,-\rangle$ modes increases with n, qualitatively similar to a Kerr nonlinearity. We define the effective Kerr nonlinearity $U_{\text{eff}} = U_{\text{eff}}(g,\Delta)$ as the energy penalty incurred in forming a two-particle polaritonic excitation in a resonator (with energy ω_2^-) from two one-particle polaritons (with total energy $2\omega_1^-$)

$$\frac{U_{\text{eff}}}{g} = \frac{\omega_2^- - 2\omega_1^-}{g} = \frac{\Delta}{2g} + 2\sqrt{\left(\frac{\Delta}{2g}\right)^2 + 1} - \sqrt{\left(\frac{\Delta}{2g}\right)^2 + 2}. \tag{3.8}$$

Figure 3.1 (c) shows these low-lying polaritonic eigenstates and the definition of U_{eff} pictorially. Interestingly, an analogous definition for the '+' polaritonic branch yields an attractive Kerr-type interaction. We note that as the distribution of energy levels with particle number n is markedly different between the models, it is only sensible to compare them in the very weakly excited regime where the above definition is meaningful.

While the above mapping 'matches' the nonlinearities of the two models by considering transitions between the one- and two-particle manifolds, we expect the single particle resonances of both systems to occur at different spectral locations.

The dominant spectral features in weakly excited systems will therefore be observed for different driving laser parameter regimes. Additionally, the mapping involves a comparison only of diagonal elements of the two governing Hamiltonians. However the different natures of the excitations of the models are not fully accounted for in such a mapping, in particular the additional internal degree of freedom possessed by the JCH model. We therefore expect the corresponding distinct off-diagonal Hamiltonian terms to lead to different physical observables between the models even under this mapping.

3.1.3 Coupled nonlinear resonators

Coupling together a 1D chain of identical (each has the same frequency) resonators via a coherent tunelling between adjacent resonators with rate J. the governing Hamiltonian is

$$\hat{H}_X = \sum_{j=1}^{M} \hat{h}_X^{\prime(j)} - J \sum_{<j,j'>} \hat{a}_j^\dagger \hat{a}_{j'}, \tag{3.9}$$

where $X \in \{JCH, BH\}$ and $\hat{h}_X^{(j)}$ describes the local nonlinearity, according to Eqns. (3.2). Systems under periodic boundary conditions are treated by including the pair $(1, M)$ in the sum over nearest neighbours $\langle j, j' \rangle$. Nearest neighbours j, j' are interchangeable, i.e. the coupling is two-way. Section 1.3 outlines some well-known key differences between the JCH and BH models in equilibrium.

3.1.4 Driving and losses

A clean experimental exploration of equilibrium ground states of the BH model [8, 9] is by now well established in the context of cold atoms in optical lattices [7, 180, 181]. However, fabrication of large-scale CRAs with sufficiently low loss to probe the phases of Fig. 1.3 (c) is still some way off, such that pumping will be necessary to maintain nontrivial states. We now describe the inclusion of driving

and losses for the purposes of our comparison in this Chapter. From this point we concern ourselves exclusively with non-equilibrium responses.

The relatively large distance between resonators in envisioned CRA setups means that external driving lasers with amplitude Ω_j and frequency ω_L can independently excite and probe each resonator j (i.e. a separate laser beam drives each resonator from the side). Here we consider the case of uniform driving $\Omega_j = \Omega, \forall j$, as described by

$$\mathcal{H}_{\rm dr} = \Omega \sum_j \left(\hat{a}_j^\dagger e^{-i\omega_L t} + \hat{a}_j e^{+i\omega_L t} \right), \tag{3.10}$$

where ω_L is the driving frequency. We note that this form of driving is not the 'familiar' type from Fabry-Perot cavities where light is shone on the outside of the Fabry Perot system. Instead, Eq. (3.10) describes the field modes in each resonator being directly driven by lasers. This form of driving is widely assumed in the CRA literature, and we follow this convention. The total Hamiltonian describing the unitary part of the CRA system's evolution is then

$$\hat{\mathcal{H}}_X^{\rm bare} = \hat{H}_X + \hat{\mathcal{H}}_{\rm dr}. \tag{3.11}$$

The explicit time dependence can be removed by transforming to a frame rotating at the laser frequency using the transformation $\hat{H}_X = \hat{T}^\dagger \hat{\mathcal{H}}_X^{\rm bare} \hat{T} + i \frac{\partial \hat{T}^\dagger}{\partial t} \hat{T}$ [182, 183], where

$$\hat{T} = e^{-i\omega_L \hat{\sigma}^+ \hat{\sigma}^- t} e^{-i\omega_L \hat{a}^\dagger \hat{a} t}. \tag{3.12}$$

After transformation, the Hamiltonian for both model systems can be written generically as

$$\hat{\mathcal{H}}_X = \sum_{j=1}^{M} \hat{h}_X^{(j)} + \sum_{j=1}^{M} \Omega_j \left(\hat{a}_j^\dagger + \hat{a}_j \right) - J \sum_{<j,j'>} \hat{a}_j^\dagger \hat{a}_{j'}. \tag{3.13}$$

The first term describes the local physics in resonator j in the rotating frame, with $X \in \{JCH, BH\}$. The second term describes the action of a coherent driving laser on each resonator j, and the last term describes the photon hopping. The local contributions $\hat{h}^{(j)}_{JCH}, \hat{h}^{(j)}_{BH}$ are identical in form to $\hat{h}'_{JC}, \hat{h}'_{BH}$, with the bare cavity frequency replaced by the detuning $\omega_c \to -\Delta_c$.

We assume a finite photon loss rate γ_p from each resonator for both models, and that the spontaneous emission rate from the excited level $|e\rangle$ of the two-level systems in the JCH system is negligible, $\gamma_a = 0$. Competition between coherent resonator driving, and photon loss leads to non-equilibrium steady state (NESS) conditions. We employ a master equation formalism [141] (Section 2.1) to describe the evolution of the system's density matrix $\rho(t)$. The NESS density matrix $\rho_{\rm ss}$ is given by the stationary point of the master equation $\dot{\rho} = \hat{\mathcal{L}}_X[\rho] = 0$, where the action of the Liouville super-operator is defined through

$$\hat{\mathcal{L}}_X[\rho_{\rm ss}] = \frac{1}{i}[\hat{H}_X, \rho_{\rm ss}] + \sum_{j=1}^{M} \frac{\gamma_p}{2}\left(2\hat{a}_j\rho_{\rm ss}\hat{a}_j^\dagger - [\hat{a}_j^\dagger\hat{a}_j, \rho_{\rm ss}]_+\right) = 0, \tag{3.14}$$

with $[\cdot,\cdot]_+$ denoting the anti-commutator operation. In general, solving Eq. (3.14) is a formidable task, owing to the exponential growth in the necessary size of a system's description with the number of cavities M. We exploit the permutational symmetry of a homogeneous minimally sized three-site cyclic resonator system to enable solution via an exact diagonalization scheme (details in Appendix C), and employ a more sophisticated TEBD based stochastic unraveling of the master equation for larger systems, as described in Sections 2.2.3 and 2.4.

Before discussing the solutions of Eq. (3.14) for an array of cavities, we first compare the stationary behavior of a single driven resonator with both Jaynes-Cummings and Kerr-type nonlinearities to illustrate their intrinsic differences in the local physics regime.

3.2 Single resonator steady states: Kerr versus Jaynes-Cummings nonlinearities

In Figures 3.2 (a) and (b) we show NESS particle numbers for both types of resonator as a function of the driving laser detuning from the bare cavity resonance. The most striking difference between the spectra is the existence of two 'wings' for the Jaynes-Cummings nonlinearity, symmetrically distributed about the cavity frequency ($\Delta_c = 0$) for this special case $\Delta/g = 0$. The driving laser frequency necessary to excite the '-' polaritons increases with the excitation number n (the converse is true for the '+' polaritons). Figure 3.2 (b) also demonstrates that the Kerr resonator always exhibits a single particle response at the bare cavity frequency, whereas the spectral location of the two single particle modes in a Jaynes-Cummings type system strongly depend on the atom-resonator coupling parameters.

The nonlinear response of the resonators can also be probed by analyzing the second order correlation function of the emitted photons from a certain resonator site. For later use, we define the generalized coherence function between any two resonators (j,k) as $g^{(2)}(j,k) = \langle \hat{a}_j^\dagger \hat{a}_k^\dagger \hat{a}_j \hat{a}_k \rangle / \langle \hat{a}_j^\dagger \hat{a}_j \rangle \langle \hat{a}_k^\dagger \hat{a}_k \rangle$ [32, 33]. In the following we refer to the on-site coherence function as $g^{(2)} \equiv g^{(2)}(j,j)$. As expected, in the strong coupling regime this quantity exhibits a dip below the coherent driving laser value $g^{(2)} = 1$ leading to photon anti-bunching when the driving laser is tuned to the corresponding single-particle modes for both models. For the Jaynes-Cummings resonator, the strongest anti-bunching is expected for laser detunings $\Delta_c = \pm g$ from the bare cavity frequency (for $\Delta = 0$). In contrast, the Kerr resonator demonstrates strongest anti-bunching when the driving laser is on resonance with the bare cavity mode, coinciding with the single particle mode at $\Delta_c = 0$. The reasonable atom-cavity coupling and cavity loss rates we have chosen ($g/\gamma = 20$) cause the correlation function to dip to a minimum $g^{(2)} \approx 0.25$ for the Jaynes-Cummings resonator, and

to $g^{(2)} \approx 0.15$ for the Kerr resonator.

Dips in the coherence function also appear when the driving laser is resonant with higher underlying quantum resonances (at equally spaced laser frequency intervals $U/2$ for the Kerr resonator, and laser frequencies $\Delta_c = \pm\frac{g}{\sqrt{n}}$ for the Jaynes-Cummings system). The magnitude of the correlation function at these resonances is highly sensitive to the magnitude of the driving laser strength and cavity loss rate.

Figures 3.2 (a) and (b) share several features common to driven dissipative nonlinear quantum systems. We see that, for both models spectral peaks corresponding to higher excitations n become successively narrower, because the monochromatic driving laser cannot be simultaneously resonant with all intermediate levels. This means all but the lowest (polaritonic or Fock) peaks involve off-resonant transitions. The peaks also become less bright with increasing n because in addition to being more difficult to populate, modes with more photons are more susceptible to photon loss. The Jaynes-Cummings system involves both atomic and photonic species, leading to different peak intensities between the models. This follows because we are only driving the photonic degree of freedom which in turn is coupled to the atomic degree of freedom in the Jaynes-Cummings resonator.

Thus the spectral signatures of driven dissipative JCH and BH systems for the case of vanishing photon hopping (single resonators) are in general quite different. However, the two models do possess broad qualitative similarities in that they both describe the interplay of coherent bosonic hopping with an on-site nonlinearity. Indeed, the BH Hamiltonian has been widely used as an approximation to treat CRAs in several works assuming a generic nonlinearity [104, 85, 105, 94]. It is natural to ask if the two models are equivalent in some regime or even if the physics of the JCH Hamiltonian can be mapped on to an effective BH model. Such a mapping would enable the large body of existing knowledge about the BH model to be applied directly to CRAs and would additionally significantly simplify numerical

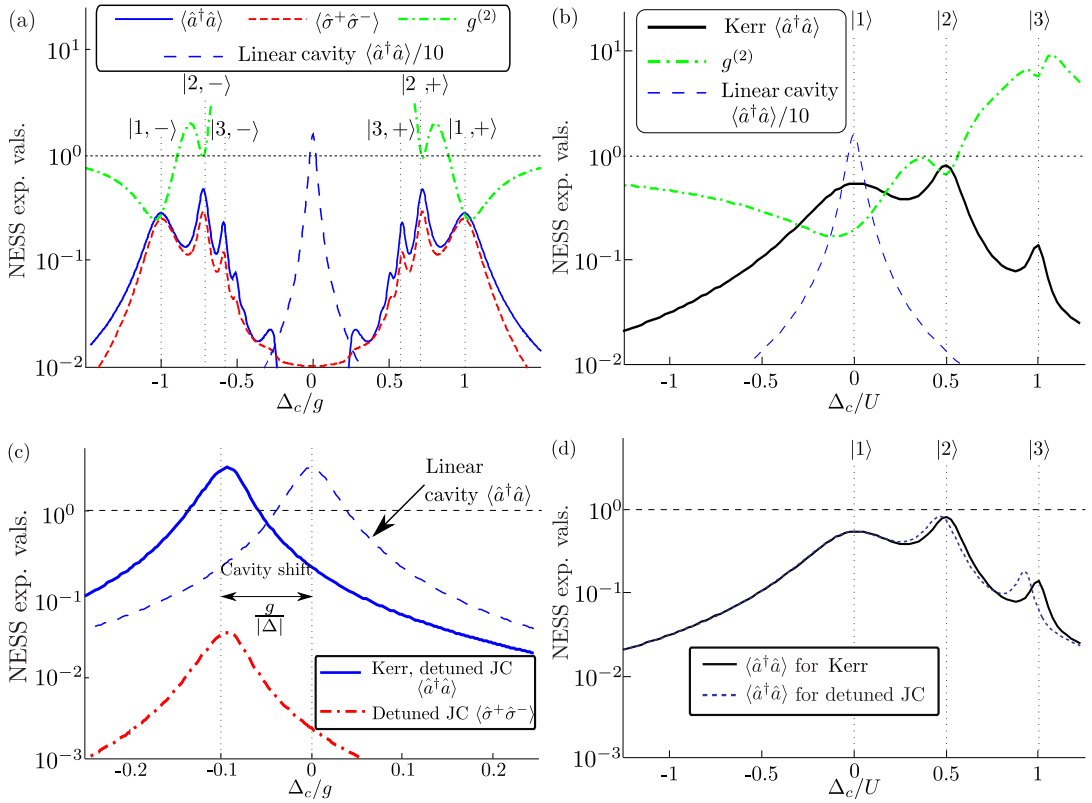


Figure 3.2. Steady state values of photonic/atomic population (solid/dashed line) and the second order photon correlation function ($g^{(2)}$, dot-dashed line) as a function of the driving laser-cavity detuning for a single driven dissipative resonator. (a) Jaynes-Cummings resonator (atom resonant with the cavity mode, $\Delta/g = 0$). The central Lorentzian (dashed curve) is the response of an empty (linear) driven-dissipative resonator $\langle\hat{a}^\dagger\hat{a}\rangle/10$. (b) Kerr-nonlinear resonator. Vertical dashed lines and labels in both plots indicate resonator resonances according to Eqns. (3.6) and (3.7), respectively. Parameters: Both systems share $\Omega/\gamma_p = 2$. Jaynes-Cummings coupling $g/\gamma_p = 20$. For the Kerr resonator: $U/\gamma_p \approx 11.7$, set using Eq. (3.8). (c) The response of a far-detuned ($\Delta/g = -10$) Jaynes-Cummings resonator for identical atom-resonator coupling, driving and loss as above. (d) Comparison of the Kerr response in (b) and that of a detuned Jaynes-Cummings resonator ($\Delta/g = -10$) with an ultra-strong nonlinearity $g'/\gamma_p \approx 1.6 \times 10^4$.

simulation. As the nonlinearity acts locally inside each resonator, we address this question below by first investigating single resonators.

3.2.1 The photonic limit of the Jaynes-Cummings model

Intuitively, we expect agreement between the models as the polaritonic JCH excitations are made more photonic in nature. For the '-' polariton species, this means setting $-g/\Delta \ll 1$. The two-level system in each resonator is then barely excited and the dispersive interaction available is capable of inducing a significant effective photon repulsion only for very large values of the coupling $g/\gamma_p \gg 1$. In this limit a Taylor expansion of the polaritonic eigen-energies $\omega_n^{\pm}$ in the small quantity $|g/\Delta|$ leads to frequencies quadratic in the particle number $n \neq 0$ as $\omega_{n,-}(g,\Delta) \approx n\,(\omega_c + g^2/\Delta) + g(g/|\Delta|)^3 n(n-1)$. We see that the off-resonant interaction induces an effective shift in the bare resonator frequency $\Delta_{\text{shift}} = -g^2/|\Delta|$, and that the energy spectrum can be written in the canonical Kerr nonlinear form with effective repulsion $U_{\text{BH}}^{\text{approx}} \equiv 2g\,(g/|\Delta|)^3$.

Figure 3.2 (c) shows the spectrum for a far detuned ($\Delta/g = -10$) driven dissipative Jaynes-Cummings resonator for the same experimentally realistic atom-cavity coupling rate g/γ_p as in Fig. 3.2 (a). We see that the response is essentially that of an empty (linear) driven dissipative resonator, albeit with a peak response at Δ_{shift} from the bare resonator frequency. The atomic excitation is an order of magnitude smaller, as expected. The effective Kerr nonlinearity is much smaller than the line-width ($U_{\text{BH}}^{\text{approx}}/\gamma_p = \frac{1}{50}$), so that nonlinear effects barely show up, apart from a slight asymmetry in the response. To observe sizable nonlinear effects for realistically achievable resonator parameters, we see that it is instead necessary to operate near the resonance point $\Delta/g \approx 0$.

For comparison, the physically unrealistic ultra-strong atom-resonator coupling

limit is shown in Fig. 3.2 (d). The response of the Kerr-nonlinear resonator shown in Fig. 3.2 (b) is reproduced, and compared with the spectrum of a Jaynes-Cummings resonator again operating in the photonic regime ($\Delta/g = -10$). The coupling strength $g/\gamma_p > 10^4$ is chosen by setting $U_{\mathrm{BH}}^{\mathrm{approx}} = U$ in the above definition of the effective Kerr nonlinearity. We see good agreement between the photon number spectra, which worsens for higher excitation peaks as higher order terms in the Taylor expansion of the polaritonic eigen-frequencies become important. So while deep in the regime satisfying $\Delta < 0$ and $|\Delta| > g$ (the photonic limit of polaritons), i.e. a detuning much larger than the frequency range over which we expect strong atom-cavity effects, the Jaynes-Cummings model can, with reasonable accuracy, be mapped on to a Kerr system, this regime is inaccessible with current technology.

3.2.2 The atomic limit of the Jaynes-Cummings model

In the opposite limit of $\Delta/g \gg 1$, the atomic component of the '-' polaritons is maximal. A Taylor expansion of the eigen-frequencies now yields: $\omega_{n,-}(g,\Delta) \approx n\left(\omega_c - g^2/\Delta\right) + g(g/\Delta)^3 n(n-1) - \Delta$, for $n \neq 0$. The ground state $|g,0\rangle$ still lies at the zero of energy. Therefore we see that to first order in g/Δ, the spectrum becomes equally spaced with the same shift in the resonator frequency as for the limit $\Delta \ll -g$, with the exception of the interval $\omega_c - \Delta$ between the ground state and the first polaritonic mode $|1,-\rangle$. In this limit $|1,-\rangle \approx |e,0\rangle$, with a small photonic component allowing transitions by the external driving laser. This may be summarized by the following effective Hamiltonian describing the 'vacuum shifted' $|n,-\rangle$ ladder of states for a single resonator in the atomic limit:

$$\hat{h}_{g/\Delta \ll 1} = (\omega_c - g^2/\Delta)\hat{a}^\dagger\hat{a} + g\left(\frac{g}{\Delta}\right)^3 \hat{a}^\dagger\hat{a}^\dagger\hat{a}\hat{a} + \Delta|g,0\rangle\langle g,0| - \Delta. \tag{3.15}$$

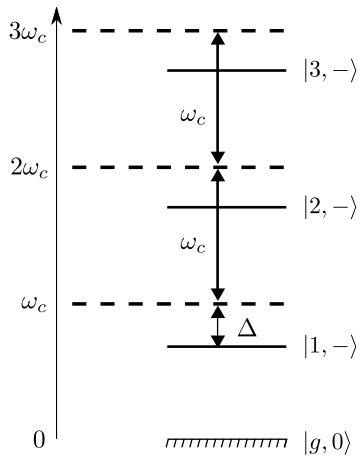


Figure 3.3. The level structure of the '-' branch of solutions for polaritons far into the 'atomic limit' when the detuning $\Delta > 0$ is much larger than the Jaynes Cummings parameter g. The spectrum is equally spaced except for the gap between the ground (vacuum) and first polaritonic states.

The level structure is shown in Fig. 3.3. Thus, population of the two-particle state from the resonantly driven single-particle mode is strongly inhibited. Higher lying levels could, however, be near-resonantly populated from the one-particle mode given an additional driving laser with frequency $\omega_L = \omega_c$.

When strictly working within the low-excitation regime, it is then appropriate to assign a large effective nonlinearity describing this energy penalty to reach the two-excitation manifold. However, care must be taken to distinguish between setups such as we consider, where only the lowest lying excitations are directly probed, and others which access the approximately harmonic ladder at larger $n > 2$.

3.3 Many-body signatures in steady state observables

Moving beyond the single resonator regime we will first analyze a minimal cyclic nonlinear CRA of $M = 3$ cavities. This case, though not truly many-body, is interesting as this is where the first experimental implementations are likely to begin

[131, 124, 184]. We consider a finite coherent photon tunneling $J \neq 0$ between adjacent cavities which splits the local polaritonic resonances into delocalized global modes.

We obtain the NESS by diagonalizing the super-operator $\hat{\mathcal{L}}$ after exploiting the permutational symmetry of the system to significantly decrease the number of unique density matrix elements and additionally retaining only basis states allowing a maximum of $P = 4$ excitations in the system, using algorithms described in Appendix C For linear cavities this permits the numerical analysis of driving strengths up to $\Omega/\gamma_p \approx 0.3$ without significant truncation errors. With a resonator nonlinearity $g, U \neq 0$, occupation of higher-lying levels is suppressed enabling accurate exact diagonalization results for yet stronger driving, confirmed by extensive quantum trajectory calculations.

Figures 3.4 (a) and (b) show generalizations of the single resonator spectra discussed above for the relatively small rate of photon hopping $J/\gamma_p = 1$. We expect the response of the systems to strongly resemble the 'local' physics in this regime, as the photon hopping is essentially a weak perturbation on top of the atom-cavity coupling.

The homogeneous nature of our chosen driving, achievable for instance by splitting a single laser source and coupling each split beam to a resonator, means that the total momentum of excitations in the NESS must be zero. The one-particle excitation in the BH system is then just the zero-momentum free-particle Bloch mode $|k=0\rangle = \frac{1}{\sqrt{M}} \sum_{j=1}^{M} \hat{a}_j^\dagger |0\rangle$ excited at a laser detuning $(\Delta_c)_{|k=0>} = -2J$, as the Kerr nonlinearity does not influence a single particle. In contrast a single excitation in the JCH system can be shared between atomic and photonic degrees of freedom leading to two delocalized generalizations of the $|1, \pm\rangle$ polaritons, denoted $|k=0, \pm\rangle = A^\pm |E\rangle + B^\pm |k{=}0\rangle$. Here $|E\rangle = \frac{1}{\sqrt{M}} \sum_{j=1}^{M} \hat{\sigma}_j^+ |0\rangle$ is a delocalized atomic excitation. The coefficients $A^\pm$ and $B^\pm$ are identical in form to the coefficients $\alpha_1^\pm$,

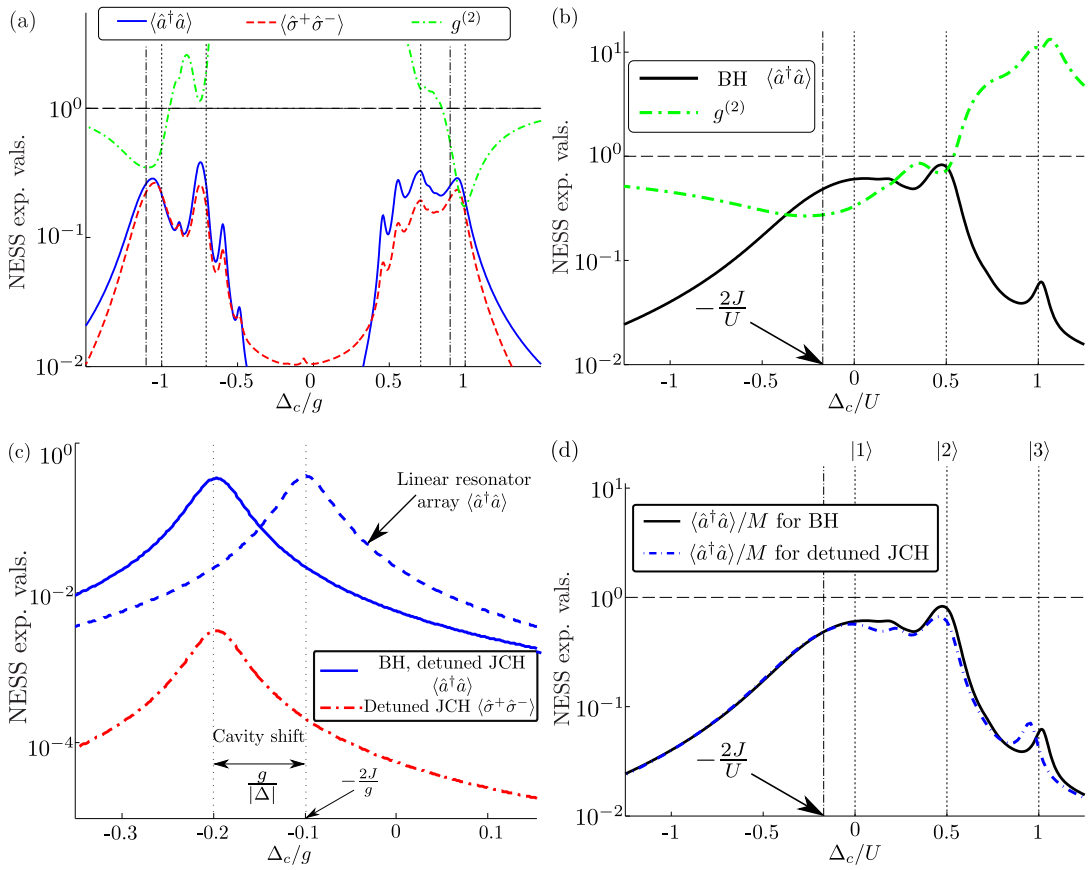


Figure 3.4. The steady state per-resonator photonic/atomic populations and $g^{(2)}$ function for homogeneously driven, cyclic three-site resonator systems described by (a) the JCH Hamiltonian (with $\Delta/\gamma_p = 2J/\gamma_p = 2$) and (b) the BH model. Vertical dashed lines indicate the location of underlying modes of an isolated resonator ($J = 0$), while vertical dash-dotted lines indicate the positions of delocalized single particle modes. The atom-resonator coupling $g/\gamma_p = 20$ for (a) and (b) is again as in Figs. 3.2, but there is now a finite photon hopping $J/\gamma_p = 1$. (c) and (d) are generalizations of the single resonator 'photonic limit' spectra of Figs. 3.2, extended to three-resonator systems with the same photon hopping. The driving rate in (c) is set at $\Omega/\gamma_p = 0.3$ to enable numerical solution, otherwise all parameters are unchanged. Note in (d) the almost complete overlap of the response of the two many-body models now in this 'photonic' limit. This agreement, however, requires an unrealistic ultra-strong value of $g/\gamma_p \approx 1.6 \times 10^4$.

$\beta_1^{\pm}$ of Eq. (3.5), after making the replacement $\Delta \to \Delta_{k=0} = \Delta - 2J$. These are resonantly excited at laser detunings $(\Delta_c)_{|k=0,\pm\rangle} = -2J - \Delta_{k=0}/2 \pm \chi^{(1)}_{k=0}$, where $\chi^{(1)}_{k=0} = \sqrt{g^2 + \Delta^2_{k=0}/4}$. As only the cavities are directly coupled there is now an additional asymmetry between photons and atoms. The resonance point for delocalized polaritons is shifted to $\Delta = 2J$ from $\Delta = 0$ found in the single resonator case. This is equivalent to setting the transition frequency of the atoms equal to the frequency of the lowest lying Bloch mode $|k{=}0\rangle$.

Relative to Figs. 3.2 (a) and (b), we see new multi-particle modes appear between the delocalized generalizations of the dressed state resonances. By an N-particle mode we mean an eigenstate of the total excitation number operator for the whole system $\hat{\mathcal{N}} = \sum_{j=1}^{M} \hat{\mathcal{N}}_j$ with eigenvalue N. For this particularly small photon hopping rate, equal to the cavity line-width, the delocalized single particle mode of the BH system is smeared into a broad hump along with delocalized two- and three- particle modes, while new features can also be discerned in the JCH spectra. Additionally, new modes appear in the JCH model at approximately the bare cavity frequency. These modes are symmetrized superpositions of '+' and '-' polaritons, and for our chosen driving strength are barely populated relative to the response of the BH model at the bare cavity frequency.

There is an asymmetry between the delocalized generalizations of the '-' and '+' wings of the JCH resonator array spectrum, despite setting $\Delta = 2J$. We note that for large photon hopping $J \gg g$ and $\Delta = 2J$, the resonator array spectrum is again symmetric about the Bloch mode frequency (not shown), though still with quantitative differences to the single resonator case. It is in the intermediate regime ($J \approx g$) that asymmetries appear, as hopping brings multiple particle global excitations into the same spectral region. A signature of this hopping-induced behavior that is particularly amenable to experimental verification is a measurement of the photon correlation at the two delocalized single-particle resonance frequencies. For

this particular driving and cavity loss rate, the values are $g^{(2)} \approx 0.18, 0.35$ for the $|k = 0, \pm\rangle$ modes respectively. Meanwhile $g^{(2)}$ reaches a minimum of ≈ 0.26 at the underlying single-particle mode of the BH system (indicated by the vertical dash-dotted line in Fig. 3.4 (b)). We note here again that if one assumes losses smaller than $g/\gamma_p = 20$ used here then the correlation minimum approaches zero and clear anti-bunching should be achieved, as expected.

The spectral response of far-detuned finite-size CRAs operating in the photonic limit ($-g/\Delta \ll 1$) is shown in Figs. 3.4 (c) and (d). These spectra are direct generalizations of those shown in Fig. 3.2. Again, we see that for our assumed atom-resonator couplings (i.e. $g/\gamma_p \approx 20$), the main effect of the atomic degree of freedom is to shift the free-particle mode by Δ_{shift}, in this case from the lowest Bloch mode. Figs. 3.4 (d) shows that (unrealistically) larger couplings 'matched' to a specific Kerr nonlinearity can reproduce the spectral features of a driven dissipative finite CRA with reasonable accuracy.

3.4 Larger resonator arrays

So far we have investigated CRA systems of a few sites operating either on-resonance (i.e. $\Delta/g = 0$), or in the photonic limit where the weak nonlinearity is captured by an effective BH interaction. We now demonstrate the effect of the changing nature of the polaritonic excitations and also investigate larger arrays of $M = 16$ sites as this parameter is varied about the strong-interaction regime $\Delta/g \approx 0$. Rather than construct a spectrum by varying the driving laser frequency, we instead selectively drive a particular spectral feature and vary Δ/g. Specifically, in Fig. 3.5 we show trajectory results for NESS particle numbers for larger ($M = 16$) JCH and BH arrays driven at their single particle resonances, corresponding to the driving laser detunings $\Delta_c = (\Delta_c)_{|k=0,-\rangle}$ and $\Delta_c = -2J$ respectively.

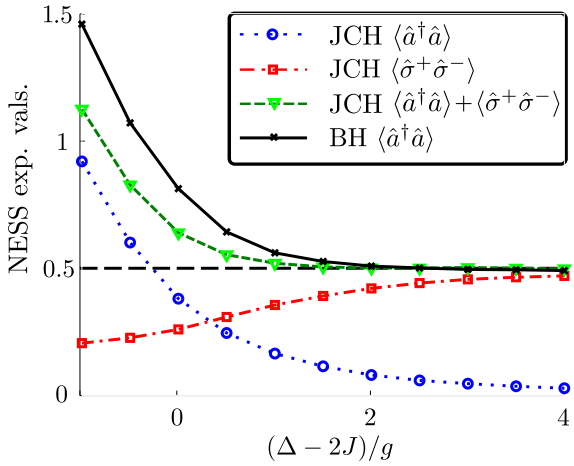


Figure 3.5. NESS particle numbers per resonator for sixteen-site Bose-Hubbard and Jaynes-Cummings CRAs driven at their single particle resonances. Parameters: photonic driving $\Omega/\gamma_p = 2$, atom-resonator coupling strength $g/\gamma_p = 20$, photon hopping rate $J/\gamma_p = 1$. Trajectory calculations retain $p = 6$ photons per resonator for the BH simulation, and $p = 5$ for the JCH. Each Jaynes-Cummings detuning Δ/g is mapped to an effective Kerr nonlinearity via Eq. (3.8) to enable a comparison.

As expected, we see the changing nature of the system's excitations reflected in a larger atomic (and smaller photonic) occupation for increasing Δ/g. For strong positive detunings, the excitations are predominantly atomic, indirectly excited via the resonator field. As we have assumed lossless atoms, the steady state corresponds to oscillations between the ground and excited states, leading to an average half atomic occupancy. Under the mapping of Eq. (3.8), this regime corresponds to a BH system with large Kerr coefficient. Under the stronger driving we have chosen for this calculation, the BH system approximately oscillates coherently between zero and one photons per resonator, with occupation of higher Fock levels suppressed. Thus, while the total excitation number for the JCH asymptotically agrees with the NESS photon number for the BH in this limit, the underlying physics is very different.

In the opposite limit $\Delta/g < 0$, the excitations of the JCH model become more photonic, and the effective Kerr nonlinearity decreases. We have already seen that

agreement between the JCH and Kerr photon number is reached far into this limit. In the intermediate regime, $\Delta/g \approx 0$, the total particle number for the JCH exhibits significant departures from the BH results. This is due both to the fact that only one component of the polaritons is driven in the JCH system, and also that this stronger driving allows access to higher-lying states ($n > 2$) outside the regime of validity for the effective Kerr strength definition. We therefore see non-trivial differences between the models both in spectra measured as a function of driving laser frequency, and as a function of the nonlinearity.

3.5 The strong nonlinearity limit: fermionization and crystallization of photons in CRAs

We have demonstrated that the NESS in resonator arrays governed by the JCH and BH Hamiltonians are in general different, and so care must be taken when interpreting numerical models which use a simplified Bose Hubbard description to extrapolate the experimentally relevant Jaynes Cummings physics. We now evaluate two non-equilibrium effects in the large nonlinearity regime recently studied assuming a BH description, with proposals to experimentally realise such effects in Jaynes-Cummings type CRA systems.

3.5.1 Fermionization in coupled resonator arrays

Recently an exploration of the ultra-strong nonlinearity regime in a three-site driven dissipative Bose-Hubbard model was undertaken [104]. For a closed coherent system it was found that as the Kerr strength U approached infinity, double occupancy of any resonator was completely suppressed. This allows the system's bosonic wavefunctions to be mapped to those of an equivalent fermionic system via a Jordan-

Wigner transformation [185]. In this interpretation double occupancy is prevented by fermionic statistics rather than a hard core bosonic interaction. The authors found that a cyclic system's N-particle eigenfunctions and corresponding energies can then be identified uniquely for a given total particle momentum. Subjecting the system to coherent driving and a finite particle loss rate from each resonator results in readily classifiable peaks in the resonator occupancy as a function of the driving laser frequency.

Figure. 3.6 (a) reproduces such a spectrum for a homogeneously driven ($\Omega_j = \Omega, \forall j$) minimal $M = 3$ resonator BH system. For the spectral range shown the only possible modes that can be observed in the hard core limit NESS are the zero momentum one-particle mode, which for the BH model coincides with the Bloch mode $|k{=}0\rangle$ of an empty resonator system, and a mode formed from two particles with opposite momenta $k = \pm 2\pi/3$. We show spectra for a strong nonlinearity $U/\gamma_p \gg 1$ (allowing for any number of photons per resonator in the calculation) and for the true fermionized limit $U \to \infty$ (when strictly $p = 1$ photon per resonator is retained in calculations) illustrating the convergence. Also shown in Fig. 3.6 (a) are NESS photon numbers for a strongly detuned JCH system operating in the 'photonic regime', again computationally retaining multiple and single photons per resonator. As expected from the discussion in Sec. 3.2, good agreement with the BH results is observed, albeit for unrealistically large values of the light-matter coupling g.

Moving beyond from the photonic limit we now explore the novel physics of ultra-strong nonlinearity in JCH systems operating in the regime of strongest interaction between resonators and atoms, i.e. $\Delta/g \approx 0$. In this regime correspondence between the models is less clear and the fully polaritonic nature of excitations must be taken into account. To recover physics which resembles hard-core photons we operate in the limit $g/\gamma_p \gg 1$, along with $g \ll \omega_c$ to satisfy the rotating wave approximation, and drive at $\omega_L \approx \omega_1^-$ near the $|1,-\rangle$ polaritonic resonance of isolated resonators.

Under these conditions the only relevant states in each resonator are the ground state and $|1,-\rangle$ polaritonic state.

Figure 3.6 (b) shows hard-core JCH model spectra for two different atom-resonator detunings $\Delta = 0$ and $\Delta = g$. Increasing the coupling g while holding the ratio Δ/g fixed leads to a qualitatively similar evolution of spectral features as in the BH model. A two-particle excitation splits from the single particle resonance and asymptotically approaches a splitting that only depends on J and Δ/g. For the coupling $g/\gamma_p \sim 800$ used, good agreement is seen in Fig. 3.6 (b) between the full JCH model and the spectrum obtained when retaining only the $p = 1$ photons per resonator necessary to describe the hard-core polariton limit. We see that even in the ultra-strong non-linearity limit of the JCH model the internal structure of polaritons (governed by the parameter Δ/g) still plays a crucial role in determining the location and amplitude of spectral features. This behavior is a result of the effective hopping, driving and loss rates for polaritons being different from the bare photon parameters. Indeed the effective polaritonic hopping rate is $J_{\text{pol}} = |\beta_1^-|^2 J$, the effective driving rate is $\Omega_{\text{pol}} = (\beta_1^-)\Omega$, while the loss rate is $\gamma_{\text{pol}} = |\beta_1^-|^2 \gamma_p$, where β_1^- is the coefficient controlling the photonic component of the $|1,-\rangle$ polaritons defined in Sec. 3.1. This reflects that the hopping, driving and loss processes involve only the photonic component of the polaritons. Thus, on resonance ($\Delta/g = 0 \Rightarrow \beta_1^- = \frac{1}{\sqrt{2}}$) we see that the peak separation is $J_{\text{pol}} = J/2$ as seen in Fig. 3.6 (b).

Focusing on experimentally measurable photonic quantities, in Fig. 3.6 (c) we track for both models as a function of their nonlinearity the photon density-density correlations measured at the two-particle peak on a single site via $g^{(2)}(j,j)$ and between neighboring sites via $g^{(2)}(j,j+1)$. The spectral location of the zero-momentum two-particle modes for the JCH and BH systems, are found using the results in Refs. [97] and [186] respectively. As outlined in Ref. [104] at small nonlinearities the two-particle peak resides within the one-particle spectral feature and so correlations

inherit Poissonian statistics from the driving laser. Larger nonlinearities split the two-particle resonance from the one-particle peak, as shown in Figs. 3.6 (a) and (b), and lead to strong bunching. For very strong nonlinearities on-site anti-bunching is expected as the two excitations are distributed in such a way that the pair of photons are never in the same resonator resulting in the nearest neighbor correlations becoming large. Such considerations, being consequences of generic nonlinear behavior, lead to qualitatively similar correlation functions for both the driven dissipative JCH and BH models. Thus fermionized photons are a feature of the on-resonance JCH model as well, once the different spectral frequencies for correlation measurements are taken into account.

3.5.2 Polariton crystallization

Another intriguing phenomenon of interacting photons in resonator systems, photon crystallization, was recently predicted to occur in a one dimensional ring of optical cavities with Kerr-type nonlinearity [105]. Driving lasers with a phase difference of $\pi/2$ between each site k, i.e. $\Omega_k = \Omega \exp(ik\pi/2)$, create a flow of bosons around the system. The contact interaction energy U was found to result in a 'crystallization' of particles as they flowed around the ring, even in the presence of dissipation. The signature of this effect was identified in the particle density-density correlations $g^{(2)}(j,k)$ between cavities j and k, measured in the system's steady state.

On-site anti-bunching is accompanied by nearest-neighbor density-density correlations stronger than correlations between more distant cavities. The conclusion drawn in Ref. [105] was that particles form 'dimers' of light, which flow around the system. We demonstrate here that this dimerization can also be seen in a JCH system outside the photonic limit. The additional degree of freedom in the atom-resonator detuning Δ allows the strength of this effect to be adjusted on demand.

We study a system of $M = 16$ coupled Jaynes-Cummings resonators under periodic boundary conditions. In addition to the relative phases, we must choose the frequency of our driving lasers. For a BH-type system, a laser detuning $\Delta_c = 0$ directly drives the single particle $k = \pi/2$ mode. For the JCH model we choose to drive the delocalized generalization of the single-particle polaritonic mode $|1, -\rangle_{k=\pi/2}$ to produce an analogous effect.

To obtain the steady states used in Fig. 3.7, we began time averaging at $g(T_{\text{start}}) = 500$. We found that $N_T = 5000$ time-steps $g(\delta t) = 0.5$, with around 100 trajectories retaining $\chi = 40$ states in the matrix product state representation, were sufficient to obtain acceptable statistical fluctuations ($\approx 0.1\%$) in the NESS expectation values we are interested in. Retaining three or four photons in the bare resonator basis was sufficient for systems in the 'atomic' regime ($\Delta \geq 0$), but more were required to properly evaluate steady state quantities for $\Delta < 0$ (results not shown).

We see in Fig. 3.7 (a) that the signatures of crystallization show up in our polaritonic system – there is a larger probability of finding photons in neighboring cavities than in cavities further apart. We have additional control over the atom-resonator detuning Δ, which allows us to tune the nature of the system's excitations either more photonic $\Delta/g < 0$, or atomic $\Delta/g > 0$. We see that the crystallization effect becomes weaker for larger Δ as the atoms and resonators are tuned away from resonance, while on-site anti-bunching is enhanced. This is a consequence of resonator photons being strongly coupled to the two-level systems, which hold most of the excitation for large Δ, but longer-range correlations tend to unity. Figure 3.7 (b) shows the actual photonic and atomic expectation values per resonator, for the three detunings considered illustrating the changing make-up and associated enhanced photon anti-bunching. Also shown for comparison in Figure 3.7 are results for the driven dissipative Kerr system like that considered in Ref. [105]. We conclude that the 'dimerization' predicted in that work for the BH model persists in CRA

calculations using the full atom-resonator Hamiltonian without approximations, and that some degree of tunability should be observable by bringing the cavities in and out of resonance while maintaining significant resonator populations.

3.6 Discussion

We have proposed and analyzed excitation number and photon coherence spectra for small to medium sized weakly driven dissipative coupled resonator systems described by the Jaynes-Cummings-Hubbard Hamiltonian. Simulations were performed using the full JCH Hamiltonian without approximations, using model parameters realizable by current state-of-the-art technology. We have also presented analogous spectra for resonator arrays governed by the Bose-Hubbard model, drawing attention to the differences in experimentally accessible observables between the two models. These differences arise primarily because of the composite nature of the elementary excitations of the JCH Hamiltonian, leading to readily identifiable unique spectral characteristics. Therefore we conclude that when simulating coupled resonator arrays the full JCH Hamiltonian must be used in calculations to properly account for the underlying physics.

Generalizations of two bosonic interaction-induced non-equilibrium phenomena were observed in the NESS of CRAs modeled retaining the richer JCH physics, with additional tunability. The fingerprints of the polaritonic equivalents of 'fermionic' photons and photon crystallization exhibit subtle departures from the pure bosonic case, detectable via experimentally accessible spectral quantities.

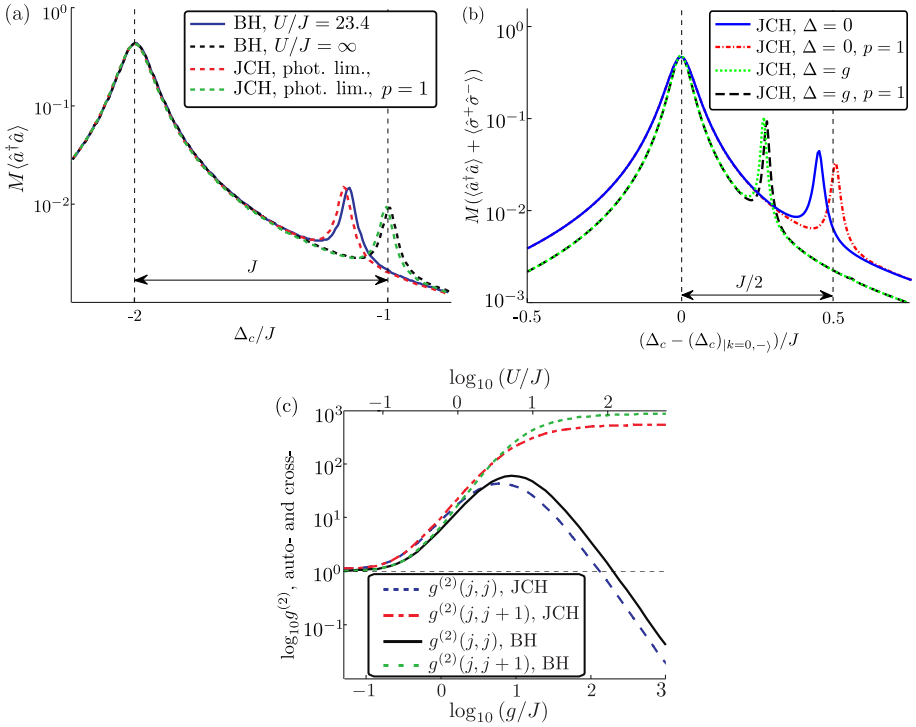


Figure 3.6. (a) The one and two particle peaks (right and left features, respectively) for a homogeneously driven three-resonator BH model in the strongly nonlinear regime (solid blue, $U/J = 23.4$), and the hard core limit ($p = 1$, dotted black). Spectra for larger U approach the hard core limit asymptotically. Parameters: photon hopping rate $J/\gamma_p = 20$, driving $\Omega/\gamma = 0.5$. Also shown are results for a strongly detuned JCH system operating in the photonic limit with $\Delta/g = -10$, and an unrealistically large atom-resonator coupling $g/\gamma_p \approx 2 \times 10^5$. (b) Analogous photon number spectra for the JCH model with $g/\gamma_p \approx 800$ (chosen according to Eq. 3.8), and the photon driving and tunneling rates as in (a), for two different atom-resonator detunings Δ/g (dashed and dash-dotted). Again, the hard-core spectra are recovered in the limit $g \to \infty$. The horizontal axis is taken relative to the single particle spectral position $(\Delta_c)_{|k=0,-\rangle}$, different for each Δ. (c) The auto- and cross- photon correlation functions measured at the two particle peak as a function of the nonlinearity in both the BH and JCH ($\Delta = 2J$) Hamiltonians. JCH systems with different couplings g are compared with Bose-Hubbard systems whose strength $U = U(g)$ (see upper horizontal axis) is obtained from Eq. 3.8. Note these calculations are performed at the lower driving $\Omega/\gamma_p = 0.25$, to avoid truncation errors at low nonlinearity.

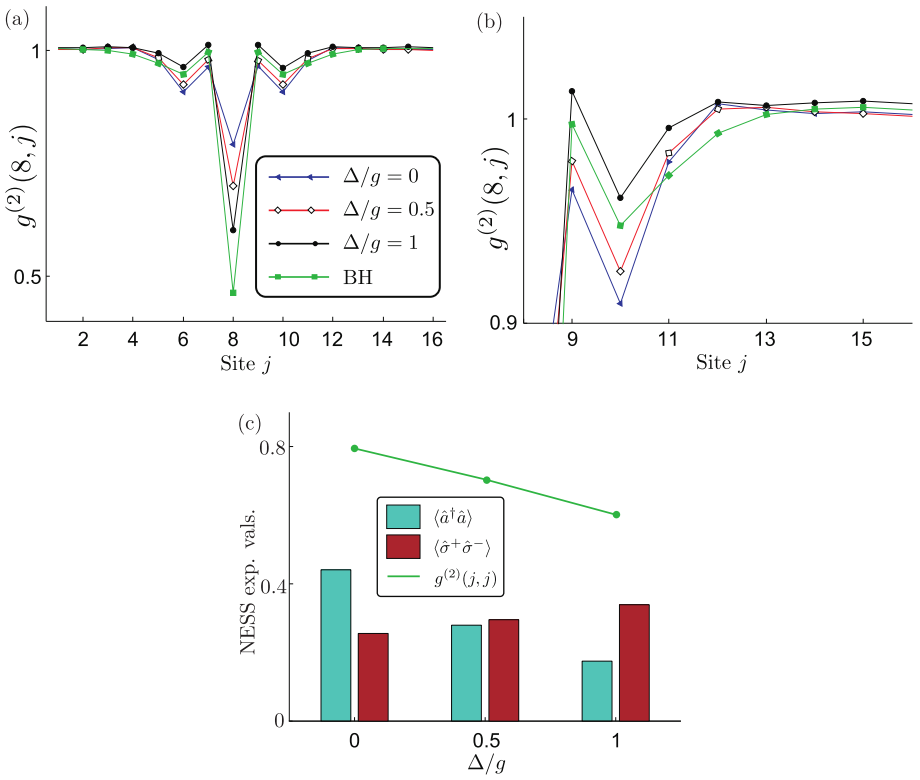


Figure 3.7. (a) Steady state photon density-density correlations for a cyclic 16 site JCH system, driven by lasers exciting the $\pi/2$ momentum mode of the system. Thin lines between markers are drawn to guide the eye. Parameters: hopping $J/\gamma_p = 2$, atom-resonator coupling $g/\gamma_p = 10$, driving strength $|\Omega_k|/\gamma_p = 2$. Also shown (solid green) are density-density correlations for a $M = 16$ site system with 'matched' Kerr nonlinearity $U/\gamma_p \approx 6$ in each resonator, and otherwise identical parameters. (b) Closer view of the correlation functions. (c) The relative atomic and photonic population in each resonator in the steady state for the three different values of atom-resonator detuning chosen, as well as the on-site photon correlation function.

Chapter 4

Robustness of bistabilities in driven photonic resonator arrays

In the last chapter, we looked at two different *physical* models describing CRAs, and showed that it is in general necessary to fully describe JCH physics when simulating resonator arrays. In this chapter, we study different approximation schemes to the fully quantum mechanical nature of CRAs, to determine the level of description necessary to accurately explore non-equilibrium CRA physics. We treat driven-dissipative quantum lattice models with differing complementary approaches, with a focus on resolving the question of the existence of multiple steady states in these systems. Multiple steady states in driven resonator arrays have been recently predicted [187], and sharp 'switching' signatures of bistability have appeared in other works [178]. In particular, we evaluate the validity of employing a non-equilibrium generalisation of a product Gutzwiller-type ansatz for the state of the system. Such an ansatz is known to qualitatively reproduce the features of ground state phase diagrams for lattice systems in the thermodynamic limit as in Section 1.3, but the utility of extension to non-equilibrium settings is not yet fully understood. Sound physical insight into phenomena such as bistability expected in extended driven-dissipative systems requires a confidence in the numerical approaches employed.

The validity and truncations introduced by common approximations must be well understood. The use of approximations of one type or another are especially relevant for these systems, as the exponential scaling of Hilbert space with system size makes full simulation of even a few sites intractable.

We find for the Gutzwiller ansatz approach non-physical results similar to those predicted by a semi-classical theory, and contrast these with rigorous fully quantum-mechanical trajectory and master equation simulations, calculated using the time evolving block decimation algorithm. Specifically, we find that bistabilities predicted by mean-field calculation schemes are inhibited once quantum correlations are correctly accounted for. A remnant of the bistability is observed as a peak in the correlations of the system, but we can conclude that no bistability is to be expected in physical realisations of coupled resonator arrays.

Throughout, we consider a minimal model which nevertheless possesses features common to more realistic quantum lattice models – coherent hopping linking adjacent sites, coherent driving, and incoherent loss processes. The model is 'minimal' in that each lattice site features just two states. However, we note that it represents a limit attainable in principle in coupled resonator arrays – the dynamics of arrays with sufficiently large nonlinearities are effectively restricted to the ground (vacuum) and lowest-lying eigenstate at each site, as discussed in Section 3.5.1.

We begin with a semi-classical treatment, in which both inter- and on-site operator expectation values are assumed to factorize, and find multiple stable stationary states. Next, we retain a full description of on-site quantum correlations while factorizing the system density matrix into a local tensor product. In equilibrium studies, mean field theory is known to qualitatively reproduce the features of ground-state phase diagrams of, for instance, the Bose Hubbard and JCH models. However, the validity of extension to non-equilibrium setting is not a priori obvious. We find that this mean-field approach also predicts bistability in our model system.

A product state ansatz is by its nature incapable of providing information on longer-range quantum and classical correlations in the system. To assess the effect of retaining all correlations, we employ the time evolving block decimation (TEBD) algorithm to simulate master equation dynamics of large lattice systems, showing that the switching behaviour is washed out. We find evidence that a single unique solution exists for all parameter regimes.

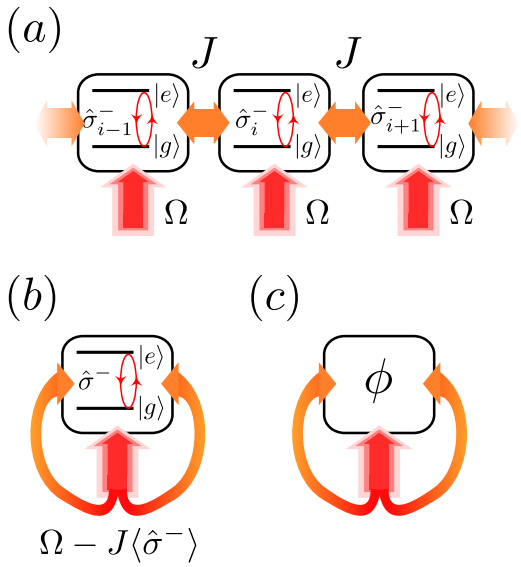


Figure 4.1. Schematics of the lattice models we consider, at different levels of approximation (by which we mean accounting for quantum correlations more or less fully). (a) The full infinite one-dimensional description. Each site i is described by a single two-level system with levels $|e\rangle, |g\rangle$ with lowering operator $\hat{\sigma}_i^-$, and is coherently coupled to each of its nearest neighbours with rate J. Vertical red arrows represent a coherent driving. (b) Breaking inter-site correlations leads to an effective single-site description, with an effective driving amplitude dependent of the state of the system itself via $\langle\hat{\sigma}^-\rangle$. (c) Further breaking on-site correlations in the semi-classical picture, the quantum operator $\hat{\sigma}^-$ is replaced by the c-number ϕ and the two-level discrete quantum nature of each site is neglected, following the procedure found in e.g. [182].

4.1 Model

We treat a system of coupled two-level systems described by the Pauli matrices, each with transition frequency ω_c, and an external driving field of frequency $\omega_L = \omega_c - \Delta_c$ inducing coherent oscillation between the levels. In a frame rotating at the driving frequency the Hamiltonian is (setting $\hbar = 1$):

$$\hat{\mathcal{H}} = \sum_j \left[\Delta_c \hat{\sigma}_j^+ \hat{\sigma}_j^- + \Omega(\hat{\sigma}_j^+ + \hat{\sigma}_j^-)\right] - J \sum_{\langle j,j' \rangle} \hat{\sigma}_j^\dagger \hat{\sigma}_{j'}. \tag{4.1}$$

Here J is the coherent tunnelling rate between neighbouring TLS, and Ω is the coherent driving amplitude. For ease of understanding in the context of the other chapters of this thesis, we emphasise that the system we study in this chapter is composed only of coupled two level systems, with no photonic degree of freedom. Where Ω represents the amplitude of a coherent photon drive in other chapters, here it is the amplitude of a field driving transitions between $|g\rangle$ and $|e\rangle$ on each site. The index j runs over the discrete lattice sites in our model, and $\langle j, j' \rangle$ denotes the set of nearest neighbours. We incorporate a generic local loss term which acts to incoherently de-excite the upper level of each TLS with characteristic rate γ_p. We take the evolution of the total system density matrix ρ to be described by a quantum master equation $\dot{\rho} = \hat{\mathcal{L}}[\rho]$, where

$$\hat{\mathcal{L}}[\rho] = \frac{1}{i}[\hat{\mathcal{H}}, \rho] + \frac{\gamma_p}{2} \sum_{j=1} \left(2\hat{\sigma}_j^- \rho \hat{\sigma}_j^+ - \hat{\sigma}_j^+ \hat{\sigma}_j^- \rho - \rho \hat{\sigma}_j^+ \hat{\sigma}_j^-\right). \tag{4.2}$$

The non-equilibrium steady state of the system is described by the density matrix $\rho_{\rm ss}$ which satisfies $\hat{\mathcal{L}}[\rho_{\rm ss}] = 0$, and NESS observables are measured with respect to this state, $\langle \hat{O} \rangle_{\rm ss} \equiv {\rm Tr}(\hat{O}\rho_{\rm ss})$.

We now begin a rigorous characterisation of the non-equilibrium steady states of the lattice model. We aim to unravel the genuine physical properties of the steady

state using increasingly sophisticated descriptions.

4.2 Semi-classical approximation

We first generate the equation of motion for the TLS dipole transition expectation $\phi_j = \langle \hat{\sigma}_j^- \rangle(t)$ from Eq. (4.2):

$$\frac{d\phi_j(t)}{dt} = \frac{1}{i}\left[\Delta_c \langle \phi_j \rangle - [\Omega - J(\phi_{j-1} + \phi_{j+1})]\left(2\langle \hat{\sigma}_j^+ \hat{\sigma}_j^- \rangle - \mathbf{I}_j\right)\right] - \frac{\gamma_p}{2}\phi_j. \tag{4.3}$$

The evolution of $\phi_j(t)$ depends on both the analogous quantity at neighbouring sites ($\phi_{j\pm1}$), and also the expectation value of a product of operators $\langle \hat{\sigma}_j^+ \hat{\sigma}_j^- \rangle$. Continuing on and evaluating equations of motion for each of these operators leads to an infinite hierarchy of coupled differential equations. Here we make two simplifying assumptions in order to proceed.

First, we shall be concerned in this work with large driven lattices, i.e. a number of lattice sites tending to infinity. A useful consequence of the resulting translational invariance is that all local observables are position-independent, e.g. $\phi_j = \phi, \forall j$. Second, in this section we replace the quantum mechanical operators by c-numbers, which is equivalent to assuming that expectation values of products of operators factorize into products of expectation values of operators. Thus $\hat{\sigma}_j^- \to \phi_j$, $\hat{\sigma}_j^+ \hat{\sigma}_j^- \to \phi_j^* \phi_j$, etc.

Making use of these assumptions in Eq. (4.3) leads to

$$\frac{d\phi}{dt} = \frac{1}{i}\left[\Delta_c \phi - (\Omega - 2J\phi)(2\phi^*\phi - 1)\right] - \frac{\gamma_p}{2}\phi. \tag{4.4}$$

The steady state reached in the long-time limit under the combined influence of driving and losses implies $\dot{\phi} = 0$. This condition yields a cubic equation in the

real-valued atomic excitation $x = \phi^*\phi$:

$$64\tilde{J}^2x^3 + 16(2\tilde{J}\tilde{\Delta}_c' - \tilde{\Omega}^2)x^2 + \left(4(\tilde{\Delta}_c')^2 + 16\tilde{\Omega}^2 + 1\right)x - 4\tilde{\Omega}^2 = 0, \qquad (4.5)$$

where we have renormalised the Hamiltonian couplings by the loss rate, $\left(\tilde{J}, \tilde{\Omega}, \tilde{\Delta}_c\right) \equiv (J/\gamma_p, \Omega/\gamma_p, \Delta_c/\gamma_p)$. Equation (4.5) exhibits either one or three real-valued solutions, depending on the physical parameter set. We have confirmed numerically that the solutions of Eq. (4.5) and their stability correspond to those of Eq. (4.4). The number and stability of solutions in phase space for this semi-classical treatment is shown in Fig. 4.2.

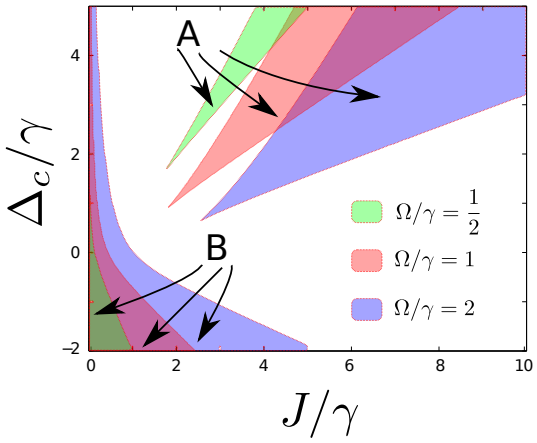


Figure 4.2. Stability regions for the semi-classical treatment of the spin model of Eq. (4.1) as a function of normalised tunnelling $\tilde{J} = J/\gamma_p$ and driving detuning $\tilde{\Delta}_c = \Delta_c/\gamma_p$, for different driving amplitudes Ω. There are three real solutions to the resulting cubic equations in the coloured regions. For the regions marked 'A', two of these solutions are stable. For the regions marked 'B', just one is stable. The white regions have only a single real solution, which is stable.

An interesting feature of Fig. 4.2 is the existence of multiple steady states arising from the cubic terms in Eq. (4.5). These are a direct consequence of the nonlinearities introduced by the self-consistent factorisation of the semiclassical approach. It is tempting therefore to discount the existence of bistable behaviour as a trivial consequence of this potentially unphysical treatment of the system. We evaluate

this idea in the following sections by examining the existence of bistable behaviour in more rigorous treatments of Eq. (4.3).

4.3 Mean field

At a higher level of description, we now keep a fully quantum representation of the local physics, while breaking inter-resonator correlations. This is done by making a product ansatz $\rho = \otimes_j \rho_j$ for the total system density matrix. Inserting this ansatz into the master equation Eq. (4.2), and again invoking translational invariance $\rho_j = \rho, \forall j$, we find the total system can be described by a single TLS governed by the effective Hamiltonian

$$\hat{\mathcal{H}}_{\mathrm{mf}} = \Delta_c \hat{\sigma}^+ \hat{\sigma}^- + \hat{\sigma}^+(\Omega - J\phi) + \hat{\sigma}^-(\Omega - J\phi^*), \tag{4.6}$$

where $\phi = \langle \hat{\sigma}^- \rangle$. This effective system is still subject to loss of excitation at the same rate γ_p as the original model, as described by a mean-field master equation $\dot{\rho} = \hat{\mathcal{L}}_{\mathrm{mf}}[\rho]$, with

$$\hat{\mathcal{L}}_{\mathrm{mf}}[\rho] = \frac{1}{i}[\hat{\mathcal{H}}_{\mathrm{mf}}, \rho] + \frac{\gamma_p}{2}\left(2\hat{\sigma}^- \rho \hat{\sigma}^+ - \hat{\sigma}^+ \hat{\sigma}^- \rho - \rho \hat{\sigma}^+ \hat{\sigma}^-\right). \tag{4.7}$$

The generator $\hat{\mathcal{L}}_{\mathrm{mf}}[\rho]$ is time-dependent via the terms $\phi(t) = \mathrm{Tr}(\rho(t)\hat{\sigma}^-)$. We see that the self-energy in the rotating frame Δ_c is also unchanged relative to the full model. The driving terms $\hat{\sigma}^{\pm}$ show that the effect of the mean-field decoupling can be interpreted as modifying the effective driving amplitude such that it depends on the state of the system itself via ϕ, i.e. $\Omega \to \Omega'(\phi) = \Omega - J\phi$. In this sense the system is 'reflexive' – the nature of the driving depends on the state of the system itself.

We now explicitly solve for the steady states of the effective system of Eq. (4.7),

and their stability. Here we derive a criterion for the stability of the self-consistent solutions to the mean field treatment of the system of coupled TLS, described by the Hamiltonian Eq. (4.6).

First we turn a matrix representation of the single-site density matrix

$$\rho = \begin{bmatrix} \rho_{11} & \rho_{12} \\ \rho_{21} & \rho_{22} \end{bmatrix} \tag{4.8}$$

into a column vector $\tilde{\rho} = [\rho_{11}, \rho_{21}, \rho_{12}, \rho_{22}]^T$. The Liouvillian generator $\hat{\mathcal{L}}$ then has the matrix representation

$$\hat{\mathcal{L}}[\phi] = \begin{bmatrix} -\gamma & -i(\Omega - J\phi) & i(\Omega - J\phi^*) & 0 \\ -i(\Omega - J\phi^*) & -\gamma/2 + i\Delta_c & 0 & i(\Omega - J\phi^*) \\ i(\Omega - J\phi) & 0 & -\gamma/2 - i\Delta_c & -i(\Omega - J\phi) \\ \gamma & i(\Omega - J\phi) & -i(\Omega - J\phi^*) & 0 \end{bmatrix}. \tag{4.9}$$

Nonlinearity enters the problem via the term $\phi = \mathrm{Tr}(\rho\hat{\sigma}^-)$, which in terms of the elements of the density matrix can be written $\phi = \rho_{12}$.

For convenience when discussing the stationary solutions $\rho^* = [\rho^*_{11}, \rho^*_{21}, \rho^*_{12}, \rho^*_{22}]^T$ of $\hat{\mathcal{L}}[\phi]\rho^* = 0$, we divide by γ so as to obtain a generator $\tilde{L}[\phi]$ independent of the loss rate. In order to discuss the stability of the self-content solutions $\tilde{\rho}^* = [\rho^*_{11}, \rho^*_{21}, \rho^*_{12}, \rho^*_{22}]^T$ which satisfy both $\tilde{\mathcal{L}}[\phi]\tilde{\rho}^* = 0$, and $\tilde{\rho}^*_{12} = \phi$, we must first transform the problem to a system of differential equations in real variables. We do this by exploiting the Hermiticity of the density matrix, defining $\tilde{\rho}_{11} = a$, $\tilde{\rho}_{12} = b + ic$

and $\tilde{\rho}_{21} = b - ic$ and $\tilde{\rho}_{22} = d$. We then have the relation

$$\begin{bmatrix} \tilde{\rho}_{11} \\ \tilde{\rho}_{21} \\ \tilde{\rho}_{12} \\ \tilde{\rho}_{22} \end{bmatrix} = \begin{bmatrix} 1 & 0 & 0 & 0 \\ 0 & 1 & -i & 0 \\ 0 & 1 & +i & 0 \\ 0 & 0 & 0 & 1 \end{bmatrix} \begin{bmatrix} a \\ b \\ c \\ d \end{bmatrix}. \tag{4.10}$$

Additionally reducing the system by using the unit trace condition $a + d = 1$, we find the evolution:

$$\frac{d}{dt} \begin{bmatrix} a \\ b \\ c \end{bmatrix} = \begin{bmatrix} -a - 2\tilde{\Omega}c \\ \tilde{J}c(2a-1) - \frac{1}{2}b + \tilde{\Delta}_c c \\ \tilde{\Omega}(2a-1) - \tilde{J}b(2a-1) - \tilde{\Delta}_c b + \frac{1}{2}c \end{bmatrix}, \tag{4.11}$$

leading to the Jacobian

$$\mathbf{J} = \begin{bmatrix} -1 & 0 & -2\tilde{\Omega} \\ 2\tilde{J}c & -\frac{1}{2} & \tilde{J}(2a-1) + \tilde{\Delta}_c \\ 2\tilde{\Omega} - 2\tilde{J}b & -\tilde{J}(2a-1) - \tilde{\Delta}_c & -\frac{1}{2} \end{bmatrix}. \tag{4.12}$$

Solving for the stationary state of Eq. (4.11) yields a cubic equation. In terms of the variable $c = \mathfrak{Im}(\tilde{\rho}_{12}) = \mathfrak{Im}(\phi)$, this cubic is

$$0 = \tilde{J}^2 c^3 + \tilde{J}\left(\tilde{J} + 2\tilde{\Delta}_c\right) c^2 + \left(\tilde{\Delta}_c^2 + 2\tilde{\Delta}_c\tilde{J} + 2\tilde{\Omega}^2 + \frac{1}{2}\right) c + \left(\tilde{\Delta}_c^2 + \frac{1}{4}\right), \tag{4.13}$$

where $\tilde{J} = J/\gamma$, $\tilde{\Omega} = \Omega/\gamma$ and $\tilde{\Delta}_c = \Delta_c/\gamma$. Characterisation of the fixed points of the system follow from the properties of the Jacobian of Eq. (4.12) [188]. Namely if the eigenvalues all have real part with a magnitude less than 0, then the system is stable at the fixed point. If any eigenvalue has a real part with a magnitude greater than 0, then the point is unstable. Finally if the largest real part of the eigenvalues

is equal to 0, the Jacobian matrix does not allow for an evaluation of the stability.

Again, multiple real and stable solutions arise because of terms cubic in the density matrix elements, as shown in Fig. 4.3 (a). These results are reminiscent of the semi-classical bistable regions of Fig. (4.2) in that there are triangular zones of multiple stable solutions in the (Δ_c, J) plane. These zones become broader at larger driving amplitudes under both a semi-classical and mean-field treatment. However, the zones occupy quantitatively different locations, and additionally the set of solutions marked 'B' in Fig. (4.2) have no equivalent under a mean-field treatment.

Figure 4.3 (b) shows the steady state reached by time evolving a system initialised in the ground state under the action of Eq. (4.7). We see that on crossing between parameter regimes with one and two stable solutions, the steady state may 'switch' sharply from one solution to another. The initial condition lies in the domain of attraction of different distinct solutions for different parameter regimes.

Bistability therefore survives the introduction of a proper treatment of local quantum and classical correlations. However, the mean-field approach is still non-linear due to the factorisation of long-range correlations. Treating these properly is the subject of the next section.

Figure. 4.4 presents an analysis of the bifurcations appearing on moving between different regions of phase space. The steady state properties of this model are surprisingly rich given its simplicity – we see supercritical pitchfork and saddle node bifurcations arising at the boundaries of phase space regions corresponding to different numbers of stable solutions.

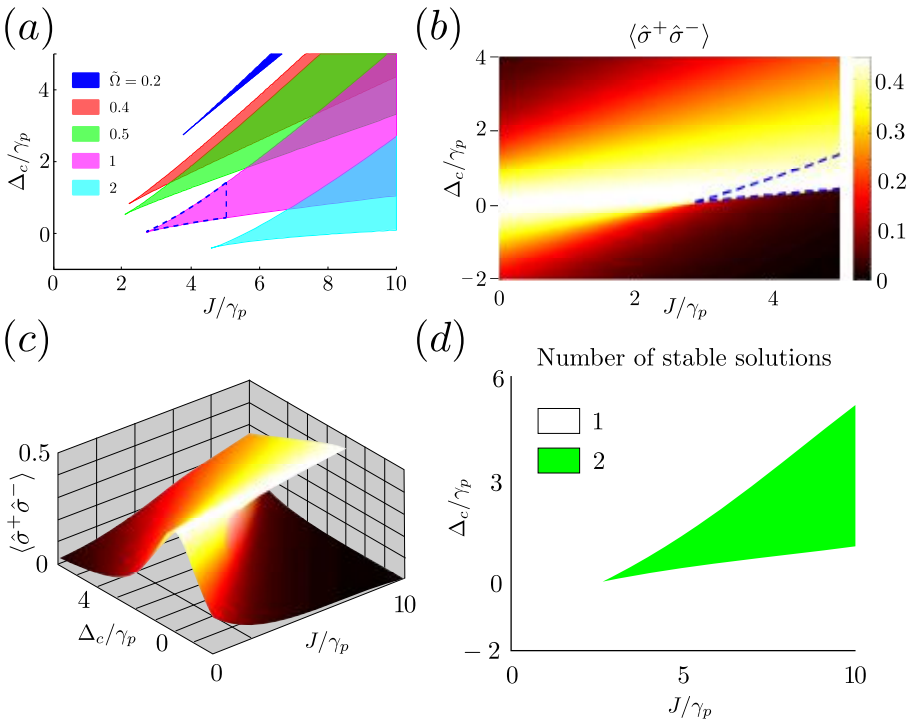


Figure 4.3. (a) Regions of bistability (coloured) in the steady state solution for the lattice model of Eq. (4.6), for different normalized drivings $\tilde{\Omega} \equiv \Omega/\gamma$. (b) Mean-field steady state population as a function of laser detuning Δ_c and resonator coupling J for the driving strength $\Omega/\gamma = 1$. The steady states are calculated by time-evolving an initial ground state under the action of Eq. (4.7). The steady state switches between distinct solutions at the boundary of the bistable region. (c) All possible stable steady state solutions as a function of laser detuning Δ_c/γ and coupling rates J/γ, showing the onset of the sharp transition at the lower boundary of the dashed triangular region of (a) and (b), corresponding to the opening up of multiple stable solutions to $\hat{\mathcal{L}}\rho = 0$. (d) The number of stable solutions at fixed drive strength $\tilde{\Omega} = 1$.

4.4 Fully quantum model

We now treat the driven-dissipative CRA in a numerically exact way, using a matrix product operator (MPO) representation for the state of the lattice [172]. We have already defined and discussed the important features of MPOs in Section 2.5, however briefly recap here for convenience.

In general, the density matrix describing a one dimensional finite system com-

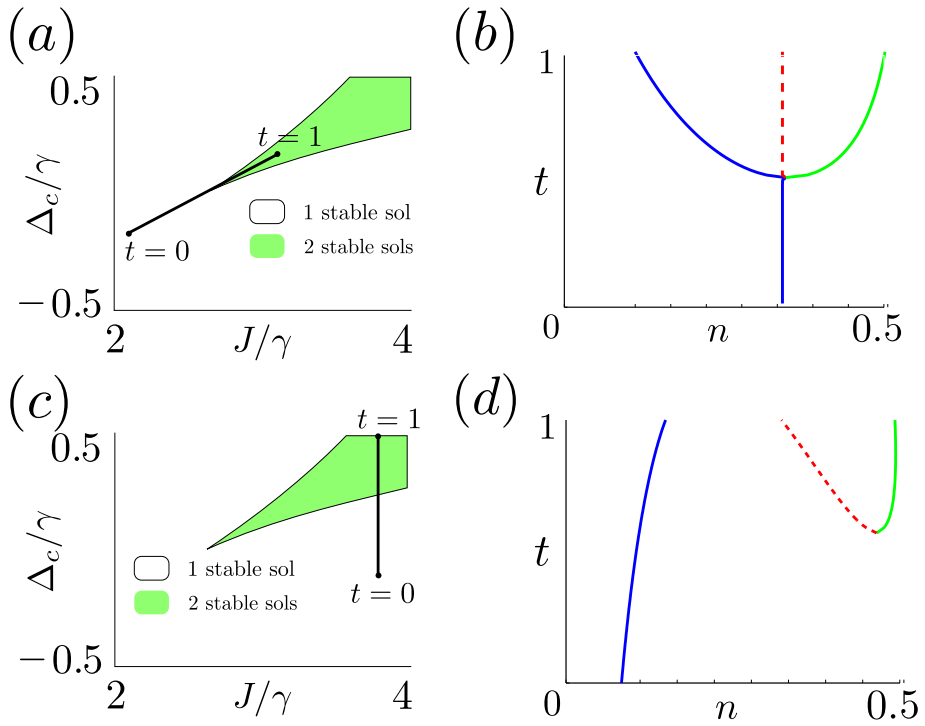


Figure 4.4. Analysis of steady states and their stability for the mean-field model. The parameter $t \in [0, 1]$ parameterises two different paths through parameter space. (a) Passing exactly through the tip of the bistable region. For the specific driving amplitude $\Omega/\gamma = 1$ of this calculation, we may show that the 'tip' of this region occurs at $(J/\gamma, \Delta_c/\gamma) = (\sqrt{31}/2, 0) \approx (2.78, 0)$. (b) Shows the corresponding solutions for the steady state atomic excitation $n = \langle \hat{\sigma}^+ \hat{\sigma}^- \rangle$. We observe a supercritical pitchfork bifurcation. (c) and (d) are analogous plots for a path at fixed coupling J into the bistable region.

posed of M sites with a local d-dimensional Hilbert space can be expanded as

$$\rho = \sum_{j_1=1}^{d^2} \cdots \sum_{j_M=1}^{d^2} c_{j_1 \cdots j_M} \left(\sigma^{[1]j_1} \cdots \sigma^{[M]j_M} \right). \tag{4.14}$$

Here $\{\sigma^{[m]j_m}\}, j_m = 1, \cdots d^2$ is a set of d^2 matrices forming a basis for the local Hilbert space of resonator m. A MPO representation expresses the expansion coefficients in the form of a product of matrices, as

$$c_{j_1 j_2 \cdots j_M} = \mathbf{\Gamma}^{[1]j_1} \lambda^{[1]} \mathbf{\Gamma}^{[2]j_2} \lambda^{[2]} \cdots \mathbf{\Gamma}^{[M]j_M}, \tag{4.15}$$

where $\mathbf{\Gamma}^{[m]j_m}$ is a matrix of dimension at most $\chi \times \chi$ for site m, indexed by the physical index j_n for that site, and $\lambda^{[m]}$ is a diagonal matrix. The utility of the MPO representation is that while formally (for $d = 2$ as we consider in this Chapter) a $\chi = 4^{M/2}$ is required to exactly represent the state of an M-site lattice, for many one-dimensional systems a small χ of order 10's – 100's is sufficient for an accurate representation. Thus an appropriate choice of the $\mathbf{\Gamma}$ matrices allows us to overcome the intractable exponential scaling of a full description. Intuitively, χ gives a measure of the inter-site correlations of either classical or quantum origin through the system. Highly correlated states require a larger χ for an accurate description. The extreme case $\chi = 1$ recovers the mean field product ansatz, as correlations between sites are completely neglected. The Gutzwiller ansatz $\rho = \otimes_j \rho_j$ is then a special case of the MPO representation. Increasing χ connects the mean-field approximation in one limit with the exact description limit $\chi \to \infty$. The density matrix product operator may be efficiently evolved the under master equation evolution of Eq. (5.2) using the time evolving block decimation (TEBD) algorithm to obtain the stationary state.

Before discussing the large system regime to connect with the infinite systems treated so far, we first examine the approach to this limit by simulating arrays of finite, increasing size.

Figure 4.5 shows calculated steady state excitation at the central site $j_c = \lfloor M/2 \rfloor + 1$ of systems of increasing size M, calculated by fixing the MPO parameter $\chi = 50$ and evolving the initial condition $|g\rangle \otimes |g\rangle \otimes \cdots \otimes |g\rangle$ until convergence is reached. For the smallest systems, the spectra are dominated by a series of peaks occurring at laser detunings consistent with transitions between two of their eigenmodes. For mesoscopic system sizes, however (beginning at roughly $M = 19$ sites), a sharp 'jump' appears, reminiscent of the mean field spectra in Fig. 4.3 (b). The gap between the upper and lower 'branches' of the spectrum widens.

The appearance of this mean field-like feature at large χ is somewhat surprising.

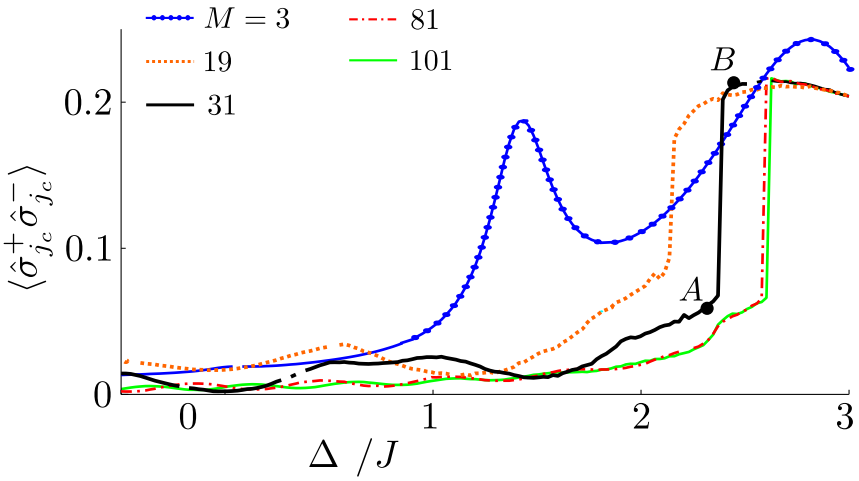


Figure 4.5. Steady state excitation $\langle \hat{\sigma}^+_{j_c} \hat{\sigma}^-_{j_c} \rangle$ at the central site j_c of finite sized systems of M sites, for increasing M, as a function of the driving detuning Δ_c. We see the emergence of a sharp MF-like transition for large enough systems. Parameters: driving $\Omega/\gamma_p = 1$, $J/\gamma_p = 4$.

Its presence in mean field calculations (corresponding to $\chi = 1$) is explicitly traceable to the unphysical de-correlation between different system sites. This de-correlation led to equations cubic in the density matrix elements, ultimately allowing for multiple distinct stable steady states. The calculations presented in Fig. 4.5 however are much higher-order, allowing limited but significant correlations to be described.

Given the evidence in Fig. 4.5, it is tempting to suspect the existence of multiple study states in the fully quantum model, qualitatively similar to results predicted by a mean-field approach. In this picture, a 'switch' from one steady state to another occurs as the (fixed) initial state passes from one steady state's domain of attraction to the other's. We find this not to be the case. Further increasing the MPO parameter χ 'washes out' the switching, as in Fig. 4.6. We note that the steady state has not converged with χ even for calculations with $\chi = 200$, which require several days for an $M = 31$ site system and a 2GHz machine. Convergence with χ is problematic in the vicinity of the 'cliff', marked with a shaded blue rectangle in Fig. 4.6. This is an indication that significant correlations are required to fully describe the NESS

in this region. Around this parameter range, the steady state exhibits markedly non-trivial long ranged correlations, as it reorganises itself between the 'low-density' and 'high-density' regimes with distinct density-density correlation signatures to the left and right of this region. In contrast results outside this region agree for even modest χ.

This picture is quantified by calculating the entropy S (defined in Section B.1.2 of Appendix B) of the steady state measured across the middle of the system, giving a measure of the entanglement of the state. Figure 4.6 (b) shows that the region near the 'cliff' feature coincides with a dramatic elevation in the total half-chain correlations of the state.

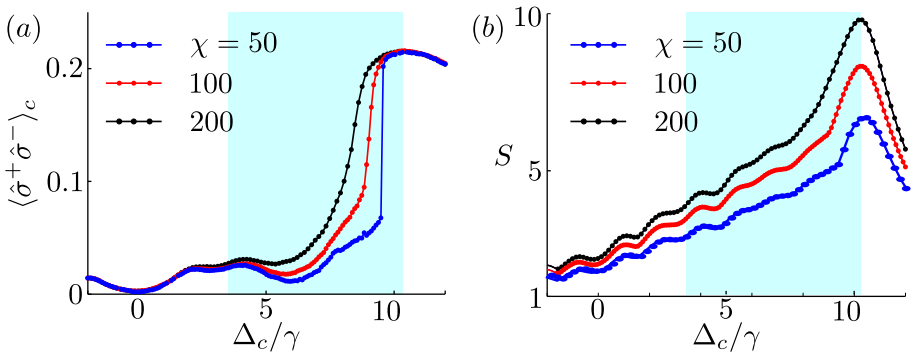


Figure 4.6. (a) Steady state excitation at the middle of an $M = 31$ site system for increasing matrix product operator parameter χ. (b) The entropy of the Schmidt coefficients S measured through the central site of the system. Physical parameters are as in Fig. 4.5, except for χ.

4.5 A quantum trajectory treatment

We have shown that an increasingly 'quantum' description of driven-dissipative lattice models destroys bistable behaviour predicted by lower-order approximations. We have also seen that accurate simulation of physically realistic phenomena is challenging even for simple systems – while simulation accuracy may be improved by increasing the internal MPS truncation parameter χ, calculation rapidly becomes

impossible for even modest χ. To address this last point, we look now at an alternative approach to calculating quantum steady states, paying particular attention to the agreement / disagreement between the two methods in the 'problem regions'. Rather than solving for quantum master equation dynamics, we instead evolve independent stochastic wave functions using TEBD, averaging over trajectories and simulation time steps to arrive at steady state expectation values. Details on the algorithm are provided in Appendix B. For the large systems we consider, expansion of these wavefunctions in the full product state basis is impossible. We therefore employ a matrix product state (MPS) representation which, similarly to matrix product operators discussed above, compresses the description of a system's wave function. Again a truncation parameter χ controls the size of the quantum correlations which the MPS may encode. We compare the two calculation schemes in Fig. 4.7.

Interestingly, convergence in trajectory results is achieved even for $\chi = 50$. This indicates that there is little quantum entanglement in the system's steady state. MPO master equation calculations in Fig. 4.6 for the same parameter sets failed to converge even for the computationally challenging case $\chi = 200$. The density matrix representing the mixed state of the lattice must encode both long-ranged quantum *and* classical correlations with the same χ. Disambiguating between the two is nontrivial, and either may contribute significantly to the difficulty in describing the state. The inability of the density matrix to capture the physics for low χ is thus an indication that classical correlations dominate the deviations from mean field and wash out the sharp transition. The convergence difficulty occurs roughly where bistability was seen in lower order approximations.

Meanwhile individual trajectories are pure quantum states, possessing only quantum long-range order. It is the averaging procedure over multiple trajectories (see Appendix B) which leads again to a statistical mixture of quantum states. A smaller

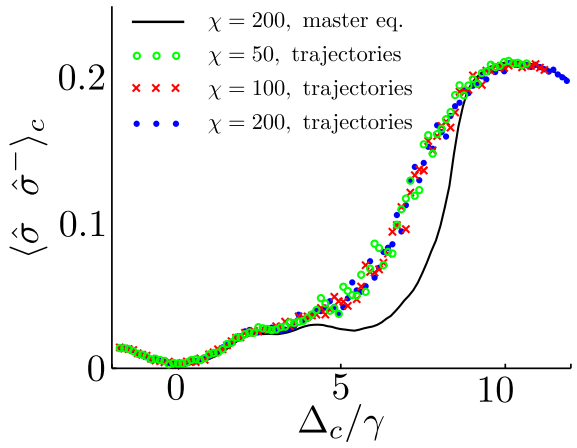


Figure 4.7. Comparison of master equation and quantum trajectory results. Only the most accurate (highest χ) master equation calculation from Fig. 4.6 is shown. We see convergence of the trajectory results (to within statistical noise) even for modest χ, which does not agree with the master equation simulation in the 'problem area'. Trajectory calculation parameters: each expectation value at fixed Δ_c is calculated as the average over $N_{\text{traj}} = 10$ trajectories. Averages for each trajectory are additionally performed over $N_T = 2 \times 10^4$ time steps of size $(\delta t)J = 10^{-2}$ beyond a time $T_{\text{start}}J = 20$ allowing for transient dynamics to die out.

χ may therefore describe the steady state more accurately than MPO calculations with larger χ for the following reason. Individual trajectories $|\Psi_i(t)\rangle$ calculated using an MPS parameter $\chi = \chi_{\text{MPS}}$ lead to a contribution to the density matrix $|\Psi_i(t)\rangle\langle\Psi_i(t)|$, with rank upper bounded by χ^2_{MPS}. However, when adding the contributions of multiple trajectories to obtain an ensemble-averaged estimate of the density matrix, it is important to note that the set of possible matrix product states of dimension χ do not form a closed vector space [189]. Instead, the rank of the estimated density matrix is upper-bounded by $N_{\text{traj}}\chi^2_{\text{MPS}}$.

This observation has significant computational implications. In general, the number of operations involved in time evolving an MPO or MPS is $N_{\text{MPO}} = Md^6\chi^3_{\text{MPO}}N_T$, $N_{\text{MPS}} = N_{\text{traj}}Md^3\chi^3_{\text{MPS}}N_T$, respectively. Here M is the number of lattice sites, d is the local dimension of Hilbert space, and N_T the number of time steps in the simulation. The number of stochastic wave functions evolved is denoted by N_{traj},

though we note that trajectory simulations are ideally suited for being run in parallel. The relative merits of using either approach is then situation-dependent. Steady states exhibiting sizeable long-ranged classical correlations require a large χ_{MPO} for an accurate description. If $\chi_{\mathrm{MPO}} \gg \chi_{\mathrm{MPS}}$ (where χ_{MPS} is the truncation parameter required for comparable convergence of trajectory results) then it may be computationally favourable to employ quantum trajectories, even compensating for the overhead of running multiple trajectories for longer simulation times.

4.6 Conclusions

We have compared steady state properties of a minimal driven-dissipative quantum lattice model predicted by increasingly accurate representations of the lattice system. We examined the semiclassical behaviour in which all quantum correlations are trivially neglected, and a mean-field type treatment where long-ranged correlations are factorised. Finally we also fully accounted for the quantum nature of the lattice using a matrix product operator formalism. We found that the lower levels of description led to unphysical artefacts in steady state observables. In particular a multiplicity of stable steady states in certain parameter regimes, manifesting as a sharp 'switch' between expectation values on changing lattice parameters. This bistability is ultimately caused by nonlinearities introduced by factorising approximations which try to embed correlation effects locally.

A study using a rigorous matrix product state description (which fully captures the physics given a large enough truncation parameter χ) showed that such artefacts are 'washed out' at a sufficiently descriptive level. It was also observed that accurate simulation of even simple systems is surprisingly difficult – the appearance of bistability coincides with a considerable increase in the complexity of the fully quantum description of the steady state. Specifically, correlations are seen to exhibit

a peak in the same region as the steady state reorganises between two qualitatively different regimes.

We note that this elevation in long-ranged correlations may be experimentally accessible in for instance coupled resonator arrays, as they appear despite the presence of loss. Such arrays feature macroscopic lattice spacing and are open to external optical probes, allowing direct measurement of cross-site photon-photon correlations which in turn reflect properties of long-ranged order in the NESS.

Finally we addressed this calculational difficulty by contrasting two schemes for calculating steady state lattice properties. We found that in certain regimes quantum trajectory simulations may outperform direct master equation simulation.

Chapter 5

Repulsively induced photon super-bunching in driven resonator arrays

The previous two Chapters presented an analysis of what constitutes a physically and computationally valid description of CRAs. Building on this foundation, we now study in the next chapters several novel phenomena observable in driven-dissipative arrays.

Our understanding of driven strongly correlated photons in CRAs is in its infancy, making it desirable to concretely connect the non-equilibrium properties of CRAs with their more familiar equilibrium structure. To this end, there have been recent efforts to identify signatures of the equilibrium quantum phase transition [12, 14, 58, 13, 11, 73, 61, 79, 71] (discussed in Section 1.3) which survive under lossy dynamics [84, 85, 86, 177, 190].

We propose an alternative scheme to chart different regions of parameter space and connect non-equilibrium observables to the underlying Hamiltonian properties. We envisage a resonator array driven to a non-equilibrium steady state (NESS) by external lasers, with the laser frequency chosen such that the unit-filled (on

average one particle per site) equilibrium ground state is selectively addressed and populated. Features arising from the details of the non-equilibrium operation appear in collected emission statistics, including a counter-intuitive many-body repulsion-induced bunching of the emitted photons, the magnitude of which is controllable via tuning Hamiltonian parameters. Unveiling the mechanism underlying this surprising bunching is the focus of this Chapter. This 'super bunching' arises in spite of relatively strong onsite repulsive interaction. Novel super bunched light sources far exceeding the bunching of thermal photons may find important applications in ghost imaging technologies [191, 192, 193] and all-optical simulation of two-photon correlations in quantum walks [194, 195].

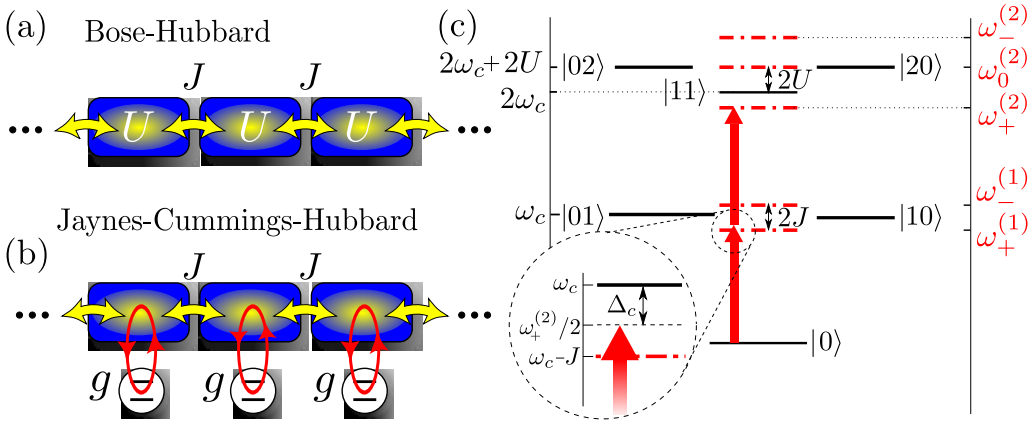


Figure 5.1. (a) Schematic of the driven-dissipative Bose-Hubbard model, featuring local coherent driving, photon tunnelling and a purely photonic Kerr nonlinearity. (b) The driven-dissipative Jaynes-Cummings model with effective photon nonlinearity generated by couplings to two-level systems. (c) Diagram showing the bare basis (solid black) and eigen-frequencies (dash dotted red) of the driven BH system for the minimal system of $M = 2$ resonators. The laser is tuned so that two laser photons (vertical red arrows) are capable of promoting the system to the lowest-lying 2-photon state.

In this work we first focus on a minimal-sized two-site resonator system. Such dimers or a photonic molecules are expected to be experimentally viable in the near future in different technologies ranging from semiconductors to Circuit QED. We initially study the dimer system for resonator nonlinearities of the repulsive Kerr-

type, as shown in Fig. 5.1 (a), to illustrate our driving scheme. We then analyze the Jaynes-Cumming type encountered when resonator modes interact with embedded effective two-level systems [45], as in Fig. 5.1 (b). In keeping with the spirit of Chapter 3 where we investigated the validity of modelling the JCH with the simpler, single species Bose-Hubbard (BH) model [137], we also demonstrate that the super-bunching signature persists under a JCH description. Moving beyond this minimal 'array', bunched emission is also demonstrated in near future experimentally accessible mesoscopic-sized systems [131, 196].

5.1 System

We consider a one-dimensional chain of M coupled single-mode optical resonators under periodic boundary conditions. Each resonator of frequency ω_c is coherently coupled to its two nearest-neighbors. External lasers coherently drive each resonator in-phase with amplitude Ω. In a frame rotating at the laser frequency ω_L, the system Hamiltonian is:

$$\hat{\mathcal{H}}^{(M)} = \sum_{j=1}^{M} \left[\Delta_c \hat{a}_j^\dagger \hat{a}_j + U \hat{a}_j^\dagger \hat{a}_j^\dagger \hat{a}_j \hat{a}_j + \Omega(\hat{a}_j^\dagger + \hat{a}_j) \right] - J \sum_{<j,j'>} \left(\hat{a}_j^\dagger \hat{a}_j' \right). \tag{5.1}$$

Here U is the Kerr nonlinear strength, J is the photon hopping rate, Ω is the photon driving strength, and $\langle j, j' \rangle$ denotes nearest neighbour resonators. We take all Hamiltonian coupling rates to be much smaller than the bare resonator frequency, $U, J, \Omega \ll \omega_c$. The operators $\hat{a}_j$ are the photon destruction operators for the photon mode in resonator j. The detuning of the driving laser frequency from the bare cavity frequency is $\Delta_c = \omega_c - \omega_L$.

Markovian photon loss processes from each cavity are incorporated via a quantum master equation formalism for the evolution of the system density matrix ρ, $\dot{\rho} =$

$\mathcal{L}^{(M)}[\rho]$, where

$$\mathcal{L}^{(M)}[\rho] = \frac{1}{i}[\hat{\mathcal{H}}^{(M)}, \rho] + \gamma_p \sum_{j=1}^{M} \hat{\mathcal{D}}_{\hat{a}_j}[\rho]. \tag{5.2}$$

The dissipative part of the dynamics is described by $\hat{\mathcal{D}}_{\hat{a}_j}[\rho] = \hat{a}_j \rho \hat{a}_j^\dagger - \frac{1}{2}(\hat{a}_j^\dagger \hat{a}_j \rho + \rho \hat{a}_j^\dagger \hat{a}_j)$. The NESS of the system is described by the density matrix $\rho_{\rm ss}$ which satisfies $\mathcal{L}[\rho_{\rm ss}] = 0$. Intra-resonator observables are measured with respect to this state, $\langle \hat{O} \rangle_{\rm ss} \equiv {\rm Tr}(\hat{O}\rho_{\rm ss})$, and may be experimentally inferred from measurements on the emitted photons using existing techniques.

5.2 Two-resonator 'dimer'

We begin by analyzing the simplest possible driven resonator 'array' consisting of just $M = 2$ resonators, which serves to illustrate clearly our scheme for accessing the unit-filled ground state. Figure 5.1 (b) shows the low-lying eigenstructure of the undriven Hamiltonian of Eq. (5.1) for $M = 2$, and our driving scheme. The two one-photon eigen-frequencies are the symmetric (+) and anti-symmetric (-) Bloch modes, and lie (in the bare frame, with $\Omega = 0$) at $\omega_\pm^{(1)} = \omega_c \mp J$, with corresponding eigenstates $|1_\pm\rangle = \frac{1}{\sqrt{2}}(|01\rangle \mp |10\rangle)$. The two-photon eigen-frequencies are $\omega_0^{(2)} = 2\omega_c + 2U$, $\omega_\pm^{(2)} = 2\omega_c + U \mp \sqrt{U^2 + 4J^2}$, with eigenstates $|2_0\rangle$, $|2_\pm\rangle$:

$$\begin{aligned}
|2_-\rangle &= \frac{-\sqrt{2}\Delta_c|11\rangle + J(|02\rangle + |20\rangle)}{\sqrt{2\Delta_c(2\Delta_c + U)}}, \\
|2_0\rangle &= \frac{1}{\sqrt{2}}(|02\rangle + |20\rangle) \\
|2_+\rangle &= \frac{\sqrt{2}(\Delta_c + U)|11\rangle + J(|02\rangle + |20\rangle)}{\sqrt{2(\Delta_c + U)(2\Delta_c + U)}},
\end{aligned}$$

where $\Delta_c = \frac{1}{2}\left(\sqrt{U^2 + 4J^2} - U\right)$ is the driving laser detuning to be discussed momentarily. The unit-filled ground state is of frequency $\omega_+^{(2)}$. This mode undergoes a qualitative change between the extreme limits of a localized state, characterized

by vanishing on-site photon number fluctutation $\mathrm{Var}(\hat{a}_j^\dagger \hat{a}_j) \to 0$ for $U \gg J$, to a coherent superposition state with $\mathrm{Var}(\hat{a}_j^\dagger \hat{a}_j) \to \frac{1}{2}$ for $U \ll J$. For increasing system size, the behavioural transition of the ground state becomes sharper, approaching the celebrated Bose-Hubbard Mott-insulating to superfluid phase transition in the infinite system limit [7].

To selectively populate the unit-filled ground state of Eq. (5.1) for a particular set of Hamiltonian parameters, we set the driving laser frequency such that two laser photons are resonant with the lowest-lying two photon mode, i.e. $2\omega_L = \omega_+^{(2)}$, implying a laser detuning

$$\Delta_c(J,U) = \frac{1}{2}\left(\sqrt{U^2 + 4J^2} - U\right). \tag{5.3}$$

Fixing $\Delta_c = \Delta_c(J,U)$ for a given hopping and nonlinearity, we now examine which features of the underlying Hamiltonian mode structure leave fingerprints on experimentally accessible photonics observables. In our non-equilibrium setting the photon number is not an integer and the photon number variance is not an informative order parameter. To compensate for these non-equilibrium effects, we instead focus on the local zero-time photon correlation function $g^{(2)} \equiv g_j^{(2)} = \langle \hat{a}_j^\dagger \hat{a}_j^\dagger \hat{a}_j \hat{a}_j \rangle / \langle \hat{a}_j^\dagger \hat{a}_j \rangle^2$, a statistical quantity directly accessible in CRA setups through standard methods like homodyne detection [30]. We note that $g^{(2)}$ measurements may be particularly valuable in weakly-driven systems, where the excitation number may be very small, but normalised statistical quantities may be collected over longer times.

Figure 5.2 (a) shows $g^{(2)}$ measured in the NESS of a BH dimer pumped at the laser detuning of Eq. (5.3), for a range of tunnelling rates and nonlinearities (J,U). The diagram is broadly divided into three regions, defined by Poissonian ($g^{(2)} \approx 1$), anti-bunched ($g^{(2)} < 1$) and bunched ($g^{(2)} > 1$) statistics. Notably, there is a critical coupling rate J_{crit} between the resonators below which bunching does not occur for

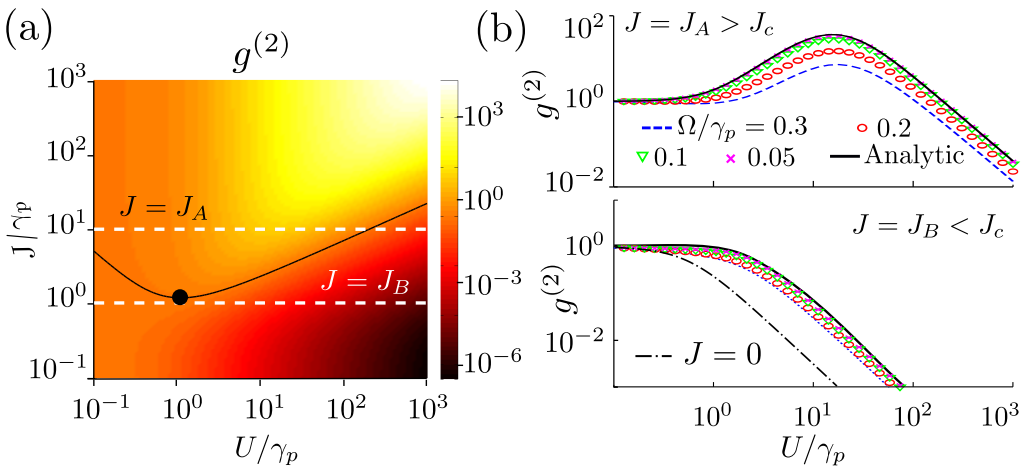


Figure 5.2. (a) Emitted photon statistics as a function of J and U for a dimer ($M = 2$) of resonators driven according to Eq. (5.3). Black curve: analytic result for $g^{(2)} = 1$. Black dot: the point $(J_c/\gamma_p, U_c/\gamma_p)$ where bunching sets in. (b) 'Slices' along the dotted lines in (a), above and below the critical hopping amplitude at which the bunching feature appears, for decreasing driving strengths, down to the infinitesimal limit (solid black lines).

any value of nonlinearity, suggesting that the bunching arises from a co-operative many body effect in the NESS. Figure 5.2 (b) shows the qualitative difference in the behaviour of the correlation function above and below this critical point. For comparison, an isolated resonator driven at it's single-particle (unit-filled) resonance never exhibits bunched signatures (see dash-dotted line in lower panel of Fig. 5.2 (b)).

At low nonlinearities $U \ll \gamma_p$, the dimer is driven at the frequency of the zero-momentum Bloch mode, and its response is approximately linear. The NESS is a coherent state, inheriting Poissonian statistics with $g^{(2)} = 1$ from the driving laser, and average population $\langle \hat{a}_j^\dagger \hat{a}_j \rangle = (2\Omega/\gamma_p)^2$, for all J. At the other extreme, taking the hardcore limit $U \gg \gamma_p$ (while also remaining in the regime $U \ll \omega_c$), no more than a single photon per resonator can be injected, and the problem is reduced to two coupled two-level systems whose statistics are completely anti bunched ($g^{(2)} = 0$), with mean excitation number per resonator $\lim_{U\to\infty}\langle \hat{a}^\dagger \hat{a} \rangle = x(2x+1)/((2x+1)^2 + xy)$, where $x \equiv (2\Omega/\gamma_p)^2$ and $y \equiv (J/\Omega)^2$.

Away from these extreme limits, in the region of parameter space where J and U are comparable, the emitted light is bunched, for hopping rates larger than a critical rate $J > J_c$. This is counter-intuitive, as we are probing a two-photon state with significant repulsion favouring separation, and yet we find an enhanced probability of photons being emitted together, relative to the statistics of the driving. This physics is reminiscent of many-boson bound states and localised breather modes in the Bose-Hubbard model [197, 198, 199, 200, 201], however we show below that our bunching is qualitatively different.

We derive features of this bunched region by considering the limit of infinitesimal driving. Figure 5.2 (b) shows that the correlation function approaches a limiting behaviour as $\Omega/\gamma_p \to 0$, an observation confirmed by perturbatively expanding the elements of the NESS density matrix $\rho_{\rm ss}$ in increasing powers of the driving strength, then solving for $g^{(2)}$ [88]. That is, we solve for $\rho_{\rm ss}$ satisfying $\mathcal{L}^{(M)}[\rho_{\rm ss}] = 0$ in a minimal basis consisting of states with at most two photons in the system, where the super-operator $\mathcal{L}^{(M)}$ is defined in Eq. (2). We recursively solve for density matrix elements at increasing powers of the weak driving strength Ω/γ_p.

For notational convenience, we label the basis states in the following way: $|00\rangle \to 1$, $|10\rangle \to 2$, $|01\rangle \to 3$, $|11\rangle \to 4$, $|20\rangle \to 5$, $|02\rangle \to 6$. The symmetry of our system under exchange of resonators $1 \Leftrightarrow 2$ allows for a considerable reduction in the necessary size of the density matrix description. The assumption that the system is very weakly driven is embodied in the assumption $\rho_{11} \approx 1$.

Following the approach in Ref. [88], we derive equations involving increasing orders of the driving strength Ω/γ_p, with the goal of calculating $g^{(2)} = \rho_{55}^2/\rho_{22}$. Here we give solutions for the elements ρ_{55} and ρ_{22}, which in turn depend on other

elements:

$$\begin{aligned}\rho_{55} &= \frac{\Omega}{2\gamma_p[(2\gamma_p)^2+(2U)^2+(4J)^2]} \\ &\times \Big[\mathrm{Im}(\rho_{25})8\sqrt{2}(\gamma_p^2+U^2+2J^2-JU) \\ &+ \mathrm{Re}(\rho_{25})8\sqrt{2}\gamma_p J - \mathrm{Im}(\rho_{24})8J(-2J+U) \\ &- \mathrm{Re}(\rho_{24})8\gamma_p J\Big]\,.\end{aligned}$$

The elements ρ_{24} and ρ_{25} are given by:

$$\begin{aligned}\rho_{24} &= \Omega\frac{2\sqrt{2}J(\sqrt{2}\rho_{22}-\rho_{15})-i(2\rho_{22}-\rho_{14})(i\Delta_c+iJ+2iU-\frac{3}{2}\gamma_p)}{\left(i\Delta_c+iJ-\frac{3}{2}\gamma_p\right)\left(i\Delta_c+iJ+2iU-\frac{3}{2}\gamma_p\right)}, \\ \rho_{25} &= \Omega\frac{\sqrt{2}J(2\rho_{22}-\rho_{14})+i(\rho_{15}-\sqrt{2}\rho_{22})(i\Delta_c+iJ-\frac{3}{2}\gamma_p)}{\left(i\Delta_c+iJ-\frac{3}{2}\gamma_p\right)\left(i\Delta_c+iJ+2iU-\frac{3}{2}\gamma_p\right)}.\end{aligned}$$

These depend on the elements ρ_{14} and ρ_{15} which are proportional to the vaccuum state population, to first order in the driving

$$\begin{aligned}\rho_{14} &= \frac{4J\Omega+2i\Omega(\gamma_p-2i\Delta_c-2iU)}{(\gamma_p-2i\Delta_c)(\gamma_p-2i\Delta_c-2iU)+4J^2}\frac{\left(1+\frac{2i(\Delta_c-J)}{\gamma_p}\right)}{1+\left(\frac{2(\Delta_c-J)}{\gamma_p}\right)^2}\left(\frac{2i\Omega}{\gamma_p}\right)\rho_{11} \\ ,\rho_{15} &= \frac{2\sqrt{2}J\Omega+\sqrt{2}i\Omega(\gamma_p-2i\Delta_c)}{(\gamma_p-2i\Delta_c)(\gamma_p-2i\Delta_c-2iU)+4J^2}\frac{\left(1+\frac{2i(\Delta_c-J)}{\gamma_p}\right)}{1+\left(\frac{2(\Delta_c-J)}{\gamma_p}\right)^2}\left(\frac{2i\Omega}{\gamma_p}\right)\rho_{11}.\end{aligned}$$

Meanwhile the denominator of $g^{(2)}$ is given by

$$\rho_{22} = \left(\frac{2\Omega}{\gamma_p}\right)^2\frac{1}{1+\left(\frac{2(\Delta_c-J)}{\gamma_p}\right)^2}\rho_{11}.$$

The correlation function $g^{(2)}=\rho_{55}^2/\rho_{22}$ does not appear to be amenable to physical insight or meaningful mathematical manipulation. Instead, further progress is made by employing a pure-state ansatz $\rho_{\mathrm{ss}}=|\Psi_{\mathrm{ss}}\rangle\langle\Psi_{\mathrm{ss}}|$, valid in the low driving

regime [101] where we observe $\mathrm{Tr}(\rho_{\mathrm{ss}}^2) \approx 1$. The state $|\Psi_{\mathrm{ss}}\rangle$ is found as the stationary state (corresponding to the zero eigenvalue) of the effective Hamiltonian $\hat{\mathcal{H}}_{\mathrm{eff}}^{(M)}$ obtained by replacing $\Delta_c \to \Delta_c - i\gamma_p/2$ in Eq. (5.1), which may be interpreted as the Hamiltonian governing a single quantum trajectory, with a vanishing probability of a quantum jump ensured by taking the limit $\Omega/\gamma_p \to 0$.

Considering only the lowest excitations and exploiting the symmetry of the two-site system, we set $|\Psi_{\mathrm{ss}}\rangle = C_{00}|00\rangle + C_1(|01\rangle + |10\rangle) + C_{11}|11\rangle + C_2(|02\rangle + |20\rangle)$. We find the following results for the wave-function coefficients, after exploiting the symmetry of the system by setting $C_{02} = C_{20} \equiv C_2$ and $C_{01} = C_{10} \equiv C_1$

$$\begin{aligned} C_{00} &\approx 1, \\ C_1 &= -\frac{\Omega C_{00}}{\Delta_c - J - i\frac{\gamma}{2}}, \\ C_2 &= -\frac{\Omega C_1}{\sqrt{2}(\Delta_c + U - i\gamma_p/2)}\left(\frac{J}{\Delta_c - i\gamma_p/2} + 1\right), \\ &\times \left[1 - \frac{J^2}{(\Delta_c - i\gamma_p/2)(\Delta_c + U - i\gamma_p/2)}\right]^{-1}. \end{aligned}$$

Here Δ_c is again the laser detuning Δ_c necessary to excite the correct mode for a given Hamiltonian parameter set (U, J) according to Eq. (5.3). From these we may explicitly obtain the correlation function as $g^{(2)} = 2|C_2|^2/|C_1|^4 = 2|C_2/C_1^2|^2$ as

$$g^{(2)} = \frac{1}{\left|1 + \frac{AU}{A^2 - J^2}\right|^2},$$

where $A = \Delta_c - i\gamma_p/2$. To solve for the parameters $(\tilde{U}, \tilde{J})_{\mathrm{crit}} \equiv (U_{\mathrm{crit}}/\gamma_p, J_{\mathrm{crit}}/\gamma_p)$ at which bunching sets in, we set $g^{(2)} = 1$, and implicitly differentiate the resulting expression, setting $d\tilde{J}/d\tilde{V} = 0$, to find the minimum resonator coupling for which

bunched statistics appear

$$\tilde{J}_{\text{crit}} = \tilde{U}^4_{\text{crit}} = \sqrt{\frac{3+2\sqrt{2}}{4}}, \tag{5.4}$$

as marked in Fig. 5.2 (a). The transition from super- to sub-Poissonian statistics (i.e. where $g^{(2)} = 1$) is found to occur at $\tilde{J} \approx \sqrt{\tilde{U}/2}$ for $J \gg J_c$, while for very large but finite U/J, the exact solution may be simplified to $g^{(2)} \approx \left(\frac{\tilde{J}}{\tilde{U}}\right)^2 \left(1 + 4\tilde{J}^2\right)$.

Figure 5.3 offers physical insight into this phenomenon, showing the emission spectrum of the system as calculated from the Fourier transform $S(\omega - \omega_L)$ of the on-site steady-state auto-correlation function $S(\tau) = \langle \hat{a}^\dagger(t+\tau)\hat{a}(t)\rangle$, as a function of increasing nonlinearity. The resonator coupling is sufficiently large ($J/\gamma_p = 10 > \tilde{J}_c$) to observe bunched emission (top panel of Fig. 5.3 (a)). At all nonlinearities, the spectrum is dominated by two bright features. These correspond to decays from the lower and upper one-particle states $|1_\mp\rangle$ to the vacuum $|0\rangle$, labelled lines A and B respectively.

Weaker features are also present, which do not significantly affect the steady state photon populations, but may strongly modify statistical quantities such as $g^{(2)}$. Line C in Figs. 5.3 (a) and (b) corresponds to emission from the highest two-particle state $|2_+\rangle$ to an intermediate level, as drawn in Fig. 5.3 (c). In the vicinity of the crossing of emission lines B and C at $\tilde{U}/\tilde{J} = (9 - \sqrt{17})/4$, the population in $|2_-\rangle$ reaches a maximum, as photons emitted as part of the line B decay process may transfer population instead to $|2_-\rangle$. Further, calculating projections into the bare basis, we find that there is a greater probability of finding the two photons of the mode $|2_-\rangle$ in the same resonator than distributed between them, relative to the driven $|2_+\rangle$ mode. This is reflected in the enhanced probability of simultaneous emission of two photons ($g^{(2)} > 1$) around this crossing. In contrast the mode $|2_+\rangle$ favours delocalising its two photons relative to the statistics of the driving laser.

Thus, we observe either approximately coherent, or anti-bunched light in all regions of parameter space except in the vicinity of the crossing of lines B and C. This underlying mechanism makes the photon bunching qualitatively different that that of discrete breather modes in dissipative nonlinear lattices [202, 203].

For resonator couplings $J < \gamma_p$, the global physics of the system resembles that of an isolated nonlinear resonator driven at it's resonance frequency, such that anti-bunching is always expected – in spectral terms, the crossing of lines B and C is hidden inside the coalesced lines A and B of Fig. 5.3.

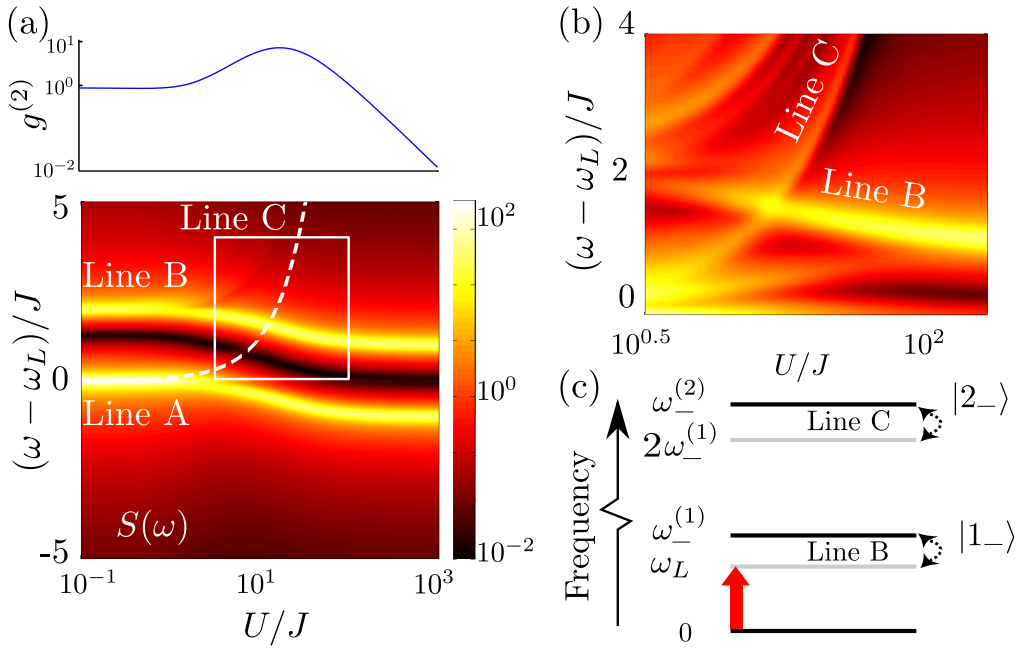


Figure 5.3. (a) Lower: Emission spectral function relative to the laser frequency $|S(\omega - \omega_L)|^2$ with increasing nonlinearity U at a fixed hopping $J/\gamma_p = 10$. At our weak driving ($\Omega/\gamma_p = 0.3$), the spectrum is dominated by transitions between the ground and one-particle manifold (bright lines A and B). Weaker features involving the two-particle manifold are also present, for instance the dashed curve highlighting line C. Upper: the zero-time correlation function $g^{(2)}$. (b) Closer view of the region of parameter space bounded by the white box in (a), but calculated at the higher driving $\Omega/\gamma_p = 1$ to highlight the crossing of the features labelled Lines B and C. (c) Transitions involved in spectral lines B and C, with only the relevant modes drawn.

5.3 Bunching in larger systems

We now investigate how the correlations presented in Fig. 5.2 (b) evolve as the system size increases, continuing to drive the commensurately-filled ground state. An analytic approach valid for arbitrary Hamiltonian couplings beyond $M = 2$ resonators is intractable. Instead, we numerically calculate the eigenvector of the effective Hamiltonian $\hat{\mathcal{H}}_{\text{eff}}^{(M)}$ with eigenvalue closest to zero (taking a series of successively weaker drivings Ω/γ_p to ensure convergence of observables). Exploiting the translational invariance of systems with periodic boundary conditions allows us to access systems of up to $M = 7$ resonators while retaining three photons per resonator in simulations using the techniques in Appendix C. Figure 5.4 shows the evolution of the counterintutive bunched region for increasing system sizes up to $M = 7$ resonators. We see a reduction in the magnitude and range of interaction strengths for which bunched light is observed as the system size increases. The bunching region is seen to retreat up the J-axis, while smaller interaction strengths U are necessary to induce the bunching. This explains the reduction in the magnitude of the effect observed for cross-sections at different resonator couplings in Figure 5.4 (a).

Rigorous quantum trajectory calculations based on the matrix product state representation and the time evolving block decimation algorithm [152, 153, 204] performed at a finite driving strength broadly agree with the results obtained via numerically exact diagonalisation of $\hat{\mathcal{H}}_{\text{eff}}^{(M)}$, as shown in Fig. 5.5. Each point corresponds to an average over 20 trajectories, and each trajectory is itself averaged over 15000 time steps. All calculations used a matrix product state parameter $\chi = 60$. This Figure shows that the bunched emission also occurs for larger system sizes M at finite driving amplitude. The phenomenon is therefore robust and may be expected in finite-sized experimental arrays. However, it also indicates that the precise features of the bunching region do depend on drive strength, as already observed

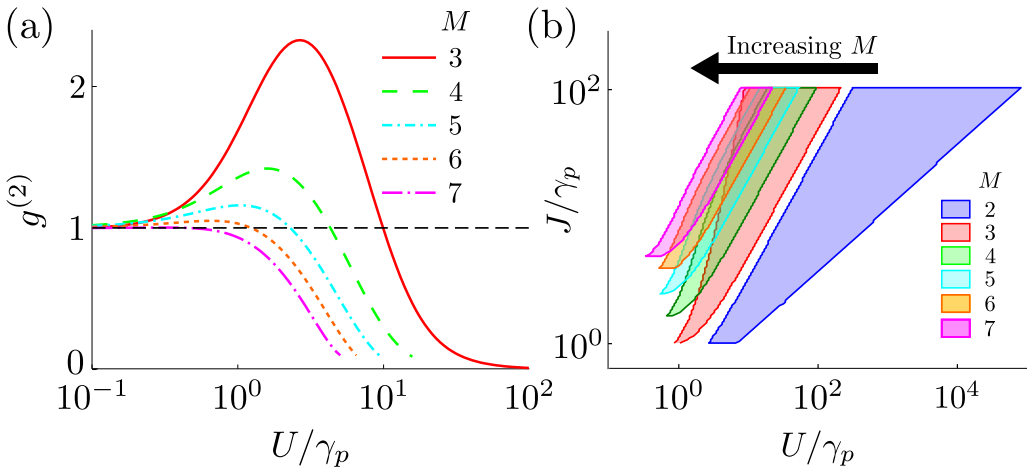


Figure 5.4. (a) Correlation function evaluated as a function of increasing nonlinearity at fixed resonator coupling $J/\gamma_p = 10^1$. Note the $M = 2$ results are not included as the bunching in this case is significantly larger. (b) Extent of the bunched region in (J, U) parameter space, as measured from $U = U_{\mathrm{LHS}}$ corresponding to the peak $g^{(2)}$, to $U = U_{\mathrm{RHS}}$ at which the correlations change from bunched to anti-bunched, for a range of resonator couplings J.

for $M = 2$ in Fig. 5.2 (b).

5.4 Photon statistics in Jaynes-Cummings arrays

Near future circuit QED systems will most probably realise a few-photon resonator nonlinearity via a Jaynes-Cummings interaction with embedded two-level systems [12], as described by the Jaynes-Cummings-Hubbard Hamiltonian in a rotating frame

$$\hat{\mathcal{H}}^{(M)}_{\mathrm{JCH}} = \sum_{j=1}^{M} \left(\Delta_c \hat{a}_j^\dagger \hat{a}_j + (\Delta_c - \Delta)\hat{\sigma}_j^+ \hat{\sigma}_j^- + \Omega(\hat{a}_j^\dagger + \hat{a}_j) \right) - J \sum_{<j,j'>} \left(\hat{a}_j^\dagger \hat{a}_j' \right). \tag{5.5}$$

Here $\Delta = \omega_c - \omega_a$ denotes the difference between the resonators' frequency and the TLS transition frequency, and $\hat{\sigma}^\pm$ denote TLS raising and lowering operators. The JCH is known to possess a localized-delocalized transition as either the hopping J is increased, or the Jaynes-Cummings parameter Δ is made more negative. This

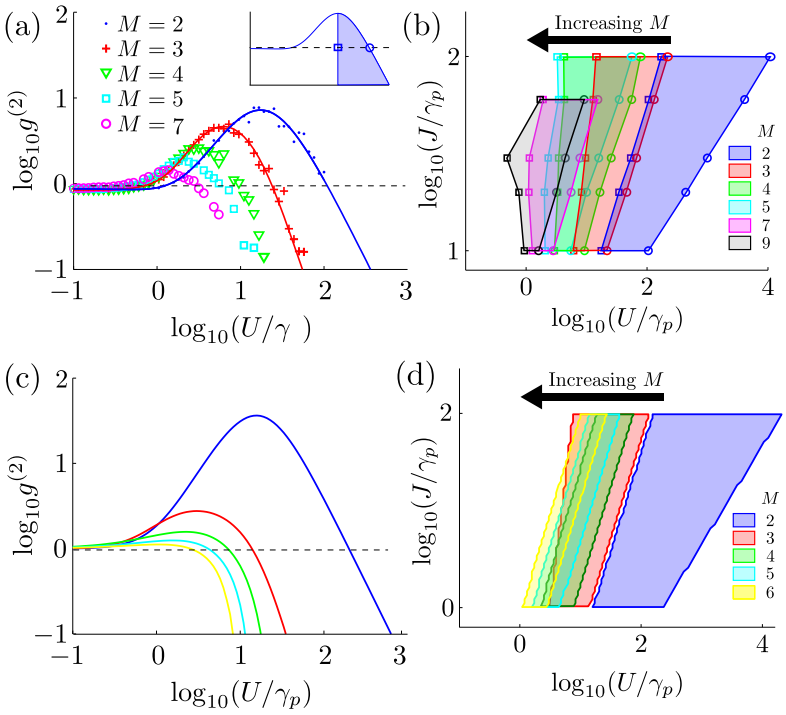


Figure 5.5. (a) Evolution of a slice along the line $J = J_A$ through the diagram of Fig. 2 (a), for increasing system size, at fixed hopping $J/\gamma_p = 10$ and driving $\Omega/\gamma_p = 0.4$. The solid blue and red lines are exact diagonalisation results for small systems. Inset: illustrates the metric we use for the width of the bunching region in (b) – squares denote the maximum bunching, and circles show where the correlation function crosses from bunched to anti bunched at $g^{(2)} = 1$. (b) Evolution of the extent of the bunching region in parameter space for increasing system size. Note that in these calculations, we have assumed open boundary conditions, in contrast to the periodic boundaries in previous calculations. (c) and (d) show results obtained by finding the stationary states of an effective quantum trajectory Hamiltonian $\hat{\mathcal{H}}_{\text{eff}}^{(M)}$.

transition is similar in some respects to the phase transition of the BH model, though also differs in fundamental ways on account of the different nature of the systems's intrinsic excitations (bosons and polaritons, respectively) [11, 73, 61, 79, 71, 137].

Figure 5.6 presents evidence that the mechanism underlying the bunched emission discussed above in the context of a the driven Bose-Hubbard model persists in this qualitatively different setting for realistic atom-resonator couplings and loss rates, and is therefore observable in near future state of the art experiments involving just two coupled resonators.

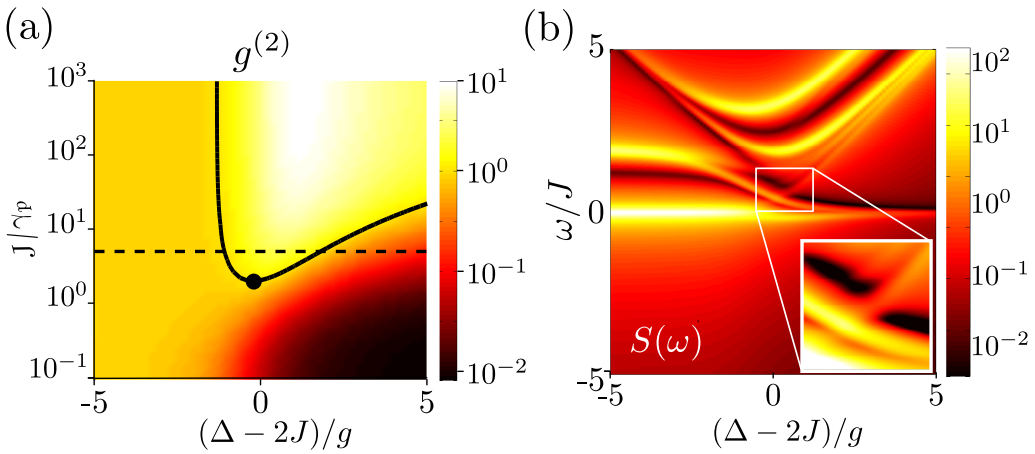


Figure 5.6. Steady state observables for a two-site Jaynes-Cummings array, driven at its lowest two-particle resonance. Parameters: $g/\gamma_p = 10$. (a) Zero-time photon correlation as a function of resonator coupling J and atom-resonator detuning Δ, playing the part of an effective photon nonlinearity. Black line shows where $g^{(2)} = 1$. (b) Spectral function $|S(\omega)|^2$ evaluated along the dashed line in (a), again showing a crossing of emission lines promoting photons to a state with enhanced probability of bunched emission.

5.5 Discussion

In this Chapter, we have proposed the selective excitation of photonic many-body modes of interest in open resonator arrays using external driving lasers, over which we have full control of frequency and amplitude. We have shown how a combination of the equilibrium Hamiltonian structure and non-equilibrium operation lead to an interaction-induced bunching in resonator photon statistics. This feature was found to persist in mesoscopic-sized arrays, and is also found under a more realistic array description, making its observation feasible in coming experiments.

Chapter 6

Frozen photons in Jaynes Cummings arrays

In this short chapter we depart from our study of non-equilibrium steady states, investigating instead a dynamical phenomenon in CRAs. Recently, there has been significant attention paid to finding novel observable non-equilibrium effects in modest-sized arrays, both in the steady state of driven-dissipative systems [190, 101, 205, 104, 94, 87], and in explorations of coherent array dynamics [90, 98, 96, 97, 206]. Resonator arrays are in many ways ideal platforms for the exploration of non-equilibrium quantum phenomena, potentially allowing relative ease of access to dynamical observables via localised measurements of photon fields, or of the atoms in each resonator.

Here we study the origin of 'frozen' states in coupled Jaynes-Cummings-Hubbard arrays in the presence of losses. For the case of half a resonator array initially populated with photons while the other half is left empty we show the emergence of self-localized or 'frozen' photonic states for specific values of the local atom-photon coupling. The resonator nonlinearity must be sufficiently large for localisation effects to set in, beyond which the photon population remains trapped in half of the system.

We analyze the dynamics in the quantum regime and discover that a semiclassical treatment similar to that first presented in [98] for the limiting case of two coupled resonators predicts a sharp transition between localised domain formation and delocalised dynamics in which photons tunnel between both halves of the system. Going beyond the semiclassical approach, fully quantum calculations confirm the frozen photon dynamics for strongly nonlinear arrays while also revealing features not present in the semiclassical calculation.

We trace the origin of this interaction-induced photon 'freezing' to the suppression of excitation of propagating modes in the system at large interaction strengths. Our findings can be seen in some ways as a photonic analog of the non-equilibrium dynamics of XXZ chains where it has been recently shown that strong nearest-neighbor interactions can lead to the formation of polarised domains which strongly influence the transport properties of spin chains [207, 140]. These ferromagnetic domains have been shown to be stable. They are spectrally separated from mobile states of the system which are capable of breaking them.

We show a related but distinct photonic equivalent. Our 'domains' of photons remain trapped over timescales large with respect to characteristic system rates due to a vanishing overlap between the initial pumped states we consider, and propagating modes of the system in the limit of large local interactions.

We discuss the possibility to experimentally probe the relevant transition by analyzing the emitted photon correlations, and we find a strong signature of the effect in the emitted photons statistics.

6.1 System

The system we consider is a one-dimensional linear array of M coupled optical resonators. Each resonator features a relevant mode of frequency ω_c, and is coherently

coupled to its nearest neighbours, as shown schematically in Fig. 5.1. A single two-level system (TLS) with transition frequency ω_0 is coherently coupled via a Jaynes-Cummings interaction to each resonator, with coupling strength g. In this work, we consider only the on-resonance case $\Delta = \omega_c - \omega_0 = 0$. The governing Hamiltonian is then the well-known Jaynes-Cummings-Hubbard (JCH) Hamiltonian:

$$\hat{\mathcal{H}} = \sum_j \left[\left(\omega_c \left(\hat{a}_j^\dagger \hat{a}_j + \hat{\sigma}_j^+ \hat{\sigma}_j^- \right) + g \left(\hat{a}_j^\dagger \hat{\sigma}_j^- + \hat{a}_j \hat{\sigma}_j^+ \right) \right] - J \sum_{\langle j,j' \rangle} \hat{a}_j^\dagger \hat{a}_{j'}. \tag{6.1}$$

Here $\hat{a}_j$ is the photon destruction operator for resonator j, and the $\hat{\sigma}_j^\pm$ are the raising / lowering operators for the TLS coupled to resonator j. The set of nearest neighbour resonators is denoted by $\langle j, j' \rangle$. The Hamiltonian $\hat{\mathcal{H}}$ commutes with the total excitation number operator

$$\hat{\mathcal{N}} = \sum_j \left(\hat{a}_j^\dagger \hat{a}_j + \hat{\sigma}_j^+ \hat{\sigma}_j^- \right). \tag{6.2}$$

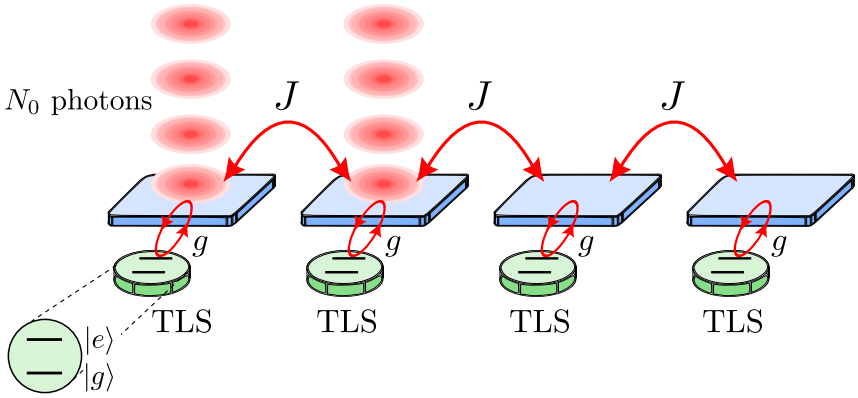


Figure 6.1. Schematic of our system and the initial conditions considered. The left half of a one dimensional array with M resonators (here $M = 4$) is initialised in a Fock state of N_0 photons (in this particular schematic, $N_0 = 4$). Each resonator is coherently coupled to its two nearest neighbours with associated tunnelling rate J. Each resonator is also coherently coupled to a two-level system (TLS) with Jaynes-Cummings coupling parameter g.

Throughout this work we shall consider a specific type of initial state. Namely,

we initialise one half of the system in a Fock state of N_0 photons, with each TLS in its ground state, as demonstrated graphically in Fig. 6.1.

$$|\Psi(0)\rangle = \prod_{j=1}^{M/2} |g, N_0\rangle_j \otimes \prod_{j=M/2+1}^{M} |g, 0\rangle_j, \tag{6.3}$$

where $|g, n\rangle_j$ denotes a photonic Fock state of n photons in resonator j.

Generalising [98] to the case of an extended system, of central interest in the following analysis will be the photon imbalance $Z(t)$ between the left (L) and right (R) halves of the system, as defined by:

$$Z(t) = \frac{\sum_{j=1}^{M/2} \langle \hat{a}_j^\dagger \hat{a}_j \rangle(t) - \sum_{j=M/2+1}^{M} \langle \hat{a}_j^\dagger \hat{a}_j \rangle(t)}{\sum_{j=1}^{M} \langle \hat{a}_j^\dagger \hat{a}_j \rangle(t)} \tag{6.4}$$

In particular, we find that time-averaging $Z(t)$ neatly encapsulates details of the photon dynamics. We denote such time averages in the following by $\bar{Z}$. Values of $\bar{Z}$ close to zero imply delocalisation of photons across the two halves of the system, either oscillating back and forth in some manner or reaching an approximately even distribution. Meanwhile $\bar{Z} \approx 1$ implies a photon population trapped in one side of the system for a substantial period of time.

6.2 Photon localisation under a semi-classical treatment

We begin our analysis of the dynamics of the system Eq. (6.1) at the semiclassical level, thereby making contact with the related previous work of [98]. We first use the Heisenberg equation of motion $\frac{d}{dt}\hat{O} = i[\hat{\mathcal{H}}, \hat{O}]$ to generate evolution equations for the photonic and TLS operator expectation values. As the semi-classical approximation entails factorising the expectation values of operator products into products

of expectation values (e.g. $\langle \hat{a}_j^\dagger \hat{\sigma}_j^- \rangle = \langle \hat{a}_j^\dagger \rangle \langle \hat{\sigma}_j^- \rangle$), we need only generate equations for the three operators $\hat{a}_j, \hat{\sigma}_j^-, \hat{\sigma}_j^z$ at each site j.

Defining $(\alpha_j, m_j, z_j) \equiv (\langle \hat{a}_j \rangle, \langle \hat{\sigma}_j^- \rangle, \langle \hat{\sigma}_j^z \rangle)$, we obtain the set of coupled differential equations for their evolution:

$$\begin{aligned} \dot{\alpha_j} &= -i\omega_c \alpha_j - igm_j + iJ((1-\delta_{j,1})\alpha_{j-1} + (1-\delta_{j,M})\alpha_{j+1}) \\ \dot{m_j} &= -2i\omega_c m_j + ig\alpha_j z_j \\ \dot{z_j} &= -2ig\left(\alpha_j m_j^* - \alpha_j^* m_j\right), \end{aligned} \tag{6.5}$$

where the delta functions take into account the open boundary conditions.

The initial conditions corresponding to our chosen state of Eq. (6.3) are

$$\begin{aligned} \alpha_j &= \begin{cases} \sqrt{N_0} : j \leq \frac{M}{2} \\ 0 : j > M/2 \end{cases}, \\ z_j &= -1, \\ m_j &= 0. \end{aligned} \tag{6.6}$$

We note that it has been shown that for the case of $M = 2$ resonators, a qualitative change in the population imbalance dynamics occurs sharply at a critical coupling $g_c \approx 2.8\sqrt{N_0}J$ [98]. Specifically, for $g < g_c$, photons move between the resonators with a characteristic tunnelling time. Around $g = g_c$, this period diverges, leading to a 'self-trapped' regime for $g > g_c$ in which the photon population remains localised in one resonator.

With these results in mind, we look now at the time averaged photon imbalance $\bar{Z}$ for larger arrays as calculated by time evolving the set of Eqns. (6.5), shown in Fig. 6.2. We see that semi-classical theory still predicts a sharp localised / de-localized transition at the critical coupling $g = g_c$, regardless of the system size

M.

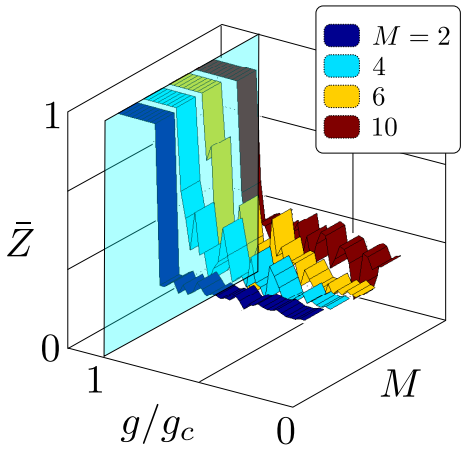


Figure 6.2. The time-averaged photon imbalance $\bar{Z}$ according to a semi-classical treatment of an M-resonator array. $\bar{Z}$ denotes the average of $Z(t)$ over a time interval $tJ \in [0, 20]$. The transparent blue plane marks the critical coupling predicted by semi-classical theory for the case of $M = 2$ resonators [98].

6.3 The fully quantum regime

Going now beyond semiclassical (SC) theory, which can only be valid in the limit of a large number of excitations, we investigate whether an analogue of the localisation predicted by the SC equations persists in the fully quantum regime of a few ($N_0 \leq 4$) excitations. Explicitly constructing a matrix representation of the Hamiltonian of Eq. (6.1) and time evolving by applying the unitary operator $\hat{\mathcal{U}}(t) = \exp(-i\hat{\mathcal{H}}t)$ to the initial state $|\Psi(t)\rangle$ becomes numerically challenging beyond even $M = 2$ resonators. The two-species nature of the Jaynes-Cummings Hubbard Hamiltonian, coupled with the necessity of retaining a sufficient number of photons per resonator in calculations so as to avoid truncation error lead to a large Hilbert space dimension. Some progress is possible by projecting the dynamics into fixed particle number subspaces, however we turn instead to a compact matrix product state (MPS) representation of the wave function, with time evolution of this ansatz facilitated by

the TEBD algorithm.

Figure 6.3 shows TEBD simulations of the local photon density in an $M = 6$ resonator array with the left half initially pumped with Fock states of $N_0 = 4$ photons, for two Jaynes-Cummings nonlinearities, one weak and one strong (relative to the photon tunnelling rate J). For weak nonlinearities photons initially oscillate between the two halves of the system, reflecting from the boundaries and eventually leading to a uniformly distributed population, i.e. zero photon imbalance $\bar{Z} \approx 0$.

For arrays with strong nonlinearities on the other hand, such as shown in Figure 6.3 (b), photons remain essentially trapped in the left-hand side of the system for very long times ($> 98\%$ of the photon population remains in the first three sites over the simulation window). The self-trapping phenomenon predicted by semiclassical theory seems then to persist in the fully quantum regime of few photons.

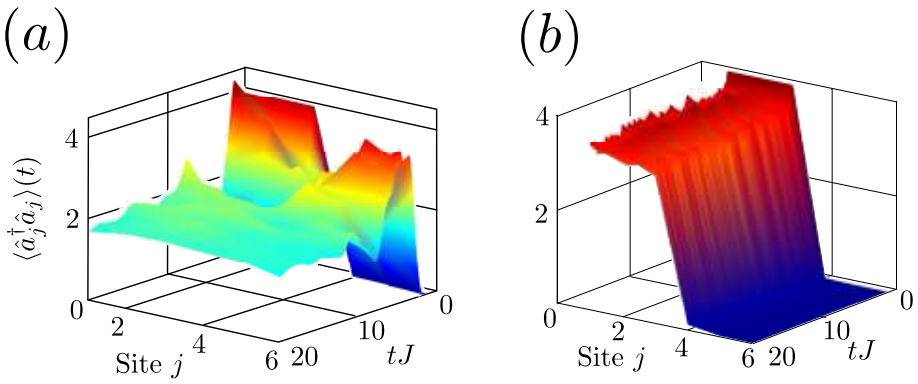


Figure 6.3. Photon number evolution for an $M = 6$ resonator system with the first three resonators pumped with $N_0 = 4$ photon Fock states at $t = 0$. (a) A weak nonlinearity $g = 0.1J$. (b) Strong Jaynes-Cummings nonlinearity $g = 15J$. The apparent reduction in the mean photon number per site over time is accounted for by the TLS excitation – we have checked that the total excitation in the system is preserved by our numerics to 1% over the simulation interval. Simulation parameters: all calculations kept a minimum of $n_{\max} = \min(N_0 M/2, 7)$ photons per resonator in the computational basis. A matrix product state truncation parameter of $\chi = 100$ was found to be sufficient to avoid cumulative errors.

Figure 6.4 however characterises the emergence of these domains of 'frozen' photons, showing that semiclassical theory is insufficient to fully capture all qualitative

details of the effect in the low-excitation regime. The Figure shows the results of rigorous TEBD simulations for arrays of different sizes, pumped with different numbers of initial photons. We see that the 'transition' between delocalized ($\bar{Z} \approx 0$) and localised ($\bar{Z} \approx 1$) dynamics becomes broader with increasing system size M, and never resembles the sharp semi-classical transition of Fig. 6.2. The qualitative trend, however, towards localisation with increasing nonlinearity g occurs irrespective of M. Figure 6.4 (b) meanwhile shows that for $N_0 > 1$, the magnitude of the initial excitation does not significantly affect the rate at which the system approaches the 'frozen' regime. Interestingly however we find that the case of a single photon per resonator pumped into the left half of the system never exhibits localisation behaviour, no matter how large the Jaynes-Cummings nonlinearity g.

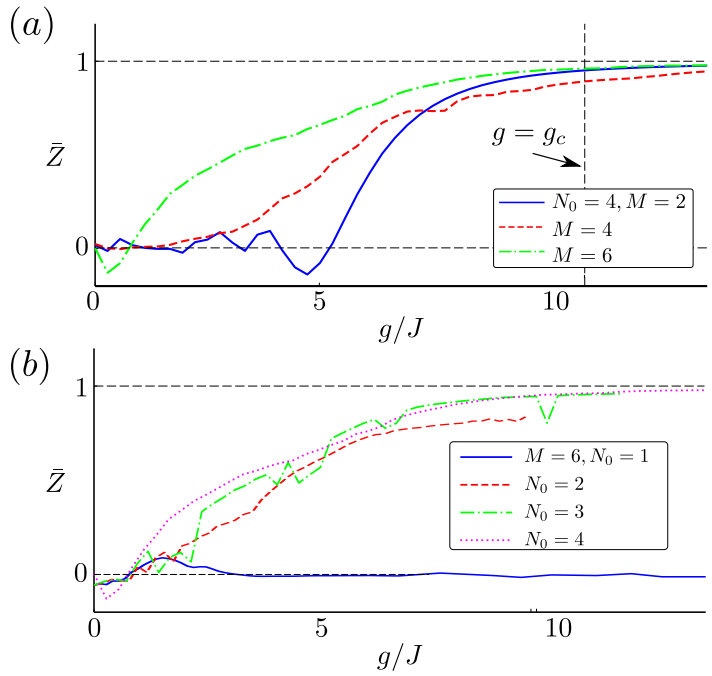


Figure 6.4. An exploration of the time averaged photon imbalance $\bar{Z}$. (a) As a function of the system size M, holding the initial excitation N_0 fixed. (b) $\bar{Z}$ as function of the initial excitation N_0, holding instead the system size fixed.

We can understand this qualitative difference in behaviour between $N_0 = 1$ and $N_0 > 1$ by examining the initial state $|\Psi(0)\rangle$ in the eigenbasis of the Hamiltonian $\hat{\mathcal{H}}$.

We work in the Hilbert subspace spanned by eigenvectors $\{\Psi_j\}$ commuting with the total excitation operator $\hat{\mathcal{N}}$ with eigenvalue $n = N_0 M/2$, and calculate the overlap of the initial state with each of these eigenstates $||\langle\Psi(0)|\Psi_j\rangle||^2$. These overlaps are presented in Fig. 6.5 for a minimal 'array' of $M = 2$ resonators with both $N_0 = 1$ and $N_0 = 4$ initial photons, as a function of the nonlinearity g. As expected, we see a shuffling of excitation between the various eigenmodes as g changes. The properties of the eigenmodes having significant overlap with the initial state for a given nonlinearity g determine the properties of the time evolution of the system. Of particular relevance is a measure of the 'photon current' through the centre of the system, or alternatively the degree of photon delocalization across the halves of the array. Both these quantities are reflected in a finite value of the expectation value $C = |\langle\hat{a}^\dagger_{M/2}\hat{a}_{M/2+1}\rangle|$. On measuring C for each of the modes $|\Psi_j\rangle$, we find that the initial state for the case of a single pumped initial photon $N_0 = 1$ has a finite overlap with 'current-carrying' modes even in the limit of a large nonlinearity g. In contrast, only non-propagating modes are substantially excited for larger excitations $N_0 > 1$, leading to the frozen domains of Fig. 6.3 (b).

6.4 Probing the frozen dynamics in an experiment

Finally we present calculations showing experimentally relevant photonic observables which give signatures of the transition between localised and delocalized dynamics. While the photon number imbalance $\bar{Z}$ between the two halves of the system may be measurable via quantum non-demolition measurements [208] on frequency shifts of the TLSs [209], we focus here on purely photonic observables that can be extracted from the emitted photons from the array. In particular, we find that measurement of

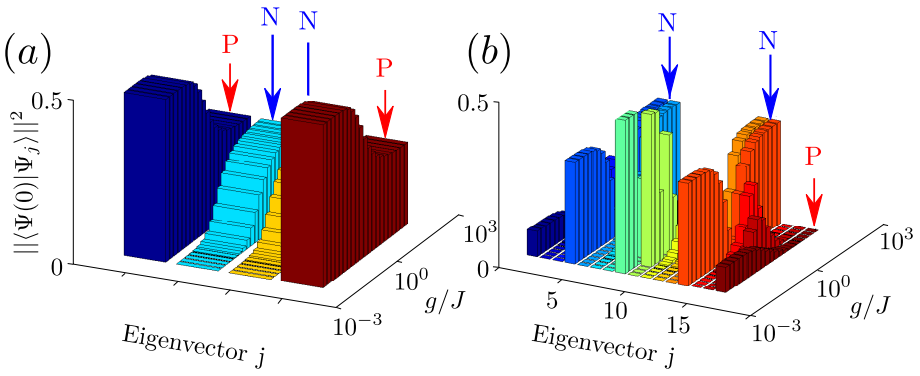


Figure 6.5. The projection of the initial state $|\Psi(t=0)\rangle$ into each of the eigenstates spanning the subspace consistent with the total number of excitation in the system, $N_0 M/2$, for the simplest case of a dimer of $M = 2$ resonators. (a) Shows overlaps for an initial excitation of just $N_0 = 1$ photon in the first resonator. (b) The corresponding projections for an initial state of $N_0 = 4$ photons. Both plots show the evolution of the different projections as the Jaynes-Cummings nonlinearity g is ramped up. Eigenmodes marked 'P' (for 'propagating') have a nonzero photon correlation function C across the two halves of the system. Modes marked 'N' have vanishing C as g increases. Note that the larger dimension of the subspace for $N_0 = 4$ results in more eigenstates in (b).

the local second order photon correlations $g_L^{(2)} = \langle \hat{a}_j^\dagger \hat{a}_j^\dagger \hat{a}_j \hat{a}_j \rangle / \langle \hat{a}_j^\dagger \hat{a}_j \rangle^2$ yields signatures of the transition. Figure. 6.6 shows that the freezing of population in one half of the system (where the photon imbalance is $\bar{Z} \approx 1$) is accompanied by a qualitative change in the on-site correlations from $g^{(2)} > 1$ to $g^{(2)} \approx 1$. Figures. 6.6 (a) and (c) show that both the photon imbalance and the time-averaged correlator $g^{(2)}$ approach a limiting behaviour as the initial number of photons grows large, with a sharp transition in observables in the vicinity of the critical point predicted by semiclassical theory $g = g_c$.

Experimentally, the photon statistics encoded in $g^{(2)}$ are mapped on to the statistics of photons leaking from resonators with finite line widths as characterised by a loss rate γ. To assess whether the correlator $g^{(2)}$ can serve as a probe of the transition in realistic settings with a finite resonator loss rate, we include Markovian photon loss processes at rate γ and TLS de-excitation at rate κ via a quantum mas-

ter equation formalism, time evolving the system density matrix ρ from the initial state of Eq. (6.3) under the evolution:

$$\dot{\rho}(t) = -i[H, \rho] + \sum_{i=L,R} (\kappa \mathcal{D}[a_i] + \gamma \mathcal{D}[\sigma_i^-]), \tag{6.7}$$

where the action of the dissipator $\mathcal{D}$ is defined as $\mathcal{D}=(2O\rho O^\dagger - O^\dagger O\rho - \rho O^\dagger O)/2$. Figures. 6.6 (b) and (d) show that the introduction of a finite loss rate acts to smear the transition, pushing localisation to larger nonlinearities g. However for sufficiently large initial photon pumping (around $N_0 \approx 7$), the statistics of the emitted photons can be used to infer a change from delocalised physics (characterised by $\bar{g}^{(2)} > 1$) to the localised case ($\bar{g}^{(2)} \approx 1$). The value of γ we use leads to a maximum ratio $g/\gamma \approx 200$, within reach of near future experiments in Circuit QED architectures [131].

6.5 Discussion

We have demonstrated the existence of a novel strongly correlated regime of 'frozen' photons in optical resonator arrays with large Jaynes Cummings type nonlinearities. For a sufficiently large initial excitation of part of the resonator array, the photon dynamics are dramatically suppressed due to a very small overlap with propagating modes of the system. As little as 2 pumped photons per resonator are sufficient to observe signatures of 'frozen' domains of photons, allowing access to the truly quantum few-excitation regime.

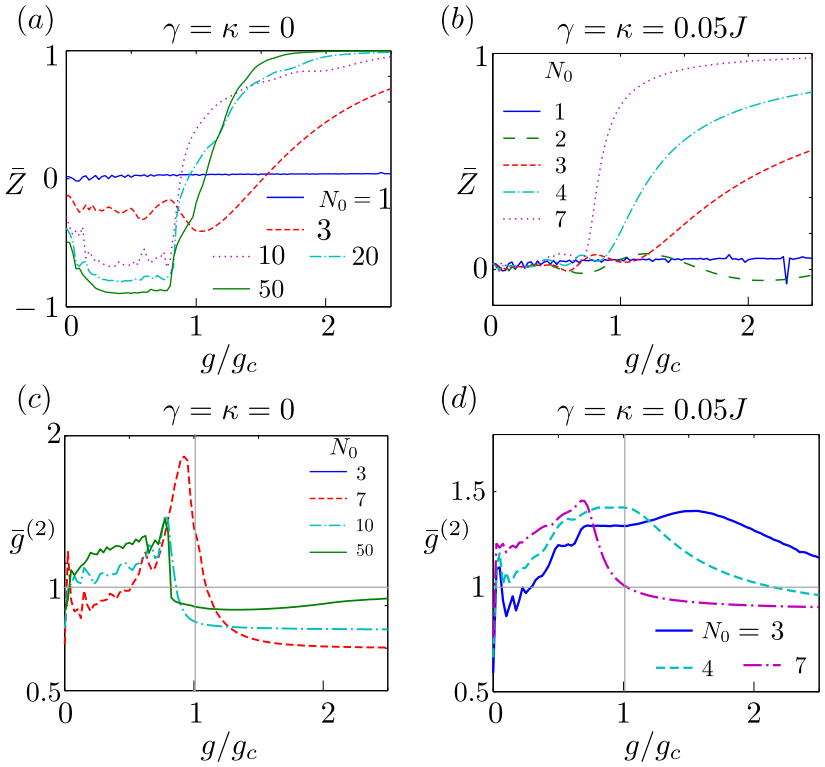


Figure 6.6. Charting the localisation - delocalization transition for a minimal $M = 2$ resonator array through both the time averaged photon imbalance $\bar{Z}$ (top row) and the time-averaged photon correlator $\bar{g}^{(2)}$ (bottom row) for increasing initial photon number N_0. $\bar{Z}$ and $\bar{g}^{(2)}$ are calculated for systems with no losses (left column), and for small finite loss rates $\gamma = \kappa = 0.05J$.

Chapter 7

Parametrically pumped resonator arrays

In this chapter, we study the physics of CRAs under a novel type of driving, suggested recently in Ref. [139]. Instead of driving the resonators directly as in previous chapters, it was proposed to drive a nonlinear material coupled to the inter-resonator fields, producing correlated pairs of photons as shown in Fig 7.1 [210]. Because of the intra-resonator nonlinearities, these pairs are injected into adjacent resonators. In a frame rotating at the driving frequency ω_L, the governing Hamiltonian is

$$\begin{aligned}\mathcal{H}_p = &- J\sum_{\langle j,j'\rangle}\left(\hat{a}_j^\dagger\hat{a}_{j'} + \text{H.c.}\right) + \sum_j \frac{U}{2}\hat{n}_j(\hat{n}_j - 1) + \Delta\sum_j\left(\hat{a}_j^\dagger\hat{a}_{j+1}^\dagger + \hat{a}_j\hat{a}_{j+1}\right)\\ &- \mu\sum_j \hat{a}_j^\dagger\hat{a}_j. \end{aligned} \tag{7.1}$$

Here $J > 0$ is the coherent tunnelling amplitude between nearest neighbour resonators, U is the local repulsive interaction strength, Δ is the amplitude of coherent parametric two-photon pumping, and $\mu = \omega_p - \omega_c$ plays the role of a chemical potential.

CRAs driven parametrically by two-photon processes in this way have been predicted to demonstrate signatures of exotic Majorana fermions – particles which are

their own anti-particles. The seminal work in [139] treated finite 1D systems with open boundary conditions, working in the ultra-strong nonlinearity limit so as to achieve the fermionised photon regime [104]. In this limit, the physics of CRAs may be mapped to a toy model for Majorana physics originally proposed by Kitaev [211], which describes a 1D p-wave superconductor of spinless fermions. The Kitaev model exhibits topological phases characterised by the existence of localised edge modes in certain parameter regimes, and has attracted a lot of attention in the context of topological quantum computers which promise a route to overcome problems of decoherence [212].

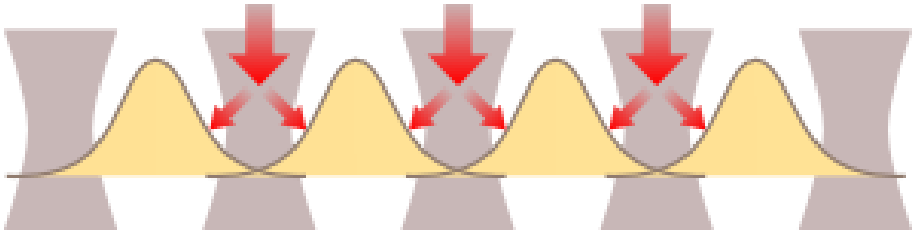


Figure 7.1. Schematic of parametric pumping in resonator arrays. Each resonator is single mode (yellow Gaussian shape), and possesses a Kerr nonlinearity U. Coherent photon hopping between nearest neighbours follows from modal overlaps. Parametric injection of correlated photons is achieved by coupling to the inter-resonator fields where strongly nonlinear materials are placed (see Supplementary material of [139]), and sufficiently large U ensures photon pairs are injected into neighbouring resonators. Figure and proposed system / driving reproduced from [139]. We note this system is intended more as an illustration of novel physics than a concrete physically implementable proposal.

The properties of more realistic systems of parametrically pumped resonator arrays with sizeable but finite nonlinearity remains unexplored. A rich phase diagram is to be expected, as the bosonic nature of the photons away from the fermonized limit comes into play, coupled with a competition between the coherence injected by the pumping, the nonlinearity, and photon tunnelling. Interesting questions arise, such as the existence of new phases, and particularly the persistence of topological behaviour as the hardcore constraint is relaxed. In this chapter, we calculate ground

state properties of both infinite- and finite-sized parametrically pumped arrays, both in the hardcore fermionised regime, and away from this idealised limit.

Before beginning our investigation of the ground states of the Hamiltonian of Eq. (7.1), we first introduce the concepts of non-local order parameters and the entanglement spectrum as useful tools in classifying topological phases in the context of the somewhat related extended Bose-Hubbard model (EBHM):

$$\mathcal{H}_V = \sum_j \frac{U}{2}\hat{n}_j(\hat{n}_j - 1) - J\sum_{\langle j,j'\rangle}\left(\hat{a}_j^\dagger \hat{a}_{j'} + \text{H.c.}\right) + V\sum_j \hat{n}_j\hat{n}_{j+1}. \tag{7.2}$$

The EBHM differs from the canonical Bose-Hubbard model in the addition of a nearest-neighbor repulsion term characterised by the rate V. Here U and J are again the on-site repulsion, and inter-site coherent tunnelling energy. This model is known to possess a range of ground-state phases at unit filling.

The extended Bose-Hubbard model is known to possess a topological phase characterised by non-local 'hidden' order parameters [213], and degeneracies in its entanglement spectrum [214, 215, 216], motivating a search for analogous intriguing states in the parametrically driven case.

We stress that the results of this chapter constitute a preliminary study of this novel system, and as such are presented somewhat phenomenologically as a basis for future more thorough explorations. To our knowledge this system has not been treated at all in the literature, and so we elucidate its novel physical features by ignoring photon loss processes, characterising it instead through its ground state properties.

7.1 Examples of topological signatures in the extended Bose-Hubbard model

In this section we solve for the ground states of infinite systems described by Hamiltonian 7.2 using imaginary time evolution under the infinite TEBD (iTEBD) scheme as introduced in Section 2.6. As the Hamiltonian of Eq. (7.2) is number-conserving, we restrict evolution to states with on average a single particle per site. To our knowledge this remarkable quantum number conserving variant of iTEBD has not been used in the calculation of ground state phase properties before.

7.1.1 Non-local order and ground state phases

Operating as we are in the unit-filled subspace, we expect $\langle \hat{n} \rangle = 1$ always. Expectation values in this chapter are to be understood to be measured relative to the ground state. Another relevant local observable is $\phi = \langle \hat{a} \rangle$, which allows us to distinguish between Mott ($\phi = 0$) and superfluid ($\phi \neq 0$) phases in the canonical Bose-Hubbard model (corresponding to the limit $V = 0$ for the EBHM).

In contrast to Mott and superfluid phases, topological phases cannot be characterised by a local order parameter, and additionally are often characterised by the presence of gapless edge modes as we explore in Section 7.3. Local observables such as ϕ yield only an incomplete characterisation of topological ground states. The existence of long-ranged order can be detected by appropriately designed non-local order parameters. Here we define 'string' order $\mathcal{O}_S$, 'parity' order $\mathcal{O}_P$, and density

wave order $\mathcal{O}_{DW}$ [217]:

$$\mathcal{O}_S^2 = \lim_{|i-j|\to\infty} \langle \delta n_i \prod_{i<l<j} (-1)^{\delta n_l} \delta n_j \rangle \tag{7.3}$$

$$\mathcal{O}_P^2 = \lim_{|i-j|\to\infty} \langle \prod_{i<l<j} (-1)^{\delta n_l} \rangle \tag{7.4}$$

$$\mathcal{O}_{DW}^2 = \lim_{|i-j|\to\infty} (-1)^{|i-j|} \langle \delta n_i \delta n_j \rangle, \tag{7.5}$$

where the density fluctuation operator $\delta n_j = \hat{n}_j - \bar{n}$ measures fluctuations relative to the mean density. Figure 7.2 shows the expected phase diagram for a unit-filled EBHM system in the thermodynamic limit as a function of on-site and inter-site interaction strengths (U and V respectively).

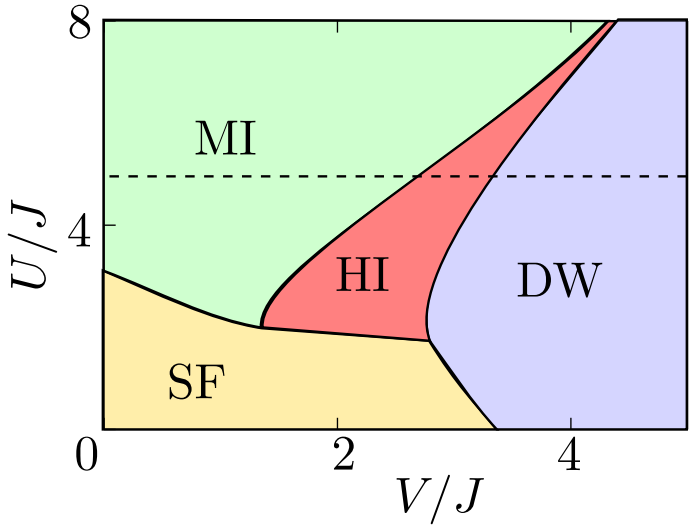


Figure 7.2. Ground state phase diagram of the unit-filled extended Bose-Hubbard model of Eq. (7.2). Reproduced from [218].

The Mott insulating (MI) and superfluid (SF) phases are familiar from the canonical Bose-Hubbard model, and indeed are the only phases present for small V. At the other extreme, when inter-site interactions dominate over all other rates ($V \to \infty$), it is energetically favourable for two particles to occupy the same site, with doubly occupied sites separated from each other by an empty site. The ground state $|\Psi\rangle_{\text{GS}} = \cdots |2\rangle \otimes |0\rangle \otimes |2\rangle \otimes |0\rangle \otimes \cdots$ in this limit is therefore 'density ordered', and is

known as the 'density-wave' (DW) phase. This phase in the extreme limit $V \to \infty$ leads to $\delta n_j = \pm 1$, with an alternating sign on each site. The negative sign in the definition of $\mathcal{O}_{\mathrm{DW}}$ then ensures a non-zero correlator.

Figure 7.2 shows a fourth phase at intermediate V, when all rates U, V, J are comparable. This 'Haldane insulator' [213, 217] is an example of a topological state of matter, and is characterised by a non-vanishing string order $\mathcal{O}_S \neq 0$. Physically, this corresponds to an ordering of fluctuations relative to a perfect unit-filled product state $|\mathbf{1}\rangle = |\cdots 11111 \cdots 11111 \cdots\rangle$. That is, deviations from the state $|\mathbf{1}\rangle$ are not randomly distributed as either $|\cdots 111110 \cdots 21111 \cdots\rangle$ or $|\cdots 111112 \cdots 01111 \cdots\rangle$, but rather a 'hole' ($|0\rangle$) is consistently preceded by an 'excitation' ($|2\rangle$), or vice versa, further illustrated in Fig. 7.3. In contrast, a Mott insulator exhibits parity ordering ($\mathcal{O}_P \neq 0$), as an excitation is always accompanied by a bound hole, but no string order as the order of these pairs is random. Figure 7.4 (b) shows long range order parameters calculated according to Eqns. (7.3) – (7.5) quantities along a slice through the phase diagram of Fig. 7.2. We see that $\mathcal{O}_{\mathrm{DW}} \neq 0$ only in the DW phase, but that both the Haldane insulator and DW phase possess string order.

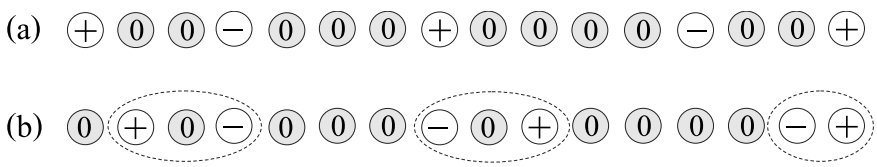


Figure 7.3. Typical configurations in the (a) HI and (b) MI ground states. The numbers represent δn (the deviation of the local occupation from the average density). The HI can be described as a charge ordered $+, -, +, \cdots$ state with an undetermined number of 0 sites between each + and −. The MI is a dilute gas of particle-hole pairs (indicated by the dotted ellipses). Figure reproduced from [219].

7.1.2 Entanglement spectra

We now introduce an alternative approach to classifying the phases in Fig. 7.2, namely calculation of the entanglement spectra. The entanglement spectrum (see also Appendix B.1.2) is defined as the set of eigenvalues $\{\lambda_\alpha\}$ of the reduced density matrix ρ_A of a lattice system split into two subsystems A and B. It provides key insights into the nature of quantum correlations in many-body systems. Recently, it has been proposed [214, 219] that topological phases can be characterized by their entanglement spectrum, as symmetries in ground state phases manifest as degeneracies in the $\{\lambda_\alpha\}$. In this way the topological phase of $S = 1$ spin chains has been explored in [215] and that of the extended Bose-Hubbard model is studied in [220].

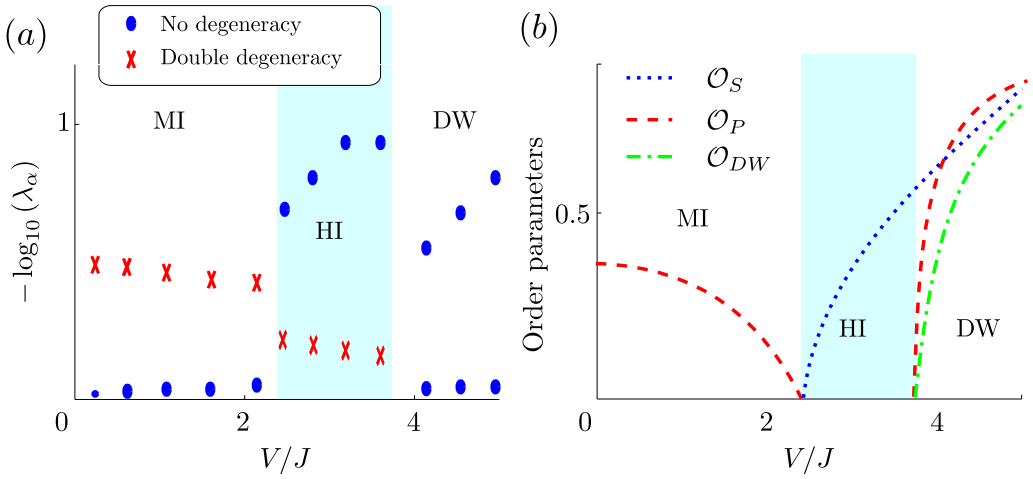


Figure 7.4. Ground state quantities calculated along the dashed line in Fig. 7.2. (a) The largest eigenvalues in the entanglement spectrum $\{\lambda_\alpha\}$. Larger eigenvalues are lower in the figure. The eigenvalue degeneracy is indicated by the type of symbol. The Mott insulating (MI) phase is characterised by a singly degenerate largest eigenvalue, with smaller eigenvalues occurring in degenerate pairs (only the first pair is shown). The Haldane insulating (HI) phase has a degeneracy in the largest eigenvalue, while the density-wave (DW) phase has no degeneracies anywhere in the entanglement spectrum. (b) Non-local order parameters as defined in Eqns. (7.3 – 7.5). The blue rectangle spans the same range of V in both (a) and (b).

We note that within the matrix product state formalism, the entanglement spec-

trum is trivially available, as the Schmidt coefficients $\{\lambda_\alpha\}$ are fundamental quantities in the state representation, making entanglement spectrum analysis attractive.

Figure 7.4 (a) shows an example of how entanglement spectra may discriminate between different phases. The Figure shows the largest eigenvalues in the Schmidt spectrum for ground states along the slice in Fig. 7.7. Three different regions are clearly visible. At low V/J (Mott insulating phase), the largest eigenvalues are non-degenerate, followed immediately by (sets of) degenerate eigenvalues. At large V/J (charge density wave phase), there are no degenerate Schmidt eigenvalues anywhere in the spectrum. Finally the topological Haldane phase at intermediate V/J, is characterised by all Schmidt spectrum eigenvalues occurring in pairs.

7.2 Infinite parametrically driven arrays

Having introduced the entanglement spectrum and non-local order parameters as useful quantities in the classification of ground state phases, we return to our central system of interest, the Hamiltonian of Eq. (7.1).

7.2.1 Limits of the model

This section explores the properties of the Hamiltonian of Eq. (7.1) in and around certain limits, with a view to building up a comprehensive picture of ground states across parameter space. We continue to solve for the ground state of infinite arrays.

'Hardcore' limit

The hardcore limit as considered in [139] (for finite arrays) assumes an infinite local nonlinearity $U \to \infty$. The occupation of each site is then truncated to either 0 or 1, and the photons exhibit fermionic behaviour [221, 104].

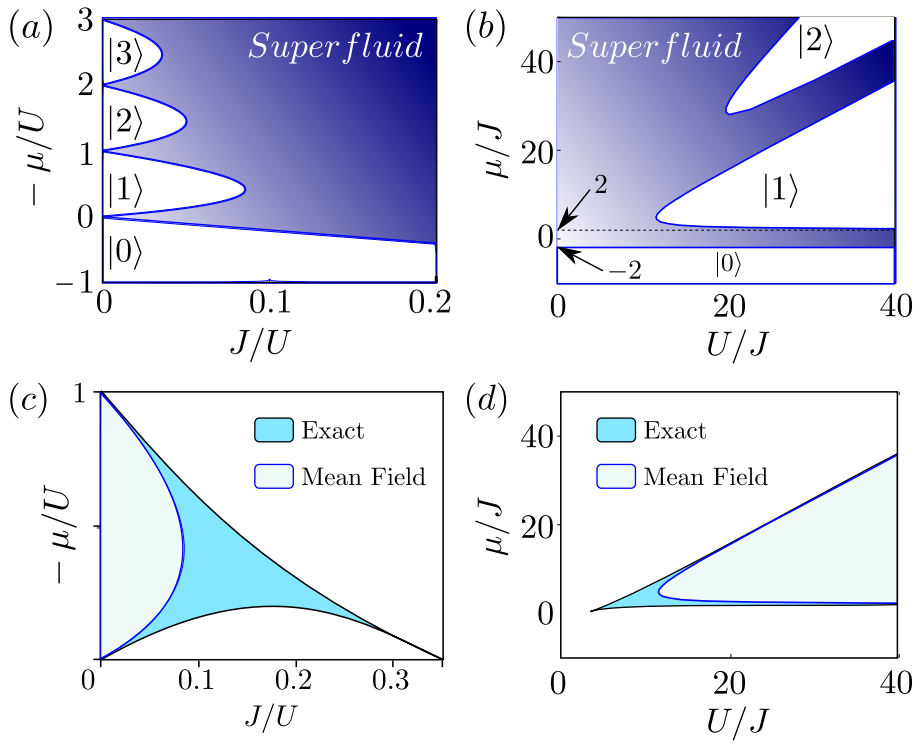


Figure 7.5. Comparison of Bose-Hubbard mean field phase diagrams for different units. (a) The 'canonical' phase diagram, constructed by fixing the interaction strength U and varying the hopping amplitude J and chemical potential J. (b) The phase diagram obtained instead by fixing J and varying U and μ. This second diagram is useful for connecting to the 'hard-core' limit $U \to \infty$. (c) and (d) show rigorous (marked 'Exact') MPS calculations showing the boundaries of the first Mott lobe, and the mean field results from (a) and (b) for comparison.

To visualise the approach to this limit, it is useful to replot the 'canonical' Bose-Hubbard phase diagram ($\Delta = 0$), which charts the (μ, J) phase space at fixed U. Figure 7.5 compares mean field and numerically exact results for the lowest-order Mott lobes at fixed U, and also at fixed J. Figure 7.5 (b) in particular shows the expected evolution of the BH phases as we approach the limit $U \to \infty$. Only the $n = 0$ and $n = 1$ lobes remain (higher occupations are forbidden), and a superfluid gap separates them, spanning $\mu \in [-2J, 2J]$. Still considering the limit $\Delta = 0$, the hopping term in the Hamiltonian leads to a band of propagating states with bandwidth $4J$. A value of the chemical potential falling anywhere inside this band

$\mu \in [-2J, 2J]$ fills the states in the band up to that energy, leading to an occupation

$$\langle \hat{n} \rangle_{\mathrm{GS}} = \begin{cases} 0 & : \mu < -2J \\ \frac{1}{\pi} \arccos\left(\frac{\mu}{2}\right) & : \mu \in [-2J, 2J]. \\ 1 & : \mu > 2J \end{cases}$$

.

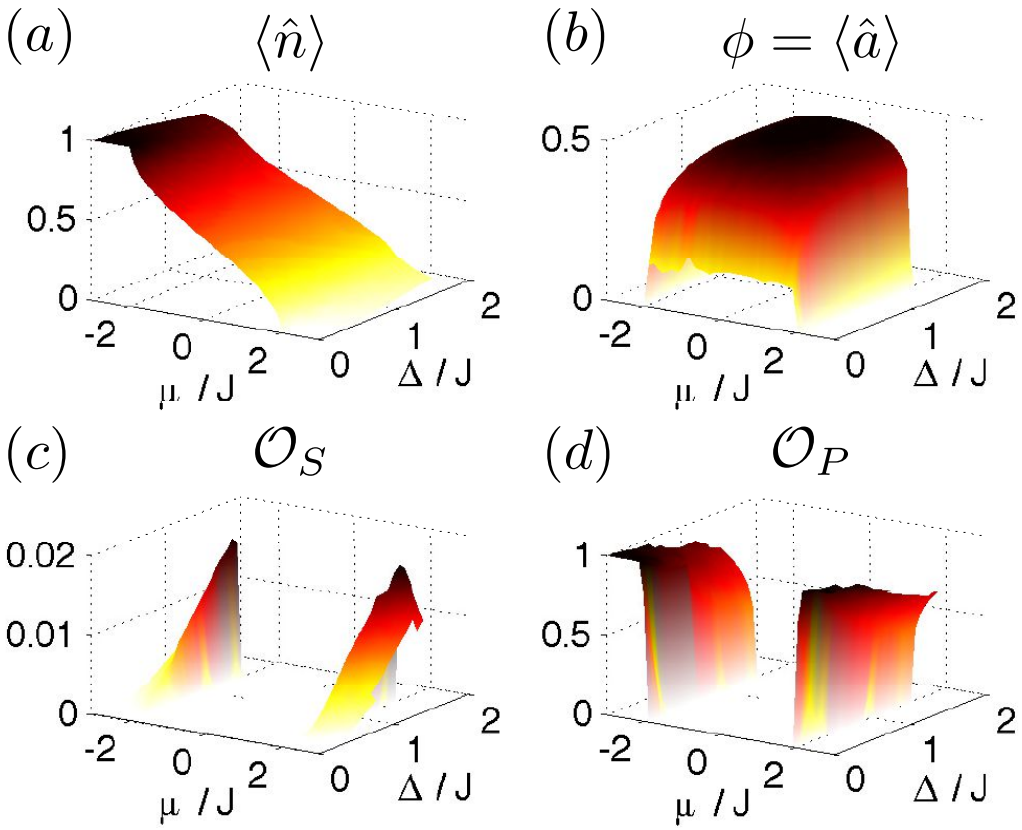


Figure 7.6. Ground state observables for the hardcore limit $U \to \infty$. (a) Ground state filling. (b) The local order parameter $\phi = \langle \hat{a}_{\mathrm{GS}} \rangle$ always vanishes outside $\mu \in [-2J, 2J]$. (c) A finite parametric driving builds up string order in the former Mott phases, which do not possess these correlations ($\mathcal{O}_S \to 0$ for $\Delta \to 0$). (d) Meanwhile a finite Δ degrades the parity ordering of the insulating regions.

Figure 7.6 shows the evolution away from this well-known Tonks-Girardeau limit ($U \to \infty$, $\Delta = 0$) as a finite driving is switched on. We see that outside the superfluid region (i.e. $|\mu| > 2J$), the driving builds up a non-zero string order,

while simultaneously degrading the parity ordering of these insulating regions. The non-number conserving driving also breaks the integer (0 or 1) filling. Interestingly, while a finite string order is present, an analysis of the entanglement spectrum (not shown) shows no degeneracies anywhere in the Schmidt spectrum, in contrast to the EBHM. The situation is different for finite systems, as we show shortly.

Zero parametric driving $\Delta \to 0$

Switching off the parametric driving term ($\Delta = 0$) recovers the canonical Bose-Hubbard model. Here we investigate the effect on the well-known BH ground state phase diagram of a small but finite parametric driving. Figure 7.7 shows the boundary of the one-particle Mott lobe as calculated by rigorous iTEBD simulations, while Figure 7.8 shows observables calculated along a cross-section through this diagram for zero, and finite driving amplitudes Δ.

We see that the driving acts to diminish the extent of the Mott lobe at $\Delta = 0$ (characterised by unit filling $\langle \hat{a}^\dagger \hat{a} \rangle = 1$ and vanishing order parameter $\phi = \langle \hat{a} \rangle = 1$). The order parameter ϕ aquires an appreciable value at hopping rates $J < J_c$ relative to the Bose-Hubbard transition point $J = J_c$.

This shift is accompanied by an increase in the mean particle number in the Mott phase from unity. Strikingly, Figure 7.8 (c) shows that the parametric driving induces non-local string order inside what was the Mott lobe, the magnitude of which increases with Δ. The magnitude of the string order is largest just inside this modified insulator, decaying away for smaller J.

Figure 7.9 shows results for a two-dimensional phase diagram in the (μ, U) plane, for different values of parametric driving strength Δ. Again, we see that the Mott lobes shrink as the driving is switched on, and we also see the appearance of string order around their edges. Deep inside the lobes, however, the ground state is more protected from the effect of the driving. This behaviour accords also with the results

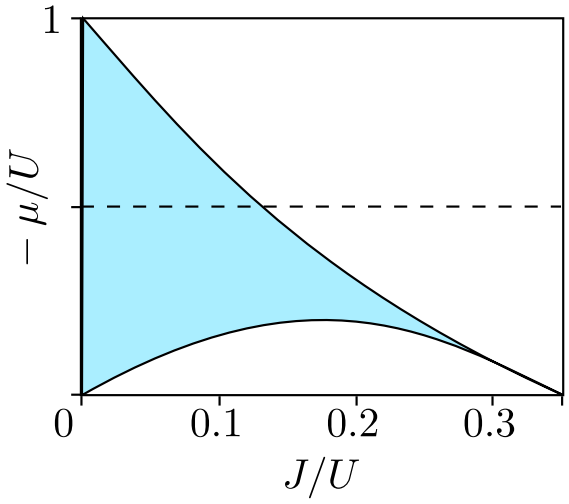


Figure 7.7. Rigorous ground state phase diagram of the Bose-Hubbard model. Blue: single-particle Mott Lobe characterised by vanishing order parameter $\phi = \langle \hat{a} \rangle_{\mathrm{GS}}$. Surrounding white region: superfluid with non-zero order parameter $\phi \neq 0$. The lobe aquires a characteristic downwards-pointing slope compared to simpler mean-field treatments. Reproduced from [59].

for the hard-core limit in Fig. 7.6. Again, we find no degeneracy signatures of topological properties in the entanglement spectrum at any point in phase space.

7.3 Finite systems

In this section we consider finite 1D chains of size M. As we show explicitly for the hard-core limit below, in certain parameter regimes topological behaviour manifests in the ground state of these systems as degenerate modes localised at the ends of the 1D chain. In addition to a degeneracy in the eigen-spectrum of the Hamiltonian, degeneracies appear in the entanglement spectrum too. The relatively small sizes of arrays we study ($M < 20$) mean that it is not possible to take the limit in Eqns. (7.3) - (7.5) to determine non-local order parameter values, and so we focus primarily on the entanglement spectra properties.

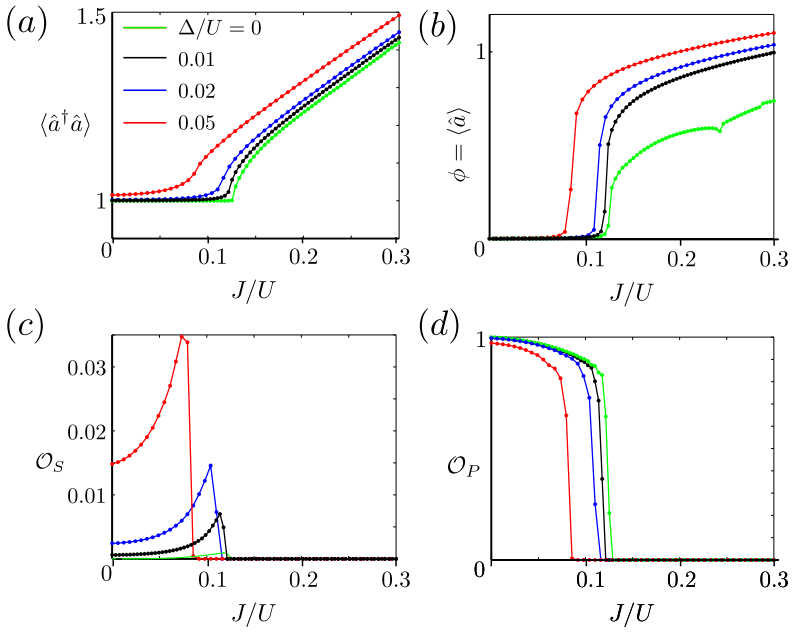


Figure 7.8. Ground state observables along the dashed line in Fig. 7.7. Parameters: fixed $\mu/U = -0.5$. (a) The ground state occupation number per site. (b) The local order parameter $\phi = \langle \hat{a} \rangle_{\mathrm{GS}}$ distinguishing between Mott ($\phi = 0$) and superfluid ($\phi \neq 0$) phases at $\Delta = 0$. (c) The non-local string order. (d) Non-local parity order.

7.3.1 Hardcore limit - Kitaev model and topological behaviour

Taking $U \to \infty$ for a finite array recovers a toy model possessing topologically non-trivial properties, first introduced by Kitaev. To gain insight into the topological nature, we define the Majorana operators

$$\begin{aligned} \hat{c}_{2j-1} &= \hat{a}_j + \hat{a}_j^\dagger, \\ \hat{c}_{2j} &= -i\left(\hat{a}_j - \hat{a}_j^\dagger\right). \end{aligned} \tag{7.6}$$

Focussing on the illustrative case $\Delta = J > 0$ and $\mu = 0$ (i.e. $\omega_c = \omega_L$), the total Hamiltonian reduces to

$$H = iJ \sum_{j=1}^{M-1} \hat{c}_{2j} \hat{c}_{2j+1}. \tag{7.7}$$

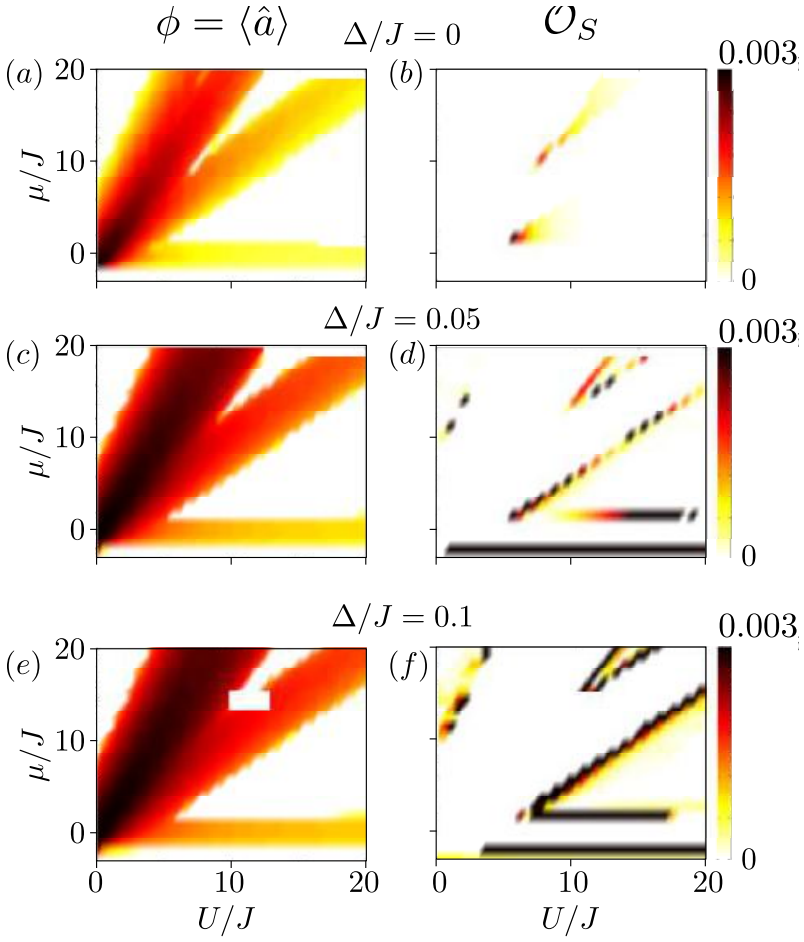


Figure 7.9. Local order parameter $\phi = \langle \hat{a}_{\mathrm{GS}} \rangle$ (left) and string order $\mathcal{O}_S$ (right) for different parametric driving rates: $\Delta/J = 0$ (top row), $\Delta/J = 0.05$ (middle row), $\Delta/J = 0.1$ (bottom row). We see the Mott lobes retreating up the U/J axis for larger driving. Strikingly, we see sizeable string ordered regions building up along the edges of Mott lobes.

Expanding out these $\hat{c}$ operators on 'virtual' nearest neighbour sites, we recover nearest the neighbour hopping of the original Hamiltonian.

Thus the Majorana operators $\hat{c}_{2j}$, $\hat{c}_{2j+1}$ from different sites are paired together. Importantly, the spectrum exhibits two zero-energy Majorana modes corresponding to the Majorana operators $\hat{c}_1$ and $\hat{c}_{2M}$ localised at the ends of the chain (note that these operators do not appear in the sum in Eq. (7.7)). A full working [211] shows that in contrast, when $|\mu| > 2J$, only Majorana operators $\hat{c}_{2j-1}$, $\hat{c}_{2j}$ from the same physical site j are paired together. The difference between these two types of pairing

are illustrated in Fig. 7.10.

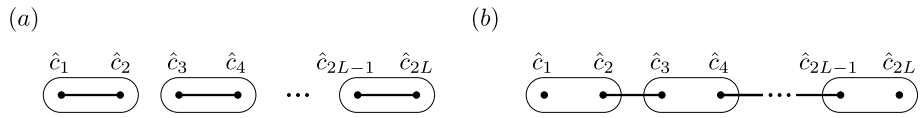


Figure 7.10. Two types of pairing in the Kitaev model

Figures 7.11 and 7.12 show these degeneracies as calculated for small systems, along with the entanglement spectral gap between the two largest Schmidt coefficients of the reduced density matrix after a bipartition at the middle of the array.

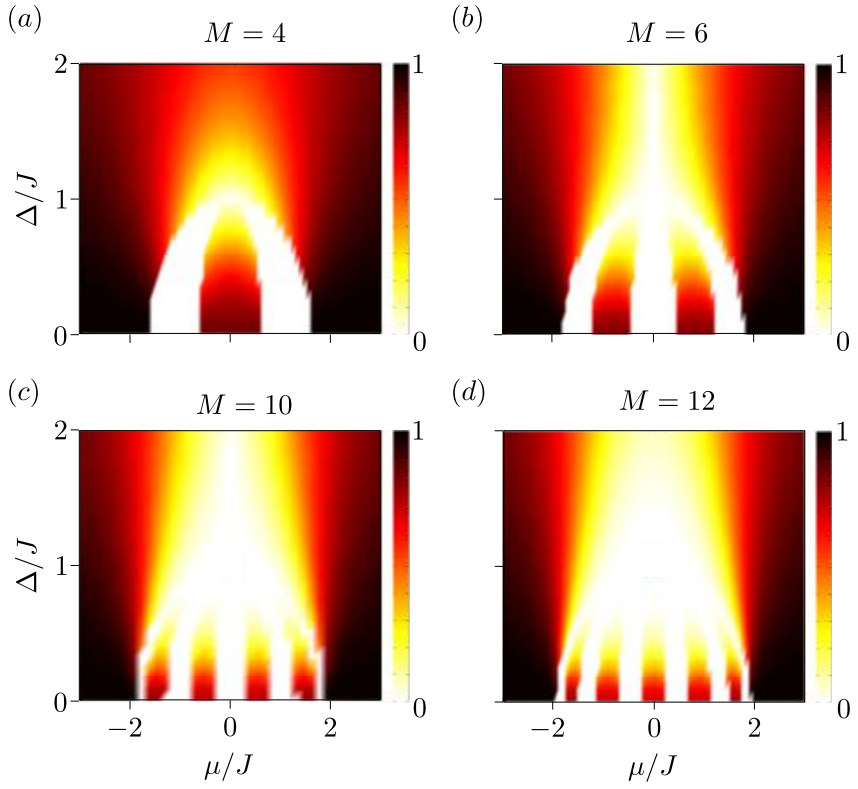


Figure 7.11. Entanglement spectral gap $\lambda_1 - \lambda_2$ between the largest and second-largest Schmidt coefficients λ_1 and λ_2 for ground states of the Kitaev model for small systems of size M.

The trend with increasing M is for the entanglement spectrum degeneracy (white) to occupy the whole region $|\mu| < 2J$. The M-dependent oscillatory structure at small drivings Δ is a finite-size effect, vanishing for larger systems.

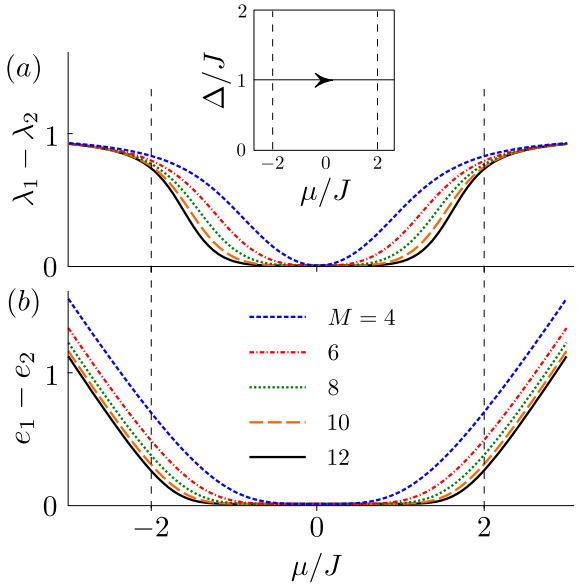


Figure 7.12. (a) Cross-section of the entanglement spectral gap through Figures 7.11. (b) Shows instead the gap between the lowest-lying eigenvalues of the governing Hamiltonian (ground state and first excited state). We see for both cases degeneracies which extend approximately across $\mu \in [-2J, 2J]$.

7.3.2 Relaxing the hardcore constraint

The topologically non-trivial behaviour of the Kitaev model is well known. Probing Majorana fermionic physics in an effective Kitaev model in a CRA setting was the primary focus of the work in [139]. Of interest is whether topological signatures may be observed in realistic arrays, possessing a large but finite resonator interaction strength U. To this end, in Fig. 7.13 we present ground state entanglement spectral gaps for finite systems of $M = 20$ resonators at different on-site interaction strengths U. Encouragingly, we observe degeneracies over a large region R of parameter space even down to an achievable nonlinearity $U/J = 10$. Interestingly, the region R is no longer constrained to $|\mu| < 2J$ as in the hard-core model of Fig. 7.13 (a). At larger drivings $\Delta/J \approx 1$, R appears to extend into the surrounding Mott lobes. We also note an asymmetry in R not present in the hardcore calculations (which possess particle-hole symmetry).

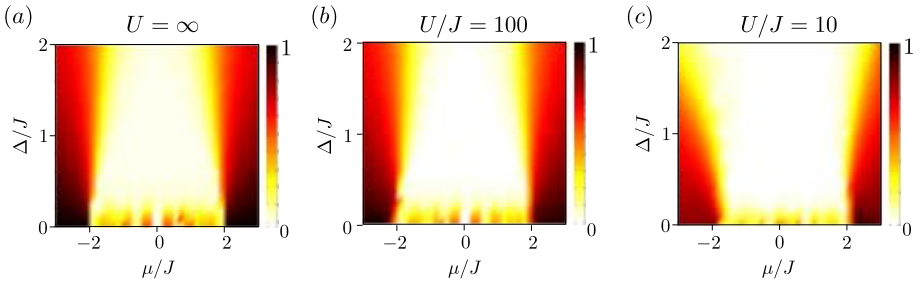


Figure 7.13. Entanglement spectral gap $\lambda_1 - \lambda_2$ for finite systems ($M = 20$) with finite nonlinearities. (a) The hard-core limit $U = \infty$. (b) $U = 100$. (c) $U = 10$.

7.4 Discussion

As noted at the beginning of this chapter, the results presented here are not intended to be an exhaustive exploration of the ground state properties of parametrically driven CRAs. Rather, we have presented an initial charting of the behaviour of this model around various limits, for both finite and infinite arrays. We found that the parametric driving induces string order inside Mott insulating lobes (but not in the surrounding superfluid). Encouragingly for the possibility of experimental observation of Majorana physics, we found evidence that topological behaviour in the well-known Kitaev model persists in more realistic resonator arrays described by finite nonlinearities.

Chapter 8

Conclusions

In this thesis we have explored the physics of driven strongly correlated photonic systems far from equilibrium. We have focused mostly on the properties of steady states of photonic resonator arrays subject to loss, maintained by a coherent driving.

8.1 Summary of results

The first part of this thesis dealt with the necessity of properly describing resonator arrays, both physically and numerically. These investigations constitute essential groundwork for further work on non-equilibrium CRAs. We demonstrated that the polaritonic nature of elementary excitations in resonator arrays as rigorously described by the Jaynes-Cummings-Hubbard Hamiltonian leads to novel physics beyond a canonical Bose-Hubbard description familiar from cold atom physics. We showed that in the low-excitation, fully quantum regime, Jaynes-Cummings signatures in steady state photonic observables cannot be 'mapped' exactly on to a purely bosonic Kerr-type description, though many similarities do exist. Despite the many differences we highlighted, we showed that fascinating novel strongly correlated photonic effects recently predicted in Bose-Hubbard type arrays persist under a more

realistic Jaynes-Cummings-Hubbard treatment, thereby supporting the candidacy of these effects to be experimentally observable in future experiments.

We then went on to demonstrate, making extensive use of a simplified 'minimal' driven lattice system, that care must be taken to rigorously account for the effects of long-ranged correlations when simulating non-equilibrium lattice dynamics. We found that commonly-used approximation schemes which amount to truncating the effect of long-ranged correlations to an effective local action introduce spurious non-physical artefacts into simulation results. In particular we focussed on the existence of bistabilities, or the potential for multiple unique stable steady states, in driven quantum arrays. Lower-order approximations were shown to lead to sharp 'switching' behaviour in non-equilibrium steady state observables, a manifestation of the nonlinearities introduced by this truncation. These signatures of bistability vanished once both classical and quantum correlations were fully accounted for.

Armed with this knowledge, Chapters 5 and 6 explored novel dynamical and steady state phenomena that may well be experimentally verifiable in near-future small arrays. Namely, we investigated the origins of a counter-intuitive bunching in the statistics of photons emitted from driven arrays featuring repulsive interactions, relating the steady state properties to an interplay between the non-equilibrium operation and the underlying Hamiltonian structure. An intriguing dynamical effect in CRAs was then presented in Chapter 6. We showed that arrays initially half-filled with photon 'walls' demonstrate a 'frozen' localisation of these photons for sufficiently large resonator nonlinearity.

Most of the results in this thesis concerned systems driven homogeneously with in-phase lasers addressing each resonator individually. However, Chapter 7 presented an analysis of the phases of a recently proposed variant on driven CRAs, in which correlated photon pairs are pumped into adjacent resonators. This novel arrangement features an interplay between injected short-range coherence, on-site

nonlinearity, and photon tunnelling processes, the physics of which has not been explored away from idealised limits. We explored both the thermodynamic limit, and finite one-dimensional systems where topologically non-trivial behaviour is expected, building up a comprehensive picture of the model's rich behaviour across parameter space.

Additionally, this work has shown that our main numerical workhorse, the combination of the quantum trajectory method with the TEBD algorithm, is an especially powerful tool in finding the NESS of open driven dissipative many-body systems. Such a numerical approach can be readily applied to calculate more complex out of equilibrium properties of coupled resonator arrays where an analytic approach is unfeasible. This might include important open problems such as determining the transport properties of linear coupled resonator arrays in the presence of photon loss, or exploring novel one-dimensional quantum states of light that are robust to experimentally realistic decay processes.

8.2 Future prospects

The present time is an exciting one for the field of strongly-correlated photon gases far from equilibrium. The study of driven-dissipative CRAs is very active and still relatively young, though dominant strands of research are beginning to emerge. Experimental efforts are underway to construct the first minimal coupled cQED arrays.

It is apparent that accompanying the experimental progress in fabricating and controlling resonator arrays in one architecture or another, numerical explorations of strongly correlated photonic states will lead and guide our understanding of these systems. Simulations of the steady state of resonator arrays are computationally challenging for reasons explored in this thesis. Though there is a growing arsenal of

numerical approaches to treat strongly correlated extended lattice systems such as the successful TEBD algorithm used extensively in our work, there is much room for improvement.

To this end, our results presented at the end of Chapter 4 regarding a comparison between master equation and trajectory simulations of open quantum lattice systems present an interesting starting point for further research into the complementary nature of the two approaches. An exploration of the relative merits of the two algorithms in computing steady state quantities in different regimes has practical and conceptual value. It is the magnitude of classical correlations across a system which decides which method is preferable, in computational terms. A comparison of the convergence of both algorithms with the matrix product state parameter χ (controlling the size of correlations describable by the states) may allow insight into the relative contribution of classical and quantum correlations in many-body systems. It is traditionally difficult to separate the effects of these two sources of correlations. We feel that the minimal system we studied in Chapter 4 serves as an ideal testbed for an exploration of these ideas, as we have already demonstrated its non-trivial physics and initiated a comparison between the two methods.

At a more conceptual level, the physics of infinite-size driven-dissipative arrays is of interest. Numerous recent works have addressed the possibility of constructing a non-equilibrium phase diagram for infinite resonator arrays described by models we have studied in this thesis. Many of these works employ a mean-field type approach to decoupled neighbouring lattice sites, thereby neglecting the effect of longer-ranged correlations. We have shown in Chapter 4 that such approximations may lead to non-physical steady state artefacts, which may be misleading in interpreting the physics of the resulting 'phase diagrams'. We have shown that matrix product representations of steady states effectively expose these artefacts. The TEBD simulations of non-equilibrium steady states that we have presented in this thesis are

appropriate only for finite sized systems, though we have 'approached' the infinite system limit in Chapters 5 and 4 by simulating systems of increasing size.

A promising and interesting route forward is to use a variant of the infinite TEBD (iTEBD) algorithm used to calculate ground state properties in Chapter 7. The initial work detailing the iTEBD algorithm [154] provided prescriptions only for solving for ground states and pure state evolution of infinite lattices. More general evolutions such as that induced by quantum master equations introduced instabilities in the algorithm. A solution was described soon after in [174], allowing simulation of driven-dissipative infinite systems. This algorithm has not, to our knowledge, been used in the literature at all, and we have also not yet implemented it.

Calculation and characterisation of steady state quantities of driven resonator arrays using the non-equilibrium iTEBD algorithm would be of great interest and novelty. It would allow for instance an evaluation of interesting recent evidence for non-equilibrium super solid signatures [106], or a verification of novel phase diagrams predicted for systems with number-conserving two-site incoherent processes [177].

While we have made significant inroads into characterising the ground-state phases of the parametrically driven CRAs considered in Chapter 7, more remains to be done. In particular, analytic perturbations around the non-interacting ($U = 0$) and strongly interacting ($U \to \infty$) limits should be possible, allowing further insight into these limits on top of our numerical explorations. Additionally, we note that the form of the governing Hamiltonian of Eq. (7.1) is only valid when the local (intra-resonator) nonlinearity is sufficiently large such that correlated photon pairs are strongly inhibited from being injected into a single resonator. The physics when this condition is not met may well be interesting, and relevant to experimental situations which can not achieve ultra-strong on-site nonlinearities. Driving processes of the form $\hat{a}_j\hat{a}_j + h.c.$ would need to be added to the Hamiltonian, leading to novel

effects.

Finally, we note that throughout this thesis we have computed intra-resonator observables such as the photon number in each resonator. Due to photon loss, such quantities are mapped on to the emitted photon fields and can thus be indirectly probed. An alternative scheme to gain insight into strongly-correlated phenomena within resonator arrays is instead to develop an input-output formalism [222, 33] for these structures. Such a formalism relates 'input' field amplitudes to those transmitted through the system, and preliminary steps towards developing the machinery necessary to deal with CRA transmutation properties has been introduced recently [223, 224]. Input-output calculations would allow theoretical insight into the experimentally relevant situation of coherent laser light being shone on CRAs, with detectors measuring transmission, without the need to probe the internal dynamics of the array.

Appendix A

Derivation of the Lindblad quantum master equation

We begin by stating in general terms the objective of the QME derivation. A closed system with Hamiltonian H is governed by the von Neumann equation (with $\hbar = 1$)

$$\frac{d}{dt}\rho(t) = -i[H, \rho(t)], \tag{A.1}$$

with solution

$$\rho(t) = U(t, t_0)\rho(t_0)U^\dagger(t, t_0). \tag{A.2}$$

Here the unitary operator $U(t, t_o) = \exp(-iH(t - t_o))$, and $\rho(t_0)$ is the initial state of the system at time $t = t_0$.

We shall be concerned with bipartite systems $S + B$, where it is logical and desirable to separate the system into two interacting subsystems S (the system) and B (the 'bath' or environment), as sketched in Fig. A.1. We assume that the total system $S + B$ is closed with Hamiltonian

$$H = H_S + H_B + H_I, \tag{A.3}$$

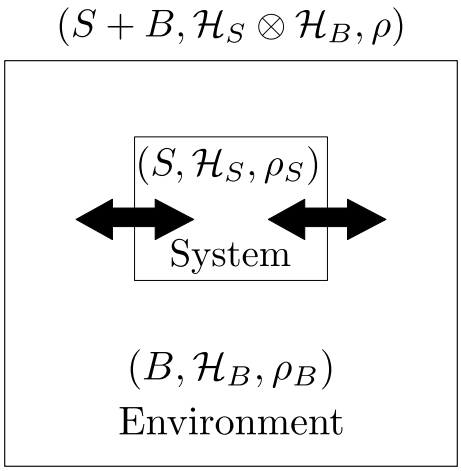


Figure A.1. Representation of the interaction between a quantum system S and its environment B. The system is described by the Hamiltonian $\mathcal{H}_S$ and reduced density matrix ρ_S. Black arrows represent the interaction between the system and environment as described by the interaction Hamiltonian $\mathcal{H}_I$.

where H_S and H_B are the free Hamiltonians of the system and reservoir, respectively. Meanwhile the interaction between the system and reservoir is described by H_I. The density matrix $\rho(t)$ for this total system evolves according to Eq. (A.1). Our ultimate aim is to derive an equation of motion for the system degrees of freedom alone, i.e. to find an evolution equation for $\rho_S(t) = \mathrm{Tr_B}\{\rho(\mathrm{t})\}$, where Tr_B denotes the partial trace of the total density matrix $\rho(t)$ over the environmental degrees of freedom. This is frequently desirable in practise, when the state of the environment B is either not of interest, or impractical to model due to its size and / or complexity.

The following sections outline the procedure to obtain the evolution of the system of interest from the total system dynamics of Eq. (A.1).

A.0.1 The Lindblad form of the master equation

Before proceeding with the derivation, we pre-empt the result. It is known that the most general form of a Markovian time-local master equation that preserves the trace, Hermiticity, and positivity of the system's density matrix ρ_S must be of

so-called Lindblad form:

$$\dot{\rho}_S = \mathcal{L}\rho = -i[H_S, \rho_S] + \sum_{\alpha,\beta=1}^{N^2-1} \gamma_{\alpha\beta} \left(A_\alpha \rho_S A_\beta^\dagger - \frac{1}{2} \left\{ A_\beta^\dagger A_\alpha, \rho_S \right\} \right), \tag{A.4}$$

where $\gamma_{\alpha\beta} = \gamma_{\beta\alpha}^*$ is a positive semi-definite matrix and the $\{A\}$ are operators in the system Hilbert space. The Lindblad form can be written in a simpler way, which we use exclusively in this thesis. Specifically, the Hermiticity of the 'damping matrix' γ allows us to diagonalise it via a unitary transformation $\sum_{\alpha\beta} U_{\alpha'\alpha}\gamma_{\alpha\beta}(U^\dagger)_{\beta\beta'} = \delta_{\alpha'\beta'}\gamma_{\alpha'}$. A new set of simplifying operators L_α may be defined through this unitary transformation as $A_\alpha = \sum_{\alpha'} U_{\alpha'\alpha} L_{\alpha'}$. Making these substitutions leads to

$$\dot{\rho}_S = \mathcal{L}\rho = -i[H_S, \rho_S] + \sum_{\alpha} \gamma_\alpha \left(L_\alpha \rho_S L_\alpha^\dagger - \frac{1}{2} \left\{ L_\alpha^\dagger L_\alpha, \rho_S \right\} \right), \tag{A.5}$$

where the γ_α are identified as the characteristic rates at which 'jump operators' L_α act on the system. For instance, in the case of a lossy single-mode resonator with field destruction operator $\hat{a}$, γ describes the loss rate of the resonator, characteristic of the jump operator $\hat{a}$ which acts to dissipate photons.

A.0.2 Evolution of the system density operator

We begin the derivation of Eq. (A.4) by transforming the von Neumann evolution equation to the interaction picture:

$$\frac{d}{dt}\tilde{\rho}(t) = -i[\tilde{H}_I(t), \tilde{\rho}(t)], \tag{A.6}$$

where the interaction picture operators are defined as

$$\tilde{\rho}(t) = e^{i(H_S+H_B)t}\rho(t)e^{-i(H_S+H_B)t}, \tag{A.7}$$

$$\tilde{H}_I(t) = e^{i(H_S+H_B)t}H_I e^{-i(H_S+H_B)t}, \tag{A.8}$$

Equation A.6 may be integrated to obtain the formal solution

$$\tilde{\rho}(t) = \tilde{\rho}(0) - i\int_0^t ds[\tilde{H}_I(s), \tilde{\rho}(s)]. \tag{A.9}$$

Inserting this solution back into Eq. (A.6) and tracing out the reservoir to obtain an equation for the system dynamics yields

$$\frac{d}{dt}\tilde{\rho}_S(t) = -\int_0^t ds\ \mathrm{tr}_B\left[\tilde{H}_I(t), [\tilde{H}_I(s), \tilde{\rho}(s)]\right]. \tag{A.10}$$

Note that in arriving at Eq. (A.10) we have assumed that $\mathrm{tr}_B[\tilde{H}_I(t), \tilde{\rho}(0)] = 0$ without loss of generality. This may be achieved by simultaneously modifying the form of the system and coupling Hamiltonians without altering the physics.

Equation (A.10) has the total system interaction picture density matrix $\tilde{\rho}$ on its right hand side. To proceed we make an approximation concerning the coupling between the system and reservoir, known as the Born approximation. This approximation assumes that the coupling between the system and the reservoir is weak, such that the state of the reservoir as described by its density matrix ρ_B is essentially unchanged by the interaction – the environment is so large that the system has no effect on its state. Mathematically, we express this as the total density matrix being separable as a tensor product at all times

$$\tilde{\rho}(t) \approx \tilde{\rho}_S(t) \otimes \tilde{\rho}_B. \tag{A.11}$$

Inserting this ansatz into Eq. (A.10) gives us a closed equation for the system density matrix ρ_S,

$$\frac{d}{dt}\rho_S(t) = -\int_0^t ds\ \mathrm{tr}_B\left[H_I(t), [H_I(s), \rho_S(s)\otimes\rho_B]\right]. \tag{A.12}$$

First Markov Approximation

While this last form is significantly simplified, and importantly no longer contains the total density matrix, it is still non-local in time. Though there are many important and interesting cases where the past history of a system determines its future evolution, in many physically relevant cases it is justifiable to make the *first Markov approximation* which amounts to assuming the future behaviour of ρ_S depends only on its current state. Mathematically, this is done by making the replacement $\rho_S(s) \to \rho_S(t)$,

$$\frac{d}{dt}\rho_S(t) = -\int_0^t ds\ \mathrm{tr}_B\left[H_I(t), [H_I(s), \rho_S(t)\otimes\rho_B]\right]. \tag{A.13}$$

Second Markov Approximation

Equation (A.14) is now local in time, however the right hand side still depends on time t. We get around this by replacing s by $t-s$ and taking the upper limit of the integral to infinity in what is known as the *second Markov approximation*. This procedure is physically justified if the integrand disappears sufficiently fast with s, relative to the time-scale of the reservoir dynamics. Put another way, for this approximation to be valid, the system dynamics must be slow compared to the 'memory' time of the reservoir, so that we cannot resolve the system dynamics at the temporal resolution characteristic of the bath. Finally, we obtain

$$\frac{d}{dt}\rho_S(t) = -\int_0^\infty ds\ \mathrm{tr}_B\left[H_I(t), [H_I(t-s), \rho_S(t)\otimes\rho_B]\right]. \tag{A.14}$$

The Born-Markov approximations leading to Equation A.14 do not ensure that the resulting evolution is of Lindblad form Eq. (A.4). Moving towards this goal, we now make what is known as the rotating wave approximation, which involves averaging over rapidly oscillating terms in the master equation. To do this, we need an explicit form for the interaction picture interaction Hamiltonian $H_I(t)$. We proceed by writing H_I in the Schrodinger picture in the most general form

$$H_I = \sum_\alpha A_\alpha B_\alpha, \tag{A.15}$$

where A and B are respectively Hermitian system and reservoir operators $A_\alpha^\dagger = A_\alpha$ and $B_\alpha^\dagger = B_\alpha$. The rotating wave approximation is more easily performed if H_I is written in terms of the eigenoperators of the system Hamiltonian H_S. Denoting the eigenvalues of H_S as ϵ and the projection onto the ϵ-eigenspace as $\Pi(\epsilon)$, we define

$$A_\alpha(\omega) = \sum_{\epsilon'-\epsilon=\omega} \Pi(\epsilon) A_\alpha \Pi(\epsilon'), \tag{A.16}$$

where the sum runs over all eigenvalues with energy difference ω and $A_\alpha = \sum_\omega A_\alpha(\omega)$. The reason we define these operators A_α is because they satisfy the commutation relations

$$[H_S, A_\alpha(\omega)] = -\omega A_\alpha(\omega) \tag{A.17}$$

$$[H_S, A_\alpha(\omega)] = +\omega A_\alpha^\dagger(\omega), \tag{A.18}$$

from which it follows that the interaction picture operators are

$$e^{iH_S t} A_\alpha(\omega) e^{-H_S t} = e^{-i\omega t} A_\alpha(\omega), \tag{A.19}$$

$$e^{iH_S t} A_\alpha^\dagger(\omega) e^{-H_S t} = e^{+i\omega t} A_\alpha^\dagger(\omega). \tag{A.20}$$

We can now use these newly introduced operators $A_\alpha(\omega)$ to write the interaction Hamiltonian in the interaction picture in the simple form

$$H_I(t) = \sum_{\alpha,\omega} e^{-i\omega t} A_\alpha(\omega) \otimes B_\alpha(t) = \sum_{\alpha,\omega} e^{+i\omega t} A_\alpha^\dagger(\omega) \otimes B_\alpha^\dagger(t), \tag{A.21}$$

where the $B_\alpha(t) = e^{iH_B t} B_\alpha e^{-iH_B t}$ are the reservoir interaction picture operators.

Inserting this form for $H_I(t)$ into the master equation Eq. (A.14), first expanding the nested commutator, we obtain

$$\begin{aligned} \frac{d}{dt}\rho_S(t) &= \int_0^\infty ds\ \mathrm{tr}_B \left\{ H_I(t-s)\rho_S(t)\rho_B H_I(t) - H_I(t)H_I(t-s)\rho_S(t)\rho_B \right\} + h.c \\ &= \sum_{\omega\omega'} \sum_{\alpha,\beta} e^{i(\omega'-\omega)} \Gamma_{\alpha\beta}(\omega) \left(A_\beta(\omega)\rho_S(t)A_\alpha^\dagger(\omega') - A_\alpha^\dagger(\omega')A_\beta(\omega)\rho_S(t) \right) \end{aligned} \tag{A.22}$$

This last line is getting closer to the desired Lindblad form of the master equation Eq. (A.4), cleanly separating the explicit state of the bath and its effect on the system from the state of the system itself. The summand is split into terms concerning only the bath, and only the system. The former are

$$\Gamma_{\alpha\beta}(\omega) = \int_0^\infty ds e^{i\omega s} \langle B_\alpha^\dagger(t) B_\beta(t-s) \rangle, \tag{A.23}$$

and can be read as one-sided Fourier transforms encoding the properties of the reservoir correlation functions $\langle B_\alpha^\dagger(t)B_\beta(t-s)\rangle = \mathrm{tr}_B\{B_\alpha^\dagger(t)B_\beta(t-s)\rho_B\}$. If we assume the reservoir density matrix ρ_B describes a stationary state of the reservoir, i.e. $[H_B, \rho_B] = 0$, then these correlation functions do not depend on time, $\langle B_\alpha^\dagger(t)B_\beta(t-s)\rangle = \langle B_\alpha^\dagger(s)B_\beta(0)\rangle$, so that further the $\Gamma_{\alpha\beta}$ are time-independent.

The time dependence of the right hand side of the master equation in the form Eq. (A.23) is only found in the system state itself $\rho_S(t)$, and in the exponential factor $\exp(\omega' - \omega)t$. We now further assume that the characteristic time scale of the system

evolution as estimated by typical inverse frequency differences $|\omega' - \omega|^{-1}, \omega \neq \omega'$ is large compared to the relaxation time of the total open system. Consequently terms in this exponential sum for which $\omega \neq \omega'$ oscillate very rapidly over the relaxation time scale, and may therefore be dropped, yielding

$$\frac{d}{dt}\rho_S(t) = \sum_{\omega} \sum_{\alpha,\beta} \Gamma_{\alpha\beta}(\omega) \left(A_\beta(\omega)\rho_S(t)A_\alpha^\dagger(\omega') - A_\alpha^\dagger(\omega')A_\beta(\omega)\rho_S(t) \right) + h.c. \quad \text{(A.24)}$$

The Γ may be decomposed as

$$\Gamma_{\alpha\beta}(\omega) = \frac{1}{2}\gamma_{\alpha\beta}(\omega) + iS_{\alpha\beta}(\omega), \quad \text{(A.25)}$$

where the Hermitian matrix S is

$$S_{\alpha\beta}(\omega) = \frac{1}{2i}\left(\Gamma_{\alpha\beta}(\omega) - \Gamma_{\beta\alpha}^*(\omega) \right), \quad \text{(A.26)}$$

and the positive 'damping matrix' γ is

$$\gamma_{\alpha\beta} = \Gamma_{\alpha\beta}(\omega) + \Gamma_{\beta\alpha}^*(\omega) = \int_{-\infty}^{\infty} ds e^{i\omega s} \langle B_\alpha^\dagger(s) B_\beta(0) \rangle. \quad \text{(A.27)}$$

Making these substitutions leads finally to the interaction picture master equation

$$\frac{d}{dt}\tilde{\rho}_S(t) = -i[H_{LS}, \tilde{\rho}_S(t)] + \mathcal{D}\left(\tilde{\rho}_S(t)\right). \quad \text{(A.28)}$$

Here the *Lamb shift* Hamiltonian induces Hamiltonian dynamics in the interaction picture, and leads to a small shift in the unperturbed system energy levels. This shift in fact is so small that H_{LS} is generally dropped from the master equation.

The dissipator meanwhile is of the required general Lindblad form

$$\mathcal{D}(\tilde{\rho}_S) = \sum_{\omega} \sum_{\alpha,\beta=1} \gamma_{\alpha\beta}(\omega) \left(A_\alpha(\omega) \rho_S A_\beta^\dagger(\omega) - \frac{1}{2} \left\{ A_\beta^\dagger(\omega) A_\alpha(\omega), \rho_S \right\} \right), \tag{A.29}$$

after diagonalisation of the matrices $\gamma_{\alpha\beta}(\omega)$. These matrices are positive (for a proof see Chapter 3 of [142]) allowing the γ to be absorbed into the A matrices.

Finally, it can be shown that transformation of the master equation Eq. (A.28) to the Schrodinger picture follows by adding the free system Hamiltonian H_S to the H_{LS}, recovering the Lindblad form Eq. (A.4).

Appendix B

Matrix product states

B.1 Entanglement properties of 1D quantum systems

Here we outline features unique to 1D systems, with an emphasis on how correlations are distributed throughout 1D systems, and use these properties to motivate the form of a highly efficient and compact description of quantum lattice states. We present these ideas in the context of pure quantum states for clarity and conciseness.

B.1.1 Schmidt decompositions

Here we define the Schmidt decomposition, a useful mathematical tool allowing deep physical insight into the structure of a quantum state. Starting with an arbitrary state $|\Psi\rangle$ on an M-site lattice, we bipartition the system into two subsystems A and B composed of m and $M-m$ sites respectively. With $\{|i\rangle_A\}$ as an orthonormal basis spanning the d^m dimensional Hilbert space of A, and $\{|j\rangle_B\}$ spanning the d^{M-m} dimensional Hilbert space of B, the state $|\Psi\rangle$ can be expressed as

$$|\Psi\rangle = \sum_{i=1}^{d^M} \sum_{j=1}^{d^{M-m}} C_{ij} |i\rangle_A \otimes |j\rangle_B, \tag{B.1}$$

where C_{ij} are the elements of a $(d^m \times d^{M-m})$ matrix C. To bring the state into the canonical Schmidt form, we break C up using a singular-value decomposition $C = UDV$, where U and V are $(d^m \times d^m)$ and $(d^{M-m} \times d^{M-m})$ unitary matrices and D is a $(d^m \times d^{M-m})$ diagonal matrix with real and non-negative elements λ_α.

Making this substitution for C leads to the so-called Schmidt decomposition

$$|\Psi\rangle = \sum_{\alpha=1}^{\chi} \lambda_\alpha \left(\sum_{i=1}^{d^m} U_{i\alpha} |i\rangle_A \right) \otimes \left(\sum_{j=1}^{d^{M-m}} V_{\alpha j} |j\rangle_B \right) \tag{B.2}$$

$$= \sum_{\alpha=1}^{\chi} \lambda_\alpha |\phi_\alpha^{[A]}\rangle \otimes |\phi_\alpha^{[B]}\rangle. \tag{B.3}$$

The $\{|\phi_\alpha^{[A]}\rangle\}$, $\{|\phi_\alpha^{[B]}\rangle\}$ are orthonormal bases spanning χ-dimensional subspaces of $\mathcal{H}_A$ and $\mathcal{H}_B$. The λ_α are called Schmidt coefficients satisfying $\sum_\alpha \lambda_\alpha^2 = 1$, and χ is known as the Schmidt rank. We take the Schmidt coefficients to be arranged in descending order $\lambda_\alpha \geq \lambda_{\alpha+1}$.

B.1.2 Entanglement spectra

Important physical information is encoded in the distribution and magnitude of the Schmidt coefficients λ_α. For example, the reduced density matrices for the two subsystems $\rho_A = \mathrm{tr}_B(|\Psi\rangle\langle\Psi|)$ and $\rho_B = \mathrm{tr}_A(|\Psi\rangle\langle\Psi|)$ assume the simple forms

$$\rho_A = \sum_{\alpha=1}^{\chi} \lambda_\alpha^2 |\phi_\alpha^{[A]}\rangle\langle\phi_\alpha^{[A]}| \tag{B.4}$$

$$\rho_B = \sum_{\alpha=1}^{\chi} \lambda_\alpha^2 |\phi_\alpha^{[B]}\rangle\langle\phi_\alpha^{[B]}|. \tag{B.5}$$

A measure of the magnitude of correlations between the two parts A and B of the system is given by the von-Neumann entropy $S = -\mathrm{tr}(\rho_A \log_2 \rho_A) = -\mathrm{tr}(\rho_B \log_2 \rho_B)$ [167]. Using the reduced density matrices as expressed in terms of Schmidt coeffi-

cients and bases, we find

$$S = -\sum_{\alpha=1}^{\chi} \lambda_\alpha^2 \log_2\left(\lambda_\alpha^2\right). \tag{B.6}$$

Crucially the spectrum $\{\lambda_\alpha^2\}$ allows us to identify the most 'important' basis states of either subsystem as those with the largest eigenvalues λ_α^2. We may approximate the full state $|\Psi\rangle$ by retaining a limited number $\chi_m < \chi$ Schmidt states. As an extreme example, a product state $|\Psi\rangle = |\phi_1^{[A]}\rangle \otimes |\phi_1^{[B]}\rangle$ has minimum possible Schmidt rank $\chi = 1$ and no entanglement, and is characterised by $S = 0$. At the other extreme, a completely random state is expected to have a spectrum composed of χ roughly equal values, so that no accurate compressed approximation is possible.

However, it turns out that for many 1D systems, the ground state and states induced by typical nearest-neighbor Hamiltonian / master equation evolution have roughly exponentially decaying entanglement spectra λ_α [225]. Consequently only a small number of eigenvalues in the entanglement spectrum are relevant. Therefore it is possible to choose a $\chi_m \ll \chi$ and avoid exponential scaling in the system description. In this way, a dramatic compression in the system's description is possible while also remaining accurate.

The MPS ansatz as introduced in the main text in Section 2.3 encapsulates the observations outlined in this section.

B.2 Operations with matrix product states

Having defined matrix product states and discussed the features of 1D systems which make them an efficient, compact representation of many quantum states of interest, we now show how observables may be calculated in this formalism. Typically, we are interested in single- and multi-site reduced density matrices, with a view to calculating local (single-site) expectation values, and more general n-point correlators

of the form $\langle\Psi|O_1 \otimes O_2 \otimes \cdots \otimes O_M|\Psi\rangle$,where $\{O_j\}$ are operators acting on the Hilbert space at site j. We demonstrate these calculations on MPS under periodic boundary conditions. The analogous manipulations for open boundary conditions are straightforward.

For simplicity in both the written expansion and graphical representation of MPS, the notation we use in this Appendix is slightly different than that used in the main text. Specifically, the two matrices $\mathbf{\Gamma}^{[m]j_m}$ and $\boldsymbol{\lambda}^{[m]}$ associated with each site in the MPS definitions of Chapter 2 are here absorbed into a single matrix $\boldsymbol{A}^{[m]j_m}$. This can be done, for instance by absorbing factors $\sqrt{\boldsymbol{\lambda}^{[m]}}$ into the $\mathbf{\Gamma}$ matrices at sites $m-1$ and m.

To begin, the full density operator $\rho = |\Psi\rangle\langle\Psi|$ is

$$\rho = \sum_{\boldsymbol{j}_{[1,M]}} \sum_{\boldsymbol{i}_{[1,M]}} \mathrm{tr}\left(\prod_{m=1}^{M} \boldsymbol{A}^{[m]j_m}\right) \mathrm{tr}\left(\prod_{m=1}^{M} \boldsymbol{A}^{*[m]j_m}\right) |\boldsymbol{j}_{[1,M]}\rangle\langle\boldsymbol{i}_{[1,M]}|, \tag{B.7}$$

after using $\mathrm{tr}(XYZ)^* = tr(X^*Y^*Z^*)$. A graphical representation of this form is given in Fig. B.1 (a). Using the additional identities $\mathrm{tr}(X)\mathrm{tr}(Y) = \mathrm{tr}(X \otimes Y)$ and $(ABC) \otimes (XYZ) = (A \otimes X)(B \otimes Y)(C \otimes Z)$, a more compact form follows as

$$\rho = \sum_{\boldsymbol{j}_{[1,M]}} \sum_{\boldsymbol{i}_{[1,M]}} \mathrm{tr}\left(\prod_{m=1}^{M} \boldsymbol{E}^{[m]j_m i_m}\right) |\boldsymbol{j}_{[1,M]}\rangle\langle\boldsymbol{i}_{[1,M]}|, \tag{B.8}$$

where the matrix $\boldsymbol{E}^{[m]i_m j_m} = \boldsymbol{A}^{[m]j_m} \otimes \boldsymbol{A}^{*[m]i_m}$, is illustrated in Fig. B.1 (b).

The reduced density matrix for site k is obtained by tracing out all physical sites but site k:

$$\rho_k = \sum_{j_k=1}^{d} \sum_{i_k=1}^{d} \mathrm{tr}\left(\left[\prod_{m=1}^{k-1} \boldsymbol{I}^{[m]}\right] \boldsymbol{E}^{[k]j_k i_k} \left[\prod_{m'=k+1}^{M} \boldsymbol{I}^{[m']}\right]\right) |j_k\rangle\langle i_k|, \tag{B.9}$$

also illustrated in Fig. B.1 (b). Here the $\boldsymbol{I}^{[m]} = \sum_{j_m=1}^{d} \boldsymbol{E}^{[m]j_m j_m}$ are called transfer

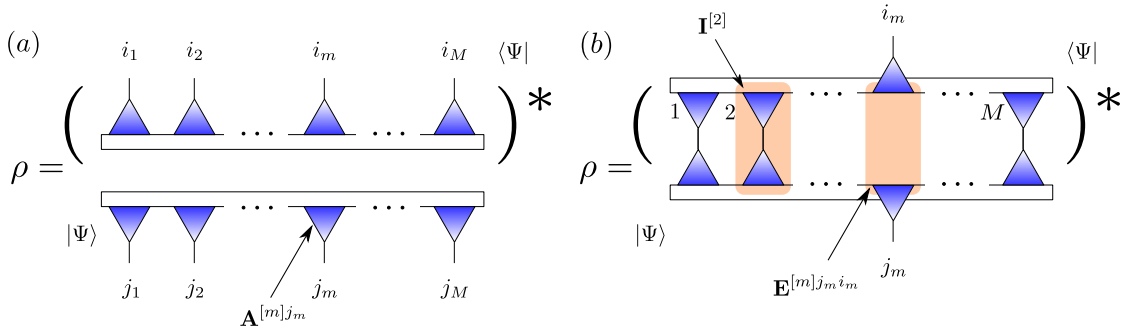


Figure B.1. (a) Schematic illustration of the full density matrix $\rho = |\Psi\rangle\langle\Psi|$ for a system described by a pure state $|\Psi\rangle$. The triangular objects represent the matrices $\boldsymbol{A}^{[m]}$. (b) Illustration of the calculation of a reduced density matrix at site m. Tracing out all sites except m is accomplished by contracting all the physical indices of the $\boldsymbol{A}$ matrices at sites $\neq m$, indicated graphically by joining the relevant 'legs' of the triangles. The resulting object has just two free indices i_m and j_m, which are the rows and columns of the density matrix ρ_m. Also indicated are the matrices $\boldsymbol{E}^{[m]j_m i_m}$ and $\boldsymbol{I}^{[m]}$.

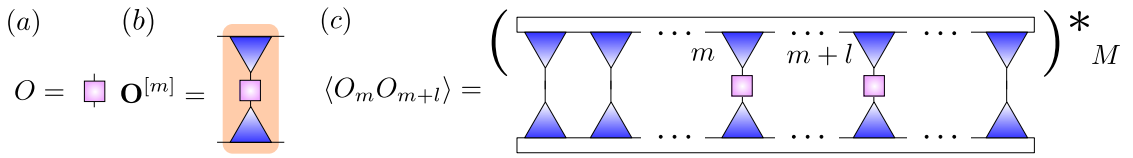


Figure B.2. Illustration of the calculation of two-site correlators $C_{l,m+l} = \langle O_m O_{m+l}\rangle$. (a) Representation of an observable O acting on one site. The two 'legs' represent the rows and columns of the appropriate matrix representation. (b) Representation of the matrix $\boldsymbol{O}^{[m]}$ formed by contraction of the state at site m with O. (c) Illustration of the contractions required to calculate $C_{l,m+l}$.

matrices, and follow from the contraction of the physical indices labelling the set of matrices. This expression for the reduced density matrix of a single site k can be generalised to the reduced density matrix of a larger number of sites. Such reduced density matrices are composed of a trace of the relevant products of $\boldsymbol{I}^{[m]}$ and $\boldsymbol{E}^{[m]j_m i_m}$ matrices. With these results, we may write a general product expectation value as

$$\langle\Psi|O_1 \otimes O_2 \otimes \cdots \otimes O_M\rangle|\Psi\rangle = \mathrm{tr}\left(\prod_{m=1}^{M} \boldsymbol{O}^{[m]}\right), \tag{B.10}$$

where the observable matrices $\boldsymbol{O}$ are defined as

$$\boldsymbol{O}^{[m]} = \sum_{j_m=1}^{d} \sum_{i_m=1}^{d} \langle j_m | O | i_m \rangle \boldsymbol{E}^{[m] j_m i_m}. \tag{B.11}$$

In this way general n-point correlators may be calculated, however we note that in most calculations many of the O_m will be the identity matrix, in which case the corresponding $\boldsymbol{O}^{[m]} = \boldsymbol{I}^{[m]}$. Exploiting certain structural properties of the $\boldsymbol{I}$ leads to efficient computation of observables, with a number of operations scaling as $\mathcal{O}(d\chi^5 M)$ and $\mathcal{O}(d\chi^3 M)$ for periodic and open boundary conditions, respectively.

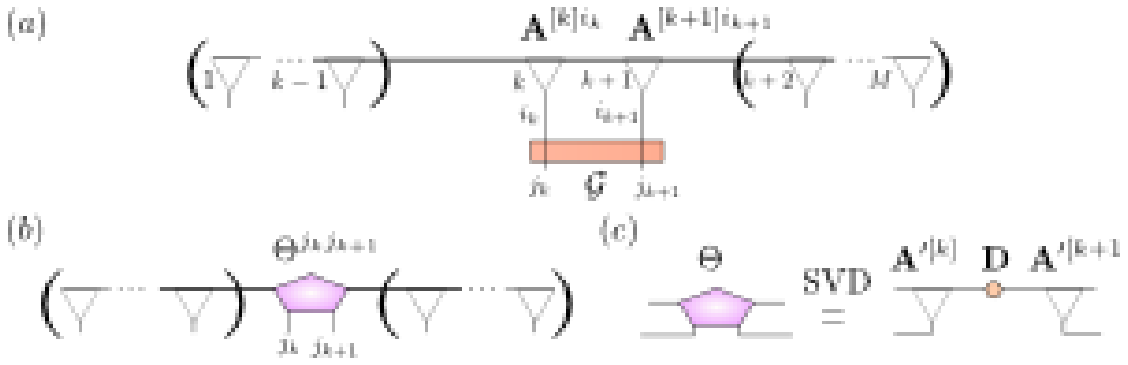


Figure B.3. (a) A gate $\mathcal{G}$ is applied to sites k, $k+1$ of an MPS with form given by Eq. (**??**). (b) The intermediate tensor Θ is not of MPS form, but can be brought back into standard form after splitting it with a singular value decomposition.

Having outlined the calculation of quantities commonly of interest, we now discuss the essential ingredient of the TEBD algorithm, which consists of applying two-site 'gates' (operators) to a MPS. The algorithm requires the application of gates only to adjacent sites $k, k+1$. The most general form of such a two-site gate is

$$\mathcal{G} = \sum_{\boldsymbol{j}_{k,k+1}} \sum_{\boldsymbol{i}_{k,k+1}} G_{i_k i_{k+1}}^{j_k j_{k+1}} |j_k\rangle |j_{k+1}\rangle \langle i_k | \langle i_{k+1}|. \tag{B.12}$$

We wish to apply $\mathcal{G}$ to an MPS of rank χ and obtain as a result another MPS of rank χ. The details are somewhat involved and beyond the scope of this background

chapter [155]. However, the procedure is illustrated graphically in Fig. B.3. Essentially, the tensor $G^{j_k j_{k+1}}_{i_k i_{k+1}}$ is *contracted* with the two 'physical legs' of the $\boldsymbol{A}$ matrix at sites $k, k+1$. This amounts to a series of multiplications and summations over these indices, represented schematically in Fig. B.3 (a) by joining the relevant 'legs' of the $\boldsymbol{A}$ matrices and the $\mathcal{G}$ tensor. The result is a single intermediate tensor Θ, which is a set of $d^2(\chi_{k-1} \times \chi_{k+1})$ matrices indexed by the two physical indices j_k, j_{k+1}. To once again achieve the canonical MPS form, this tensor is reshaped into a 2D $d\chi_{k-1} \times d\chi_{k+1}$ matrix. A singular value decomposition splits this matrix into two new matrices $\boldsymbol{A}'^{[k]}$, $\boldsymbol{A}'^{[k+1]}$, as well as a diagonal matrix $\boldsymbol{D}$, which can be absorbed into the $\boldsymbol{A}$ matrices. During the course of these manipulations, the Schmidt rank χ'_k may have increased, perhaps exceeding the fixed MPS parameter χ. To deal with this, only the Schmidt states corresponding to the χ largest Schmidt coefficients λ_α of the singular value decomposition are retained. The final MPS is therefore truncated. However, it can be shown that the overlap error in applying a single gate is [226]

$$\epsilon = 1 - |\langle \Psi' | \Psi'_{\mathrm{tr}} | = \sum_{\alpha_k = \chi_m}^{\chi'_k} \left(\lambda'^{[k]}_{\alpha_k}\right)^2 \tag{B.13}$$

Monitoring the magnitude of the discarded Schmidt coefficients therefore yields information on the accuracy of the operation.

B.3 Time evolving matrix product states

B.3.1 The Suzuki-Trotter approximation

In this thesis we will only be concerned with time-independent Hamiltonian and Liouvillian operators. The time evolution for a pure state $|\Psi(t)\rangle$ under the action of a Hamiltonian $\hat{H}$ is then $|\Psi(t)\rangle = \exp(-i\hat{H}t)|\Psi(0)\rangle$.

For all but the smallest systems, the evolution operator $U(t) = \exp(-i\hat{H}t)$ can

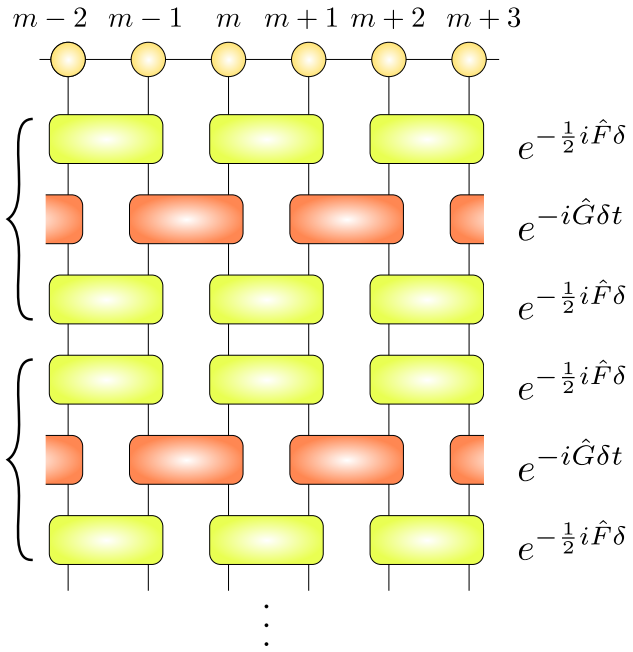


Figure B.4. Simplified schematic of a TEBD simulation time-step. Gates are applied to even pairs $\exp(-\frac{1}{2}i\hat{F}\delta t)$, then odd pairs $\exp(-i\hat{G}\delta t)$ then even pairs again $\exp(-\frac{1}{2}i\hat{F}\delta t)$.

not be represented exactly. To simulate time evolution, we therefore discretise the total integration time T into $T/\delta t$ steps as $t_n = (n-1)\delta t$, with $n = \{1, \ldots, T/\delta t\}$. We then approximate the action of $U(t)$ by repeatedly applying $U(\delta t)$.

$$U(t) = \exp\left(-i\hat{H}t\right) \approx \prod_{n=1}^{T} \exp\left(-i\hat{H}\delta t\right) + \mathcal{O}(\delta t^2). \tag{B.14}$$

This discretisation simplifies the time integration by breaking it into smaller steps. However, computing $U_{\delta t} = \exp\left(-i\hat{H}\delta t\right)$ still requires exponential resources as it acts over the full state space.

Progress is possible for our Hamiltonians of interest, namely those with at most nearest-neighbor interactions. Local terms (those acting on only a single site) can be written as two-site terms $\hat{O}_j \otimes I_{j+1}$. We may then break such lattice Hamiltonians

into a sum of terms acting on nearest neighbours $\hat{H} = \hat{F} + \hat{G}$, where

$$\hat{F} = \sum_{\text{odd j}} \hat{H}_{j,j+1}, \tag{B.15}$$

$$\hat{G} = \sum_{\text{even j}} \hat{H}_{j,j+1}, \tag{B.16}$$

so that $U_{\delta t} = \exp[-i(\hat{F} + \hat{G})\delta t]$. All terms within $\hat{F}$ or $\hat{G}$ commute amongst themselves, allowing a factorisation into a product of local unitaries when either of these operators is exponentiated

$$e^{-i\hat{F}\delta t} = \prod_{\text{odd j}} e^{-i\hat{H}_{j,j+1}\delta t}, \tag{B.17}$$

$$e^{-i\hat{G}\delta t} = \prod_{\text{even j}} e^{-i\hat{H}_{j,j+1}\delta t}, \tag{B.18}$$

In general however, $\hat{F}$ and $\hat{G}$ do not commute. An approximation to the full evolution operator $U_{\delta t}$ follows by employing a Suzuki Trotter expansion [168], which approximates $U_{\delta t}$ by a product of individual exponentiations of $\hat{F}$ and $\hat{G}$. Importantly, Suzuki-Trotter expansions are a unitary approximation to the exact evolution operator, and therefore preserve the norm of the state (under coherent evolution). The simplest such expansion assumes that $\hat{F}$ and $\hat{G}$ commute:

$$\hat{U}_{\delta t} = \exp(-i\hat{F}\delta t)\exp(-i\hat{G}\delta t) + O(\delta t^2). \tag{B.19}$$

A second order expansion

$$\hat{U}_{\delta t} = \exp(-i\frac{1}{2}\hat{F}\delta t)\exp(-i\hat{G}\delta t)\exp(-i\frac{1}{2}\hat{F}\delta t) + O(\delta t)^3, \tag{B.20}$$

is illustrated schematically in Fig. B.4. Errors scale linearly with number of time steps [227]. Throughout this thesis we use this second order expansion, which is

stable regardless of whether the gates are unitary (coherent evolution) or not (ground state calculations, trajectory simulations) [228].

B.3.2 The TEBD algorithm

The preceding sections have outlined the ingredients of the TEBD algorithm, which consists of applying two-site Suzuki-Trotter approximations of unitary generators to MPS representations of quantum states, yielding further states of MPS form at each time step [152, 153]. Expectation values are calculated as discussed in Section B.2, allowing an efficient and accurate characterisation of the dynamics of quantum lattice models.

Appendix C

Exact diagonalisation notes

In this Appendix we present several schemes to reduce the size of the description of a system's density matrix in a direct product basis, with a view towards facilitating the calculation of the non-equilibrium steady state (NESS) of larger quantum systems than is possible with straight-forward diagonalisation. The systems we have in mind are homogeneous (each site of the system is identical) periodic lattice systems, possibly with permutational invariance. Though we have sophisticated schemes based on the quantum trajectory (QT) and Time Evolving Block Decimation (TEBD) methods to time evolve a system towards it's NESS, explicit rapid diagonalisation of small systems is highly desirable. However, the exponential growth of Hilbert and Liouville space with system size/on-site dimension makes the diagonalisation of even quite small systems challenging.

C.0.3 Set-up

Let's say we have a permutationally invariant system of M cavities, and each cavity has a local dimension of D. For instance, if we limit the number of bosons in a purely bosonic cavity to n_{max}, $D = n_{max} + 1$, and we can label our local basis states as $|\ 0\rangle, |\ 1\rangle, \cdots, |\ n_{max}\rangle$. If additionally we have a single two-level system in

each cavity, we have $D = 2(n_{max} + 1)$, and our basis states are $\mid e, 0\rangle, \mid e, 1\rangle, \cdots, \mid e, n_{max}\rangle, \mid g, 0\rangle, \mid g, 1\rangle, \cdots, \mid g, n_{max}\rangle$

The hopping of particles between cavities must be homogeneous, and any driving (coherent of incoherent) must be the same on all cavities.

Labelling the elements of Hilbert and Liouville spaces

To proceed, we replace the explicit labels for the local basis elements by a single number s in the range $[0, D]$. Then the i^{th} basis element of the M-cavity system can be written $\mid s_1^i s_2^i \cdots s_M^i\rangle$, and $i \in [1, D^M]$. The total number of elements in the system's Hamiltonian basis is $N_H = D^M$, whereas Liouville space (where the density matrix resides) has dimension $D^M \times D^M$, with density matrices containing a total of D^{2M} elements.

We represent the i^{th} element of Hilbert space by $(s_1^i s_2^i \cdots s_M^i)$, and of Liouville space by a vector of length $2M$:

$$\mid t_1^i t_2^i \cdots t_M^i\rangle\langle s_1^i s_2^i \cdots s_M^i \mid \equiv (t_1^i t_2^i \cdots t_M^i)(s_1^i s_2^i \cdots s_M^i). \tag{C.1}$$

For our purposes, we wish to order elements by their physical indices, so we regroup the density matrix basis elements as $(t_1^i s_1^i)(t_2^i s_2^i) \cdots (t_M^i s_M^i)$. The super-script i is chosen to run down the columns of the density matrix, as shown below:

$$\rho \equiv \begin{array}{c|ccc} & (s_1^1 s_2^1 \cdots s_M^1) & \cdots & (s_1^{N_H} s_2^{N_H} \cdots s_M^{N_H}) \\ \hline (t_1^1 t_2^1 \cdots t_M^1) & \rho_1 & \cdots & \vdots \\ (t_1^2 t_2^2 \cdots t_M^2) & \rho_2 & \cdots & \vdots \\ \vdots & \vdots & \vdots & \vdots \\ (t_1^{N_H} t_2^{N_H} \cdots t_M^{N_H}) & \rho_{N_H} & \cdots & \rho_{N_\rho} \end{array} \tag{C.2}$$

In the following, we shall be working with a 'flattened' version of the density matrix,

i.e. we reshape the density matrix into a column vector $\tilde{\rho}$ according to:

$$\tilde{\rho} \equiv \begin{bmatrix} \rho_1 \\ \rho_2 \\ \vdots \\ \rho_{N_\rho} \end{bmatrix} \equiv \begin{bmatrix} (t_1^1 s_1^1)(t_2^1 s_2^1)\cdots(t_M^1 s_M^1) \\ (t_1^2 s_1^1)(t_2^2 s_2^1)\cdots(t_M^2 s_M^1) \\ \vdots \\ (t_1^{N_H} s_1^{N_H})(t_2^{N_H} s_2^{N_H})\cdots(t_M^{N_H} s_M^{N_H}) \end{bmatrix}, \tag{C.3}$$

i.e. a vector of length N_ρ. Though we shall be working with density matrices primarily, the discussion concerning the restriction of dynamics to a subspace involving only a certain maximum number of excitations in the system in Section C.0.4 requires only an analysis of Hilbert space basis elements. We thus order kets in the basis:

$$\Psi \equiv \begin{bmatrix} \Psi_1 \\ \Psi_2 \\ \vdots \\ \Psi_{N_\rho} \end{bmatrix} \equiv \begin{bmatrix} (s_1^1 s_2^1 \cdots s_M^1) \\ (s_1^2 s_2^2 \cdots s_M^2) \\ \vdots \\ (s_1^{N_H} s_2^{N_H} \cdots s_M^{N_H}) \end{bmatrix}, \tag{C.4}$$

Condition for NESS

To find the NESS, we must solve for the stationary density matrix, which satisfies

$$\mathcal{L}\rho_{ss} = 0, \tag{C.5}$$

where $\mathcal{L}$ is the master equation Liovillian super-operator. Equation (C.5) is written in terms of the density matrix ρ – now we wish to recast it in terms of the flattened density vector $\tilde{\rho}$, in the form $\tilde{\mathcal{L}}\tilde{\rho}_{ss} = 0$.

In MATLAB, transforming the matrix pre- and post- multiplications by an arbitrary operator O (of dimension N_H) into pre-multiplications by the equivalent super-operator $\tilde{O}_{pre/post}$ (of dimension N_ρ) may be achieved with

```
Osuperpre = kron(speye(NH), O);

Osuperpost = kron(O.', speye(NH));
```

Then we have $OM \to \tilde{O}_{pre}\tilde{M}$, and $MO \to \tilde{O}_{post}\tilde{M}$, for an arbitrary matrix M.

Eq. (6.7) is solved for the NESS $\tilde{\rho}_{ss}$ by finding the zero eigen-vector of the superoperator $\tilde{L}$. Fortunately, $\tilde{L}$ is very sparse, so that sparse matrix routines in MATLAB can be exploited. However, it's dimensions still scale exponentially with system size, so that, for instance, a three cavity systems with two-level atoms in each cavity can only be explicitly diagonalised when we allow a single photon per cavity.

Our task now is to find ways to reduce the size of the description of our system, i.e. find smaller representations than the most general one $\tilde{\rho}$, hopefully without losing physical information about the system, so that we can diagonalise the matrix $\tilde{L}$.

C.0.4 N-excitation sector

The first strategy we look at is restricting the *total* number of excitations in the system to some maximum number N. By constructing Hilbert and Liouville spaces as above, starting from a certain on-site basis, we allow for quite a large maximum number of excitations, for instance Mn_{max}, or $M(n_{max}+1)$ in the case of our coupled cavities. If we are interested in only very weakly excited systems, this can be overkill. To restrict ourselves to states that have N excitations or less, we can filter the elements of Hilbert space, $\Psi \equiv (\Psi_1, \Psi_2, \cdots \Psi_{N_H}$, as in Eq. C.4. If a function $n(s)$ returns the number of excitations in the on-site ket $\mid s\rangle$, then $n_i = \sum_j n(s^i_j)$ is the number of excitations in the basis ket Ψ_i. We can then construct two lists, Ψ_{keep} and $\Psi_{discard}$, containing the basis element numbers i of the kets satisfying $n_i \leq N$ and $n_i > N$.

We want to 'throw out' the elements in $\Psi_{discard}$. In practise, this is done by deleting the rows and columns indexed by $\Psi_{discard}$ of any matrix operator O constructed in the full Hilbert basis. We can do this via a matrix operation $O \to \mathbf{S}^T O \mathbf{S}$, where $\mathbf{S}$ is a shrinking matrix having dimensions $N_H \times N_{keep}$. The i^{th} column of $\mathbf{S}$ has a 1 in row $\Psi_{keep}(i)$. Then any operator O written in the full basis has a representation $\mathbf{S}^T O \mathbf{S}$ in the reduced basis.

All our operators can be shrunk in such a way, and the super-operators are then formed as usual.

C.0.5 Permutationally invariant subsystems

The second scheme we look at applies to systems which possess permutation invariance, i.e. the system is left unchanged under any permutation of its subsystems. For instance, a periodic system of three identical subsystems (we will take as our example systems of optical cavities with either only bosons, or a combination of bosons and a single two level system inside). Also, any fully connected system, each of whose subsystems is connected in an identical way with all other subsystems, is permutationally invariant. This could be an interesting limit to look at for coupled cavity systems, as it is a geometry that is not one-dimensional.

The idea is that the steady state density matrix will have many duplicate entries, corresponding to all the elements in the matrix that correspond to coherences that are permutationally invariant.

Determining which elements are equal

Ordering our density matrix basis as in Eq. (C.3), we apply the following algorithm to generate lists of identical elements. Firstly, a list of all possible permutations $P_i, i \in [1, \cdots, M!]$ of the site indices is generated (there are $M!$ permutations possi-

ble). Starting at the top of the list, we apply each of the permutations in turn to the current basis element i, yielding $(t^1_{P(1)}s^1_{P(1)})(t^1_{P(2)}s^1_{P(2)})\cdots(t^1_{P(M)}s^1_{P(M)})$. Any other elements which match this permuted label are then connected via permutation of site numbers, and so in the steady state the corresponding density matrix elements will be equal. For instance, in a three-cavity system with on-site dimension 3, the elements (12)(22)(31) and (22)(12)(31) are linked under the permutation $1 \leftrightarrow 2$. In this way, we build up a list of identical or 'connected' elements C_i, $i \in 1, \cdots, N_c$, where N_c is the number of distinct connected element lists. Each C_i is itself a list of numbers containing the indices of the density matrix basis which are connected.

What this means is that there are onl N_c independent density matrix elements, and so we should be able to re-write our condition for stationarity, Eq. (6.7), in terms of a reduced density vector $\tilde{\rho}'$, of length N_c, with a corresponding reduced super-operator Liouvillian $\tilde{L}'$ of dimension $N_c \times N_c$.

Shrinking the Liouvillian operator

Unlike the restriction to an N-excitation sector above, we cannot just throw away the rows and columns of the super-operator corresponding to identical elements.

If we think about the matrix product $\mathbf{x} = \mathcal{L}\tilde{\rho}$, where $\tilde{\rho}$ is the 'vectorised' density matrix, then $\mathbf{x}_i = \sum_k \mathcal{L}_{ik}\tilde{\rho}_k$. If additionally we know that the set of elements $(j_1, j_2, ...j_N)$ of $\tilde{\rho}$ are equal, then we can remove the elements $j_2, ..., j_N$ from the flattened density matrix vector by adding the corresponding columns of $\mathcal{L}$ to the j_1^{th} column, and deleting the corresponding rows in $\mathcal{L}$. We therefore shrink the super-operator, while keeping it square and also retaining full information about the steady state. The column-adding procedure can be done via matrix multiplication – we can define an *addition matrix* $\mathbf{A} = \mathbf{A}(C)$ such that $O\mathbf{A}$ returns the matrix O with the columns corresponding to the elements in each C_i added together in the column corresponding to the first element in C_i. For instance, if we know the elements

$2, 15, 27$ are identical, then we want to add the 15th and 27th columns to the 2nd column, then delete the 15th and 27th rows and columns.

If we wish to add column k of a matrix O to column j, such that column $j \rightarrow$ column j + column k, and column $k \rightarrow$ column k, we define the matrix $\mathbf{A}$:

$$\mathbf{A} = \mathbb{I} + \delta_{k,j}, \tag{C.6}$$

i.e. the identity matrix with a 1 also in the $(k, j)^{th}$ element. We can add as many of these off-diagonal ones as we like, corresponding to different columns being added together. Then $O\mathbf{A}$ has the appropriate columns added together.

The shrunken super-operator is then $\tilde{L} = \mathbf{S}_{perm}^{T} \mathcal{L} \mathbf{A} \mathbf{S}_{perm}$, which is then diagonalised to find the independent elements of ρ_{ss}, and those deleted elements are then filled in according to the compiled lists of connected elements C, and finally the steady state density matrix is renormalised to have trace 1.

C.0.6 Constructing the Liouvillian directly in the shrunken basis

Typically, the most time-consuming part of the algorithms defined above involve the compilation of the connected element lists. If many calculations must be done (for instance computing spectra), it would be a waste of time to first construct the full Liouvillian, then identify connected elements, and shrink it for each calculation. We would rather construct the Liouvillian directly in the shrunken basis.

To this end, we can define all the necessary super-operators directly in the shrunken basis. Then each new calculation, with different couplings, will just change the coefficients of these superoperators, and the shrunken Liouvillian is just a sum of pre-existing matrices. Very fast.

Combination of the above two methods

If we are interested in a weakly excited, permutationally invariant system, then we can combine the methods above. Say we want to construct the super-operator corresponding to pre-multiplication by an operator O in the full basis. Then after constructing the matrices $\mathbf{S}, \mathbf{A}, \mathbf{S}_{perm}$ for a particular set (M, N), the operator becomes:

$$O \to \tilde{O} = \mathbf{S}_{perm}^{T} spre(\mathbf{S}^{T} O \mathbf{S}) \mathbf{A} \mathbf{S}_{perm},$$

where the operation $spre(\bullet)$ denotes the operation transforming a pre-multiplying matrix to a super-operator.

Appendix D

Example trajectory code

```
function example_traj_code_main(job_number)
% Numerically exact trajectory code for a Bose Hubbard dimer (two-site
% system)

global r h c1 c2;

if ischar(job_number), job_number = str2num(job_number); end;

save_prefix = 'BH_traj_';
save_name = [save_prefix num2str(job_number) '.mat'];

% Parameters:

M = 2  % Number of sites in ring
n_max = 4;  % Photon truncation parameter

dim_H = (n_max+1)^M;    % Dimension of Hilbert space

gamma = 0.1;    % Photon loss rate
Omega = 1*gamma;  % Driving amplitude
```

```
J = 1;  % Coherent tunnelling between resonators

U = 1.5;    % Kerr nonlinearity

% c1 and c2 are the Lindblad loss operators at each resonator
c1 = sqrt(gamma)*tensor_matrix(a_n(n_max+1), 2, 1);
c2 = sqrt(gamma)*tensor_matrix(a_n(n_max+1), 2, 1);

ad = a_n_dag(n_max+1);  % Photon creation operator
a = a_n(n_max+1);   % Photon destruction operator

% Number operator at first resonator
n1 = tensor_matrix(ad, 2, 1)*tensor_matrix(a, 2, 1);

% Create the unitary system Hamiltonian
h = bhm_hamiltonian_multi_site_pbc(M, n_max, ...
    delta_omega_d, J, U, Omega);
% The effective Hamiltonian H_{\rm eff}
h = h - 1i*c1'*c1/2 - 1i*c2'*c2/2;

% Time vector
ti = 0; % Initial time
tf = 2000; % Final time
tgrid = 10000;    % Num grid points
t = linspace(ti, tf, tgrid);    % Time grid

y00 = kron([1;zeros(n_max,1)],[1;zeros(n_max,1)]);

% Solver parameters
ntraj = 1;    % Number of trajectories
rand('state',sum(100*clock));   % Initialise random number generator
```

```
rho_store = zeros(dim_H, dim_H, ntraj);

photon_number_store = zeros(1,tgrid);

% Main loop over trajectories
for loop_traj = 1:ntraj

    % Display simulation progress
    disp(['Trajectory ' num2str(loop_traj) ' of ' num2str(ntraj)]);
    ts = ti;
    y = y00;    % Initial conditions
    y0 = y00;

    r = rand(1);    % Draw a random number

    for loop=1:length(t)-1

        time_interval = [t(loop) t(loop+1)];

        % Call the ode solver up to the time of the next jump
        [TS, YS] = ode45(@odefun, time_interval, y0);
        y = YS(end,:).';   % Last solution
        y0 = y;
        ynorm = y/sqrt(y'*y);

        % Check if a jump has occured
        norm = sqrt(y'*y)
        if norm < r

            % Calculate probabilities of different jumps:
            y_with_jump_1 = c1*y;
```

```
            y_with_jump_2 = c2*y;
            p1 = y_with_jump_1'*y_with_jump_1;
            p2 = y_with_jump_2'*y_with_jump_2;

            norm = p1+p2;
            p1 = p1/norm;
            p2 = p2/norm;

            % Choose a jump:
            if rand < p1
                c = c1;
            else
                c = c2;
            end

            y0 = c*y;   % Apply quantum jump
            y0 = y0/sqrt(y0'*y0);   % Normalise

            r = rand(1);    % Choose a new random number

        end

        num_1 = ynorm'*n1*ynorm
        photon_number_store(loop) = num_1;

    end

end

rho_ss = get_steady_state_rho(M, n_max, ...
    delta_omega_d, J, U, Omega, gamma);
rho_store(:,:,loop) = rho_ss;
```

```
save(save_name, 'n_max', 'M', 'U_list', 'gamma', ...
    'Omega', 'J', 'rho_store', 'job_number')
disp(['Saved data to file ' save_name '. Quitting...'])

end

%%%%%%%%%%%%%%%%% Auxillary functions %%%%%%%%%%%%%%%%%%%%%%
function H = bhm_hamiltonian_multi_site_pbc(M, n_max,...
    delta_omega_d, J, U, Omega)
% Function to return the Bose Hubbard Hamiltonian for periodic
% boundary conditions
% M - number of lattice sites
% n_max (maximum photon number at which we truncate Fock space
% delta_omega_d - difference between resonator frequency and
% driving frequency:
% J - photon hopping, U - Kerr repulsion

a = a_n(n_max + 1); % Destruction operator for one site
ad = a_n_dag(n_max + 1); % Creation operator

num = ad*a;    % Number operator

ket_g = [0;1];
ket_e = [1;0];

H = sparse((n_max+1)^M,(n_max+1)^M);   % Initialise Hamiltonian

for m = 1:M-1     % Loop over the lattice sites

    a_m = tensor_matrix(a, M, m);
    a_dag_m = tensor_matrix(ad, M, m);
```

```
    a_m_plus_1 = tensor_matrix(a, M, m+1);
    a_dag_m_plus_1 = tensor_matrix(ad, M, m+1);
    num_m = tensor_matrix(num, M, m);

    hopping_term = a_dag_m*a_m_plus_1 + a_dag_m_plus_1*a_m;

    % Assemble the Hamiltonian for each lattice site contribution
    H = H + delta_omega_d*num_m - J*hopping_term + ...
          + U*a_dag_m*a_dag_m*a_m*a_m + Omega*(a_m + a_dag_m);

end

% Need to also include the last on-site term:
a_M = tensor_matrix(a, M, M);
a_dag_M = tensor_matrix(ad, M, M);
num_M = tensor_matrix(num, M, M);

% Add the last site's on-site interaction contribution
H = H + delta_omega_d*num_M + U*a_dag_M*a_dag_M*a_M*a_M + ...
      + Omega*(a_M + a_dag_M);

% Now need the terms which make periodic boundary conditions
% (i.e. hoppings between sites 1 and M)
b_1 = tensor_matrix(a, M, 1);
b_dag_1 = tensor_matrix(ad, M, 1);
hopping_term_pbc = a_dag_M*b_1 + b_dag_1*a_M;

H = H - J*hopping_term_pbc;

end
%%%%%%%%%%%%%%%5
function operator = a_n(n_max)
```

```
% Destruction operator in Fock basis
operator = spdiags(sqrt([0:n_max].'), 1, n_max, n_max);

end
%%%%%%%%%%%%%%%%
function operator = a_n_dag(n_max)
% Creation operator in Fock basis
operator = spdiags(sqrt([1:n_max-1].'), -1, n_max, n_max);

end
%%%%%%%%%%%%%%
function matrix_big = tensor_matrix(matrix, M, index)
% Function to return the tensor product: I * I * ...
% * matrix * I * ... * I, where matrix is in the
% index'th position, and '*' denotes a tensor multiplication,
% and there are M matrices all together in the product

% The identity matrix to be tensored successively
id = speye(size(matrix));
% Initialise the output matrix (NB kron(1, matrix) = matrix)
matrix_big = 1;

for k = 1:M

    if (k == index)
        next_matrix = matrix;
    else
        next_matrix = id;
    end

    matrix_big = kron(matrix_big, next_matrix);
```

```
end


end
%%%%%%%%%%%%%%
function dy = odefun(t, y)
% ODE kernel which solves the effective Hamiltonian part of the equation
global h
dy = -i*h*y;


end
```

Bibliography

[1] P. A. Lee, N. Nagaosa, and X. G. Wen. Doping a mott insulator: Physics of high-temperature superconductivity. *Reviews of Modern Physics*, 78(1):17, 2006.

[2] H. L. Stormer, D. C. Tsui, and A. C. Gossard. The fractional quantum hall effect. *Reviews of Modern Physics*, 71(2):S298, 1999.

[3] E. Jané, G. Vidal, W. Dür, P. Zoller, and J.I. Cirac. Simulation of quantum dynamics with quantum optical systems. *Quantum Information & Computation*, 3(1):15–37, 2003.

[4] H.S.J. Van der Zant, F.C. Fritschy, W.J. Elion, L.J. Geerligs, and J.E. Mooij. Field-induced superconductor-to-insulator transitions in josephson-junction arrays. *Physical review letters*, 69(20):2971, 1992.

[5] A. van Oudenaarden and J.E. Mooij. One-dimensional mott insulator formed by quantum vortices in josephson junction arrays. *Physical review letters*, 76(26):4947, 1996.

[6] R. Fazio and H. S. J. van der Zant. Quantum phase transitions and vortex dynamics in superconducting networks. *Phys. Rep.*, 355:235–334, 2001.

[7] D. Jaksch, C. Bruder, J.I. Cirac, C.W. Gardiner, and P. Zoller. Cold bosonic atoms in optical lattices. *Phys. Rev. Lett.*, 81(15):3108–3111, 1998.

[8] M.P.A. Fisher, P.B. Weichman, G. Grinstein, and D.S. Fisher. Boson localization and the superfluid-insulator transition. *Phys. Rev. B*, 40(1):546–570, 1989.

[9] M. Greiner, O. Mandel, T. Esslinger, T.W. Hänsch, and I. Bloch. Quantum phase transition from a superfluid to a Mott insulator in a gas of ultracold atoms. *Nature*, 415(6867):39–44, 2002.

[10] B. Paredes, A. Widera, V. Murg, O. Mandel, S. Fölling, I. Cirac, G.V. Shlyapnikov, T.W. Hänsch, and I. Bloch. Tonks–Girardeau gas of ultracold atoms in an optical lattice. *Nature*, 429(6989):277–281, 2004.

[11] M. Aichhorn, M. Hohenadler, C. Tahan, and P.B. Littlewood. Quantum Fluctuations, Temperature, and Detuning Effects in Solid-Light Systems. *Phys. Rev. Lett.*, 100(21):216401, 2008.

[12] D.G. Angelakis, M.F. Santos, and S. Bose. Photon-blockade-induced Mott transitions and XY spin models in coupled cavity arrays. *Phys. Rev. A*, 76(3):31805, 2007.

[13] M.J. Hartmann, F.G.S.L. Brandão, and M.B. Plenio. Strongly interacting polaritons in coupled arrays of cavities. *Nature Physics*, 2:849–855, 2006.

[14] A.D. Greentree, C. Tahan, J.H. Cole, and L.C.L. Hollenberg. Quantum phase transitions of light. *Nature Physics*, 2(12):856–861, 2006.

[15] F. Illuminati. Quantum optics: Light does matter. *Nature Physics*, 2(12):803–804, 2006.

[16] I. Carusotto and C. Ciuti. Quantum fluids of light. *arXiv preprint arXiv:1205.6500*, 2012.

[17] J.F. Sherson, C. Weitenberg, M. Endres, M. Cheneau, I. Bloch, and S. Kuhr. Single-atom-resolved fluorescence imaging of an atomic mott insulator. *Nature*, 467(7311):68–72, 2010.

[18] W.S. Bakr, A. Peng, M.E. Tai, R. Ma, J. Simon, J.I. Gillen, S. Foelling, L. Pollet, and M. Greiner. Probing the superfluid–to–mott insulator transition at the single-atom level. *Science*, 329(5991):547–550, 2010.

[19] R. Zwanzig. *Nonequilibrium statistical mechanics*. Oxford University Press, 2001.

[20] T. Prosen. Third quantization: a general method to solve master equations for quadratic open Fermi systems. *New Journal of Physics*, 10:043026, 2008.

[21] T. Prosen and B. Žunkovič. Exact solution of Markovian master equations for quadratic Fermi systems: thermal baths, open XY spin chains and non-equilibrium phase transition. *New Journal of Physics*, 12:025016, 2010.

[22] M. Žnidarič. Exact solution for a diffusive nonequilibrium steady state of an open quantum chain. *Journal of Statistical Mechanics: Theory and Experiment*, 2010(05):L05002, 2010.

[23] M. Žnidarič. Solvable quantum nonequilibrium model exhibiting a phase transition and a matrix product representation. *Physical Review E*, 83(1):011108, 2011.

[24] T. Prosen. Open xxz spin chain: Nonequilibrium steady state and a strict bound on ballistic transport. *Physical Review Letters*, 106(21):217206, 2011.

[25] T. Prosen. Exact nonequilibrium steady state of a strongly driven open xxz chain. *Physical Review Letters*, 107(13):137201, 2011.

[26] D. Karevski, V. Popkov, and G.M. Schütz. Exact matrix product solution for the boundary-driven lindblad xxz chain. *Physical Review Letters*, 110(4):047201, 2013.

[27] O. Golinelli and K. Mallick. The asymmetric simple exclusion process: an integrable model for non-equilibrium statistical mechanics. *Journal of Physics A: Mathematical and General*, 39(41):12679, 2006.

[28] B. Derrida. An exactly soluble non-equilibrium system: the asymmetric simple exclusion process. *Physics Reports*, 301(1):65–83, 1998.

[29] K.M. Birnbaum, A. Boca, R. Miller, A.D. Boozer, T.E. Northup, and H.J. Kimble. Photon blockade in an optical cavity with one trapped atom. *Nature*, 436(7047):87–90, 2005.

[30] J.M. Raimond and S. Haroche. *Exploring the quantum*. Oxford University Press, Oxford, 2006.

[31] D.J. Griffiths. *Introduction to electrodynamics*, volume 3. prentice Hall Upper Saddle River, NJ, 1999.

[32] L. Mandel and E. Wolf. *Optical coherence and quantum optics*. Cambridge Univ Pr, 1995.

[33] D.F. Walls, G. Milburn, and J. Gerard. *Quantum optics*. Springer, 2008.

[34] S. Barnett and P.M. Radmore. *Methods in theoretical quantum optics*, volume 15. Oxford University Press, 2002.

[35] J.C. Garrison and R.Y. Chiao. *Quantum optics*. Oxford Univ. Press, 2008.

[36] B.W. Shore and P.L. Knight. Topical Review. The Jaynes-Cummings Model. *J. Mod. Opt*, 40(7):1195–1238, 1993.

[37] E. Jaynes and F. Cummings. Comparison of Quantum and Semiclassical Radiation Theories with Application to the Beam Maser. *Proceedings of the IEEE*, 51(1):89, 1963.

[38] T. A. Fulton and G. J. Dolan. Observation of single-electron charging effects in small tunnel junctions. *Phys. Rev. Lett.*, 59:109–112, Jul 1987.

[39] M. A. Kastner. The single-electron transistor. *Rev. Mod. Phys.*, 64:849–858, Jul 1992.

[40] H. J. Carmichael. Photon antibunching and squeezing for a single atom in a resonant cavity. *Phys. Rev. Lett.*, 55:2790–2793, Dec 1985.

[41] A. Imamoğlu, H. Schmidt, G. Woods, and M. Deutsch. Strongly interacting photons in a nonlinear cavity. *Phys. Rev. Lett.*, 79(8):1467–1470, 1997.

[42] A. Faraon, I. Fushman, D. Englund, N. Stoltz, and ans Vučkovi&cacute J. Pierre, P. Coherent generation of non-classical light on a chip via photon-induced tunnelling and blockade. *Nature Physics*, 4(11):859–863, 2008.

[43] A. Reinhard, T. Volz, M. Winger, A. Badolato, K.J. Hennessy, E.L. Hu, and A. Imamoğlu. Strongly correlated photons on a chip. *Nature Photonics*, 6(2):93–96, 2011.

[44] F. Bello and D.M. Whittaker. Photon antibunching and nonlinear effects for a quantum dot coupled to a semiconductor cavity. *Phys. Rev. B*, 82(11):115328, 2010.

[45] J.M. Fink, M. Göppl, M. Baur, R. Bianchetti, P.J. Leek, A. Blais, and A. Wallraff. Climbing the jaynes–cummings ladder and observing its nonlinearity in a cavity qed system. *Nature*, 454(7202):315–318, 2008.

[46] C. Lang, D. Bozyigit, C. Eichler, L. Steffen, J.M. Fink, A.A. Abdumalikov Jr, M. Baur, S. Filipp, M.P. da Silva, A. Blais, et al. Observation of resonant photon blockade at microwave frequencies using correlation function measurements. *Physical Review Letters*, 106(24):243601, 2011.

[47] S. E. Harris, J. E. Field, and A. Imamoğlu. Nonlinear optical processes using electromagnetically induced transparency. *Phys. Rev. Lett.*, 64:1107–1110, Mar 1990.

[48] E. Arimondo. V coherent population trapping in laser spectroscopy. *Progress in optics*, 35:257–354, 1996.

[49] M. Fleischhauer, A. Imamoğlu, and J.P. Marangos. Electromagnetically induced transparency: Optics in coherent media. *Reviews of Modern Physics*,

77(2):633, 2005.

[50] A. Imamoğlu, H. Schmidt, G. Woods, and M. Deutsch. Strongly interacting photons in a nonlinear cavity. *Physical Review Letters*, 79(8):1467, 1997.

[51] M.J. Hartmann and M.B. Plenio. Strong photon nonlinearities and photonic Mott insulators. *Phys. Rev. Lett.*, 99(10):103601, 2007.

[52] M.J. Werner and A. Imamoğlu. Photon-photon interactions in cavity electromagnetically induced transparency. *Phys. Rev. A*, 61(1):11801, 1999.

[53] T. Lauprêtre, C. Proux, R. Ghosh, S. Schwartz, F. Goldfarb, and F. Bretenaker. Photon lifetime in a cavity containing a slow-light medium. *Optics letters*, 36(9):1551–1553, 2011.

[54] C. Chin, R. Grimm, P. Julienne, and E. Tiesinga. Feshbach resonances in ultracold gases. *Rev. Mod. Phys.*, 82:1225–1286, Apr 2010.

[55] A. Yariv, Y. Xu, R.K. Lee, and A. Scherer. Coupled-resonator optical waveguide: a proposal and analysis. *Opt. Lett.*, 24(11):711–713, 1999.

[56] S. Sachdev. *Quantum phase transitions*. Wiley Online Library, 2007.

[57] W. Krauth, M. Caffarel, and J.P. Bouchaud. Gutzwiller wave function for a model of strongly interacting bosons. *Physical Review B*, 45(6):3137, 1992.

[58] D. Rossini and R. Fazio. Mott-insulating and glassy phases of polaritons in 1D arrays of coupled cavities. *Phys. Rev. Lett.*, 99(18):186401, 2007.

[59] M. Pino, J. Prior, and S.R. Clark. Capturing the re-entrant behavior of one-dimensional bose–hubbard model. *physica status solidi (b)*, 250(1):51–58, 2013.

[60] E.K. Irish, C.D. Ogden, and M.S. Kim. Polaritonic characteristics of insulator and superfluid states in a coupled-cavity array. *Phys. Rev. A*, 77(3):33801, 2008.

[61] J. Koch and K. Le Hur. Superfluid–Mott-insulator transition of light in the Jaynes-Cummings lattice. *Phys. Rev. A*, 80(2):23811, 2009.

[62] A. Kay and D.G. Angelakis. Reproducing spin lattice models in strongly coupled atom-cavity systems. *EPL (Europhysics Letters)*, 84:20001, 2008.

[63] M.J. Hartmann, F.G.S.L. Brandão, and M.B. Plenio. Effective spin systems in coupled microcavities. *Phys. Rev. Lett.*, 99(16):160501, 2007.

[64] J. Cho, D.G. Angelakis, and S. Bose. Simulation of high-spin Heisenberg models in coupled cavities. *Phys. Rev. A*, 78(6):62338, 2008.

[65] M.J. Hartmann, F.G.S.L. Brandao, and M.B. Plenio. Quantum many-body phenomena in coupled cavity arrays. *Laser & Photon Rev.*, 2(6):527–556, 2008.

[66] O. Viehmann, J. von Delft, and F. Marquardt. Observing the nonequilibrium dynamics of the quantum transverse-field ising chain in circuit qed. *arXiv preprint arXiv:1208.1354*, 2012.

[67] P.B. Li, Y. Gu, Q.H. Gong, and G.C. Guo. Generation of ising interaction and cluster states in a one-dimensional coupled resonator waveguide. *The European Physical Journal D*, 55(1):205–209, 2009.

[68] J. Cho, D.G. Angelakis, and S. Bose. Fractional quantum hall state in coupled cavities. *Phys. Rev. Lett.*, 101(24):246809, 2008.

[69] R.B. Laughlin. Anomalous quantum hall effect: an incompressible quantum fluid with fractionally charged excitations. *Physical Review Letters*, 50(18):1395–1398, 1983.

[70] A. Nunnenkamp, J. Koch, and S.M. Girvin. Synthetic gauge fields and homodyne transmission in jaynes–cummings lattices. *New Journal of Physics*, 13:095008, 2011.

[71] A. Mering, M. Fleischhauer, P.A. Ivanov, and K. Singer. Analytic approximations to the phase diagram of the jaynes-cummings-hubbard model. *Phys. Rev. A*, 80(5):053821, 2009.

[72] M.I. Makin, J.H. Cole, C. Tahan, L.C.L. Hollenberg, and A.D. Greentree. Quantum phase transitions in photonic cavities with two-level systems. *Phys. Rev. A*, 77(5):53819, 2008.

[73] S. Schmidt and G. Blatter. Strong coupling theory for the jaynes-cummings-hubbard model. *Physical review letters*, 103(8):86403, 2009.

[74] D. Rossini, R. Fazio, and G. Santoro. Photon and polariton fluctuations in arrays of qed-cavities. *EPL (Europhysics Letters)*, 83:47011, 2008.

[75] J. Zhao, A.W. Sandvik, and K. Ueda. Insulator to superfluid transition in coupled photonic cavities in two dimensions. *arXiv*, 806.

[76] M. Knap, E. Arrigoni, and W. Von Der Linden. Spectral properties of coupled cavity arrays in one dimension. *Phys. Rev. B*, 81(10):104303, 2010.

[77] P. Pippan, H.G. Evertz, and M. Hohenadler. Excitation spectra of strongly correlated lattice bosons and polaritons. *Phys. Rev. A*, 80(3):33612, 2009.

[78] J. Quach, M.I. Makin, C.H. Su, A.D. Greentree, and L.C.L. Hollenberg. Band structure, phase transitions, and semiconductor analogs in one-dimensional solid light systems. *Phys. Rev. A*, 80(6):63838, 2009.

[79] S. Schmidt and G. Blatter. Excitations of strongly correlated lattice polaritons. *Physical review letters*, 104(21):216402, 2010.

[80] N. Na, S. Utsunomiya, L. Tian, and Y. Yamamoto. Strongly correlated polaritons in a two-dimensional array of photonic crystal microcavities. *Phys. Rev. A*, 77(3):31803, 2008.

[81] M. Schiró, M. Bordyuh, B. Öztop, and H.E. Türeci. Phase transition of light in cavity qed lattices. *Physical Review Letters*, 109(5):053601, 2012.

[82] H. Gimperlein, S. Wessel, J. Schmiedmayer, and L. Santos. Ultracold atoms in optical lattices with random on-site interactions. *Physical review letters*, 95(17):170401, 2005.

[83] C.W. Wu, M. Gao, Z.J. Deng, H.Y. Dai, P.X. Chen, and C.Z. Li. Quantum phase transition of light in a one-dimensional photon-hopping-controllable resonator array. *Physical Review A*, 84(4):043827, 2011.

[84] A. Tomadin. Non-equilibrium phase transition in driven-dissipative nonlinear cavity arrays. *Quantum*, pages 1–4, 2009.

[85] A. Tomadin, V. Giovannetti, R. Fazio, D. Gerace, I. Carusotto, H.E. Türeci, and A. Imamoğlu. Signatures of the superfluid-insulator phase transition in laser-driven dissipative nonlinear cavity arrays. *Phys. Rev. A*, 81(061801):061801, 2010.

[86] K. Liu, L. Tan, C.H. Lv, and W.M. Liu. Quantum phase transition in an array of coupled dissipative cavities. *Physical Review A*, 83(6):063840, 2011.

[87] T. Grujic, S.R. Clark, D. Jaksch, and D.G. Angelakis. Repulsively induced photon superbunching in driven resonator arrays. *Physical Review A*, 87(5):053846, 2013.

[88] S. Ferretti, L.C. Andreani, H.E. Türeci, and D. Gerace. Photon correlations in a two-site nonlinear cavity system under coherent drive and dissipation. *Phys. Rev. A*, 82(1):013841, 2010.

[89] M. Knap, E. Arrigoni, W. von der Linden, and J.H. Cole. Emission characteristics of laser-driven dissipative coupled-cavity systems. *Phys. Rev. A*, 83(2):23821, 2011.

[90] M.I. Makin, J.H. Cole, C.D. Hill, A.D. Greentree, and L.C.L. Hollenberg. Time evolution of the one-dimensional Jaynes-Cummings-Hubbard Hamiltonian. *Phys. Rev. A*, 80(4):43842, 2009.

[91] S. Bose, D. Angelakis, and D. Burgarth. Transfer of a polaritonic qubit through a coupled cavity array. *Journal of Modern Optics*, 54(13):2307, 2007.

[92] R. Chakrabarti and G. Sreekumari. Quantum communication through Jaynes-Cummings-Hubbard arrays. *Arxiv preprint arXiv:1103.0640*, 2011.

[93] S. Felicetti, G. Romero, D. Rossini, R. Fazio, and E. Solano. Photon transfer in ultrastrongly coupled three-cavity arrays. *arXiv preprint arXiv:1304.6221*, 2013.

[94] D. Gerace, H.E. Türeci, A. Imamoğlu, V. Giovannetti, and R. Fazio. The quantum-optical Josephson interferometer. *Nature Physics*, 5(4):281–284, 2009.

[95] Y. Liu, X.W. Xu, A. Miranowicz, and F. Nori. From blockade to transparency: controllable photon transmission through a circuit qed system. *Arxiv preprint arXiv:1203.6419*, 2012.

[96] P. Longo, P. Schmitteckert, and K. Busch. Few-photon transport in low-dimensional systems. *Physical Review A*, 83(6):063828, 2011.

[97] M.T.C. Wong and C.K. Law. Two-polariton bound states in the jaynes-cummings-hubbard model. *Physical Review A*, 83(5):055802, 2011.

[98] S. Schmidt, D. Gerace, A.A. Houck, G. Blatter, and H.E. Türeci. Nonequilibrium delocalization-localization transition of photons in circuit quantum electrodynamics. *Physical Review B*, 82(10):100507, 2010.

[99] N. Schetakis, T. Grujic, S.R. Clark, D. Jaksch, and D.G. Angelakis. Frozen photons in jaynes cummings arrays. *J. Phys. B Jaynes Cummings physics special issue, forthcoming*, 2013.

[100] T.C.H. Liew and V. Savona. Single photons from coupled quantum modes. *Phys. Rev. Lett.*, 104(18):183601, 2010.

[101] M. Bamba, A. Imamoğlu, I. Carusotto, and C. Ciuti. Origin of strong photon antibunching in weakly nonlinear photonic molecules. *Phys. Rev. A*, 83(2):021802, 2011.

[102] D.G. Angelakis, S. Bose, and S. Mancini. Steady-state entanglement between hybrid light-matter qubits. *EPL (Europhysics Letters)*, 85:20007, 2009.

[103] D.G. Angelakis, L. Dai, and L.C. Kwek. Coherent control of long-distance steady-state entanglement in lossy resonator arrays. *EPL (Europhysics Letters)*, 91:10003, 2010.

[104] I. Carusotto, D. Gerace, H.E. Tureci, S. De Liberato, C. Ciuti, and A. Imamoğlu. Fermionized photons in an array of driven dissipative nonlinear cavities. *Phys. Rev. Lett.*, 103(3):33601, 2009.

[105] M.J. Hartmann. Polariton crystallization in driven arrays of lossy nonlinear resonators. *Phys. Rev. Lett.*, 104(11):113601, 2010.

[106] J. Jin, D. Rossini, R. Fazio, M. Leib, and M.J. Hartmann. Photon solid phases in driven arrays of non-linearly coupled cavities. *arXiv preprint arXiv:1302.2242*, 2013.

[107] J.D. Joannopoulos, S.G. Johnson, and J.N. Winn. *Photonic crystals: molding the flow of light*. Princeton Univ Pr, 2008.

[108] G.P. Agrawal. *Nonlinear fiber optics*. Springer, 2000.

[109] F.H. Julien and A. Alexandrou. QUANTUM DOTS: Enhanced: Controlling Artificial Atoms. *Science*, 282(5393):1429, 1998.

[110] A. Badolato, K. Hennessy, M. Atatüre, J. Dreiser, E. Hu, P.M. Petroff, and A. Imamoğlu. Deterministic coupling of single quantum dots to single nanocavity modes. *Science*, 308(5725):1158, 2005.

[111] K. Hennessy, A. Badolato, M. Winger, D. Gerace, M. Atatüre, S. Gulde, S. Fält, E.L. Hu, A. Imamoğlu, et al. Quantum nature of a strongly coupled single quantum dot–cavity system. *Nature*, 445(7130):896–899, 2007.

[112] K. Busch, G. Von Freymann, S. Linden, S.F. Mingaleev, L. Tkeshelashvili, and M. Wegener. Periodic nanostructures for photonics. *Physics reports*, 444(3-6):101–202, 2007.

[113] M. Notomi, E. Kuramochi, and T. Tanabe. Large-scale arrays of ultrahigh-q coupled nanocavities. *Nature Photonics*, 2(12):741–747, 2008.

[114] D.G. Angelakis, P.L. Knight, and E. Paspalakis. Photonic crystals and inhibition of spontaneous emission: an introduction. *Contemporary Physics*, 45(4):303–318, 2004.

[115] P. Russell. Photonic crystal fibers. *science*, 299(5605):358–362, 2003.

[116] J.C. Knight. Photonic crystal fibres. *Nature*, 424(6950):847–851, 2003.

[117] F. Morichetti, C. Ferrari, A. Canciamilla, and A. Melloni. The first decade of coupled resonator optical waveguides: bringing slow light to applications. *Laser & Photonics Reviews*, 6(1):74–96, 2012.

[118] Y. Xu, R.K. Lee, and A. Yariv. Propagation and second-harmonic generation of electromagnetic waves in a coupled-resonator optical waveguide. *JOSA B*, 17(3):387–400, 2000.

[119] Y. Chen and S. Blair. Nonlinearity enhancement in finite coupled-resonator slow-light waveguides. *Optics Express*, 12(15):3353–3366, 2004.

[120] J.B. Khurgin and R.S. Tucker. *Slow light: science and applications*. CRC press, 2008.

[121] M. Trupke, E.A. Hinds, S. Eriksson, E.A. Curtis, Z. Moktadir, E. Kukharenka, and M. Kraft. Microfabricated high-finesse optical cavity with open access and small volume. *Applied Physics Letters*, 87(21):211106–211106, 2005.

[122] M. Trupke, J. Goldwin, B. Darquié, G. Dutier, S. Eriksson, J. Ashmore, and E.A. Hinds. Atom detection and photon production in a scalable, open, optical microcavity. *Phys. Rev. Lett.*, 99(6):63601, 2007.

[123] J. Goldwin, M. Trupke, J. Kenner, A. Ratnapala, and E.A. Hinds. Fast cavity-enhanced atom detection with low noise and high fidelity. *Nature communications*, 2:418, 2011.

[124] G. Lepert, M. Trupke, E.A. Hinds, H. Rogers, J.C. Gates, and P.G.R. Smith. Demonstration of uv-written waveguides, bragg gratings and cavities at 780 nm, and an original experimental measurement of group delay. *Optics Express*, 19(25):24933–24943, 2011.

[125] G. Lepert, E.A. Hinds, H.L. Rogers, J.C. Gates, and P.G.R Smith. Array of fabry-p\'erot waveguide resonators with tunable coupling. *arXiv preprint arXiv:1304.7013*, 2013.

[126] J.B. Trebbia, H. Ruf, P. Tamarat, and B. Lounis. Efficient generation of near infra-red single photons from the zero-phonon line of a single molecule. *arXiv preprint arXiv:1011.6153*, 2010.

[127] J. Hwang and E.A. Hinds. Dye molecules as single-photon sources and large optical nonlinearities on a chip. *New Journal of Physics*, 13(8):085009, 2011.

[128] A. Blais, R.S. Huang, A. Wallraff, S.M. Girvin, and R.J. Schoelkopf. Cavity quantum electrodynamics for superconducting electrical circuits: An architecture for quantum computation. *Physical Review A*, 69(6):062320, 2004.

[129] O. Astafiev, A.M. Zagoskin, A.A. Abdumalikov, Y.A. Pashkin, T. Yamamoto, K. Inomata, Y. Nakamura, and J.S. Tsai. Resonance fluorescence of a single artificial atom. *Science*, 327(5967):840, 2010.

[130] L. Frunzio, A. Wallraff, D. Schuster, J. Majer, and R. Schoelkopf. Fabrication and characterization of superconducting circuit qed devices for quantum computation. *Applied Superconductivity, IEEE Transactions on*, 15(2):860–863, 2005.

[131] A.A. Houck, H.E. Türeci, and J. Koch. On-chip quantum simulation with superconducting circuits. *Nature Physics*, 8(4):292–299, 2012.

[132] M.H. Devoret, S. Girvin, and R. Schoelkopf. Circuit-qed: How strong can the coupling between a josephson junction atom and a transmission line resonator be? *Annalen der Physik*, 16(10-11):767–779, 2007.

[133] A. Wallraff, D.I. Schuster, A. Blais, L. Frunzio, R.S. Huang, J. Majer, S. Kumar, S.M. Girvin, and R.J. Schoelkopf. Strong coupling of a single photon to a superconducting qubit using circuit quantum electrodynamics. *Nature*, 431(7005):162–167, 2004.

[134] J.Q. You and F. Nori. Atomic physics and quantum optics using superconducting circuits. *Nature*, 474(7353):589–597, 2011.

[135] K. Srinivasan and O. Painter. Linear and nonlinear optical spectroscopy of a strongly coupled microdisk–quantum dot system. *Nature*, 450(7171):862–865, 2007.

[136] P.E. Barclay, K. Srinivasan, O. Painter, B. Lev, and H. Mabuchi. Integration of fiber-coupled high-Q SiNx microdisks with atom chips. *Phys. Rev. Lett.*, 89(13), 2006.

[137] T. Grujic, S. R. Clark, D. Jaksch, and D. G. Angelakis. Non-equilibrium many-body effects in driven nonlinear resonator arrays. *New Journal of Physics*, 14(10):103025, 2012.

[138] C.M. Savage and H.J. Carmichael. Single atom optical bistability. *IEEE Journal of Quantum Electronics*, 24(8):1495–1498, 1988.

[139] C.E. Bardyn and A. Imamoğlu. Majorana-like modes of light in a one-dimensional array of nonlinear cavities. *Physical review letters*, 109(25):253606, 2012.

[140] J.J. Mendoza-Arenas, T. Grujic, D. Jaksch, and S.R. Clark. Dephasing enhanced transport in non-equilibrium strongly-correlated quantum systems. *arXiv preprint arXiv:1302.5629*, 2013.

[141] H. Carmichael. *An Open Systems Approach to Quantum Optics*. Springer Verlag, 1991.

[142] H.P. Breuer and F. Petruccione. *The theory of open quantum systems*. Oxford University Press, USA, 2002.

[143] F. Verstraete, V. Murg, and J.I. Cirac. Matrix product states, projected entangled pair states, and variational renormalization group methods for quantum spin systems. *Advances in Physics*, 57(2):143–224, 2008.

[144] J.I. Cirac and F. Verstraete. Renormalization and tensor product states in spin chains and lattices. *Journal of Physics A: Mathematical and Theoretical*, 42(50):504004, 2009.

[145] D. Perez-Garcia, F. Verstraete, M.M. Wolf, and J.I. Cirac. Matrix product state representations. *Quantum Information & Computation*, 7(5):401–430, 2007.

[146] U. Schollwöck. The density-matrix renormalization group in the age of matrix product states. *Annals of Physics*, 326(1):96–192, 2011.

[147] T. Giamarchi. *Quantum physics in one dimension*. Oxford University Press, Oxford, 2004.

[148] S. Ghosh, J.E. Sharping, D.G. Ouzounov, and A.L. Gaeta. Resonant optical interactions with molecules confined in photonic band-gap fibers. *Physical review letters*, 94(9):093902, 2005.

[149] K.P. Nayak, P.N. Melentiev, M. Morinaga, F.L Kien, V.I. Balykin, and K. Hakuta. Optical nanofiber as an efficient tool for manipulating and probing atomic fluorescence. *Optics Express*, 15(9):5431–5438, 2007.

[150] M. Bajcsy, S. Hofferberth, V. Balic, T. Peyronel, M. Hafezi, A.S. Zibrov, V. Vuletic, and M.D. Lukin. Efficient all-optical switching using slow light within a hollow fiber. *Physical review letters*, 102(20):203902, 2009.

[151] S. Vorrath, S.A. Möller, P. Windpassinger, K. Bongs, and K. Sengstock. Efficient guiding of cold atoms through a photonic band gap fiber. *New Journal of Physics*, 12(12):123015, 2010.

[152] G. Vidal. Efficient classical simulation of slightly entangled quantum computations. *Phys. Rev. Lett.*, 91(14):147902, 2003.

[153] G. Vidal. Efficient simulation of one-dimensional quantum many-body systems. *Phys. Rev. Lett.*, 93(4):40502, 2004.

[154] G. Vidal. Classical simulation of infinite-size quantum lattice systems in one spatial dimension. *Physical review letters*, 98(7):70201, 2007.

[155] A.J. Daley, C. Kollath, U. Schollwöck, and G. Vidal. Time-dependent density-matrix renormalization-group using adaptive effective hilbert spaces. *Journal of Statistical Mechanics: Theory and Experiment*, 2004(04):P04005, 2004.

[156] Tensor Network Theory (TNT) library. `http://ccpforge.cse.rl.ac.uk/gf/project/tntlibrary/`.

[157] S. Clarke. *Strongly correlated one-dimensional systems of cold atoms in optical lattices*. PhD thesis, 2007.

[158] C. Moler and C. Van Loan. Nineteen dubious ways to compute the exponential of a matrix, twenty-five years later. *SIAM review*, 45(1):3–49, 2003.

[159] C.W. Gardiner, A.S Parkins, and P. Zoller. Wave-function quantum stochastic differential equations and quantum-jump simulation methods. *Phys. Rev. A*, 46(7):4363–4381, 1992.

[160] P. Zoller and C.W. Gardiner. Quantum noise in quantum optics: the stochastic schrödinger equation. In *Fluctuations Quantiques/Quantum Fluctuations*, volume 1, page 79, 1997.

[161] M.B. Plenio and P.L. Knight. The quantum-jump approach to dissipative dynamics in quantum optics. *Rev. of Mod. Phys.*, 70(1):101–144, 1998.

[162] J. Dalibard, Y. Castin, and K. Mølmer. Wave-function approach to dissipative processes in quantum optics. *Phys. Rev. Lett.*, 68(5):580–583, 1992.

[163] R. Dum, A.S. Parkins, P. Zoller, and C.W. Gardiner. Monte Carlo simulation of master equations in quantum optics for vacuum, thermal, and squeezed reservoirs. *Phys. Rev. A*, 46(7):4382–4396, 1992.

[164] C. Mejia-Monasterio and H. Wichterich. Heat transport in quantum spin chains. *The European Physical Journal-Special Topics*, 151(1):113–125, 2007.

[165] M. Michel, O. Hess, H. Wichterich, and J. Gemmer. Transport in open spin chains: A Monte Carlo wave-function approach. *Phys. Rev. B*, 77(10):104303, 2008.

[166] A.J. Daley, J.M. Taylor, S. Diehl, M. Baranov, and P. Zoller. Atomic three-body loss as a dynamical three-body interaction. *Physical review letters*, 102(4):40402, 2009.

[167] M.A. Nielsen and I.L. Chuang. *Quantum computation and quantum information*. Cambridge university press, 2010.

[168] M. Suzuki. Fractal decomposition of exponential operators with applications to many-body theories and monte carlo simulations. *Physics Letters A*, 146(6):319–323, 1990.

[169] S.R. White et al. Density matrix formulation for quantum renormalization groups. *Physical Review Letters*, 69(19):2863–2866, 1992.

[170] S.R. White. Density-matrix algorithms for quantum renormalization groups. *Physical Review B*, 48(14):10345, 1993.

[171] U. Schollwöck. The density-matrix renormalization group. *Rev. Mod. Phys.*, 77(1):259–315, 2005.

[172] M. Zwolak and G. Vidal. Mixed-state dynamics in one-dimensional quantum lattice systems: a time-dependent superoperator renormalization algorithm. *Physical review letters*, 93(20):207205, 2004.

[173] F. Verstraete, J.J. Garcia-Ripoll, and J.I. Cirac. Matrix product density operators: simulation of finite-temperature and dissipative systems. *Physical review letters*, 93(20):207204, 2004.

[174] R. Orus and G. Vidal. Infinite time-evolving block decimation algorithm beyond unitary evolution. *Physical Review B*, 78(15):155117, 2008.

[175] S. Diehl, A. Micheli, A. Kantian, B. Kraus, HP Büchler, and P. Zoller. Quantum states and phases in driven open quantum systems with cold atoms. *Nature Physics*, 4(11):878–883, 2008.

[176] S. Diehl, A. Tomadin, A. Micheli, R. Fazio, and P. Zoller. Dynamical Phase Transitions and Instabilities in Open Atomic Many-Body Systems. *Phys. Rev. Lett.*, 105(1):15702, 2010.

[177] A. Tomadin, S. Diehl, and P. Zoller. Nonequilibrium phase diagram of a driven and dissipative many-body system. *Phys. Rev. A*, 83(1):13611, 2011.

[178] F. Nissen, S. Schmidt, M. Biondi, G. Blatter, H.E. Türeci, and J. Keeling. Nonequilibrium dynamics of coupled qubit-cavity arrays. *Physical Review Letters*, 108(23):233603, 2012.

[179] T. Hümmer, G.M. Reuther, P. Hänggi, and D. Zueco. Nonequilibrium phases in hybrid arrays with flux qubits and nitrogen-vacancy centers. *Physical Review A*, 85(5):052320, 2012.

[180] D. Jaksch and P. Zoller. The cold atom Hubbard toolbox. *Annals of Physics*, 315(1):52–79, 2005.

[181] M. Lewenstein, A. Sanpera, V. Ahufinger, B. Damski, A. Sen, and U. Sen. Ultracold atomic gases in optical lattices: mimicking condensed matter physics and beyond. *Adv. Phys.*, 56:243–279, 2007.

[182] M.A. Armen and H. Mabuchi. Low-lying bifurcations in cavity quantum electrodynamics. *Phys. Rev. A*, 73(6):63801, 2006.

[183] M. Armen. Bifurcations in single atom cavity QED. 2009.

[184] M. Notomi. Manipulating light with strongly modulated photonic crystals. *Reports on progress in physics*, 73(9):096501, 2010.

[185] M. Girardeau. Relationship between Systems of Impenetrable Bosons and Fermions in One Dimension. *J. Math. Phys.*, 1(6):516, 1960.

[186] J. Javanainen, O. Odong, and J.C. Sanders. Dimer of two bosons in a one-dimensional optical lattice. *Phys. Rev. A*, 81(4):043609, 2010.

[187] A. Le Boité, G. Orso, and C. Ciuti. Steady-state phases and tunneling-induced instabilities in the driven dissipative bose-hubbard model. *Physical Review Letters*, 110(23):233601, 2013.

[188] P. Glendinning. *Stability, instability and chaos: an introduction to the theory of nonlinear differential equations*. Cambridge university press, 1994.

[189] J.J. García-Ripoll. Time evolution of matrix product states. *New Journal of Physics*, 8(12):305, 2006.

[190] A. Tomadin, V. Giovannetti, R. Fazio, D. Gerace, I. Carusotto, H.E. Türeci, and A. Imamoglu. Signatures of the superfluid-insulator phase transition in laser-driven dissipative nonlinear cavity arrays. *Physical Review A*, 81(6):061801, 2010.

[191] R.S. Bennink, S.J. Bentley, and R.W. Boyd. two-photon coincidence imaging with a classical source. *Physical review letters*, 89(11):113601, 2002.

[192] M.I. Kolobov. *Quantum Imaging*. Springer, 2007.

[193] T.B. Pittman, Y.H. Shih, D.V. Strekalov, and A.V. Sergienko. Optical imaging by means of two-photon quantum entanglement. *Physical Review A*, 52(5):3429–3432, 1995.

[194] A. Peruzzo, M. Lobino, J.C.F. Matthews, N. Matsuda, A. Politi, K. Poulios, X.Q. Zhou, Y. Lahini, N. Ismail, K. Wörhoff, et al. Quantum walks of correlated photons. *Science*, 329(5998):1500–1503, 2010.

[195] Y. Bromberg, Y. Lahini, R. Morandotti, and Y. Silberberg. Quantum and classical correlations in waveguide lattices. *Physical review letters*, 102(25):253904, 2009.

[196] A. Majumdar, A. Rundquist, M. Bajcsy, V. D. Dasika, S.R. Bank, and J. Vučković. Design and analysis of photonic crystal coupled cavity arrays for quantum simulation. *Phys. Rev. B*, 86(19):195312, 2012.

[197] A.C. Scott, J.C. Eilbeck, and H. Gilhøj. Quantum lattice solitons. *Physica D: Nonlinear Phenomena*, 78(3):194–213, 1994.

[198] V. Fleurov, R. Schilling, and S. Flach. Tunneling of a quantum breather in a one-dimensional chain. *Physical Review E*, 58(1):339, 1998.

[199] S. Aubry, S. Flach, K. Kladko, and E. Olbrich. Manifestation of classical bifurcation in the spectrum of the integrable quantum dimer. *Physical review letters*, 76(10):1607–1610, 1996.

[200] G. Kalosakas and A.R. Bishop. Small-tunneling-amplitude boson-hubbard dimer: Stationary states. *Physical Review A*, 65(4):043616, 2002.

[201] K. Winkler, G. Thalhammer, F. Lang, R. Grimm, J.H. Denschlag, A.J. Daley, A. Kantian, H.P. Büchler, and P. Zoller. Repulsively bound atom pairs in an optical lattice. *Nature*, 441(7095):853–856, 2006.

[202] P. Maniadis and S. Flach. Mechanism of discrete breather excitation in driven micro-mechanical cantilever arrays. *EPL (Europhysics Letters)*, 74(3):452, 2007.

[203] D. Zueco, P.J. Martínez, L.M. Floría, and F. Falo. Mode-locking of mobile discrete breathers. *Physical Review E*, 71(3):036613, 2005.

[204] S.R. White and A.E. Feiguin. Real-time evolution using the density matrix renormalization group. *Phys. Rev. Lett.*, 93(7):76401, 2004.

[205] M. Leib and M.J. Hartmann. Bose–hubbard dynamics of polaritons in a chain of circuit quantum electrodynamics cavities. *New Journal of Physics*, 12(9):093031, 2010.

[206] M.J. Hartmann and M.B. Plenio. Migration of bosonic particles across a Mott insulator to a superfluid phase interface. *Phys. Rev. Lett.*, 100(7):70602, 2008.

[207] G. Benenti, G. Casati, T. Prosen, and D. Rossini. Negative differential conductivity in far-from-equilibrium quantum spin chains. *EPL (Europhysics Letters)*, 85(3):37001, 2009.

[208] J. Majer, J.M. Chow, J.M. Gambetta, J. Koch, B.R. Johnson, J.A. Schreier, L. Frunzio, D.I. Schuster, A.A. Houck, A. Wallraff, et al. Coupling superconducting qubits via a cavity bus. *Nature*, 449(7161):443–447, 2007.

[209] D.I. Schuster, A.A. Houck, J.A. Schreier, A. Wallraff, J.M. Gambetta, A. Blais, L. Frunzio, J. Majer, B. Johnson, M.H. Devoret, et al. Resolving photon number states in a superconducting circuit. *Nature*, 445(7127):515–518, 2007.

[210] C.E. Bardyn and A. Imamoğlu. Supplementary material of 'majorana-like modes of light in a one-dimensional array of nonlinear cavities'. *Physical review letters*, 109(25):253606, 2012.

[211] A.Y. Kitaev. Unpaired majorana fermions in quantum wires. *Physics-Uspekhi*, 44(10S):131, 2001.

[212] C. Nayak, S.H. Simon, A. Stern, M. Freedman, and S.D. Sarma. Non-abelian anyons and topological quantum computation. *Reviews of Modern Physics*, 80(3):1083, 2008.

[213] E.G. Dalla Torre, E. Berg, and E. Altman. Hidden order in 1d bose insulators. *Physical review letters*, 97(26):260401, 2006.

[214] H. Li and F. D. M. Haldane. Entanglement spectrum as a generalization of entanglement entropy: Identification of topological order in non-abelian fractional quantum hall effect states. *Physical review letters*, 101(1):010504, 2008.

[215] F. Pollmann, A.M. Turner, E. Berg, and M. Oshikawa. Entanglement spectrum of a topological phase in one dimension. *Physical Review B*, 81(6):064439, 2010.

[216] X. Deng and L. Santos. Entanglement spectrum of one-dimensional extended bose-hubbard models. *Physical Review B*, 84(8):085138, 2011.

[217] E. Berg, E.G. Dalla Torre, T. Giamarchi, and E. Altman. Rise and fall of hidden string order of lattice bosons. *Physical Review B*, 77(24):245119, 2008.

[218] R. Rossini, M. Gibertini, V. Giovannetti, and R. Fazio. Topological pumping in the one-dimensional bose-hubbard model. *Physical Review B*, 87(8):085131, 2013.

[219] M. Levin and X.G. Wen. Detecting topological order in a ground state wave function. *Physical review letters*, 96(11):110405, 2006.

[220] A. Kitaev and J. Preskill. Topological entanglement entropy. *Physical review letters*, 96(11):110404, 2006.

[221] D.E. Chang, V. Gritsev, G Morigi, V. Vuletic, M.D. Lukin, and E.A. Demler. Crystallization of strongly interacting photons in a nonlinear optical fibre. *Nature Physics*, 4(11):884–889, 2008.

[222] C.W. Gardiner and M.J. Collett. Input and output in damped quantum systems: Quantum stochastic differential equations and the master equation. *Phys. Rev. A*, 31:3761–3774, Jun 1985.

[223] S. Fan, E.K. Kocabaş, Şükrü, and J.T. Shen. Input-output formalism for few-photon transport in one-dimensional nanophotonic waveguides coupled to a qubit. *Physical Review A*, 82(6):063821, 2010.

[224] E. Rephaeli and S. Fan. Few-photon single-atom cavity qed with input-output formalism in fock-space. 2012.

[225] J. Eisert, M. Cramer, and M.B. Plenio. Colloquium: Area laws for the entanglement entropy. *Reviews of Modern Physics*, 82(1):277, 2010.

[226] F. Verstraete and J.I. Cirac. Matrix product states represent ground states faithfully. *Physical Review B*, 73(9):094423, 2006.

[227] D. Gobert, C. Kollath, U. Schollwöck, and G. Schütz. Real-time dynamics in spin-1/2 chains with adaptive time-dependent density matrix renormalization group. *Physical Review E*, 71(3):036102, 2005.

[228] T.H. Johnson, S.R. Clark, and D. Jaksch. Dynamical simulations of classical stochastic systems using matrix product states. *Physical Review E*, 82(3):036702, 2010.